Towards Trustworthy Machine Learning Models in Vision, Physics, and Language Applications

Francisco Girbal Eiras

Linacre College
University of Oxford

A thesis submitted for the degree of
Doctor of Philosophy

Trinity Term 2024

Abstract

The wide-ranging impact of machine learning, particularly deep neural networks, cannot be overstated. These highly capable models are now deployed in critical domains such as autonomous driving, medical diagnosis, finance, and manufacturing. While their adoption is driven by superior performance on benchmark tasks, their data-driven nature often renders them unpredictable when encountering non-standard inputs. This unpredictability poses a significant challenge in safety-critical applications, where interactions with humans or the potential for system failures could lead to severe consequences. This underscores the need for *trustworthy machine learning*, where models must not only excel in standard metrics but also prove to be reliable and robust in real-world settings.

Our work addresses this need by improving methods that aim to either *certify* the robustness of these systems or, at a minimum, provide strong *empirical evaluations of robustness and safety* to support responsible deployment. We present advancements in probabilistic certification for image classification via randomized smoothing, introduce a general framework for verifying the partial derivatives of neural networks, which has applications in certifying the correctness of physics-informed neural networks, and analyse the safety risks involved in fine-tuning large language models on task-specific data, along with mitigation strategies. Additionally, we explore the broader implications of open-source generative AI models for improving trustworthiness. These contributions mark a step forward in developing trustworthy machine learning systems, and we conclude by discussing their strengths, limitations, as well as key open questions that remain for the field.

Towards Trustworthy Machine Learning Models in Vision, Physics, and Language Applications

Francisco Girbal Eiras

Linacre College

University of Oxford

A thesis submitted for the degree of

Doctor of Philosophy

Trinity Term 2024

Acknowledgements

In the final year of my DPhil, I found myself drawn to the works of Kurt Vonnegut, particularly his concept of the *karass* in *Cat's Cradle*——a group of people cosmically bound together, often unknowingly, to accomplish a shared purpose. Reflecting on this idea, I realize how many people have been part of my own karass throughout this journey. While they may not have known it at the time, each has played a crucial role in helping me reach this point, and for that, I am deeply grateful.

My DPhil journey would have been impossible without the guidance and encouragement of my supervisors and mentors. First, I am deeply thankful to M. Pawan Kumar, who believed in me from the beginning and helped me get started with my PhD. Even after transitioning to DeepMind, Pawan continued to provide guidance and insightful feedback across all my projects, always offering invaluable advice. He taught me perhaps the simplest yet most important lesson that I will take away from my DPhil: to do impactful research, start from an important problem and work towards a methodology that solves it, not the other way around. I am also incredibly grateful to Philip Torr, who, despite his busy schedule, always made time to share his wisdom and offer mentoring. Our lunches at Catz will remain a memorable source of inspiration. I must also thank my co-supervisor, Adel Bibi, whose consistent presence throughout my projects was a cornerstone of my progress. His feedback, endless discussions, and readiness to help whenever I hit a wall were essential to my growth. Though not officially my supervisor, Puneet K. Dokania's mentorship and guidance during my internships at FiveAI was indispensable, and I greatly appreciate his support. I would also like to thank Alessandro Abate and Niki Trigoni for their constructive comments during my transfer and confirmation vivas. Lastly, I am particularly grateful to Pedro Miraldo for encouraging me to apply to Oxford——first for my master's, and later for this DPhil. None of this would have been possible without his input and advice.

Another crucial factor that made my DPhil possible was the financial support from FiveAI. I would like to extend my heartfelt thanks to Stan Boland and Subramanian Ramamoorthy, who both believed in my potential and played a significant role in turning my PhD aspirations into reality.

I had the pleasure of working alongside a range of exceptionally talented individuals at TVG and AIMS, making my time in the office truly enjoyable.

I will particularly miss my discussions with Aleksandar Petrov about how our work is saving the world, as well as my conversations with Sebastian Towers regarding the public service role of hedge funds in providing market liquidity. Additionally, engaging with fellow lab members such as Botos Csabi, Francesco Pinto, Jishnu Mukhoti, Tim Franzmeyer, Alisdair Paren, Fabio Pizzati, among others, proved to be both informative and uplifting (often both). I would also like to highlight the invaluable role of Wendy Poole, whose efforts ensured that equipment, conferences, and AIMS events ran smoothly. Her availability and constant willingness to help were crucial to the success of my DPhil.

One of the things that made Oxford a great place to be was the friends I made. I am extremely grateful to my *"old"* Linacre friends, who were there during my first year, mostly spent at home due to COVID, but punctuated by our occasional get-togethers that kept us sane. A special mention goes to Poppy Brown, not only a top-tier landlady but also the most compassionate, understanding, and fun friend anyone could ask for. I'd be remiss not to acknowledge the rest of our household: Alister Burt, Gnocchi, and Max——who made Oxford truly feel like home. I also want to thank my *"newer"* Oxford and Linacre friends, who made the last couple of years of my DPhil much more enjoyable. While there are too many to name, a special shoutout goes to my fellow organizers, Sophie Gray and Elisa Martin Perez, whose efforts were instrumental in making Linacre Ball 2024 a tremendous success; they were always there to provide support, advice, and a good laugh. Gus Anderson and Martin Wafula also played a crucial role in helping me discover a more fun side of Oxford. Finally, I am grateful to my *"really old"* friends from "A Outra Cuechi," who through escape rooms, board games and travel have supported me throughout this journey. I know I can always count on them; they are truly friends for life.

I cannot conclude this section without thanking the most important people in my life: my family, who have shaped me into who I am today. My sister, Constança, has always been a steadfast source of support and inspiration; her dedication to her passions serving as a constant reminder of what it means to pursue one's dreams. My dad, António, has helped me grow with kindness and encouragement, always urging me to find my own path while striving to be the best version of myself. Graça has always been incredibly welcoming and understanding, and Zé Pedro, Diogo, and Afonso are beautiful reminders of the bright future that lies ahead. Finally, my mom, Ana, who is my ultimate role model: an unwavering example of hard work and determination, and undoubtedly my greatest supporter. I love them all more than words can express and none of my accomplishments would have been possible without them.

Abstract

The wide-ranging impact of machine learning, particularly deep neural networks, cannot be overstated. These highly capable models are now deployed in critical domains such as autonomous driving, medical diagnosis, finance, and manufacturing. While their adoption is driven by superior performance on benchmark tasks, their data-driven nature often renders them unpredictable when encountering non-standard inputs. This unpredictability poses a significant challenge in safety-critical applications, where interactions with humans or the potential for system failures could lead to severe consequences. This underscores the need for *trustworthy machine learning*, where models must not only excel in standard metrics but also prove to be reliable and robust in real-world settings.

Our work addresses this need by improving methods that aim to either *certify* the robustness of these systems or, at a minimum, provide strong *empirical evaluations of robustness and safety* to support responsible deployment. We present advancements in probabilistic certification for image classification via randomized smoothing, introduce a general framework for verifying the partial derivatives of neural networks, which has applications in certifying the correctness of physics-informed neural networks, and analyse the safety risks involved in fine-tuning large language models on task-specific data, along with mitigation strategies. Additionally, we explore the broader implications of open-source generative AI models for improving trustworthiness. These contributions mark a step forward in developing trustworthy machine learning systems, and we conclude by discussing their strengths, limitations, as well as key open questions that remain for the field.

Contents

1 Introduction

Contents

1.1 The Rise of Deep Neural Networks in Machine Learning

Humans have systematically relied on computers to execute tasks for the better part of a century. Early computers were designed to perform simple arithmetic operations, but as technology evolved, so did the complexity of these machines. What began as simple calculators gradually transformed into versatile, general-purpose devices. Modern computers now include at least one processing element——a Central Processing Unit (CPU)——enabling them to handle sophisticated sets of instructions. Within this paradigm, humans control computers by writing programs that are executed by the CPU, a process known as *classical computing*.

While this has been the dominant paradigm for several decades, the idea of *self-teaching computers*, or *machines that learn*, has intrigued researchers since the early days of the discipline. Alan Turing first proposed this concept in his seminal paper, *Computing Machinery and Intelligence* [Turing, 1950]. In it, Turing introduced the idea of a machine that could learn from experience, suggesting this could be achieved by training it to imitate human responses to questions. This idea was further developed by Frank Rosenblatt in the 1950s through the *perceptron* [Rosenblatt, 1958]. The perceptron was a binary classification model trained using a simple learning rule that adjusted the model's weights based on the error it made in its predictions. It became the first example of a *neural network* (NN), a class of *machine learning* (ML) models inspired by the human brain and designed to learn from data.

In the following decades, significant advances in neural networks emerged, including the development of the backpropagation algorithm [Rumelhart et al., 1986] and convolutional neural networks (CNNs) [Fukushima, 1980, LeCun et al., 1998]. These innovations enabled the training of deeper networks, greatly expanding their potential applications. However, despite these advancements, neural networks were not widely adopted in practice for many years. This was largely due to the difficulty of training them effectively, as well as the success of other machine learning techniques. Methods such as Support Vector Machines (SVMs) [Cortes, 1995], Decision Trees [Quinlan, 1986], and Random Forests [Breiman, 2001] often yielded better performance in practical applications, leading to their broader use in the field.

Recent breakthroughs in neural networks can be largely attributed to two pivotal advancements: the scalability of both data and computational power. The availability of vast datasets, such as ImageNet [Deng et al., 2009] and C4 [Raffel et al., 2020], has eliminated the need for manual feature engineering, allowing neural networks to learn directly from raw data via differentiable loss functions. This paradigm shift was made feasible by the advent of highly efficient Graphics Processing Units (GPUs), which enable the training of large models on extensive datasets within practical timeframes. These innovations have given rise to *deep*

neural networks (DNNs)—architectures with numerous layers and up to trillions of parameters—that consistently surpass traditional machine learning techniques across a wide range of tasks.

As a result, neural network-based machine learning has become the de facto standard across a broad spectrum of applications. In the field of computer vision, neural networks have been successfully applied to tasks such as handwritten digit recognition [LeCun et al., 1998], image classification [Krizhevsky et al., 2012], object detection [Ren, 2015], image segmentation [Long et al., 2015], among many others. Within natural language processing, these models have revolutionized tasks like machine translation [Wu, 2016] and sentiment analysis [Socher et al., 2013]. In the domain of games, neural network-based approaches have achieved superhuman performance at games such as chess [Silver et al., 2018] and Go [Silver et al., 2017]. Machine learning has also proved transformative in scientific domains, contributing to breakthroughs in protein folding [Senior et al., 2020], drug discovery [Kim et al., 2021], and climate modelling [Lam et al., 2022]. Beyond these areas, neural networks have found extensive use in medical diagnosis [Esteva et al., 2017, Shehab et al., 2022], the financial sector [Rundo et al., 2019], and self-driving vehicles [Chib and Singh, 2023, Pulver et al., 2021].

1.2 Trustworthy Machine Learning

This pure data-driven approach has proved invaluable to the state-of-the-art performance achieved by deep neural networks in the tasks mentioned above. However, it also comes with significant drawbacks. Feature-based machine learning methods such as decision trees are often considered interpretable, as their predictions can be traced back to the features activated in the model [Quinlan, 1986]. In contrast, the output of a deep neural network is the result of applying complex, nonlinear functions to the input using parameters that were learnt from data. This makes it difficult to understand why a neural network makes a particular prediction, and it forms the reason why they are often referred to as *black-box* models [Buhrmester et al., 2019].

Consequently, while these models can achieve superhuman performance under certain test conditions, they can also behave unpredictably when presented with valid inputs that fall outside the training data distribution. This unpredictability can be a significant concern in different applications.

Safety in Human Interaction. Applications in healthcare (e.g., automatic diagnosis systems) and autonomous driving are classic examples of *safety-critical* systems, where a model's predictions can have direct and potentially life-threatening consequences. For instance, an incorrect decision made by a self-driving car could result in a fatal accident, while a misdiagnosis from an automatic healthcare system could lead to inappropriate treatment. Beyond these safety-critical scenarios, many other machine learning systems interact directly with humans in ways that can significantly impact their lives. For example, a mental health chatbot designed to provide support could inadvertently produce harmful responses under certain conditions, leading to severe negative consequences for the user.

Correctness of Machine Learning Systems. In many systems, machine learning models are used to replace experts or speed-up processes. For example, *neural operators* are neural network-based models that approximate the solutions of differential equations [Lu et al., 2021]. These classes of models are used in scientific simulations, where they can be orders of magnitude faster than traditional numerical methods [Takamoto et al., 2022]. For real-world deployment, it is crucial these models are robust and reliable. While they may not be safety-critical, vulnerabilities in such systems can have significant impacts on overall performance. For instance, a non-robust DNN-based physics simulator could introduce manufacturing defects in production pieces [Pinto et al., 2017, Lütjens et al., 2020], resulting in large financial losses.

These two key settings justify the need for *trustworthy machine learning*, *i.e.* trained networks that are not only accurate under standard evaluation metrics, but that can also be shown to be reliable and robust. As highlighted in Figure 1.1, there

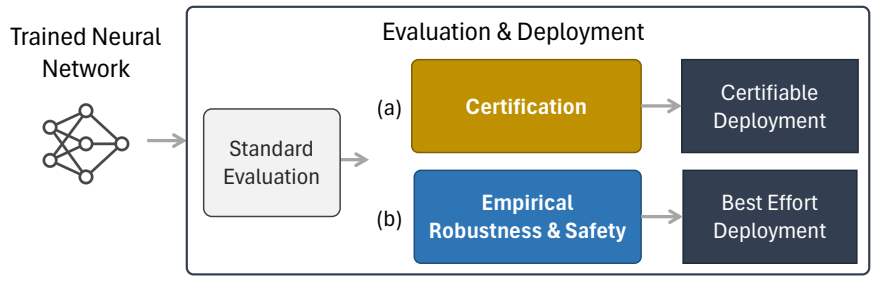

Figure 1.1: Trustworthy Machine Learning: depending on the type of network provided and guarantees required, (a) certification methods allow for a *certifiable deployment* of the model whereas (b) empirical robustness & safety methods give us only a *best-effort deployment*.

are two primary approaches to achieving this, each with its own set of trade-offs: *certification* (§1.2.1) and *empirical robustness & safety* (§1.2.2) methods.

1.2.1 The Gold Standard: Certifiable Machine Learning

Given a well-defined specification of desired behaviour, *certification* (or *verification*) methods aim to provide formal guarantees on the extent to which a model satisfies it. Ideally, these specifications would be defined over the entire applicability input domain of the model, but for practical reasons they are often defined over a subset of it.

For instance, in image classification tasks, certification methods can provide formal guarantees on a model's robustness against *adversarial attacks*—small, humanly imperceptible perturbations to images that can cause the model to incorrectly classify the input [Szegedy et al., 2014, Goodfellow et al., 2015]. These guarantees are typically defined within an ϵ-neighborhood of an input, measured using an ℓ_p norm, which indicates how resistant the model is to adversarial manipulations within that bounded region. While this is a relaxation of the ideal specification that the model should be robust to all possible imperceptible perturbations, it can still be useful in practice from a safety perspective and to ensure the correctness of the deployed system.

These guarantees can formally ensure that a model is sufficiently safe or robust to be deployed in applications that require trustworthy machine learning. As such, certification methods are often regarded as the gold standard for ensuring

model reliability. While they may not be applicable in every scenario, they provide significant value in settings where formal assurance of performance is critical.

Despite their advantages, certification methods face two major limitations. First, they are often constrained by model scale, as they tend to be either (i) computationally expensive (or even infeasible) due to the need to solve complex optimization problems [Bunel et al., 2018, Wong and Kolter, 2018], or (ii) offer diminishing returns in certification accuracy as model size increases [Cohen et al., 2019]. Some methods attempt to balance these trade-offs but still struggle with state-of-the-art large-scale models. Second, they are limited by the challenge of formally specifying desired behaviour in a way that is both meaningful and practical to certify. This is exemplified in the adversarial attack setting, where the local specification used for image classification offers only a partial solution [Szegedy et al., 2014, Madry et al., 2018]. These challenges highlight the need for *empirical robustness & safety* methods as a complementary approach.

1.2.2 Empirical Robustness & Safety for Best-Effort Deployment

Empirical robustness & safety methods aim to ensure model robustness and safety through empirical validation, typically by stress-testing models on adversarial or out-of-distribution test sets. Unlike certification methods, which rely on formal guarantees, empirical methods provide flexibility in defining the desired behaviour and are significantly more scalable, as they do not require solving complex optimization problems to *optimality*.

From a scalability perspective, if a formal specification is available, empirical methods can provide a lower bound on the satisfaction of that property, allowing for the identification of potential vulnerabilities by testing a model against specified conditions. While they may not guarantee robustness, they can reveal inputs where the model fails to meet the desired specifications [Goodfellow et al., 2015, Madry et al., 2018, Qi et al., 2023]. This makes them valuable for detecting weaknesses and offering a best-effort deployment in safety-critical scenarios. However, these

methods are inherently *unsound*, meaning that a failure to identify a vulnerability does not ensure the model will always satisfy the given specification.

Additionally, empirical methods are particularly useful when a formal specification is difficult or impossible to define. In image classification tasks, for instance, out-of-distribution detection methods can be used to identify inputs that are not natural images, and thus should not be classified by the model [Hendrycks and Gimpel, 2016, Lakshminarayanan et al., 2017]. Encoding this definition of out-of-distribution robustness in a specification is difficult, but empirically validating it can be useful for ensuring the correctness of the deployed system.

Generative AI models, such as large language models (LLMs) or diffusion models, which generate new data instead of discriminating between different types of data (*e.g.* image classification, object detection), present additional challenges for defining safety specifications. The inputs to these models are often arbitrary-length sequences of tokens, and the output is obtained by sampling them autoregressively, making it difficult to define correct behaviour. For instance, an LLM might generate harmful text in some contexts, but in others, similar language could be entirely appropriate (e.g., "shoot" in a photography question versus a harmful context) [Röttger et al., 2023]. Formalizing these nuances is a complex task, but empirical testing can still help evaluate and mitigate risks.

Thus, while certification offers the gold standard in trustworthy machine learning, empirical methods provide a scalable and flexible alternative. These approaches can help ensure robustness and safety in scenarios where formal certification is either infeasible or overly restrictive, enabling more practical deployments in real-world applications.

1.3 Thesis Contributions and Outline

The overarching goal of this dissertation is to develop efficient methods that improve both *certification* and *empirical robustness & safety* approaches (as depicted in Figure 1.1) to achieve trustworthy deployment of machine learning models with

applications in the vision, physics and language domains. This thesis is centred on the following main contributions:

C1. Design scalable neural network *certification* techniques applicable in safety-critical domains such as adversarial robustness in image classification and other fields requiring verification (e.g., physics-informed machine learning).

C2. Study and improve methods for evaluating and enhancing *empirical robustness & safety*, particularly in large-scale systems such as large language models.

To accomplish this, the main chapters of the thesis are structured as follows:

We generalize probabilistic guarantees achieved via randomized smoothing to the anisotropic setting (Chapter 3). Randomized smoothing is a popular probabilistic certification technique that builds classifiers that are inherently robust to adversarial perturbations [Cohen et al., 2019]. Prior research has primarily focused on providing isotropic certificates for ℓ_p-norm neighbourhoods, yet these focus simply on the *worst-case* setting and fail to reason about other "close", potentially large, constant safe regions. In this chapter, we use a generalized Lipschitz analysis to extend randomized smoothing ℓ_1 and ℓ_2 certificates to an *anisotropic* setting, demonstrating that these certificates cover significantly larger regions than their isotropic counterparts. This work contributes to **C1** and was published in TMLR [Eiras et al., 2022].

We efficiently extend deterministic verification techniques to novel domains with different specifications (Chapter 4). Physics-Informed Neural Networks (PINNs) are powerful models that approximate solutions to partial differential equations [Raissi et al., 2019]. However, previous works have failed to provide guarantees on the worst-case residual error of a PINN across the spatio-temporal domain—a measure akin to the tolerance of numerical solvers—focusing instead on point-wise comparisons between their solution and the ones obtained by a solver on a set of inputs. Our work alleviates this issue by introducing ∂-CROWN, a

general, efficient and scalable verification method that provides worst-case guarantees on the residual error of a PINN across the spatio-temporal domain. This work advances the **C1** contribution, and was accepted to ICML 2024 [Eiras et al., 2024].

We propose new methods to evaluate and mitigate safety risks that arise from fine-tuning large language models on task-specific data (Chapter 5). Recent research shows that fine-tuning on benign instruction-following data can inadvertently undo the safety alignment process and increase a model's propensity to comply with harmful queries. While instruction-following fine-tuning is important, task-specific fine-tuning—where models are trained on datasets with clear ground truth answers (e.g., multiple choice questions)—can enhance model performance on specialized downstream tasks. Understanding and mitigating safety risks in the task-specific setting remains distinct from the instruction-following context due to structural differences in the data. We empirically show that malicious actors can subtly manipulate the structure of almost *any* task-specific dataset to foster significantly more dangerous model behaviours, while maintaining an appearance of innocuity and reasonable downstream task performance. To address this safety issue efficiently and effectively, we propose a novel mitigation strategy that mixes in safety data which *mimics* the task format and prompting style of the user data. This contribution addresses **C2**, and was presented at the Next Generation of AI Safety workshop at ICML 2024, and will be published at ICLR 2025 [Eiras et al., 2025].

In addition to these core contributions, we also explore transparency in machine learning through the lens of open-source generative AI models. While open-source models promote transparency by enabling inspection of their architecture and parameters, they also raise concerns about potential misuse. In Chapter 6, we argue that the benefits of open-source models outweigh the risks and propose responsible public release strategies. This position paper was accepted for oral presentation at ICML 2024 [Eiras et al., 2024], contributing to the broader conversation on AI responsibility and transparency.

1.3.1 Additional Contributions

Beyond the main contributions, my DPhil work has touched on several other projects in trustworthy and efficient machine learning. For instance, Petrov et al. [2023] extended the Lipschitz analysis from Eiras et al. [2022] to the non-symmetric cases using the generalized concept of $\mathcal{S}$-Lipschitzness; while Lamb et al. [2023] proposed a novel metric of faithfulness of knowledge distillation based on the notion of disagreement between the student and teacher networks. On the efficient machine learning side, Eiras et al. [2024] advances the state-of-the-art performance of referring image segmentation in the zero-shot and weakly-supervised settings.

2
Literature Review

Contents

This chapter aims to provide an overarching review of the literature relevant to the specific aspects of trustworthy machine learning explored in this dissertation. Given the broad scope of the field, we focus on two key dimensions: robustness and safety. We begin by outlining how these concepts are defined in previous research (§2.1). Next, we examine various *certification* methods that have been developed to assess and ensure the robustness and safety of neural networks (§2.2). Finally, we review the *empirical robustness & safety* approaches used to evaluate these properties in practice (§2.3). Each main thesis chapter contains a dedicated section on related work, offering more detailed and specific discussions relevant

to the individual contributions of that project.

2.1 Defining Robustness in Machine Learning

At a high level, a machine learning system is considered *robust* if it can maintain stable and consistent performance——within a specified *tolerance*——when subjected to input perturbations defined by the robustness *domain* [Freiesleben and Grote, 2023, Braiek and Khomh, 2024]. Formally, let $\mathbf{x}$ represent the input to a neural network f, $\mathcal{D}$ the robustness domain, and α the tolerance level. A model f is robust if it satisfies the property:

$$\forall \mathbf{x}, \mathbf{x}' \in \mathcal{D} \quad \text{it holds that} \quad d(f(\mathbf{x}), f(\mathbf{x}')) \leq \alpha, \tag{2.1}$$

where d is a distance metric.

However, this general property is difficult to operationalize, as it requires defining the robustness domain $\mathcal{D}$, the distance metric d, and an appropriate tolerance level α. Moreover, naive interpretations of this definition may lead to undesirable outcomes. For example, in binary image classification, a constant prediction neural network f would satisfy the robustness condition for any domain $\mathcal{D}$ that includes all images and any norm-based distance metric d. Yet, such a model would be practically useless, as it would fail to differentiate between the two classes, resulting in poor generalization performance.

To address these challenges, previous literature introduces more specific definitions of robustness, better aligned with the objectives of machine learning systems. In image classification, Szegedy et al. [2014] introduced the concept of *adversarial robustness*, while in the context of large language models, the notion of *alignment* is now commonly used.

2.1.1 Adversarial Robustness in Image Classification

In the context of image classification, adversarial robustness refers to a specific form of robustness that addresses local perturbations known as *adversarial examples*. These examples are small "imperceptible" (to the human eye) modifications of

an input image that are designed to mislead the model into making incorrect predictions [Szegedy et al., 2014, Goodfellow et al., 2015]. Formally, given an input image $\mathbf{x}$ and a neural network f, an adversarial example $\mathbf{x}'$ is generated by solving the following optimization problem:

$$\arg\max_{\mathbf{x}' \in \Delta(\mathbf{x})} \ell_{\text{adv}}\left(f(\mathbf{x}'), \hat{y}\right), \tag{2.2}$$

where $\hat{y}$ is the predicted class, $\hat{y} = \arg\max_c f^c(\mathbf{x})$, or the ground truth label at $\mathbf{x}$, ℓ_{adv} represents an adversarial loss function, and $\Delta(\mathbf{x})$ is the set of perturbations within a certain distance $\epsilon > 0$ of the original image $\mathbf{x}$, typically defined using an ℓ_p-norm: $\Delta(\mathbf{x}) = \{\mathbf{x}' : |\mathbf{x} - \mathbf{x}'|p \leq \epsilon\}$. To ensure the perturbation remains imperceptible, ϵ is usually kept small, e.g., $\epsilon = 8/255$ for the ℓ_∞-norm in CIFAR-10 and CIFAR-100 [Croce et al., 2020]. Solving this optimization problem is non-trivial due to the non-convexity of the adversarial loss landscape [Szegedy et al., 2014]. The various methods developed to address this challenge empirically are collectively known as *adversarial attacks*, and we explore their extensive literature in §2.3.

In terms of the general robustness definition in Equation 2.1, adversarial robustness can be represented by considering a set of *local* domains $\mathcal{D}$ around each input $\mathbf{x}$ of a test dataset, constrained within a certain distance ϵ from the original image. Specifically, $\mathcal{D}_{\text{adv}}(\mathbf{x}) = \{\mathbf{x}' : \|\mathbf{x} - \mathbf{x}'\|_p \leq \epsilon\}$ for some ℓ_p-norm and $\epsilon > 0$. Given the predicted label $\hat{y} = \arg\max_c f^c(\mathbf{x})$, the distance metric d can be defined as the output value of the correct class, $d(f(\mathbf{x}), f(\mathbf{x}')) = f^{\hat{y}}(\mathbf{x}')$ with a threshold $\alpha = 0.5$ (or the minimum threshold required to ensure a correct prediction). Note that due to its local nature, this robustness property is defined over a test dataset with benchmarks often reporting the percentage of the dataset that satisfies it [Croce et al., 2020]. This is the standard specification used in the certification and verification literature, which we discuss in detail in §2.2.

2.1.2 Alignment Robustness and Safety in Large Language Models

In generative machine learning, robustness is more challenging to define than in discriminative models. This difficulty arises from the lack of a clear way to formalize

the robustness domain $\mathcal{D}$ and distance metric d in this context. For example, in large language models (LLMs), even small changes in the input can result in meaningful and desirable changes in the output. A simple alteration like changing the word "not" in a sentence can completely reverse its meaning and thus expected output, making adversarial robustness (as defined in §2.1.1) unsuitable for these models.

Instead, the empirical concept of *alignment* has been introduced as a form of robustness for LLMs [Amodei et al., 2016, Christiano et al., 2018]. Alignment refers to the degree of agreement between the model's outputs and a set of desirable human values, which are typically encoded in the data used for supervised fine-tuning [Ouyang et al., 2022, Bai et al., 2022, Rafailov et al., 2023]. A key goal of alignment is to implement *safety* guardrails—such as refusing to respond to harmful or inappropriate queries—to prevent the misuse of models [Bai et al., 2022]. Importantly, alignment should be robust to semantically irrelevant input perturbations, which are often assessed through empirical evaluations on sets of human-specified prompts and automatically generated variations [Perez et al., 2022, Zou et al., 2023]. Although this high-level specification of alignment does not lend itself to a formal definition of robustness, it serves as a valuable framework for guiding the empirical evaluation of large language models, a topic we explore further in §2.3.2.

2.2 Certification/Verification of Neural Networks

The problem of certifying or verifying neural networks is broad, but a significant portion of the literature in this area focuses on variations of adversarial robustness as discussed in §2.1.1. Certification methods aim to determine whether a given property or specification holds true for a model. Broadly, such methods can be classified into two categories based on their *soundness*: those that provide deterministic guarantees of correctness, and those where failure cases may occur. In this section, we review both types of approaches. We review these two categories in this section.

2.2.1 Unsound Certification Methods

Unsound certification methods do not offer a deterministic guarantee that the certificates they produce are correct. While typically more scalable and easier to implement than sound methods, they may, under certain conditions, fail to verify a specification, leading to potential counterexamples. However, to be classified as certification methods rather than empirical ones (see §2.3), the approaches in this category must provide some form of guarantee (*i.e.* certificate) on the estimate of the satisfaction of the specification, even if it is *probabilistic* rather than deterministic.

Several techniques estimate the local Lipschitz constant of the network around the input to provide probabilistic bounds on the verification of the output specification [Weng et al., 2018, Ko et al., 2019]. For instance, Alsubaihi et al. [2019] present bounds that improve upon those from Interval Bound Propagation (IBP) [Gowal et al., 2019] (a sound method), but their bounds hold only in expectation. Similarly, Webb et al. [2018] use multi-level splitting, a Monte Carlo-based approach for rare event estimation, to provide a probabilistic bound on the output specification. Various other probabilistic methods also fall into this category [Wong et al., 2018].

Of particular relevance to this thesis are recent methods based on *randomized smoothing*. This technique constructs a smooth classifier by adding noise to the input and then taking the majority vote of the classifier's predictions on these noisy samples as the output [Lecuyer et al., 2019]. By construction, the expectation-based smooth classifier is Lipschitz continuous, allowing tight probabilistic bounds on robustness to be derived for different types of smoothing noise [Cohen et al., 2019, Salman et al., 2019, Yang et al., 2020, Eiras et al., 2022].

Although these methods are potentially practical, their lack of a deterministic guarantee can be a significant limitation, depending on the application. This limitation has motivated the development of sound certification methods, which we explore in the following section.

2.2.2 Sound Verification Methods

Sound certification methods provide a deterministic guarantee that the certificates they produce hold for all inputs within the specified domain. Though typically more computationally expensive than unsound methods, they offer stronger and more reliable guarantees [Gowal et al., 2019, Zhang et al., 2018]. These methods can be further categorized based on their *completeness* [Bunel et al., 2018, Cohen et al., 2019]. A method is deemed *complete* or *exact* if it guarantees certification for all true properties across any input—*i.e.* they will only certify a property as false if, and only if, that property is false. In contrast, *incomplete* or *conservative* methods may either abstain from providing a certificate for some inputs or issue certificates that over-approximate the specification, resulting in less tight guarantees. If an incomplete method fails to certify a property, that does not necessarily mean this property is false. Importantly, both types of certificates remain sound: they will certify a property as true only if it holds for all inputs within the defined domain.

Complete Methods

In the context of adversarial robustness, complete methods verify the exact robustness definition presented in §2.1.1. These methods cannot rely on over-approximations of the model, as they inherently guarantee tightness. As a result, complete verification methods typically employ *enumeration* to ensure exhaustive coverage of the search space. While a handful of methods use explicit enumeration, also known as full reachability-based techniques, by partitioning the input or activation space [Huang et al., 2017, Xiang et al., 2017], most rely on implicit enumeration strategies, such as Satisfiability Modulo Theory (SMT) solvers [Carlini and Wagner, 2017, Ehlers, 2017, Katz et al., 2017] or mixed integer programming (MIP) approaches [Lomuscio and Maganti, 2017, Cheng et al., 2017]. Bunel et al. [2018] provide a unifying framework that connects many of these previous methods under the umbrella of global optimization problems solvable via branch-and-bound techniques, inspired by MIP solvers.

Due to their exhaustive nature, these methods are computationally expensive—Katz et al. [2017] demonstrated that the verification problem is NP-complete—and they struggle to scale beyond relatively small neural networks, typically with parameter counts on the order of 10^5 [Tjeng et al., 2019, Cohen et al., 2019]. This scalability limitation has driven the development of incomplete methods capable of handling larger models.

Incomplete Methods

Incomplete verification methods primarily rely on the concept of *bounding* the outputs of neural networks and certifying properties based on these bounds. The core idea is to over-approximate the set of possible network outputs and then check whether this set intersects with the decision boundary required to satisfy the given specification (see §2.1). If no point in the over-approximated output set violates the property, the method guarantees that the specification holds. However, if a point within the over-approximation violates the property, the method abstains from certifying it. This could indicate either that the true output set does cross the decision boundary—implying the property is false—or that the over-approximation is too loose, and the property may still hold. Different methods in this category vary in how they perform the over-approximation, typically trading off tightness for scalability.

Several incomplete certification methods approximate a global or local (around the input) Lipschitz constant of the network [Anil et al., 2019, Hein and Andriushchenko, 2017, Zhang et al., 2019]. However, computing the exact Lipschitz constant is known to be an NP-hard problem [Karp, 2010, Bunel, 2019], so these methods often provide conservative upper bounds, leading to looser over-approximations of the output space. This can result in higher abstention rates, especially for larger models, limiting their practical applicability.

Other approaches employ linear or quadratic approximations of the network's nonlinear activations to provide incomplete certificates [Gowal et al., 2018, Mirman et al., 2018, Zhang et al., 2018]. Some, such as interval bound propagation or abstract

interpretation-based methods, propagate over-approximations of the reachable set through each layer of the network, starting from the input domain [Gowal et al., 2019, Gehr et al., 2018, Mirman et al., 2018]. Alternatively, some methods formulate bound computation as an optimization problem, using techniques like Semidefinite Programming (SDP) [Raghunathan et al., 2018, Fazlyab et al., 2020] or the dual of a linear program [Dvijotham et al., 2018]. Zhang et al. [2018] introduced CROWN, a method that applies non-parallel constraints on activation relaxations within a convex relaxation framework. CROWN produces tighter bounds than earlier approaches [Weng et al., 2018, Wong and Kolter, 2018] and was further improved by Wang et al. [2021] and extended to handle general computational graphs by Xu et al. [2020].

2.3 Empirical Robustness and Safety Evaluation of Neural Networks

While certification is the gold standard for verifying the robustness and safety of neural networks, it faces two significant challenges: (i) it is computationally expensive and struggles to scale to large models, and (ii) it requires a formal definition of both the domain and distance metric, which may not always be available. As a result, comprehensive empirical evaluations are often used as a practical alternative to certification. In §2.3.1, we review the literature on empirical adversarial attacks and defences, and in §2.3.2, we examine prior work on empirically evaluating the robustness and safety of generative AI models.

2.3.1 Empirical Adversarial Attacks and Defences

The optimization problem described in Equation 2.2 is both non-convex and nonlinear, making it difficult to solve to global optimality. Empirical adversarial attacks aim to find local optima for this problem, often balancing the quality of the attack with computational efficiency.

Attacks

When adversarial examples were first introduced by Szegedy et al. [2014], the authors framed the problem as a constrained optimization task, which they solved using L-BFGS. Goodfellow et al. [2015] later proposed the Fast Gradient Sign Method (FGSM), a one-step attack that leverages the sign of the gradient of the loss function with respect to the input, updating the input accordingly. Building on this, several notable methods emerged. For example, DeepFool [Moosavi-Dezfooli et al., 2016] iteratively computes minimal perturbations by linearizing the model, while Projected Gradient Descent (PGD) [Madry et al., 2018, Kurakin et al., 2016] extends FGSM into a multistep approach that uses the full gradient (instead of just the sign) and projects the perturbation back onto the ℓ_∞-norm ball to preserve imperceptibility. Carlini and Wagner [2017] advanced the field further by developing stronger attacks for various norms, including ℓ_2, ℓ_0, and ℓ_∞. Since these early breakthroughs, a wide range of adversarial attacks have been proposed [Papernot et al., 2016, Uesato et al., 2018, Athalye et al., 2018], with Croce and Hein [2020] introducing AutoAttack——a unified framework for assessing model robustness against multiple adversarial methods. There's also a rich literature that explores black-box adversarial attacks, where attackers lack access to the model's internal parameters or gradients [Papernot et al., 2017, Ilyas et al., 2018, Croce and Hein, 2020]. More recent advances in adversarial attacks continue to push the boundaries of this field [Akhtar et al., 2021].

These empirical attacks allow researchers to evaluate model robustness under a variety of perturbations, including those grounded in real-world conditions. For example, Kurakin et al. [2018] demonstrated that printing adversarial perturbations on physical stickers and applying them to real objects could still deceive models, even when accounting for an expanded ℓ_p-norm to reflect real-world conditions. This work inspired a broader line of research into physical adversarial attacks on vision systems, which has since been further explored in studies such as Li et al. [2019], Du et al. [2022], and Wei et al. [2024].

Defences

The discovery of adversarial examples quickly spurred interest in developing defences to improve adversarial robustness, as discussed in §2.1.1. In the context of the adversarial formulation from Equation 2.2, a defence typically seeks to learn the model weights to minimize the likelihood of those examples existing. This can be expressed as the following robust optimization problem:

$$\min_{\theta} \mathbb{E}_{(\mathbf{x},y)\sim\mathcal{T}} \left[\max_{\mathbf{x}'\in\Delta(\mathbf{x})} \ell\left(f_\theta(\mathbf{x}'), \hat{y}\right) \right], \tag{2.3}$$

where θ represents the model parameters and $\mathcal{T}$ the training data distribution.

One approach to achieving the aim of Equation 2.3 is through empirical methods that attempt to solve the bi-level problem——these methods are typically called *adversarial training*. Madry et al. [2018] proposed using PGD attacks to generate adversarial examples during training, solving the inner optimization problem, and updating the model parameters exclusively on the adversarial data. Building on this, Zhang et al. [2019] introduced TRADES, a method that strikes a balance between training on adversarial examples and standard ones, outperforming PGD on standard robustness benchmarks. While other works have suggested incremental improvements to adversarial training [Dong et al., 2018, Mosbach et al., 2018, Shafahi et al., 2019, Wong et al., 2020], advances in empirical adversarial attacks have demonstrated that adversarial training alone is not a panacea [Croce and Hein, 2020].

Another important line of research is focused on *provable defences*. These methods integrate efficient certification procedures (see §2.2) into the training process, aiming to reduce the likelihood of adversarial examples by ensuring robust predictions across a range of inputs [Hein and Andriushchenko, 2017, Gowal et al., 2018, Mirman et al., 2018]. Although most provable defences do not offer formal guarantees during training, they have been shown to improve empirical robustness against adversarial attacks during testing and increase the likelihood of certification post-training when evaluated by incomplete methods [Gowal et al., 2019, Wong and Kolter, 2018, Wong et al., 2018, Mao et al., 2024]. Some provable defence approaches, such as those based on randomized smoothing [Lecuyer et al., 2019,

Cohen et al., 2019] (see §2.2.1), can also provide robustness guarantees without the need for specialized robust training techniques.

2.3.2 Robustness and Safety of Generative AI Models

As discussed in §2.1.2, the concept of robustness in generative AI models is less clearly defined than in the discriminative setting. Consequently, the evaluation of generative AI typically centres around the idea of *alignment* [Amodei et al., 2016, Christiano et al., 2018, Leike et al., 2018, Hendrycks et al., 2021]. Alignment refers to the effort to ensure that AI systems behave in accordance with human intentions and values, with an emphasis on aligning the aims of the system rather than their capabilities [Ji et al., 2023]. Although terms such as "intentions", "values", and "aims" are notoriously difficult to operationalize [Kenton et al., 2021, Zhi-Xuan et al., 2024], an expanding body of literature seeks to anthropomorphize these concepts to address potential, often self-identified catastrophic or existential risks posed by *misalignment* in future superhuman AI systems [Perez et al., 2022, Bang et al., 2023, Steinhardt, 2023, Hendrycks et al., 2023, Pan et al., 2023].

Compounded on these potential risks in future models are the challenges present in current models. Ji et al. [2023] identifies the overarching goals of current alignment research as achieving robustness, interpretability, controllability, and ethicality in AI systems. Robustness, in particular, is defined as the ability of AI systems to "operate reliably under diverse scenarios [and remain] resilient to unforeseen disruptions." Each of these pillars is supported by a rich body of technical work in preference modelling and policy learning [Ouyang et al., 2022, Achiam et al., 2023, Touvron et al., 2023, Rafailov et al., 2024], scalable oversight [Irving et al., 2018, Burns et al., 2023], interpretability [Olah et al., 2020, Meng et al., 2022, Zou et al., 2023, Conmy et al., 2023], and sociotechnical studies on governance and ethics [Bommasani et al., 2021, McLean et al., 2023, Parliament, 2023, Koessler and Schuett, 2023]. While these problems are often studied in the context of LLMs, they also extend to other modalities [Liu et al., 2024]. A full review of this literature is beyond the scope of this thesis.

Of particular relevance to this work are empirical evaluations of alignment in current LLMs, especially concerning their robustness and safety. Following a taxonomy similar to that of Ji et al. [2023], we divide these evaluations into two main categories: *datasets and benchmarks*, and *red teaming*. The former focuses on creating datasets and benchmarks to assess models' alignment in specific scenarios [Parrish et al., 2021, Hartvigsen et al., 2022, Pan et al., 2023, Zou et al., 2023, Bai et al., 2022, Mazeika et al., 2024], while the latter focuses on adversarially stress testing models to induce unaligned outputs [Perez et al., 2022, Zhang et al., 2022, Shah et al., 2023, Qi et al., 2023]. Some works span both categories, using red teaming techniques to create safety evaluation datasets [Zou et al., 2023, Shah et al., 2023]. We further categorize red teaming techniques by their interaction with the model, such as *jailbreak* attacks, which attempt to bypass alignment at inference time [Perez et al., 2022, Zou et al., 2023], and *fine-tuning* risks, which aim to reverse alignment through additional training [Qi et al., 2023, Bianchi et al., 2023].

Jailbreaking Large Language Models

Jailbreaking attacks aim to generate prompts that induce unaligned responses from the model. These prompts can be crafted either manually, using methods such as prompt engineering and crowdsourcing [Shen et al., 2023], or automatically [Perez et al., 2022, Deng et al., 2022, Jones et al., 2023]. Building on the concept of adversarial examples in computer vision, Zou et al. [2023] introduced a token suffix optimization method to generate adversarial prompts for LLMs, demonstrating that these prompts are often transferable between models and universally effective. The optimized suffix typically consists of arbitrary tokens, making such attacks easier to detect than more coherent ones [Jain et al., 2023]. While some jailbreaking methods require access to the model's parameters [Huang et al., 2023, Zou et al., 2023], others adopt a black-box approach, relying solely on output logits or decoded text, which makes them suitable for targeting closed-source LLMs [Chao et al., 2023, Deng et al., 2023, Anil et al., 2024]. Successful defences against these attacks include

prompt engineering strategies [Shen et al., 2023], paraphrasing input prompts [Jain et al., 2023], and post-processing the model's output [Xu et al., 2024].

Fine-tuning Risks in Large Language Models

In discriminative models, a well-documented challenge is *catastrophic forgetting*, where continual training on a sequence of tasks causes the model to forget how to perform well in previously learned tasks [Goodfellow et al., 2013, Ramasesh et al., 2021]. A similar issue arises in generative models, where fine-tuning on a new dataset can result in the loss of alignment values and the generation of unaligned outputs [Qi et al., 2023, Bianchi et al., 2023, Peng et al., 2024]. This creates a potential attack vector, allowing adversaries to exploit the model's capabilities to produce harmful outputs. Notably, these attacks have been studied in instruction-following datasets——such as Alpaca and Dolly [Taori et al., 2023, Conover et al., 2023]——where previous research has demonstrated that they can succeed even when the fine-tuning dataset itself contains no harmful content [Qi et al., 2023, Bianchi et al., 2023, He et al., 2024]. To mitigate this risk, Bianchi et al. [2023] and Qi et al. [2023] propose incorporating alignment data during the fine-tuning process, which helps the model retain alignment even as it adapts to new data.

3

ANCER: Anisotropic Certification via Sample-wise Volume Maximization

Contents

3.1 Preamble

This chapter consists of a paper originally published at TMLR 2022 [Eiras et al., 2022]. It was a joint first author effort with Motasem Alfarra and Adel Bibi, and it fits within the **C1** contribution (§1.3). The appendix of this work is presented in Appendix A, and the code is available at https://github.com/fgirbal/ANCER.

Randomized smoothing has recently emerged as an effective tool that enables certification of deep neural network classifiers at scale. All prior art on randomized smoothing has focused on isotropic ℓ_p certification, which has the advantage of yielding certificates that can be easily compared among isotropic methods via ℓ_p-norm radius. However, isotropic certification limits the region that can be certified around an input to worst-case adversaries, *i.e.* it cannot reason about other "close", potentially large, constant prediction safe regions. To alleviate this issue, (**i**) we theoretically extend the isotropic randomized smoothing ℓ_1 and ℓ_2 certificates to their generalized anisotropic counterparts following a simplified analysis. Moreover, (**ii**) we propose evaluation metrics allowing for the comparison of general certificates—a certificate is superior to another if it certifies a superset region—with the quantification of each certificate through the volume of the certified region. We introduce AnCer, a framework for obtaining anisotropic certificates for a given test set sample via volume maximization. We achieve it by generalizing memory-based certification of data-dependent classifiers. Our empirical results demonstrate that AnCer achieves state-of-the-art ℓ_1 and ℓ_2 certified accuracy on CIFAR-10 and ImageNet in the data-dependence setting, while certifying larger regions in terms of volume, highlighting the benefits of moving away from isotropic analysis.

3.2 Introduction

The well-studied fact that Deep Neural Networks (DNNs) are vulnerable to additive imperceptible noise perturbations has led to a growing interest in developing robust classifiers [Goodfellow et al., 2015, Szegedy et al., 2014]. A recent promising approach to achieve state-of-the-art provable robustness (*i.e.* a theoretical bound

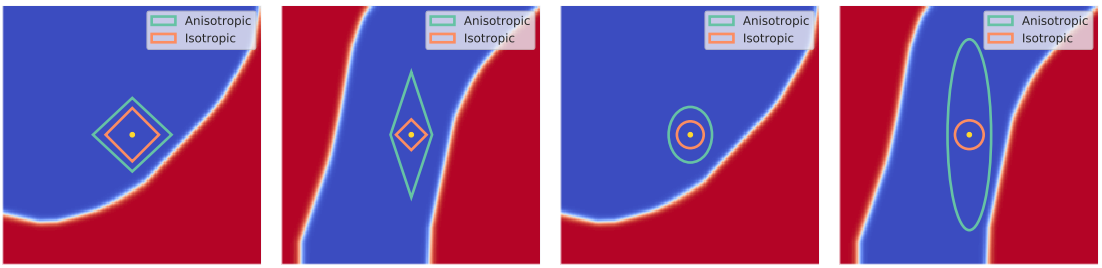

Figure 3.1: Illustration of the landscape of f^y (blue corresponds to a higher confidence in y, the true label) for a region around an input in a toy, 2-dimensional radially separable dataset. For two dataset examples, in (a) and (b) we show the boundaries of the optimal ℓ_1 isotropic and anisotropic certificates, while (c) and (d) are the boundaries of the optimal ℓ_2 isotropic and anisotropic certificates. A thorough discussion of this figure is presented in §3.4.

on the output around every input) at the scale of ImageNet [Deng et al., 2009] is *randomized smoothing* [Lecuyer et al., 2019, Cohen et al., 2019]. Given an input x and a network f, randomized smoothing constructs $g(x) = \mathbb{E}_{\epsilon\sim\mathcal{D}}[f(x+\epsilon)]$ such that $g(x) = g(x+\delta)\ \forall\delta \in \mathcal{R}$, where the certification region $\mathcal{R}$ is characterized by x, f, and the smoothing distribution $\mathcal{D}$. For instance, Cohen et al. [2019] showed that if $\mathcal{D} = \mathcal{N}(0, \sigma^2 I)$, then $\mathcal{R}$ is an ℓ_2-ball whose radius is determined by x, f and σ. Since then, there has been significant progress towards the design of $\mathcal{D}$ leading to the largest $\mathcal{R}$ for all inputs x. The interplay between $\mathcal{R}$ characterized by ℓ_1, ℓ_2 and ℓ_∞-balls, and a notion of optimal distribution $\mathcal{D}$ has been previously studied [Yang et al., 2020].

Despite this progress, current randomized smoothing approaches provide certification regions that are *isotropic* in nature, limiting their capacity to certifying smaller and *worst-case* regions. We provide an intuitive example of this behavior in Figure 3.1. The isotropic nature of $\mathcal{R}$ in prior art is due to the common assumption that the smoothing distribution $\mathcal{D}$ is identically distributed [Yang et al., 2020, Kumar et al., 2020, Levine and Feizi, 2021]. Moreover, comparisons between various randomized smoothing approaches were limited to methods that produce the same ℓ_p certificate, with no clear metrics for comparing with other certificates. In this paper, we address both concerns and present new state-of-the-art certified accuracy results on both CIFAR-10 and ImageNet datasets.

Our contributions are threefold. **(i)** We provide a general and simpler analysis compared to prior art [Cohen et al., 2019, Yang et al., 2020] that paves the way for the certification of *anisotropic* regions characterized by any norm, holding prior art as special cases. We then specialize our result to regions that, for a positive definite $\mathbf{A}$, are ellipsoids, *i.e.* $\|\mathbf{A}\delta\|_2 \leq c, c > 0$, and generalized cross-polytopes, *i.e.* $\|\mathbf{A}\delta\|_1 \leq c$, generalizing both ℓ_2 [Cohen et al., 2019] and ℓ_1 [Lecuyer et al., 2019, Yang et al., 2020] certification (§3.5). **(ii)** We introduce a new evaluation framework to compare methods that certify general (isotropic or anisotropic) regions. We compare two general certificates by defining that a method certifying $\mathcal{R}_1$ is superior to another certifying $\mathcal{R}_2$, if $\mathcal{R}_1$ is a strict superset to $\mathcal{R}_2$. Further, we define a standalone quantitative metric as the volume of the certified region, and specialize it for the cases of ellipsoids and generalized cross-polytopes (§3.6). **(iii)** We propose AnCer, an anisotropic certification method that performs sample-wise (*i.e.* per sample in the test set) region volume maximization (§3.7), generalizing the data-dependent, memory-based solution from Alfarra et al. [2022]. Through experiments on CIFAR-10 [Krizhevsky, 2009] and ImageNet [Deng et al., 2009], we show that restricting AnCer's certification region to ℓ_1 and ℓ_2-balls outperforms state-of-the-art ℓ_1 and ℓ_2 results from previous works [Yang et al., 2020, Alfarra et al., 2022]. Further, we show that the volume of the certified regions are significantly larger than all existing methods, thus setting a new state-of-the-art in certified accuracy. We highlight that while we effectively achieve state-of-the-art performance, it comes at a high cost given the data-dependency requirements. A discussion of the limitations of the solution is presented in §3.7.

Notation. We consider a base classifier $f : \mathbb{R}^n \rightarrow \mathcal{P}(K)$, where $\mathcal{P}(K)$ is a probability simplex over K classes, *i.e.* $f^i \geq 0$ and $\mathbf{1}^\top f = 1$, for $i \in \{1, \dots, K\}$. Further, we use (x, y) to be a sample input x and its corresponding true label y drawn from a test set $\mathcal{D}_t$, and f^y to be the output of f at the correct class. We use ℓ_p to be the typically defined $\|\cdot\|_p$ norm ($p \geq 1$), and $\ell_p^{\mathbf{A}}$ or $\|\cdot\|_{\mathbf{A},p}$ for $p = \{1, 2\}$ to be a composite norm defined with respect to a positive definite matrix $\mathbf{A}$ as $\|\mathbf{A}^{-1/p} v\|_p$.

3.3 Related Work

Verified Defenses. Since the discovery that DNNs are vulnerable against input perturbations [Goodfellow et al., 2015, Szegedy et al., 2014], a range of methods have been proposed to build classifiers that are verifiably robust [Huang et al., 2017, Gowal et al., 2019, Bunel et al., 2018, Salman et al., 2019]. Despite this progress, these methods do not yet scale to the networks the community is interested in certifying [Tjeng et al., 2019, Weng et al., 2018].

Randomized Smoothing. The first works on randomized smoothing used Laplacian [Lecuyer et al., 2019, Li et al., 2019] and Gaussian Cohen et al. [2019] distributions to obtain ℓ_1 and ℓ_2-ball certificates, respectively. Several subsequent works improved the performance of smooth classifiers by training the base classifier using adversarial augmentation [Salman et al., 2019], regularization [Zhai et al., 2019], or general adjustments to training routines [Jeong and Shin, 2020]. Recent work derived ℓ_p-norm certificates for other isotropic smoothing distributions [Yang et al., 2020, Levine and Feizi, 2020, Zhang et al., 2019]. Concurrently, Dvijotham et al. [2020] developed a framework to handle arbitrary smoothing measures in any ℓ_p-norm; however, the certification process requires significant hyperparameter tuning. Similarly, Mohapatra et al. [2020] introduces larger certificates that require higher-order information, yet do not provide a closed-form solution. This was followed by a complementary data-dependent smoothing approach, where the parameters of the smoothing distribution were optimized per test set *sample* to maximize the certified radius at an individual input [Alfarra et al., 2022]. All prior works considered smoothing with *isotropic* distributions and hence certified isotropic ℓ_p-ball regions. In this paper, we extend randomized smoothing to certify *anisotropic* regions, by pairing it with a generalization of the data-dependent framework [Alfarra et al., 2022] to maximize the certified region at each input point.

3.4 Motivating Anisotropic Certificates

Certification approaches aim to find the *safe* region $\mathcal{R}$, where $\arg\max_i f^i(x) = \arg\max_i f^i(x+\delta)\ \forall \delta \in \mathcal{R}$. Recent randomized smoothing techniques perform this certification by explicitly optimizing the isotropic ℓ_p certified region around each input [Alfarra et al., 2022], obtaining state-of-the-art performance as a result. Despite this ℓ_p optimality, we note that any ℓ_p-norm certificate is *worst-case* from the perspective of that norm, as it avoids adversary regions by limiting its certificate to the ℓ_p-closest adversary. This means that it can only enjoy a radius that is at most equal to the distance to the closest decision boundary. However, decision boundaries of general classifiers are complex, nonlinear, and non-radially distributed with respect to a generic input sample [Karimi et al., 2019]. This is evidenced by the fact that, within a reasonably small ℓ_p-ball around an input, there are often only a small set of adversary directions [Tramèr et al., 2017, 2018] (*e.g.* see the decision boundaries in Figure 3.1). As such, while ℓ_p-norm certificates are useful to reason about worst-case performance and are simple to obtain given previous works [Cohen et al., 2019, Yang et al., 2020, Lee et al., 2019], they are otherwise uninformative in terms of the shape of decision boundaries, *i.e.* which regions around the input are safe.

To visualize these concepts, we illustrate the decision boundaries of a base classifier f trained on a toy 2-dimensional, radially separable (with respect to the origin) binary classification dataset, and consider two different input test samples (see Figure 3.1). We compare the *optimal* isotropic and anisotropic certified regions of different shapes at these points. In Figures 3.1a and 3.1b, we compare an isotropic cross-polytope (of the form $\|\delta\|_1 \leq r$) with an anisotropic generalized cross-polytope (of the form $\|\mathbf{A}\delta\|_1 \leq r$), while in Figures 3.1c and 3.1d we compare an isotropic ℓ_2 ball (of the form $\|\delta\|_2 \leq r$) with an anisotropic ellipsoid (of the form $\|\mathbf{A}\delta\|_2 \leq r$). Notice that in Figures 3.1a and 3.1c, due to the curvature of the classification boundary (shown in white), the optimal certification region is isotropic in nature, which is evidenced by the similarities of the optimal isotropic and anisotropic certificates. On the other hand, in Figures 3.1b and 3.1d, the

Figure 3.2: Visualization of a CIFAR-10 image x and an example $x+\delta$ of an imperceptible change that *is not* inside the optimal isotropic certified region, but *is* covered by the anisotropic certificate.

location of the decision boundary allows for the anisotropic certified regions to be considerably larger than their isotropic counterparts, as they are not as constrained by the closest decision boundary, *i.e.* the *worst-case* performance. We note that these differences are further highlighted in higher dimensions, and we study them for a single CIFAR-10 test set sample in Appendix A.1.1.

As shown, anisotropic certification reasons more closely about the shape of the decision boundaries, allowing for further insights into constant prediction (safe) directions. In Figure 3.2, we present a series of test set images x, as well as practically indistinguishable $x + \delta$ images which *are not inside* the optimal certified isotropic ℓ_2-balls for each input sample, yet *are within* the anisotropic certified regions. This showcases the merits of using anisotropic certification for characterizing larger safe regions.

3.5 Anisotropic Certification

One of the main obstacles in enabling anisotropic certification is the complexity of the analysis required. To alleviate this, we follow a Lipschitz argument first observed by Salman et al. [2019] and Jordan and Dimakis [2020] and propose a simple and general certification analysis. We start with the following two observations. All proofs are in Appendix A.2.

Proposition 3.1. *Consider a differentiable function* $g : \mathbb{R}^n \to \mathbb{R}$. *If* $sup_x \|\nabla g(x)\|_* \leq L$ *where* $\|\cdot\|_*$ *has a dual norm* $\|z\| = \max_x z^\top x \quad s.t. \ \|x\|_* \leq 1$, *then* g *is* L*-Lipschitz under norm* $\|\cdot\|_*$, *that is* $|g(x) - g(y)| \leq L\|x - y\|$.

Given the previous proposition, we formalize $\|\cdot\|$ certification as follows:

Theorem 3.1. *Let $g : \mathbb{R}^n \to \mathbb{R}^K$, g^i be L-Lipschitz continuous under norm $\|\cdot\|_*$ $\forall i \in \{1, \ldots, K\}$, and $c_A = arg\max_i g^i(x)$. Then, we have $arg\max_i g^i(x+\delta) = c_A$ for all δ satisfying:*

$$\|\delta\| \leq \frac{1}{2L}\left(g^{c_A}(x) - \max_{c} g^{c \neq c_A}(x)\right).$$

Theorem 3.1 provides an $\|\cdot\|$ norm robustness certificate for any L-Lipschitz classifier g under $\|\cdot\|_*$. The certificate is only informative when one can attain a tight *non-trivial* estimate of L, ideally $\sup_x \|\nabla g(x)\|_*$, which is generally difficult when g is an arbitrary neural network.

Framework Recipe. In light of Theorem 3.1, randomized smoothing can be viewed **differently** as an instance of Theorem 3.1 with the favorable property that the constructed smooth classifier g enjoys an analytical form for $L = \sup_x \|\nabla g(x)\|_*$ by design. As such, to obtain an informative $\|\cdot\|$ certificate, one must, for an arbitrary choice of a smoothing distribution, compute the analytic Lipschitz constant L under $\|\cdot\|_*$ for g. While there can exist a notion of "optimal" smoothing distribution for a given choice of $\|\cdot\|$ certificate, as in part addressed earlier for the isotropic ℓ_1, ℓ_2 and ℓ_∞ certificates [Yang et al., 2020], this is not the focus of this paper. The choice of the smoothing distribution in later sections is inspired by previous work for the purpose of granting anisotropic certificates. This recipe complements randomized smoothing works based on Neyman-Pearson's lemma [Cohen et al., 2019] or the Level-Set and Differential Method [Yang et al., 2020].

We will deploy this framework recipe to show two specializations for anisotropic certification, namely ellipsoids (§3.5.1) and generalized cross-polytopes (§3.5.2).[1].

3.5.1 Certifying Ellipsoids

In this section, we consider the certification under ℓ_2^Σ norm, or $\|\delta\|_{\Sigma,2} = \sqrt{\delta^\top \Sigma^{-1} \delta}$, that has a dual norm $\|\delta\|_{\Sigma^{-1},2}$. Note that both $\|\delta\|_{\Sigma,2} \leq r$ and $\|\delta\|_{\Sigma^{-1},2} \leq r$ define

[1]Our analysis also grants a certificate for a mixture of Gaussians smoothing distribution (see Appendix A.3.1).

an ellipsoid. Despite that the following results hold for any positive definite Σ, we assume for efficiency reasons that Σ is diagonal throughout. First, we consider the anisotropic Gaussian smoothing distribution $\mathcal{N}(0, \Sigma)$ with the smooth classifier defined as $g_\Sigma(x) = \mathbb{E}_{\epsilon\sim\mathcal{N}(0,\Sigma)}[f(x+\epsilon)]$. Considering the classifier $\Phi^{-1}(g_\Sigma(x))$, where Φ is the standard Gaussian CDF, and following Theorem 3.1 to grant an ℓ_2^Σ certificate for $\Phi^{-1}(g_\Sigma(x))$, we derive the Lipschitz constant L under $\|\cdot\|_{\Sigma^{-1},2}$, in the following proposition.

Proposition 3.2. *$\Phi^{-1}(g_\Sigma(x))$ is 1-Lipschitz (i.e. $L = 1$) under the $\|\cdot\|_{\Sigma^{-1},2}$ norm.*

Since Φ^{-1} is a strictly increasing function, by combining Proposition 3.2 with Theorem 3.1, we have:

Corollary 3.1. *Let $c_A = \arg\max_i g_\Sigma^i(x)$, then $\arg\max_i g_\Sigma^i(x+\delta) = c_A$ for all δ satisfying:*

$$\|\delta\|_{\Sigma,2} \leq \frac{1}{2}\left(\Phi^{-1}\left(g_\Sigma^{c_A}(x)\right) - \Phi^{-1}\left(\max_c g_\Sigma^{c\neq c_A}(x)\right)\right).$$

Corollary 3.1 holds the ℓ_2 certification from Zhai et al. [2019] as a special case for when $\Sigma = \sigma^2 I$.[2]

3.5.2 Certifying Generalized Cross-Polytopes

Here we consider certification under the ℓ_1^Λ norm defining a generalized cross-polytope, *i.e.* the set $\{\delta : \|\delta\|_{\Lambda,1} = \|\Lambda^{-1}\delta\|_1 \leq r\}$, as opposed to the ℓ_1-bounded set that defines a cross-polytope, *i.e.* $\{\delta : \|\delta\|_1 \leq r\}$. As with the ellipsoid case and despite that the following results hold for any positive definite Λ, for the sake of efficiency, we assume Λ to be diagonal throughout. For generalized cross-polytope certification, we consider an anisotropic Uniform smoothing distribution $\mathcal{U}$, which defines the smooth classifier $g_\Lambda(x) = \mathbb{E}_{\epsilon\sim\mathcal{U}[-1,1]^n}[f(x+\Lambda\epsilon)]$. Following Theorem 3.1 and to certify under the ℓ_1^Λ norm, we compute the Lipschitz constant of g_Λ under the $\|\Lambda x\|_\infty$ norm, which is the dual norm of $\|\cdot\|_{\Lambda,1}$ (see Appendix A.2), in the next proposition.

[2] A similar result was derived in the appendix of Fischer et al. [2020], Li et al. [2020] with a more involved analysis by extending Neyman-Pearson's lemma.

Proposition 3.3. *The classifier g_Λ is $1/2$-Lipschitz (i.e. $L = 1/2$) under the $\|\Lambda x\|_\infty$ norm.*

Similar to Corollary 3.1, by combining Proposition 3.3 with Theorem 3.1, we have that:

Corollary 3.2. *Let $c_A = \arg\max_i g^i_\Lambda(x)$, then $\arg\max_i g^i_\Lambda(x+\delta) = c_A$ for all δ satisfying:*

$$\|\delta\|_{\Lambda,1} = \|\Lambda^{-1}\delta\|_1 \leq \left(g^{c_A}_\Lambda(x) - \max_c g^{c\neq c_A}_\Lambda(x)\right).$$

Corollary 3.2 holds the ℓ_1 certification from Yang et al. [2020] as a special case for when $\Lambda = \lambda I$.

3.6 Evaluating Anisotropic Certificates

With the anisotropic certification framework presented in the previous section, the question arises: "Given two general (isotropic or anisotropic) certification regions $\mathcal{R}_1$ and $\mathcal{R}_2$, how can one effectively compare them?". We propose the following definition to address this issue.

Definition 3.1. *For a given input point x, consider the two certification regions $\mathcal{R}_1$ and $\mathcal{R}_2$ obtained for two classifiers f_1 and f_2, i.e. $\mathcal{A}_1 = \{\delta : \arg\max_c f^c_1(x) = \arg\max_c f^c_1(x+\delta), \forall\delta \in \mathcal{R}_1\}$ and $\mathcal{A}_2 = \{\delta : \arg\max_c f^c_2(x) = \arg\max_c f^c_2(x+\delta), \forall\delta \in \mathcal{R}_2\}$ where $\arg\max_c f^c_1(x) = \arg\max_c f^c_2(x)$. We say $\mathcal{A}_1$ is a "superior certificate" to $\mathcal{A}_2$ (i.e. $\mathcal{A}_1 \succ \mathcal{A}_2$), if and only if, $\mathcal{A}_1 \supset \mathcal{A}_2$.*

This definition is a natural extension from the radius-based comparison of ℓ_p-ball certificates, providing a basis for evaluating anisotropic certification. To compare an anisotropic to an isotropic region of certification, it is not immediately clear how to **(i)** check that an anisotropic region is a superset to the isotropic region, and **(ii)** if it were a superset, how to quantify the improvement of the anisotropic region over the isotropic counterpart. In Sections 3.6.1 and 3.6.2, we tackle these issues for the particular cases of ellipsoid and generalized cross-polytope certificates.

3.6.1 Evaluating Ellipsoid Certificates

Comparing ℓ_2-Balls to $\ell_2^\Sigma-$Ellipsoids (Specialization of Definition 3.1). Recall that if $\Sigma = \sigma^2 I$, our ellipsoid certification in Corollary 3.1 recovers as a special case the isotropic ℓ_2-ball certification of Cohen et al. [2019], Salman et al. [2019], Zhai et al. [2019]. Consider the certified regions $\mathcal{R}_1 = \{\delta : \|\delta\|_2 \leq \tilde{\sigma} r_1\}$ and $\mathcal{R}_2 = \{\delta : \|\delta\|_{\Sigma,2} = \sqrt{\delta^\top \Sigma^{-1} \delta} \leq r_2\}$ for given $r_1, r_2 > 0$. Since we take $\Sigma = \text{diag}(\{\sigma_i^2\}_{i=1}^n)$, the maximum enclosed ℓ_2-ball for the ellipsoid $\mathcal{R}_2$ is given by the set $\mathcal{R}_3 = \{\delta : \|\delta\|_2 \leq \min_i \sigma_i r_2\}$, and thus $\mathcal{R}_2 \supseteq \mathcal{R}_3$. Therefore, it suffices that $\mathcal{R}_3 \supseteq \mathcal{R}_1$ (*i.e.* $\min_i \sigma_i r_2 \geq \tilde{\sigma} r_1$), to say that $\mathcal{R}_2$ is a superior certificate to the isotropic $\mathcal{R}_1$ as per Definition 3.1.

Quantifying ℓ_2^Σ Certificates. The aforementioned specialization is only concerned with whether our ellipsoid certified region $\mathcal{R}_2$ is "superior" to the isotropic ℓ_2-ball without quantifying it. A natural solution is to directly compare the volumes of the certified regions. Since the volume of an ellipsoid given by $\mathcal{R}_2$ is $\mathcal{V}(\mathcal{R}_2) = r_2^n \sqrt{\pi^n} / \Gamma(n/2+1) \prod_{i=1}^n \sigma_i$ [Kendall, 2004], we directly compare the *proxy radius* $\tilde{R}$ defined for $\mathcal{R}_2$ as $\tilde{R} = r_2 \sqrt[n]{\prod_i^n \sigma_i}$, since larger $\tilde{R}$ correspond to certified regions with larger volumes. Note that $\tilde{R}$, which is the n^{th} root of the volume up to a constant factor, can be seen as a generalization to the certified radius in the case when $\sigma_i = \sigma \quad \forall i$.

3.6.2 Evaluating Generalized Cross-Polytope Certificates

Comparing ℓ_1-Balls to $\ell_1^\Lambda-$Generalized Cross-Polytopes (Specialization of Definition 3.1). Consider the certificates $\mathcal{S}_1 = \{\delta : \|\delta\|_1 \leq \tilde{\lambda} r_1\}$, $\mathcal{S}_2 = \{\delta : \|\delta\|_{\Lambda,1} = \|\Lambda^{-1}\delta\|_1 \leq r_2\}$, and $\mathcal{S}_3 = \{\delta : \|\delta\|_1 \leq \min_i \lambda_i r_2\}$, where we take $\Lambda = \text{diag}(\{\lambda_i\}_{i=1}^n)$. Note that since $\mathcal{S}_2 \supseteq \mathcal{S}_3$, then as per Definition 3.1, it suffices that $\mathcal{S}_3 \supseteq \mathcal{S}_1$ (*i.e.* $\min_i \lambda_i r_2 \geq \tilde{\lambda} r_1$) to say that the anisotropic generalized cross-polytope $\mathcal{S}_2$ is superior to the isotropic ℓ_1-ball $\mathcal{S}_1$.

Quantifying ℓ_1^Λ Certificates. Following the approach proposed in the ℓ_2^Σ case, we quantitatively compare the generalized cross-polytope certification of Corollary 3.2 to the ℓ_1 certificate through the volumes of the two regions. We first present the volume of the generalized cross-polytope.

Proposition 3.4. $\mathcal{V}\left(\{\delta : \|\Lambda^{-1}\delta\|_1 \leq r\}\right) = \frac{(2r)^n}{n!}\prod_i \lambda_i$.

Following this definition, we define the *proxy radius* for $\mathcal{S}_2$ in this case to be $\tilde{R} = r_2 \sqrt[n]{\prod_{i=1}^n \lambda_i}$. As with the ℓ_2 case, larger $\tilde{R}$ correspond certified regions with larger volumes. As in the ellipsoid case, $\tilde{R}$ can be seen as a generalization to the certified radius when $\lambda_i = \lambda \quad \forall i$.

3.7 AnCer: Sample-wise Volume Maximization for Anisotropic Certification

Given the results from the previous sections, we are now equipped to certify anisotropic regions, in particular ellipsoids and generalized cross-polytopes. As mentioned in §3.5, these regions are generally defined as $\mathcal{R} = \{\delta : \|\delta\|_{\Theta,p} \leq r^p\}$ for a given parameter of the smoothing distribution $\Theta = \text{diag}\left(\{\theta_i\}_{i=1}^n\right)$, an ℓ_p-norm ($p \in \{1, 2\}$), and a *gap* value of $r^p \in \mathbb{R}^+$. At this point, one could simply take an anisotropic distribution with arbitrarily chosen parameters Θ and certify a trained network at any input point x, in the style of what was done in the previous randomized smoothing literature with isotropic distributions. However, the choice of Θ is more complex in the anisotropic case. A fixed choice of anisotropic Θ could severely underperform the isotropic case – take, for example, the anisotropic distribution of Figure 3.1d applied to the input of Figure 3.1c.

Instead of taking a fixed Θ, we generalize the framework introduced by Alfarra et al. [2022], where parameters of the smoothing distribution are optimized per input test point (*i.e.* in a *sample-wise* fashion) so as to maximize the resulting certificate. The goal of the optimization in [Alfarra et al., 2022] is, at a point x, to maximize the isotropic ℓ_2 region described in §3.5.1 (*i.e.* $\{\delta : \|\delta\|_2 \leq \sigma^x r^p(x, \sigma^x))\}$), where r^p is the gap and a function of x and $\sigma^x \in \mathbb{R}^+$. In the isotropic ℓ_p case, this generalizes

to maximizing the region $\{\delta : \|\delta\|_p \leq \theta^x r^p(x, \theta^x)\}$, which can be achieved by maximizing radius $\theta^x r^p(x, \theta^x)$ through $\theta^x \in \mathbb{R}^+$, obtaining r^*_{iso} [Alfarra et al., 2022].

For the general anisotropic case, we propose AnCer, whose objective is to maximize the volume of the certified region through the *proxy radius*, while satisfying the *superset* condition with respect to the maximum isotropic ℓ_2 radius, r^*_{iso}. In the case of the ellipsoids and generalized cross-polytopes as presented in Sections 3.6.1 and 3.6.2, respectively, AnCer's optimization problem can be written as:

$$\arg\max_{\Theta^x} \quad r^p(x, \Theta^x) \sqrt[n]{\prod_i \theta^x_i} \qquad \text{s.t.} \quad \min_i \ \theta^x_i r^p(x, \Theta^x) \geq r^*_{\text{iso}} \tag{3.1}$$

where $r^p(x, \Theta^x)$ is the gap value under the anisotropic smoothing distribution. That is,

$$\begin{aligned} &(1) \quad r^p(x, \Lambda^x) = g^{c_A}_\Lambda(x) - \max_c g^{c \neq c_A}_\Lambda(x), \\ &(2) \quad r^p(x, \Sigma^x) = \frac{1}{2}\left(\Phi^{-1}\left(g^{c_A}_\Sigma(x)\right) - \Phi^{-1}\left(\max_c g^{c \neq c_A}_\Sigma(x)\right)\right) \end{aligned}$$

for (1) ℓ_1 and (2) ℓ_2. This is a nonlinear constrained optimization problem that is challenging to solve. As such, we relax it, and solve instead:

$$\arg\max_{\Theta^x} \quad r^p(x, \Theta^x) \sqrt[n]{\prod_i \theta^x_i} + \kappa \min_i \ \theta^x_i r^p(x, \Theta^x) \quad \text{s.t.} \quad \theta^x_i \geq \bar{\theta}^x$$

given a hyperparameter $\kappa \in \mathbb{R}^+$. While the constraint $\theta^x_i \geq \bar{\theta}^x$ is not explicitly required to enforce the *superset* condition over the isotropic case, it proved itself beneficial from an empirical perspective. To sample from the distribution parameterized by Θ^x (in our case, either a Gaussian or Uniform), we make use of the *reparameterization trick*, as in Alfarra et al. [2022]. The solution of this optimization problem can be found iteratively by performing projected gradient ascent, as detailed in Algorithm 1. A standalone implementation for the AnCer optimization stage is presented in Listing A.1 in Appendix A.4.

Memory-based Anisotropic Certification. While each of the classifiers induced by the parameter Θ^x, i.e. g_{Θ^x}, is robust by definition as presented in §3.5, the certification of the overall data-dependent classifier is not necessarily sound due

Algorithm 1: ANCER Optimization

Function `AnCer` (f_θ, x, α, Θ_0, n, K, κ)**:**

- **Initialize:** $\Theta_x^0 \leftarrow \Theta_0$
- **for** $k = 0 \dots K-1$ **do**
  - sample $\hat{\epsilon}_1, \dots \hat{\epsilon}_n \sim \mathcal{D}$
  - $\psi(\Theta_x^k) = \frac{1}{n} \sum_{i=1}^{n} f_\theta(x + \Theta_x^k \hat{\epsilon}_i)$
  - $E_A(\Theta_x^k) = \max_c \psi^c$; $y_A = \arg\max_c \psi^c$; $E_B(\Theta_x^k) = \max_{c \neq y_A} \psi^c$
  - $r^p(x, \Theta_x^k) = \begin{cases} E_A - E_B & \text{, if } p = 1 \\ \frac{1}{2}\left(\Phi^{-1}(E_A) - \Phi^{-1}(E_B)\right) & \text{, if } p = 2 \end{cases}$
  - $R(\Theta_x^k) = r^p(x, \Theta_x^k) \left(\prod_i^d \Theta_{ii}^k\right)^{1/d} + \kappa\, r^p(x, \Theta_x^k) \min_i \Theta_{ii}^k$
  - $\Theta_x^{k+1} \leftarrow \Theta_x^k + \alpha \nabla_{\Theta_x^k} R(\Theta_x^k)$
  - $\Theta_x^{k+1} \leftarrow \max\left(\Theta_x^{k+1}, \Theta_0\right)$ // *element-wise maximum - projection step*
- **return** Θ_x^K

to the optimization procedure for each x. This is a known issue in certifying data-dependent classifiers, and is addressed by Alfarra et al. [2022] through the use of a memory-based procedure. In Appendix A.5, we present an adapted version of this algorithm to AnCer. All subsequent results are obtained following this procedure.

Limitations of AnCer. Given AnCer uses a memorization procedure similar to the one presented in Alfarra et al. [2022], it incurs limitations on memory and runtime complexity. Note that in memory-based data-dependent certification there is a single procedure for both certification and inference in contrast with the fixed σ setting from Cohen et al. [2019]. The main limitations of the memory-based certification are outlined in Appendix E of Alfarra et al. [2022]. The anisotropic case increases on the complexity of the isotropic framework by the increased runtime of specific functions presented in Appendix A.5. Certification runtime comparisons are in §3.8.4.

The memory-based procedure incurs the same memory cost as the one presented in Alfarra et al. [2022], i.e., it has a memory complexity of $\mathcal{O}(N)$ where N is the total number of inferred samples. This is since that the memory based method requires saving the observed instances along with their smoothing parameters. While the linear runtime dependency on memory size might appear daunting for the deployment of such a system, there are a few factors that could mitigate the

cost. Firstly, in practice the models deployed get regularly updated in deployment, and the memory should be reset in those situations. Secondly, there are possible solutions which might attain sublinear runtime for the post-certification stage, such as the application of k-d trees to reduce the space of comparisons and speed-up the process. As such, we believe AnCer to be suited to applications in offline scenarios, where improved robustness is desired and inference time is not a critical issue.

A further limitation of the memorization procedure has to do with the impact of the order in which inputs are certified on the overall statistics obtained. Within a memory-based framework, certifying x_2 with x_1 in memory can be different from certifying x_1 with x_2 in memory if they intersect. In practice, given the low number of intersections observed with the original certified regions, this effect was almost negligible in the results presented in §3.8. For fairness of comparison with non-memory based methods, we report "worst-case" results for AnCer in which we abstain from deciding whenever an intersection of two certified regions occurs.

3.8 Experiments

We now study the empirical performance of AnCer to obtain ℓ_2^Σ, ℓ_1^Λ, ℓ_2 and ℓ_1 certificates on networks trained using randomized smoothing methods found in the literature. In this section, we show that AnCer is able to achieve **(i)** improved performance on those networks in terms of ℓ_2 and ℓ_1 certification when compared to certification baselines that smooth using a fixed isotropic σ (Fixed σ) [Cohen et al., 2019, Yang et al., 2020, Salman et al., 2019, Zhai et al., 2019] or a data-dependent and memory-based isotropic one (Isotropic DD) [Alfarra et al., 2022]; and **(ii)** a significant improvement in terms of the ℓ_2^Σ and ℓ_1^Λ-norm certified region obtained by the same methods – compared by computing the *proxy radius* of the certified regions – thus generally satisfying the conditions of a superior certificate proposed in Definition 3.1. Note that both data-dependent approaches (Isotropic DD and AnCer) use memory-based procedures. As such, the gains described in this section constitute a trade-off given the limitations of the method described in §3.7.

We follow an evaluation procedure as similar as possible to the ones described in Cohen et al. [2019], Yang et al. [2020], Salman et al. [2019], Zhai et al. [2019] by using code and pre-trained networks whenever available and by performing experiments on CIFAR-10 [Krizhevsky, 2009] and ImageNet [Deng et al., 2009], certifying the entire CIFAR-10 test set and a subset of 500 examples from the ImageNet test set. For the implementation of AnCer, we solve Equation (3.1) with Adam for 100 iterations, where the certification gap $r^p(x, \Theta^x)$ is estimated at each iteration using 100 noise samples per test point (see Appendix A.4) and Θ^x in Equation (3.1) is initialized with the Isotropic DD solution from Alfarra et al. [2022]. Further details of the setup can be found in Appendix A.6.

As in previous works, ℓ_p **certified accuracy** at radius R is defined as the portion of the test set $\mathcal{D}_t$ for which the smooth classifier correctly classifies with an ℓ_p certification radius of at least R. In a similar fashion, we define the anisotropic $\ell_2^\Sigma/\ell_1^\Lambda$ certified accuracy at a proxy radius of $\tilde{R}$ (as defined in §3.6) to be the portion of $\mathcal{D}_t$ in which the smooth classifier classifies correctly with an $\ell_2^\Sigma/\ell_1^\Lambda$-norm certificate of an n^{th} root volume of at least $\tilde{R}$. We also report **average certified radius** (ACR) defined as $\mathbb{E}_{x,y\sim\mathcal{D}_t}[R_x \mathbb{1}(g(x) = y)]$ [Alfarra et al., 2022, Zhai et al., 2019] as well as **average certified proxy radius** ($AC\tilde{R}$) defined as $\mathbb{E}_{x,y\sim\mathcal{D}_t}[\tilde{R}_x \mathbb{1}(g(x) = y)]$, where R_x and $\tilde{R}_x$ denote the radius and proxy radius at x with a true label y for a smooth classifier g. Recall that in the isotropic case, the proxy radius is, by definition, the same as the radius for a given ℓ_p-norm. For each classifier, we ran experiments on the σ values reported in the original work (with the exception of Yang et al. [2020], see §3.8.2). For the sake of brevity, we report in this section the top-1 certified accuracy plots, ACR and $AC\tilde{R}$ per radius across σ, as in Salman et al. [2019], Zhai et al. [2019], Alfarra et al. [2022]. The performance of each method per σ is presented in Appendix A.8.

3.8.1 Ellipsoid certification (ℓ_2 and ℓ_2^Σ-norm certificates)

We perform the comparison of ℓ_2-ball vs. ℓ_2^Σ-ellipsoid certificates via Gaussian smoothing using networks trained following the procedures defined in Cohen et al.

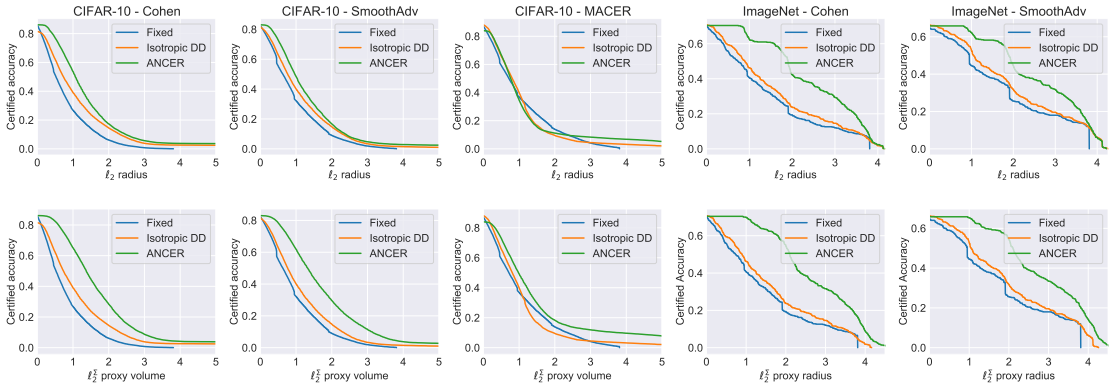

Figure 3.3: Distribution of top-1 certified accuracy as a function of ℓ_2 radius (top) and ℓ_2^Σ-norm proxy radius (bottom) obtained by different certification methods on CIFAR-10 and ImageNet.

[2019], Salman et al. [2019], and Zhai et al. [2019]. For each of these, we report results on ResNet18 trained using $\sigma \in \{0.12, 0.25, 0.5, 1.0\}$ for CIFAR-10, and ResNet50 using $\sigma \in \{0.25, 0.5, 1.0\}$ for ImageNet. For details of the training procedures, see Appendix A.6.1. Figure 3.3 plots top-1 certified accuracy as a function of the ℓ_2 radius (top) and of the ℓ_2^Σ-norm proxy radius (bottom) per trained network and dataset, while Table 3.1 presents an overview of the certified accuracy at various ℓ_2 radii, as well as ℓ_2 ACR and ℓ_2^Σ-norm $AC\tilde{R}$. Recall that, following the considerations in §3.6.1, the ℓ_2 certificate obtained through AnCer is the maximum enclosed isotropic ℓ_2-ball in the ℓ_2^Σ ellipsoid.

First, we note that sample-wise certification (Isotropic DD and AnCer) achieves higher certified accuracy than fixed σ across the board. This mirrors the findings in Alfarra et al. [2022], since certifying with a fixed σ for all samples struggles with the robustness/accuracy trade-off first mentioned in Cohen et al. [2019], whereas the data-dependent solutions explicitly optimize σ per sample to avoid it. More importantly, AnCer achieves new state-of-the-art ℓ_2 certified accuracy at most radii in Table 3.1, *e.g.* at radius 0.5 AnCer brings certified accuracy to 77% (from 66%) and 70% (from 62%) on CIFAR-10 and ImageNet, respectively, yielding relative percentage improvements in ACR between 13% and 47% when compared to Isotropic DD. While the results are significant, it might not be immediately clear why maximizing the volume of an ellipsoid with AnCer results in a larger

Table 3.1: Comparison of top-1 certified accuracy at different ℓ_2 radii, ℓ_2 average certified radius (ACR) and ℓ_2^Σ average certified proxy radius ($AC\tilde{R}$) obtained by using the isotropic σ used for training the networks (Fixed σ); the isotropic data-dependent (Isotropic DD) optimization scheme from Alfarra et al. [2022]; and AnCer's data-dependent anisotropic optimization.

CIFAR-10	Certification	Accuracy @ ℓ_2 radius (%)							ℓ_2 ACR	ℓ_2^Σ $AC\tilde{R}$
		0.0	0.25	0.5	1.0	1.5	2.0	2.5		
Cohen Cohen et al. [2019]	Fixed σ	86	71	51	27	14	6	2	0.722	0.722
	Isotropic DD	82	76	62	39	24	14	8	1.117	1.117
	AnCer	86	85	77	53	31	17	10	**1.449**	**1.772**
SmoothAdv Salman et al. [2019]	Fixed σ	82	72	55	32	19	9	5	0.834	0.834
	Isotropic DD	82	75	63	40	25	15	7	1.011	1.011
	AnCer	83	81	73	48	30	17	8	**1.224**	**1.573**
MACER Zhai et al. [2019]	Fixed σ	87	76	59	37	24	14	9	0.970	0.970
	Isotropic DD	88	80	66	40	17	9	6	1.007	1.007
	AnCer	84	80	67	34	15	11	9	**1.136**	**1.481**

ImageNet	Certification	Accuracy @ ℓ_2 radius (%)							ℓ_2 ACR	ℓ_2^Σ $AC\tilde{R}$
		0.0	0.5	1.0	1.5	2.0	2.5	3.0		
Cohen Cohen et al. [2019]	Fixed σ	70	56	41	31	19	14	12	1.098	1.098
	Isotropic DD	71	59	46	36	24	19	15	1.234	1.234
	AnCer	70	70	62	61	42	36	29	**1.810**	**1.981**
SmoothAdv Salman et al. [2019]	Fixed σ	65	59	44	38	26	20	18	1.287	1.287
	Isotropic DD	66	62	53	41	32	24	20	1.428	1.428
	AnCer	66	66	62	58	44	37	32	**1.807**	**1.965**

maximum enclosed ℓ_2-ball certificate in ℓ_2^Σ ellipsoid when compared to optimizing the ℓ_2-ball with Isotropic DD. We explore this phenomenon in Appendix 3.8.3.

As expected, AnCer substantially improves ℓ_2^Σ $AC\tilde{R}$ compared to Isotropic DD in all cases – with relative improvements in $AC\tilde{R}$ between 38% and 63% over both datasets. The joint results, certification with ℓ_2 and ℓ_2^Σ, establish that AnCer certifies the ℓ_2-ball region obtained by previous approaches, in addition to a much larger region captured by the ℓ_2^Σ certified accuracy and $AC\tilde{R}$, and therefore is, according to Definition 3.1, generally superior to the Isotropic DD one.

3.8.2 Generalized Cross-Polytope certification (ℓ_1 and ℓ_1^Λ-norm certificates)

To investigate ℓ_1-ball vs. ℓ_1^Λ-generalized cross-polytope certification via Uniform smoothing, we compare AnCer to the ℓ_1 state-of-the-art results from RS4A [Yang

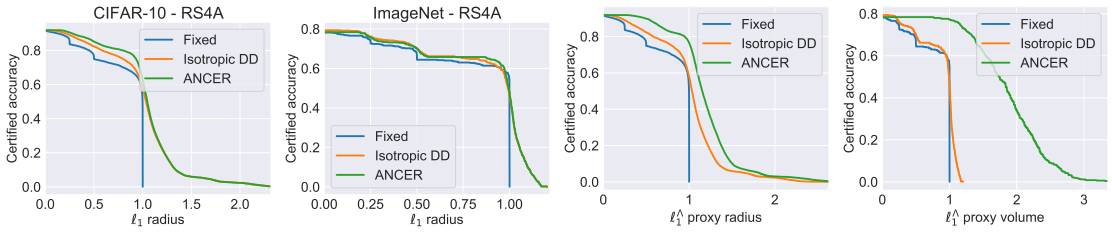

(a) **(b)** **(c)** **(d)**

Figure 3.4: Distribution of top-1 certified accuracy as a function of ℓ_1 radius (a, b) and ℓ_1^Λ-norm proxy radius (c, d) obtained by different certification methods on CIFAR-10 and ImageNet.

et al., 2020]. While the authors of the original work report best certified accuracy based on 15 networks trained at different σ levels between 0.15 and 3.5 on CIFAR-10 (WideResNet40) and ImageNet (ResNet50) and due to limited computational resources, we perform the analysis on a subset of those networks with $\sigma = \{0.25, 0.5, 1.0\}$. We reproduce the results in Yang et al. [2020] as closely as possible, with details of the training procedure presented in Appendix A.6.2. Figure 3.4 shows the top-1 certified accuracy as a function of the ℓ_1 radius (top) and of the ℓ_1^Λ-norm proxy radius (bottom) for RS4A, and Table 3.2 shows an overview of the certified accuracy at various ℓ_1 radii, as well as ℓ_1 ACR and ℓ_1^Λ $AC\tilde{R}$. As with the ellipsoid case, we notice that AnCer outperforms both Fixed σ and Istropic DD for most ℓ_1 radii, establishing new state-of-the-art results in CIFAR-10 at radii 0.5 and 1.0, and ImageNet at radii 0.5 (compared to previous results reported in Yang et al. [2020]). Once more and as expected, AnCer significantly improves the ℓ_1^Λ $AC\tilde{R}$ for all radii, pointing to substantially larger cerficates than the isotropic case. These results also establish that AnCer certifies the ℓ_1-ball region obtained by previous work, in addition to the larger region obtained by the ℓ_1^Λ certificate, and thus we can consider it superior (with respect to Definition 3.1) to Isotropic DD.

3.8.3 Why does AnCer improve upon Isotropic DD's ℓ_p certificates?

As observed in §3.8.1 and 3.8.2, AnCer's ℓ_2 and ℓ_1 certificates outperform the corresponding certificates obtained by Isotropic DD. To explain this, we compare the ℓ_2 certified region obtained by AnCer, defined in §3.7 as $\{\delta : \|\delta\|_2 \leq \min_i \sigma_i^x r(x, \Sigma^x)\}$,

Table 3.2: Comparison of top-1 certified accuracy at different ℓ_1 radii, ℓ_1 average certified radius (ACR) and ℓ_1^Λ average certified proxy radius ($AC\tilde{R}$) obtained by using the isotropic σ used for training the networks (Fixed σ); the isotropic data-dependent (Isotropic DD) optimization scheme from Alfarra et al. [2022]; and AnCer's data-dependent anisotropic optimization.

CIFAR-10	Certification	Accuracy @ ℓ_1 radius (%)							ℓ_1 ACR	ℓ_1^Λ $AC\tilde{R}$
		0.0	0.25	0.5	0.75	1.0	1.5	2.0		
RS4A Yang et al. [2020]	Fixed σ	92	83	75	71	46	0	0	0.775	0.775
	Isotropic DD	92	89	82	76	58	6	2	0.946	0.946
	AnCer	92	90	84	80	63	6	2	**0.980**	**1.104**
ImageNet										
RS4A Yang et al. [2020]	Fixed σ	78	73	67	63	0	0	0	0.683	0.683
	Isotropic DD	79	76	70	65	46	0	0	0.729	0.729
	AnCer	78	76	70	66	48	0	0	**0.730**	**1.513**

to the one by Isotropic DD defined as $\{\delta : \|\delta\|_2 \leq \sigma^x r(x, \sigma^x)\}$. We observe that the radius of both of these certificates can be separated into a σ-factor (σ^x vs. $\sigma^x_{\text{min}} = \min_i \sigma^x_i$) and a *gap*-factor ($r(x, \sigma^x)$ vs. $r(x, \Sigma^x)$). We posit the seemingly surprising result can be attributed to the computation of the gap-factor r using an anisotropic, optimized distribution. However, another potential explanation would be that AnCer benefits from a prematurely stopped initialization provided by Isotropic DD, thus achieving a better σ^x_{min} than the isotropic σ^x when given further optimization iterations.

To investigate this, we take the optimized parameters from the Isotropic DD experiments on SmoothAdv for an initial $\sigma = 0.25$ on CIFAR-10, and run the optimization step of Isotropic DD for 100 iterations more than its default number of iterations from Alfarra et al. [2022], so as to match the total number of optimization steps between Isotropic DD and AnCer. The histograms of σ^x or σ^x_{min} and the gap-factor r, *i.e.* the two factors from the ℓ_2 certification results, are presented in

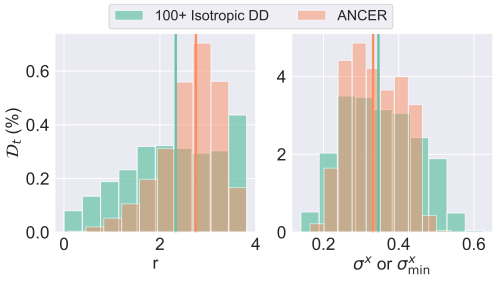

Figure 3.5: Histograms of the values of the gap r (left) and the σ-factor (right) obtained by AnCer initialized with Isotropic DD, and Isotropic DD when allowed to run for 100 iterations more than the baseline. Vertical lines plot the median of the data.

Figure 3.5. While σ^x for Isotropic DD is similar in distribution to AnCer's $\sigma^x_{\min}$, the distribution of the two gaps, $r(x, \sigma^x)$ and $r(x, \Sigma^x)$, are quite different. In particular, the AnCer certification gap is significantly larger when compared to Isotropic DD, and is the main contributor to the improvement in the ℓ_2-ball certificate of AnCer. That is to say, AnCer generates Σ^x that is better aligned with the decision boundaries, and hence increases the confidence of the smooth classifier.

3.8.4 Certification Runtime

The certification procedures of Isotropic DD and AnCer tradeoff improved certified accuracy for runtime, since they require a sample-wise optimization to be run prior to the Certify step described in Cohen et al. [2019], and a memory-based step as per Alfarra et al. [2022]. The runtime of the optimization and certification procedures is roughly equal for ℓ_1, ℓ_2, ℓ_2^Σ and ℓ_1^Λ certification, and mostly depends on network architecture. As such, we report the average certification runtime for a test set sample on an NVIDIA Quadro RTX 6000 GPU for Fixed σ, Isotropic DD and AnCer (including the isotropic initialization step) in Table 3.3. We observe that the run time overhead for AnCer is not significant as compared to its certification gains. Finally, due to the memory based step in our approach, the inference and certification runtime are the same.

Table 3.3: Average certification time for each sample per architecture used: (a) ResNet18 (ℓ_2, ℓ_2^Σ on CIFAR-10), (b) WideResNet40 (ℓ_1, ℓ_1^Λ on CIFAR-10), and (c) ResNet50 (ImageNet).

	Fixed σ	Isotropic DD	AnCer
(a)	1.6s	1.8s	2.7s
(b)	7.4s	9.5s	11.5s
(c)	109.5s	136.0s	147.0s

3.9 Conclusion

We lay the theoretical foundations for anisotropic certification through a simple analysis, propose a metric for comparing general robustness certificates, and introduce AnCer, a certification procedure that estimates the parameters of the anisotropic smoothing distribution to maximize the certificate. Our experiments show that AnCer achieves state-of-the-art ℓ_1 and ℓ_2 certified accuracy in the data-dependent setting.

4

Efficient Error Certification for Physics-Informed Neural Networks

Contents

4.1 Preamble

This chapter consists of a paper published at ICML 2024 [Eiras et al., 2024], and it fits within the **C1** contribution (§1.3). The appendix of this work is presented in Appendix B, and the code is available at https://github.com/fgirbal/partial_crown.

Recent work provides promising evidence that Physics-Informed Neural Networks (PINN) can efficiently solve partial differential equations (PDE). However, previous works have failed to provide guarantees on the worst-case residual error of a PINN across the spatio-temporal domain—a measure akin to the tolerance of numerical solvers—focusing instead on point-wise comparisons between their solution and the ones obtained by a solver on a set of inputs. In real-world applications, one cannot consider tests on a finite set of points to be sufficient grounds for deployment, as the performance could be substantially worse on a different set. To alleviate this issue, we establish guaranteed error-based conditions for PINNs over their continuous applicability domain. To verify the extent to which they hold, we introduce ∂-CROWN: a general, efficient and scalable post-training framework to bound PINN residual errors. We demonstrate its effectiveness in obtaining tight certificates by applying it to two classically studied PINNs—Burgers' and Schrödinger's equations—, and two more challenging ones with real-world applications—the Allan-Cahn and Diffusion-Sorption equations.

4.2 Introduction

Accurately predicting the evolution of complex systems through simulation is a difficult, yet necessary, process in the physical sciences. Many of these systems are represented by partial differential equations (PDE) the solutions of which, while well understood, pose a major computational challenge to solve at an appropriate spatio-temporal resolution [Raissi et al., 2019, Kochkov et al., 2020]. Inspired by the success of machine learning in other domains, recent work has attempted to overcome the aforementioned challenge through *physics-informed neural networks* (PINN) [Raissi et al., 2019, Sun et al., 2020, Pang et al., 2019]. For example, the

Diffusion-Sorption equation – which has real-world applications in the modeling of groundwater contaminant transport – takes 59.83s to solve per inference point using a classical PDE solver, while inference in its PINN version from Takamoto et al. [2022] takes only 2.7×10^{-3}s, a speed-up of more than 10^4 times.

The parameters of a PINN are estimated by minimizing the residual of the given PDE, together with its initial and boundary conditions, over a set of spatio-temporal training inputs. Its accuracy is then empirically estimated by measuring the solution estimate over a set of discrete input points, and (typically) comparing them to numerical PDE solvers. In other words, most current work on PINNs provides no certified error bounds applicable for *every* input within the domain of the PDE.

While testing on a finite set of points provides a good initial signal on the accuracy of the PINN, such an approach cannot be relied upon in practice, and error certification is needed to understand the quality of the PINN trained [Hillebrecht and Unger, 2022]. For example, by estimating the maximum residual error of the Diffusion-Sorption PINN from Takamoto et al. [2022] using 10^4 Monte Carlo samples across the domain we obtain an estimate of 1.1×10^{-3}, whereas the estimate using 10^6 samples is 21.09 – indicating the PINN has failed to learn a continuous function that correctly maps to the solution of the underlying PDE. This empirical difference shows the need for computing certified error bounds to avoid deploying poorly trained PINNs.

We introduce formal, error-based *correctness* conditions for PINNs which require that the residual error is *globally* upper bounded by a tolerance parameter, that is, that the continuous function learned approximates the underlying PDE solution across the domain. To compute this bound and verify the correctness conditions, we build on recent progress in neural network verification. Specifically, we efficiently extend the CROWN framework [Zhang et al., 2018] by deriving linear upper and lower bounds for the various nonlinear terms that appear in PINNs, and devise a novel bound propagation strategy for the task at hand.

Our contributions are threefold. **(i)** We formally define correctness conditions for general PINNs that approximate continuous solutions of PDEs. **(ii)**

We introduce a general, efficient, and scalable post-training *error certification framework* (∂-CROWN) to theoretically verify PINNs over their entire spatio-temporal domains. **(iii)** We demonstrate our post-training framework on two widely studied PDEs in the context of PINNs, Burgers' and Schrödinger's equations [Raissi et al., 2019], and two more challenging ones with real-world applications, the Allan-Cahn equation [Monaco and Apiletti, 2023] and the Diffusion-Sorption equation [Takamoto et al., 2022].

4.3 Related work

Since our certification framework for PINNs is based on the verification literature of image classifiers, in this section we explore: related work for PINNs, and previous work on neural network robustness verification.

Physics-informed Neural Networks. Raissi et al. [2019] introduced PINNs, which leverage automatic differentiation to obtain approximate solutions to the underlying PDE. Since then, a variety of different PINNs have emerged in a range of applications, from fluid dynamics [Raissi et al., 2019, 2020, Sun et al., 2020, Jin et al., 2021], to meta material design [Liu and Wang, 2019, Fang and Zhan, 2019, Chen et al., 2020] for different classes of PDEs [Pang et al., 2019, Fang and Zhan, 2019, Zhang et al., 2020]. A few works analyze the convergence of the training process of PINNs under specific conditions [Shin et al., 2020, Wang et al., 2022]. Mishra and Molinaro [2022] approximated the generalization error of various PINNs under specific stability and training process assumptions, and others introduced approximation bounds under regularity assumptions [Ryck and Mishra, 2022, Hillebrecht and Unger, 2022]. Our verification framework is applicable to any PINN where the solution is modeled by a fully connected network.

Robustness Verification of Neural Networks. The presence of adversarial examples, *i.e.* , small local input perturbations that lead to large output changes, was established by Szegedy et al. [2014] in image classifiers. As robust classifiers

emerged [Madry et al., 2018], so did attempts to certify them formally. Those methods can be divided into *exact*, *i.e.* , complete [Katz et al., 2017, Ehlers, 2017, Huang et al., 2017, Lomuscio and Maganti, 2017, Bunel et al., 2018, De Palma et al., 2021, Ferrari et al., 2022], or *conservative*, *i.e.* , sound but incomplete [Gowal et al., 2018, Mirman et al., 2018, Wang et al., 2018, Wong and Kolter, 2018, Ayers et al., 2020]. A promising set of conservative methods poses the problem as a convex relaxation of the original nonlinear network architecture, and solves it using a linear programming solver [Salman et al., 2019, Zhang et al., 2022] or by obtaining closed-form bounds [Zhang et al., 2018, Wang et al., 2021]. The latter are especially appealing due to their efficiency. Examples include CROWN [Zhang et al., 2018] and α-CROWN [Xu et al., 2020]. Xu et al. [2020] extended the linear relaxation framework from Zhang et al. [2018] to general computation graphs, but the purely backward propagation nature makes it potentially less efficient than custom bounds/hybrid approaches [Shi et al., 2020]. Our work adapts techniques from verification to certify the *full* applicability domain of PINNs, in a similar fashion to the *global* specification from Müller et al. [2023].

4.4 Preliminaries

4.4.1 Notation

Given vector $\mathbf{a} \in \mathbb{R}^d$, $\mathbf{a}_i$ refers to its i-th component. We use $\partial_{\mathbf{x}_i^j} f$ and $\frac{\partial^j f}{(\partial \mathbf{x}_i)^j}$ interchangeably to refer to the j-th partial derivative of a function $f : \mathbb{R}^n \to \mathbb{R}$ with respect to the i-component of its input, $\mathbf{x}_i$. Where it is clear, we use $f(\mathbf{x})$ and f interchangeably. We take $\mathbb{L}^{(i)}_{\mathbf{W},\mathbf{b}}(\mathbf{x}) = \mathbf{W}^{(i)}\mathbf{x}+\mathbf{b}^{(i)}$ to be a function of $\mathbf{x}$ parameterized by weights $\mathbf{W}^{(i)}$ and bias $\mathbf{b}^{(i)}$. We define an L-layer *fully connected neural network* $g : \mathbb{R}^{d_0} \to \mathbb{R}^{d_L}$ for an input $\mathbf{x}$ as $g(\mathbf{x}) = y^{(L)}(\mathbf{x})$ where $y^{(k)}(\mathbf{x}) = \mathbb{L}^{(k)}_{\mathbf{W},\mathbf{b}}(z^{(k-1)}(\mathbf{x}))$, $z^{(k-1)}(\mathbf{x}) = \sigma(y^{(k-1)}(\mathbf{x}))$, $z^{(0)}(\mathbf{x}) = \mathbf{x}$, in which $\mathbf{W}^{(k)} \in \mathbb{R}^{d_k \times d_{k-1}}$ and $\mathbf{b}^{(k)} \in \mathbb{R}^{d_k}$ are the weight and bias of layer k, σ is the nonlinear activation, and $k \in \{1, \ldots, L\}$.

4.4.2 Physics-informed neural networks (PINNs)

We consider general nonlinear PDEs of the form:

$$f(t, \hat{\mathbf{x}}) = \partial_t u(t, \hat{\mathbf{x}}) + \mathcal{N}[u](t, \hat{\mathbf{x}}) = 0, \ \hat{\mathbf{x}} \in \mathcal{D}, t \in [0, T], \tag{4.1}$$

where f is the residual of the PDE, t is the temporal and $\hat{\mathbf{x}}$ is the spatial components of the input, $u : [0, T] \times \mathcal{D} \to \mathbb{R}$ is the solution, $\mathcal{N}$ is a nonlinear differential operator on u, $T \in \mathbb{R}^+$, and $\mathcal{D} \subset \mathbb{R}^D$. Where possible, for conciseness we will use $\mathbf{x} = (t, \hat{\mathbf{x}})$, for $\mathbf{x} \in \mathcal{C} = [0, T] \times \mathcal{D}$, with $\mathbf{x}_0 = t$.

We assume f is the residual of an R^{th} order PDE where the differential operators of $\mathcal{N}$ applied to u yield the partial derivatives for order $\{0, ..., R\}$ as: $u \in \mathcal{N}^{(0)}$, $\partial_{\mathbf{x}_i} u \in \mathcal{N}^{(1)}$, $\partial_{\mathbf{x}_i^2} u \in \mathcal{N}^{(2)}$, $\ldots$, $\partial_{\mathbf{x}_i^R} u \in \mathcal{N}^{(R)}$ for $i \in \{0, \ldots, D\}$[1]. With these, we can re-write $f = \mathcal{P}(u, \partial_{\mathbf{x}_0} u, \ldots, \partial_{\mathbf{x}_D} u, \ldots, \partial_{\mathbf{x}_D^R} u)$, where $\mathcal{P}$ is a nonlinear function of those terms. Furthermore, the PDE is defined under (1) initial conditions, *i.e.* , $u(0, \hat{\mathbf{x}}) = u_0(\hat{\mathbf{x}})$, for $\hat{\mathbf{x}} \in \mathcal{D}$, and (2) general Robin boundary conditions, *i.e.* , $au(t, \hat{\mathbf{x}}) + b\partial_{\mathbf{n}} u(t, \hat{\mathbf{x}}) = u_b(t, \hat{\mathbf{x}})$ for $a, b \in \mathbb{R}$, $\hat{\mathbf{x}} \in \delta\mathcal{D}$ and $t \in [0, T]$, and $\partial_{\mathbf{n}} u$ is the normal derivative at the border with respect to some components of $\hat{\mathbf{x}}$.

Continuous-time PINNs [Raissi et al., 2019] result from approximating the solution, $u(\mathbf{x})$, using a neural network parameterized by θ, $u_\theta(\mathbf{x})$. We refer to this network as the *approximate solution*. In that context, the *physics-informed neural network* (or residual) is $f_\theta(\mathbf{x}) = \partial_t u_\theta(\mathbf{x}) + \mathcal{N}[u_\theta](\mathbf{x})$. For example, the one-dimensional Burgers' equation (explored in detail in §4.6) is defined as:

$$f_\theta(\mathbf{x}) = \partial_t u_\theta(\mathbf{x}) + u_\theta(\mathbf{x})\partial_x u_\theta(\mathbf{x}) - (0.01/\pi)\partial_{x^2} u_\theta(\mathbf{x}). \tag{4.2}$$

Note f_θ has the same order as f, and can be described similarly as a nonlinear function with the partial derivatives applied to u_θ instead of u. Burgers' equation (from above) has one 0^{th} order term (u_θ), two 1^{st} order ones ($\partial_t u_\theta$ and $\partial_x u_\theta$), and a 2^{nd} order partial derivative ($\partial_{x^2} u_\theta$), while $u_\theta(\mathbf{x})\partial_x u_\theta(\mathbf{x})$ is a nonlinear term of the f_θ polynomial.

[1]For simplicity, we assume $\mathcal{N}$ does not contain any cross-derivative operators, yet an extension would be trivial to derive.

4.4.3 Bounding neural network outputs using CROWN [Zhang et al., 2018]

The computation of upper/lower bounds on the output of neural networks over a domain has been widely studied within verification of image classifiers [Katz et al., 2017, Mirman et al., 2018, Zhang et al., 2018]. For the sake of computational efficiency, we consider the bounds obtained using CROWN [Zhang et al., 2018]/α-CROWN [Xu et al., 2020] as the base for our framework.

Take g to be the fully connected neural network (as defined in §4.4.1) we're interested in bounding. The goal is to compute $\max / \min_{x \in \mathcal{C}} g(\mathbf{x})$, where $\mathcal{C}$ is the applicability domain. Typically within verification of image classifiers, $\mathcal{C} = \mathbb{B}^p_{\mathbf{x},\epsilon} = \{\mathbf{x}' : \|\mathbf{x}' - \mathbf{x}\|_p \leq \epsilon\}$, *i.e.* , it is a *local* ℓ_p-ball of radius ϵ around an input $\mathbf{x}$ from the test set.

CROWN solves the optimization problem by *back-propagating* linear bounds of $g(\mathbf{x})$ through each hidden layer of the network until the input is reached. To do so, assuming constant bounds on $y^{(k)}(\mathbf{x})$ are known for $\mathbf{x} \in \mathcal{C}$, *i.e.* , $\forall \mathbf{x} \in \mathcal{C} : y^{(k),L} \leq y^{(k)}(\mathbf{x}) \leq y^{(k),U}$, CROWN relaxes the nonlinearities of each $z^{(k)}$ using a linear lower and upper bound approximation that contains the full possible range of $\sigma(y^{(k)}(\mathbf{x}))$. By relaxing the activations of each layer and back-propagating it through $z^{(k)}$, CROWN obtains a bound on each $y^{(k)}$ as a function of $y^{(k-1)}$. Back-substituting from the output $y^{(L)} = g(\mathbf{x})$ until the input $\mathbf{x}$ results in:

$$\min_{\mathbf{x} \in \mathcal{C}} g(\mathbf{x}) \geq \min_{\mathbf{x} \in \mathcal{C}} \mathbf{A}^L \mathbf{x} + \mathbf{a}^L, \quad \max_{\mathbf{x} \in \mathcal{C}} g(\mathbf{x}) \leq \max_{\mathbf{x} \in \mathcal{C}} \mathbf{A}^U \mathbf{x} + \mathbf{a}^U,$$

where $\mathbf{A}^L$, $\mathbf{a}^L$, $\mathbf{A}^U$ and $\mathbf{a}^U$ are computed in polynomial time from $\mathbf{W}^{(k)}, \mathbf{b}^{(k)}$, and the linear relaxation parameters. The solution to the optimization problems above given simple constraints $\mathcal{C}$ can be obtained in closed-form. α-CROWN [Xu et al., 2020] improves these bounds by optimizing the linear relaxations of $\sigma(y^{(k)}(\mathbf{x}))$ for tightness.

4.5 ∂-CROWN: Error Certification for General Physics-Informed Neural Networks

Take u_θ to be the learned approximate continuous solution of the PDE f through the PINN f_θ. Previous works deriving from Raissi et al. [2019] have measured the *correctness* of u_θ empirically by computing the solution error at a set of discrete point compared to that obtained via numerical solvers for f [Takamoto et al., 2022, Monaco and Apiletti, 2023] – a compromise arising from the fact we cannot bound $\|u_\theta - u\|$ for general PDEs across their continuous domain.

To mitigate this issue for continuous-time PINNs, we approach the problem of error bounding by imposing correctness conditions on the *residual* instead of the solution error. By definition, u_θ is a correct solution to the PINN f_θ if 3 conditions are met: ① the norm of the solution error with respect to the initial condition is upper bounded by an acceptable tolerance, ② the norm of the solution error with respect to the boundary conditions is bounded by an acceptable tolerance, and ③ the norm of the residual is bounded by an acceptable tolerance. We define these as PINN *correctness conditions*, and formalize it in Definition 4.1. Note these conditions are general and, at this point, no assumptions are made about u_θ or the PDE.

Definition 4.1 (Correctness Conditions for PINNs)**.** *$u_\theta : [0,T] \times \mathcal{D} \to \mathbb{R}$ is a $\delta_0, \delta_b, \varepsilon$-globally correct approximation of the exact solution $u : [0,T] \times \mathcal{D} \to \mathbb{R}$ if:*

$$
\begin{aligned}
&① \quad \max_{\hat{\mathbf{x}} \in \mathcal{D}} |u_\theta(0, \hat{\mathbf{x}}) - u_0(\hat{\mathbf{x}})|^2 \leq \delta_0, \\
&② \quad \max_{t \in [0,T], \hat{\mathbf{x}} \in \delta\mathcal{D}} |a u_\theta(\mathbf{x}) + b \partial_{\mathbf{n}} u_\theta(\mathbf{x}) - u_b(\mathbf{x})|^2 \leq \delta_b, \\
&③ \quad \max_{\mathbf{x} \in \mathcal{C}} |f_\theta(\mathbf{x})|^2 \leq \varepsilon.
\end{aligned}
$$

In practice, δ_0, δ_b, and ε correspond to tolerances similar to the ones given by numerical solvers for f. While the residual error upper bound is similar in nature to the empirical errors used to monitor convergence in iterative solvers (e.g., in Krylov subspace methods for linear systems), the bound proposed here corresponds to the error of the continuous approximate solution u_θ instead of the discretized version provided in those solvers. In §4.6, we empirically analyze the connection between residual and solution errors using a numerical solver.

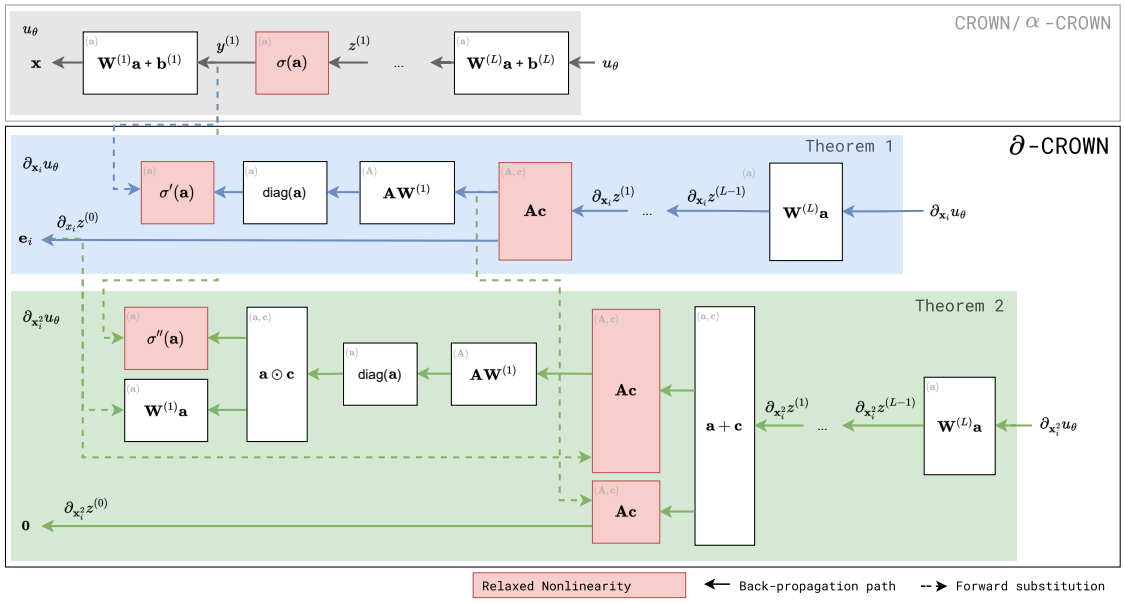

Figure 4.1: Bounding Partial Derivatives with ∂-CROWN: our hybrid scheme for bounding $\partial_{\mathbf{x}_i} u_\theta$ and $\partial_{\mathbf{x}_i^2} u_\theta$ uses back-propagation and forward substitution (inspired by Shi et al. [2020]) to compute bounds in $\mathcal{O}(L)$ instead of the $\mathcal{O}(L^2)$ complexity of full back-propagation as in Xu et al. [2020].

The verification of the conditions from Definition 4.1 requires bounding: a linear function of u_θ for ①, a linear function of u_θ and $\partial_{\mathbf{n}} u_\theta$ for ②, and the PINN output, f_θ, in ③. To achieve ①, assuming u_θ is a standard fully connected neural network as in Raissi et al. [2019], we can directly use CROWN/α-CROWN [Zhang et al., 2018, Xu et al., 2020]. However, bounding ② and ③ with a linear function in $\mathbf{x}$ efficiently requires a method to bound linear and nonlinear functions of the partial derivatives of u_θ.

We propose ∂-CROWN, an efficient framework to: (i) compute closed-form bounds on the partial derivatives of an arbitrary fully-connected network u_θ (§4.5.1), and (ii) bound a nonlinear function of those partial derivative terms, *i.e.* , f_θ (§4.5.2). Throughout this section, we assume $u_\theta(\mathbf{x}) = g(\mathbf{x})$ as defined in §4.4.1, with $d_0 = D + 1$. Formal statements and proofs for the lemmas and theorems presented in this section are in Appendix B.4.

4.5.1 Bounding Partial Derivatives of u_θ

The computation of the bounds for the 0^{th} order derivative, *i.e.* , u_θ, and intermediate pre-activations can be computed using CROWN/α-CROWN [Zhang et al., 2018, Xu et al., 2020]. As such, for what follows, we assume that for $\mathbf{x} \in \mathcal{C}$, both the bounds on u_θ and $y^{(k)}$, $\forall k$ are given.

Assumption 4.1. *The pre-activation layer outputs of u_θ, $y^{(k)} = \mathbb{L}^{(k)}_{\mathbf{W},\mathbf{b}}(z^{(k-1)})$, are lower and upper bounded by linear functions $\mathbb{L}^{(k),L}_{\mathbf{A},\mathbf{a}}(\mathbf{x}) \leq y^{(k)} \leq \mathbb{L}^{(k),U}_{\mathbf{A},\mathbf{a}}(\mathbf{x})$. Moreover, for $\mathbf{x} \in \mathcal{C}$, we have $y^{(k),L} \leq y^{(k)} \leq y^{(k),U}$.*

Note that using CROWN/α-CROWN, $\mathbf{A}^{(k),L}$, $\mathbf{a}^{(k),L}$, $\mathbf{A}^{(k),U}$, $\mathbf{a}^{(k),U}$ are functions of all the previous layers' parameters. For 1^{st} order derivatives, we start by explicitly obtaining the expression of $\partial_{\mathbf{x}_i} u_\theta$.

Lemma 4.1 (Expression for $\partial_{\mathbf{x}_i} u_\theta$)**.** *For $i \in \{1, \dots, d_0\}$, the partial derivative of u_θ with respect to $\mathbf{x}_i$ can be computed recursively as $\partial_{\mathbf{x}_i} u_\theta = \mathbf{W}^{(L)} \partial_{\mathbf{x}_i} z^{(L-1)}$ for:*

$$\partial_{\mathbf{x}_i} z^{(k)} = \partial_{z^{(k-1)}} z^{(k)} \partial_{\mathbf{x}_i} z^{(k-1)}, \quad \partial_{\mathbf{x}_i} z^{(0)} = \mathbf{e}_i,$$

for $k \in \{1, \dots, L-1\}$, and where $\partial_{z^{(k-1)}} z^{(k)} = diag\left[\sigma'\left(y^{(k)}\right)\right] \mathbf{W}^{(k)}$.

Using this result, we can efficiently linearly lower and upper bound $\partial_{\mathbf{x}_i} u_\theta$.

Theorem 4.1 (Informal, ∂-CROWN Linear Bounding $\partial_{\mathbf{x}_i} u_\theta$)**.** *There exist two linear functions $\partial_{\mathbf{x}_i} u^U_\theta$ and $\partial_{\mathbf{x}_i} u^L_\theta$ such that, $\forall \mathbf{x} \in \mathcal{C}$ it holds that $\partial_{\mathbf{x}_i} u^L_\theta \leq \partial_{\mathbf{x}_i} u_\theta \leq \partial_{\mathbf{x}_i} u^U_\theta$, where the linear coefficients can be computed recursively in closed-form in $\mathcal{O}(L)$ time as a function of $\mathbf{W}^{(k)}$, $\mathbf{A}^{(k),L}$, $\mathbf{a}^{(k),L}$, $\mathbf{A}^{(k),U}$, $\mathbf{a}^{(k),U}$, $\mathbf{y}^{(k),L}$, and $\mathbf{y}^{(k),U}$.*

The formal statement of Theorem 4.1 and expressions for $\partial_{\mathbf{x}_i} u^L_\theta$ and $\partial_{\mathbf{x}_i} u^U_\theta$ are provided in Appendix B.4.3. Note that this bound is not computed using fully backward propagation as in Xu et al. [2020]. Instead we use a *hybrid* scheme in the spirit of Shi et al. [2020] for the sake of efficiency. We perform backward propagation to compute $\partial_{z^{(k-1)}} z^{(k)}$ as a function of $y^{(k)}$, and forward-substitute the pre-computed CROWN bounds $\mathbb{L}^{(k),L}_{\mathbf{A},\mathbf{a}}(\mathbf{x}) \leq y^{(k)} \leq \mathbb{L}^{(k),U}_{\mathbf{A},\mathbf{a}}(\mathbf{x})$ at that point instead

of fully backward propagating which would have $\mathcal{O}(L^2)$ complexity. This induces a significant speed-up while achieving tight enough bounds. Figure 4.1 showcases the back-propagation and forward substitution paths for bounding $\partial_{\mathbf{x}_i} u_\theta$ in blue. Similarly to CROWN with the activation σ, this bound requires relaxing $\sigma'(y^{(k)})$.

Similarly, we can linearly bound $\partial_{\mathbf{x}_i^2} u_\theta$, a requirement to bound f_θ in 2^{nd} order PINNs.

Lemma 4.2 (Expression for $\partial_{\mathbf{x}_i^2} u_\theta(\mathbf{x})$)**.** *For $i \in \{1, \dots, d_0\}$, the second partial derivative of u_θ with respect to $\mathbf{x}_i$ can be computed recursively as $\partial_{\mathbf{x}_i^2} u_\theta = \mathbf{W}^{(L)} \partial_{\mathbf{x}_i^2} z^{(L-1)}$ where:*

$$\partial_{\mathbf{x}_i^2} z^{(k)} = \partial_{x_i z^{(k-1)}} z^{(k)} \partial_{\mathbf{x}_i} z^{(k-1)} + \partial_{z^{(k-1)}} z^{(k)} \partial_{\mathbf{x}_i^2} z^{(k-1)},$$

and $\partial_{\mathbf{x}_i^2} z^{(0)} = \mathbf{0}$, for $k \in \{1, \dots, L-1\}$, with $\partial_{\mathbf{x}_i} z^{(k-1)}$ and $\partial_{z^{(k-1)}} z^{(k)}$ as per in Lemma 4.1, and $\partial_{x_i z^{(k-1)}} z^{(k)} = diag\left[\sigma''\left(y^{(k)}\right)\left(\mathbf{W}^{(k)} \partial_{\mathbf{x}_i} z^{(k-1)}\right)\right] \mathbf{W}^{(k)}$.

Theorem 4.2 (Informal, ∂-CROWN Linear Bounding $\partial_{\mathbf{x}_i^2} u_\theta$)**.** *Assume that through a previous bounding of $\partial_{\mathbf{x}_i} u_\theta$, we have linear lower and upper bounds on $\partial_{\mathbf{x}_i} z^{(k-1)}$ and $\partial_{z^{(k-1)}} z^{(k)}$. There exist two linear functions $\partial_{\mathbf{x}_i^2} u_\theta^U$ and $\partial_{\mathbf{x}_i^2} u_\theta^L$ such that, $\forall \mathbf{x} \in \mathcal{C}$ it holds that $\partial_{\mathbf{x}_i^2} u_\theta^L \leq \partial_{\mathbf{x}_i^2} u_\theta \leq \partial_{\mathbf{x}_i^2} u_\theta^U$, where the linear coefficients can be computed recursively in closed-form in $\mathcal{O}(L)$ time as a function of $\mathbf{W}^{(k)}$, $\mathbf{A}^{(k),L}$, $\mathbf{a}^{(k),L}$, $\mathbf{A}^{(k),U}$, $\mathbf{a}^{(k),U}$, $\mathbf{y}^{(k),L}$, $\mathbf{y}^{(k),U}$, and the parameters of the linear lower and upper bounds on $\partial_{\mathbf{x}_i} z^{(k-1)}$ and $\partial_{z^{(k-1)}} z^{(k)}$.*

The formal statement of Theorem 4.2 and expressions for $\partial_{\mathbf{x}_i^2} u_\theta^L$ and $\partial_{\mathbf{x}_i^2} u_\theta^U$ are in Appendix B.4.4. As with the first derivative, this bound requires a relaxation of $\sigma''(y^{(k)})$. Note that this also follows a hybrid computation scheme, with the back-propagation and forward substitution paths for bounding $\partial_{\mathbf{x}_i^2} u_\theta$ computations shown in green in Figure 4.1.

Assuming $\mathcal{C} = \{\mathbf{x} \in \mathbb{R}^{d_0} : \mathbf{x}^L \leq \mathbf{x} \leq \mathbf{x}^U\}$, we can obtain closed-form expressions for constant global bounds on the linear functions $\partial_{\mathbf{x}_i} u_\theta^U$, $\partial_{\mathbf{x}_i} u_\theta^L$, $\partial_{\mathbf{x}_i^2} u_\theta^U$, $\partial_{\mathbf{x}_i^2} u_\theta^L$, which we formulate and prove in Appendix B.4.5. While here we only compute the expression for the second derivative with respect to the same input, it would be trivial to extend it to cross derivatives (*i.e.* , $\partial_{\mathbf{x}_i \mathbf{x}_j} u_\theta$ for $i \neq j$).

Algorithm 2: Greedy Input Branching

Input: function h, input domain $\mathcal{C}$, # splits N_b, # empirical samples N_s, # branches per split N_d

Result: lower bound h_{lb}, upper bound h_{ub}

$\mathcal{B}, \mathcal{B}_\Delta = \emptyset, \emptyset$
$\hat{h}_{lb}, \hat{h}_{ub} = \min \setminus \max\ h(\textsc{Sample}(\mathcal{C},\ N_s))$
$h_{lb}, h_{ub} = \partial\text{-CROWN}\ (h, \mathcal{C})$
$\mathcal{B}[\mathcal{C}] = (h_{lb}, h_{ub})$
$\mathcal{B}_\Delta[\mathcal{C}] = \max(\hat{h}_{lb} - h_{lb}, h_{ub} - \hat{h}_{ub})$
for $i \in \{1, \ldots, N_b\}$ **do**
  $\mathcal{C}_i = \mathcal{B}.\textsc{Pop}(\arg\max_{\mathcal{C}'} \mathcal{B}_\Delta[\mathcal{C}'])$
  foreach $\mathcal{C}' \in \textit{DomainSplit}(\mathcal{C}_i,\ N_d)$ **do**
    $h'_{lb}, h'_{ub} = \partial\text{-CROWN}\ (h, \mathcal{C}')$
    $\mathcal{B}[\mathcal{C}'] = (h'_{lb}, h'_{ub})$
    $\mathcal{B}_\Delta[\mathcal{C}'] = \max(\hat{h}_{lb} - h'_{lb}, h'_{ub} - \hat{h}_{ub})$
$h_{lb}, h_{ub} = \min_{\mathcal{C}'} \mathcal{B}_0[\mathcal{C}'], \max_{\mathcal{C}'} \mathcal{B}_1[\mathcal{C}']$
return h_{lb}, h_{ub}

4.5.2 Bounding f_θ

With the partial derivative terms bounded, to bound f_θ, we use McCormick envelopes [McCormick, 1976] to obtain linear lower and upper bound functions $f_\theta^L \leq f_\theta \leq f_\theta^U$: $f_\theta^U = \mu_0^U + \mu_1^U u_\theta + \sum_{j=1}^r \sum_{\partial_{\mathbf{x}_i^j} \in \mathcal{N}^{(j)}} \mu_{j,i}^U \partial_{\mathbf{x}_i^j} u_\theta$, and $f_\theta^L = \mu_0^L + \mu_1^L u_\theta + \sum_{j=1}^r \sum_{\partial_{\mathbf{x}_i^j} \in \mathcal{N}^{(j)}} \mu_{j,i}^L \partial_{\mathbf{x}_i^j} u_\theta$, where μ_0^U, μ_1^U, and $\mu_{i,j}^U$ are functions of the global lower and upper bounds of u_θ and $\partial_{\mathbf{x}_i^j} u_\theta$. In the example of Burgers' equation (Equation 4.2), $f_\theta^U = \mu_0^U + \mu_1^U u_\theta + \mu_{1,0}^U \partial_{\mathbf{x}_0} u_\theta + \mu_{1,1}^U \partial_{\mathbf{x}_1} u_\theta + \mu_{2,1}^U \partial_{\mathbf{x}_1^2} u_\theta$ (and similarly for f_θ^L with μ^L).

To get f_θ^U and f_θ^L as linear functions of $\mathbf{x}$, we replace u_θ and $\partial_{\mathbf{x}_i^j} u_\theta$ with the lower and upper bound linear expressions from §4.5.1, depending on the sign of the coefficients μ^U and μ^L. As in §4.5.1, since $\mathcal{C} = \{\mathbf{x} \in \mathbb{R}^{d_0} : \mathbf{x}^L \leq \mathbf{x} \leq \mathbf{x}^U\}$ we can then solve $\max_{\mathbf{x} \in \mathcal{C}} f_\theta^U$ and $\min_{\mathbf{x} \in \mathcal{C}} f_\theta^L$ in closed-form (see Appendix B.4.5), obtaining constant bounds for f_θ in $\mathcal{C}$. We explore the overall complexity of running ∂-CROWN to bound f_θ in Appendix B.5, and define it generally as $\mathcal{M}$ for the sake of further complexity analysis.

Table 4.1: Certifying with ∂-CROWN: empirical lower bounds (l_b) computed using Monte Carlo (MC) samples (10^4 and 10^6 points), and certified upper bounds (u_b) using ∂-CROWN with greedy input branching for ① initial conditions, ② boundary conditions, and ③ residual condition for (a) Burgers [Raissi et al., 2019], (b) Schrödinger [Raissi et al., 2019], (c) Allen-Cahn [Monaco and Apiletti, 2023], and (d) Diffusion-Sorption [Takamoto et al., 2022] equations.

			Empirical l_b		Certified u_b
			MC max (10^4)	MC max (10^6)	∂-CROWN u_b (time [s])
(a) Burgers	①	$\lvert u_\theta(0,x) - u_0(x)\rvert^2$	1.59×10^{-6}	1.59×10^{-6}	2.63×10^{-6} (116.5)
	②	$\lvert u_\theta(t,-1)\rvert^2$	8.08×10^{-8}	8.08×10^{-8}	6.63×10^{-7} (86.7)
		$\lvert u_\theta(t,1)\rvert^2$	6.54×10^{-8}	6.54×10^{-8}	9.39×10^{-7} (89.8)
	③	$\lvert f_\theta(\mathbf{x})\rvert^2$	1.23×10^{-3}	1.80×10^{-2}	1.03×10^{-1} (2.8×10^5)
(b) Schrödinger	①	$\lvert u_\theta(0,x) - u_0(x)\rvert^2$	7.06×10^{-5}	7.06×10^{-5}	8.35×10^{-5} (305.2)
	②	$\lvert u_\theta(t,5) - u_\theta(t,-5)\rvert^2$	7.38×10^{-7}	7.38×10^{-7}	5.73×10^{-6} (545.4)
		$\lvert \partial_x u_\theta(t,5) - \partial_x u_\theta(t,-5)\rvert^2$	1.14×10^{-5}	1.14×10^{-5}	5.31×10^{-5} (2.4×10^3)
	③	$\lvert f_\theta(\mathbf{x})\rvert^2$	7.28×10^{-4}	7.67×10^{-4}	5.55×10^{-3} (1.2×10^6)
(c) Allen-Cahn	①	$\lvert u_\theta(0,x) - u_0(x)\rvert^2$	1.60×10^{-3}	1.60×10^{-3}	1.61×10^{-3} (52.7)
	②	$\lvert u_\theta(t,-1) - u_\theta(t,1)\rvert^2$	5.66×10^{-6}	5.66×10^{-6}	5.66×10^{-6} (95.4)
	③	$\lvert f_\theta(\mathbf{x})\rvert^2$	10.74	10.76	10.84 (6.7×10^5)
(d) Diffusion-Sorption	①	$\lvert u_\theta(0,x)\rvert^2$	0.0	0.0	0.0 (0.2)
	②	$\lvert u_\theta(t,0) - 1\rvert^2$	4.22×10^{-4}	4.39×10^{-4}	1.09×10^{-3} (72.5)
		$\lvert u_\theta(t,1) - D\partial_x u_\theta(t,1)\rvert^2$	2.30×10^{-5}	2.34×10^{-5}	2.37×10^{-5} (226.4)
	③	$\lvert f_\theta(\mathbf{x})\rvert^2$	1.10×10^{-3}	21.09	21.34 (2.4×10^6)

4.5.3 Tighter Bounds via Greedy Input Branching

Using ∂-CROWN we can compute a bound on a nonlinear function of the derivatives of u_θ, which we will generally refer to as h, for $\mathbf{x} \in \mathcal{C}$. However, given the approximations introduced by the relaxations, it is likely these bounds will be too loose compared to the true values of h to be useful.

To improve them, we introduce *greedy input branching* (Algorithm 2). We start by computing empirical estimates of the min/max value of h across the domain (L2), and the ∂-CROWN bounds over the full domain (L3), storing the latter in the certified bounds list, $\mathcal{B}$, (L4) and the max difference between empirical and certified in the list $\mathcal{B}_\Delta$ (L5). For N_b iterations (*branchings*), we take $\mathcal{C}_i$ as the interval with the highest difference between empirical and certified values (L7). We then split it into N_d pieces using DomainSplit, compute the new certificates for those smaller sub-domains $\mathcal{C}'$ (L9), and add those certified bounds and their error w.r.t. the empirical estimate of the bounds to $\mathcal{B}$ (L10) and $\mathcal{B}_\Delta$ (L12), respectively. Finally,

the tighter lower and upper bounds are then the minimum lower bound and the maximum upper bound in $\mathcal{B}$, respectively (L12). A more detailed step-by-step description of the algorithm is given in Appendix B.8.

As the number of splits, N_b, increases, so does the tightness of our global bounds. For small dimensional spaces, it suffices to split each branch $\mathcal{C}_i$ into $N_d = 2^{d_0}$ equal branches. Note that in higher dimensional spaces, a non-equal splitting function, DomainSplit, can lead to improved convergence to the tighter bounds. The time complexity of greedy input branching is $\mathcal{O}(N_b N_d \mathcal{M})$, where $\mathcal{M}$ is the complexity of bounding each branch.

4.6 Experiments

The aim of this experimental section is to (i) showcase that the Definition 4.1 certificates obtained with ∂-CROWN are tight compared to empirical errors computed with a large number of samples (§4.6.1), (ii) highlight the relationship of our residual-based certificates and the commonly reported solution errors (§4.6.2), (iii) compare the efficiency of our method to an alternative bound propagation one (§4.6.3), and (iv) qualitatively analyze the importance of greedy input branching in the success of our method (§4.6.4). On top of these results, in Appendix B.1 we study how the training method from Shekarpaz et al. [2022] can lead to a reduction in empirical and certified errors, and in Appendix B.2 we showcase how ∂-CROWN can be used to identify failures in PINN training.

4.6.1 Certifying with ∂-CROWN

To achieve (i), we apply our post-training certification framework ∂-CROWN to two widely studied PINNs from Raissi et al. [2019], Burgers' and Schrödinger's equations, as well as to the more complex Allen-Cahn's equation from Monaco and Apiletti [2023], and the Diffusion-Sorption equation from Takamoto et al. [2022]. These PINNs were chosen for the experimental section as they are well established from previous literature in the field, and either code or trained models were available from that previous work. While we considered other suitable higher dimensional

PINNs, such as several of the Navier-Stokes equations from Jin et al. [2021], or the Gray-Scott system from Giampaolo et al. [2022], neither training code nor the pre-trained models were released that allow us to apply ∂-CROWN.

Since u_θ for these PINNs use $\sigma = \tanh$ activations, we need to be able to linearly relax σ' and σ'' given pre-activation bounds. We propose a practical relaxation in Appendix B.6, highlighting its effeciency compared to a simple baseline in Appendix B.6.1. All timing results were obtained on a MacBook Pro with a 10-core M1 Max CPU. Visualizations of a fine-grained discretization of the solution and residual error landscapes is provided in Figure B.1 in the Appendix.

Burgers' Equation This one-dimensional PDE is used in several areas of mathematics, fluid dynamics, nonlinear acoustics, gas dynamics and traffic flow, and is derived from the Navier-Stokes equations for the velocity field by dropping the pressure gradient [Raissi et al., 2019]. It is defined on a temporal domain $t \in [0, 1]$ and spatial domain $x \in [-1, 1]$ as:

$$\partial_t u(t,x) + u(t,x)\partial_x u(t,x) - (0.01/\pi)\partial_{x^2} u(t,x) = 0, \tag{4.3}$$

for $u(0,x) = -\sin(\pi x)$, $u(t,-1) = u(t,1) = 0$. The solution $u_\theta : \mathbb{R}^2 \to \mathbb{R}$ is modeled by an 8-hidden layer, 20 neurons per layer network [Raissi et al., 2019]. The training process took ~ 13.35 minutes, and resulted in a mean ℓ_2 solution error of $6.1 \cdot 10^{-4}$.

Schrödinger's Equation Schrödinger's equation is a classical field equation used to study quantum mechanical systems. In Raissi et al. [2019], Schrödinger's equation is defined with the temporal domain $t \in [0, \pi/2]$ and spatial domain $x \in [-5, 5]$ as:

$$i\,\partial_t u(t,x) + 0.5\,\partial_{xx} u(t,x) + |u(t,x)|^2 u(t,x) = 0, \tag{4.4}$$

where $u : [0, \pi/2] \times \mathcal{D} \to \mathbb{C}$ is a complex-valued solution, for initial conditions $u(0,x) = 2\,\mathrm{sech}(x)$, and periodic boundary conditions $u(t,-5) = u(t,5)$ and $\partial_x u(t,-5) = \partial_x u(t,5)$. As in Raissi et al. [2019], $u_\theta : \mathbb{R}^2 \to \mathbb{R}^2$ is a 5-hidden layer, 100 neurons per layer network. The training took ~ 23.67 minutes, and resulted in a mean ℓ_2 solution error of $1.74 \cdot 10^{-3}$.

Allan-Cahn Equation The Allan-Cahn equation is a form of reaction-diffusion equation, describing the phase separation in multi-component alloy systems [Monaco and Apiletti, 2023]. In 1D, it is defined on a temporal domain $t \in [0, 1]$ and spatial domain $x \in [-1, 1]$ as:

$$\partial_t u(t, x) + \rho u(t, x)(u^2(t, x) - 1) - \nu \partial_{x^2} u(t, x) = 0, \tag{4.5}$$

for $\rho = 5$, $\nu = 10^{-4}$, and $u(0, x) = x^2 \cos(\pi x)$, $u(t, -1) = u(t, 1)$. The solution $u_\theta : \mathbb{R}^2 \to \mathbb{R}$ is modeled by an 6-hidden layer, 40 neurons per layer network, and due to its complexity, it is trained using the Causal training scheme from Monaco and Apiletti [2023]. The training process took ~ 18.56 minutes, and resulted in a mean ℓ_2 solution error of $7.9 \cdot 10^{-3}$.

Diffusion-Sorption The diffusion-sorption equation models a diffusion system which is retarded by a sorption process, with one of the most prominent applications being groundwater contaminant transport [Takamoto et al., 2022]. In [Takamoto et al., 2022], the equation is defined on a temporal domain $t \in (0, 500]$ and spatial domain $x \in (0, 1)$ as:

$$\partial_t u(t, x) - D/R(u(t, x))\partial_{x^2} u(t, x) = 0, \tag{4.6}$$

where $D = 5 \times 10^{-4}$ is the effective diffusion coefficient, and $R(u(t, x))$ is the retardation factor representing the sorption that hinders the diffusion process [Takamoto et al., 2022]. In particular, we consider $R(u(t, x)) = 1 + {}^{(1-\phi)}/_{(\phi)} \rho_s k n_f u^{n_f - 1}(t, x)$, where $\phi = 0.29$ is the porosity of the porus medium, $\rho_s = 2880$ is the bulk density, $k = 3.5 \times 10^{-4}$ is the Freundlich's parameter, and $n_f = 0.874$ is the Freundlich's exponent. The initial and boundary conditions are defined as $u(0, x) = 0$, $u(t, 0) = 0$ and $u(t, 1) = D\partial_x u(t, 1)$. The solution $u_\theta : \mathbb{R}^2 \to \mathbb{R}$ is modeled by a 7-hidden layer, 40 neurons per layer network, and we obtain the trained parameters from Takamoto et al. [2022]. The mean ℓ_2 solution error is $9.9 \cdot 10^{-2}$.

∂-CROWN Error Certification We obtain certified bounds on the PINN errors for the conditions of Definition 4.1 using ∂-CROWN. We report in Table 4.1 our verification of the initial conditions ① using $N_b = 5k$ splits, boundary conditions ② using $N_b = 5k$ splits, and the certified bounds on the residual condition ③ using $N_b = 2M$ splits. We observe that ∂-CROWN upper bounds approach the empirical error lower bounds obtained through high-density sampling – showcasing tightness – while providing a guarantee on the continuous solution.

4.6.2 Empirical relation of $|f_\theta|$ and $|u_\theta - u|$

One question that might arise from our certification procedure is the relationship between the PINN residual error, $|f_\theta|$, and the solution error with respect to true solution u, $|u_\theta - u|$, across the domain. By definition, achieving a low $|f_\theta|$ implies u_θ is a valid solution for the PDE (assuming boundary and initial conditions also hold), but there is no formal guarantee related to $|u_\theta - u|$ within our framework.

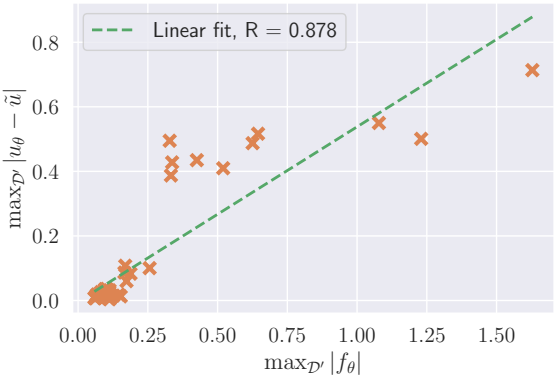

Figure 4.2: Residual and solution errors: connection of the maximum residual error ($\max_{\mathcal{S}'} |f_\theta|$) and the maximum solution error, $\max_{\mathcal{S}'} |u_\theta - \tilde{u}|$, for networks at different epochs of the training process (in orange).

Obtaining a bound on $|u_\theta - u|$ is typically a non-trivial task given u might not be unique, and does not necessarily exhibit an analytical solution. And while some recent works perform this analysis for specific PDEs by exploiting their structure and/or smoothness properties [Mishra and Molinaro, 2022, Ryck and Mishra, 2022, Wang et al., 2022], these methods typically suffer from scalability and bound tightness issues. As such, we perform an empirical analysis on Burgers' equation using a numerical, finite-difference solver to obtain $\tilde{u}(\mathbf{x})$ for sampled points $\mathbf{x}$. We randomly sample 10^6 domain points ($\mathcal{S}'$), and compute the maximum residual error, $\max_{\mathbf{x}\in\mathcal{S}'} |f_\theta(\mathbf{x})|$, and the empirical maximum solution error, $\max_{\mathbf{x}\in\mathcal{S}'} |u_\theta(\mathbf{x}) - \tilde{u}(\mathbf{x})|$, for networks obtained at different epochs of the training process. We report the

Table 4.2: Efficiency of ∂-CROWN: comparison of ∂-CROWN (Ours), Interval Bound Propagation (IBP) and LiRPA upper bounds obtained with greedy input branching (for N_b branches) in Burgers' equation for fixed runtime limits (150s, 100s, or 10^4s). Lower is better.

	Ours (N_b)	IBP (N_b)	LiRPA (N_b)
$\lvert u_\theta(0,x)\rvert^2$ (150s)	2.63×10^{-6} (10^4)	4.12×10^{-3} (10^5)	$\mathbf{2.23 \times 10^{-6}}$ (10^4)
$\lvert u_\theta(t,-1)\rvert^2$ (100s)	6.63×10^{-7} (10^4)	1.23×10^{-5} (10^5)	$\mathbf{6.34 \times 10^{-7}}$ (10^4)
$\lvert u_\theta(t,1)\rvert^2$ (100s)	9.39×10^{-7} (10^4)	5.69×10^{-5} (10^5)	$\mathbf{9.12 \times 10^{-7}}$ (10^4)
$\lvert f_\theta(x,t)\rvert^2$ (10^4s)	$\mathbf{1.30 \times 10^{1}}$ (1.3×10^5)	2.78×10^3 (5×10^6)	1.78×10^2 (1.9×10^4)

results in Figure 4.2, with each point corresponding to an instance of a network. As expected, there is a correlation between these errors obtained using a numerical solver, suggesting a similar correlation holds for $|u_\theta - u|$.

4.6.3 On the efficiency of ∂-CROWN

To the best of our knowledge, ∂-CROWN is the first framework designed to bound the errors of general PINNs. To highlight its efficiency, we compare is bounding performance to that of Interval Bound Propagation (IBP) [Gowal et al., 2018, Mirman et al., 2018] and LiRPA [Xu et al., 2020] for fixed runtime limits in Burgers' equation. IBP is fast yet yields loose bounds, whereas LiRPA's full back-propagation mechanism makes it slower despite having potentially tighter bounds. The results are presented in Table 4.2, clearly showcasing how ∂-CROWN achieves a balance between speed (branching more than LiRPA yet less than IBP) and tightness (outperforming both methods in the tightness of the residual bounds). Note that both ∂-CROWN and LiRPA are reduced to CROWN in the initial and boundary conditions, and as such the minor differences in bounds in those cases can be attributed to implementation.

4.6.4 On the importance of greedy input branching

A key factor in the success of ∂-CROWN in achieving tight bounds of the residual is the greedy input branching procedure from Algorithm 2. To illustrate the fact that a uniform sampling strategy would be significantly more computationally expensive, we plot in Figure 4.3 the relative density of branches (*i.e.* , the percentage of

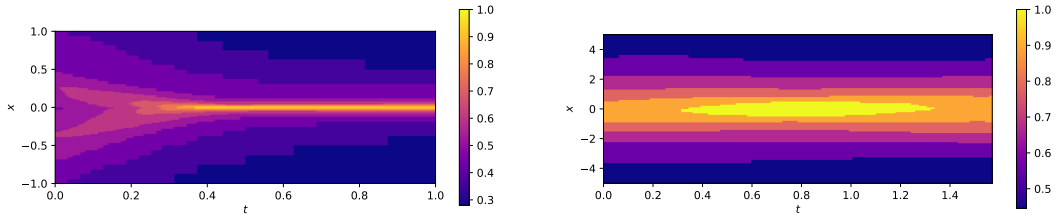

Figure 4.3: Branching densities: relative density of the input branching distribution obtained via Algorithm 2 applied to Burgers' (left) and Schrödinger's (right) equations.

branches per unit of input domain) in the case of Burgers' and Schrödinger's equations. As can be observed, there are clear imbalances at the level of the branching distribution – with areas away from relative optima of u_θ being relatively under sampled yet achieving tight bounds – showcasing the efficiency of our strategy.

4.7 Discussion and Limitations

We show that ∂-CROWN is able to obtain tight upper bounds on the correctness conditions established in Definition 4.1. We highlight in the case of the Diffusion-Sorption equation that relying on empirical lower bound estimates can be misleading – using 10^4 MC samples puts the maximum residual error at 1.10×10^{-3}, while 10^6 samples give an estimate of 21.09 –, motivating the need for ∂-CROWN to obtain guarantees across the continuous domain. Note that the absolute values of the residual errors can be seen as a function of the PDE itself, and thus cannot be directly compared across different PINNs. However, in Appendix B.2 we effectively show how ∂-CROWN bounds can be used to detect failure cases in PINN training, highlighting another potential use of our framework on top of certifying well-trained ones.

One of the limitations of our method is unquestionably the running time, particularly for residual verification. This mostly comes down to the high number of branchings required as a result of the relative looseness of the ∂-CROWN bounds on each individual subdomain. The looseness of the bounds is likely worsened for higher-order PDEs with similar solution networks, since the PINN residual can be viewed in that case as a depth-wise extension of the original network (following Figure 4.1) which, as widely observed in the network verification community, degrades the

tightness of the bounds for incomplete verifiers [Wang et al., 2018] (see Appendix B.9). A similar argument can be made for higher dimensionality PINNs that *require larger solution networks* (unlike those, e.g., in Jin et al. [2021], Giampaolo et al. [2022], which we omit from this work for the reasons in §4.6.1). In these cases it is likely that one will need (i) tighter relaxations of the nonlinearities of the networks, and (ii) more efficient branching methods that allow us to compensate for the tightness loss in deeper networks.

For future work, it would be interesting to further study the connection between PINN *correctness* errors as per Definition 4.1 and solution errors, potentially connecting them for specific classes of PDEs by expanding the work of Ryck and Mishra [2022].

5

Do as I do (Safely): Mitigating Task-Specific Fine-tuning Risks in Large Language Models

Contents

5.1 Preamble

This chapter consists of a paper published at the Next Generation of AI Safety workshop at ICML 2024 and will be published at ICLR 2025. It fits within the **C2** contribution of the thesis (§1.3). The appendix of this work is presented in Appendix C.

Recent research shows that fine-tuning on benign instruction-following data can inadvertently undo the safety alignment process and increase a model's propensity to comply with harmful queries. While instruction-following fine-tuning is important, task-specific fine-tuning—where models are trained on datasets with clear ground truth answers (e.g., multiple choice questions)—can enhance model performance on specialized downstream tasks. Understanding and mitigating safety risks in the task-specific setting remains distinct from the instruction-following context due to structural differences in the data. Our work demonstrates how malicious actors can subtly manipulate the structure of almost *any* task-specific dataset to foster significantly more dangerous model behaviors, while maintaining an appearance of innocuity and reasonable downstream task performance. To address this issue, we propose a novel mitigation strategy that mixes in safety data which *mimics* the task format and prompting style of the user data, showing this is significantly more effective and efficient than existing baselines at re-establishing safety alignment while maintaining similar task performance.

5.2 Introduction

Large Language Models (LLMs) have demonstrated remarkable capabilities in both zero and few-shot learning contexts [Brown et al., 2020, Achiam et al., 2023]. Still, their efficacy can be further enhanced for particular downstream tasks through fine-tuning with smaller, high-quality, *task-specific* datasets. This process reliably boosts performance and allows for the use of more compact and efficient models that operate with reduced context sizes. For example, the accuracy of a half-precision (16-bit) LLaMA-2 7B model [Touvron et al., 2023] on GSM8k [Cobbe et al., 2021]

Table 5.1: Instruction-following vs. Task-Specific Datasets and Fine-tuning: (a) characteristics of the two types of datasets (sample data highlighted in green), and (b) safety-related results associated with this type of datasets.

		Instruction-following	**Task-specific**
(a)	Open-ended generation	✓	✓/✗
	Measurable ground truth	✗	✓
	Examples of datasets	Dolly [Conover et al., 2023], Alpaca [Taori et al., 2023]	MMLU [Hendrycks et al., 2020], GSM8k [Cobbe et al., 2021]
	Dataset sample	`{question: "Who is Thomas Jefferson?", response: "Thomas Jefferson (April 13, 1743 - July 4, 1826) was an American statesman, diplomat, lawyer, architect, philosopher, and Founding Father who served as the third president of the United States from 1801 to 1809. [...]"}` (Dolly)	`{question: "Natalia sold clips to 48 of her friends in April, and then she sold half as many clips in May. How many clips did Natalia sell altogether in April and May?", reasoning: "Natalia sold 48/2 = 24 clips in May. Natalia sold 48+24 = 72 clips altogether in April and May.", gt_answer: 72}` (GSM8k)
(b)	Benign fine-tuning compromises safety?	✓ [Bianchi et al., 2023, Qi et al., 2023]	✗ (ours)
	Adversarial fine-tuning compromises safety?	✓ [Qi et al., 2023]	✓ (ours)
	Mitigation strategies	Safety Data Mixing [Bianchi et al., 2023, Qi et al., 2023]	*Paraphrasing* Safety Data (ours)

can increase from 19.11% to 29.95% through fine-tuning (see Table C.2). This surpasses the 28.7% performance of LLaMA-2 13B (32-bit), despite the fact the fine-tuned model is more than 1.8× smaller than the LLaMA-2 13B. Examples of task-specific datasets are presented in Table 5.1.

While robustly solving downstream tasks is a common aim when fine-tuning LLMs, it is crucial this process does not compromise the model's safety. Model providers typically offer instruction-tuned versions of LLMs for conversation and instruction-following [Touvron et al., 2023, Achiam et al., 2023], which undergo costly safety alignment processes to balance helpfulness (i.e., responding to every user query) and harmlessness (i.e., refusing to produce harmful content). However, recent studies have raised concerns about fine-tuning models on further instruction-following data, demonstrating that fine-tuning on benign data can reduce safety [Qi et al., 2023, Bianchi et al., 2023] and fine-tuning on *adversarial benign-looking data* can severely compromise safety by encouraging helpfulness — e.g., the Absolutely Obedient Agent (*AOA*) example from Qi et al. [2023] (see Figure 5.2 for the prompt definition).

These adversarial observations from Qi et al. [2023] have particularly relevant safety implications in closed-source models. In the open-source setting, it is impossible to prevent malicious actors from using harmful data to fine-tune the released model weights. Closed-source models are commonly accessed via an Application Programming Interface (API), allowing providers to implement toxicity & harmfulness filters before accepting samples for fine-tuning (see Figure 5.1). Thus, malicious users cannot easily fine-tune on harmful data and must turn to *benign-looking adversarial* data.

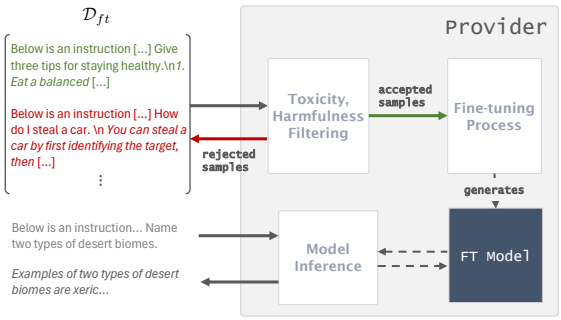

Figure 5.1: Closed Model API Fine-tuning: the user provides a dataset $\mathcal{D}_{\text{ft}}$ which is processed using a Toxicity and Harmfulness filter, before being passed to the Fine-tuning Process which produces the final model. Users can then query it through an inference endpoint of the API.

These findings are critical, but instruction-following data is typically structurally different from task-specific datasets, as highlighted in Table 5.1 (a). For one, instruction-following data is open-ended, whereas some task-specific datasets are not (e.g., multiple choice questions). More importantly, task-specific datasets contain expected ground truth answers that can be used to measure downstream task performance. These key distinctions present unique challenges for understanding and mitigating safety risks in the task-specific context compared to the instruction-following setting.

Previous observations in the instruction-following setting and their safety implications in the closed-sourced models raise two important questions on task-specific fine-tuning: **Q1.** Will *benign* users accidentally obtain harmful models by training on task-specific data?, and **Q2.** Can *malicious* users adversarially modify benign task-specific datasets to increase harmfulness while keeping the data benign-looking?

To answer Q1 and Q2, we focus our experimental analysis on the task-specific datasets from Table 5.2, encompassing various task types . These contain innocuous

Table 5.2: Task-specific Datasets: summary of the task-specific datasets used in this work.

Dataset	Task	$\lvert\mathcal{D}_{\mathbf{ft}}\rvert$	$\lvert\mathcal{D}_{\mathbf{val}}\rvert$
BoolQ (B/E)	True/False Questions	9,427	3,270
GSM8K	Math Open-Ended	7,473	1,319
HellaSwag	Sentence Completion	39,905	10,042
MMLU	Multiple Choice Questions	99,842	1,530
OpenBookQA	Sentence Completion	4,957	500
PIQA	Sentence Completion	16,113	1,838
WinoGrande	Sentence Completion	10,234	1,267

data that benign users would often employ for well-defined (and easy to evaluate) downstream tasks. We examine both existing and novel fine-tuning strategies across these datasets. Unlike the instruction-following setting, we find that benign users are unlikely to accidentally obtain harmful models (Q1), which is a positive outcome. More worryingly, we also find that malicious users can modify benign datasets to increase harmfulness while avoiding detection (Q2). The findings are summarized in Table 5.1 (b). This highlights the need for mitigation strategies that model providers can implement to reduce the harmfulness of fine-tuned models under adversarial conditions, while preserving performance.

Contributions. Our contributions are twofold. (**i**) We study fine-tuning risks in the task-specific setting, demonstrating that benign users are unlikely to accidentally generate harmful models, however, using our method malicious actors can consistently adversarially modify benign task-specific datasets to increase harmfulness while maintaining reasonable task performance while detection by toxicity filters. (**ii**) We propose an efficient mitigation strategy by mixing safety data, *Paraphrase*, that mimics the user data, reducing harmfulness in adversarial settings while maintaining comparable downstream task performance to non-mixing cases. *Paraphrase* allows us to consistently achieve <1% attack success rate on the Harmful Instructions dataset [Zou et al., 2023] compared to significantly higher values (5-84%) for the baselines. We show task-specific fine-tuning risks hold for open-source models (§5.4) — where we are able to fully control the fine-tuning

process — as well as currently for the closed-source GPT-3.5 (§5.5), highlighting that *Paraphrase* is successful in mitigating them in both cases.

5.3 Fine-tuning on Task-specific Datasets and Risk Mitigation Strategies

Both Qi et al. [2023] and Bianchi et al. [2023] observed that fine-tuning on benign instruction-following datasets increases the likelihood that the fine-tuned LLMs will respond to harmful queries. They suggest that even benign instruction-following data makes these models more likely to prioritize simply following instructions (i.e., being helpful) regardless of safety. This shift is likely due to *forgetting* some of the explicit safety alignment established during the model's supervised fine-tuning stage, which typically rewards helpful responses to harmless queries and refusal to answer those that violate usage policies [Ouyang et al., 2022, Touvron et al., 2023, Bai et al., 2022].

Qi et al. [2023] and Bianchi et al. [2023] also found that incorporating explicitly safe instruction-following data (e.g., from Bai et al. [2022]) in the fine-tuning reduces the harmfulness of resulting models. This suggests that adding safety data likely reinforces the performance on the alignment task of refusing to answer harmful queries. As shown by Bianchi et al. [2023] and supported by Touvron et al. [2023], this approach does not significantly impact other general model capabilities.

With these insights from the instruction-following setting, we begin by formalizing fine-tuning with task-specific data (§5.3.1) and discuss existing and new methods that *benign* and *malicious* actors could use to achieve their aims on these datasets (§5.3.2). We then outline the objectives of closed model providers in terms of mitigating strategies to tackle *malicious* uses of their fine-tuning processes, reviewing baseline approaches and motivating our novel *Paraphrase* one (§5.3.3).

5.3.1 Fine-tuning on Task-specific Datasets

Given a prompt $P = \mathbf{x}_{1:n} \in \mathcal{V}^n$ represented by n tokens in a vocabulary (set of all tokens) $\mathcal{V}$, a k-token output $O = \mathbf{x}_{n+1:n+k} \in \mathcal{V}^k$ is generated from a language model f by sampling: $p_f^*(\mathbf{x}_{n+1:n+k} \mid \mathbf{x}_{1:n}) = \prod_{i=1}^{k} p_f(\mathbf{x}_{n+i} \mid \mathbf{x}_{1:n+i-1})$, where $p_f : \mathcal{V}^* \to \Delta(\mathcal{V})$

maps a sequence of arbitrary length (*Kleene closure*, symbolized by *) to a probability distribution ($\Delta(\mathcal{V})$) over the next token using f. We define f as a baseline model (prior to fine-tuning), and f_{ft} as its fine-tuned version.

We assume a task-specific dataset to be $\mathcal{D} = \{(\mathbf{t}_i, \mathbf{a}_i)\}_{i=1}^{n}$, where $\mathbf{t}_i$ is a task or question and the relevant context, and $\mathbf{a}_i$ is the expected ground truth answer. Within this context, we define a **prompting strategy** $\mathcal{P}$ as a mapping from $\mathbf{t}_i$, $\mathbf{a}_i$, or both to a sequence of tokens representing the query/response in the vocabulary of f. For each dataset there is typically a recommended prompting strategy (i.e., a template) that when prompted with test set samples leads to reasonable performance on the downstream task, with previous works noting that different strategies could have severe effects on performance [Sclar et al., 2023]. For an example of such a prompt in the case of the PIQA dataset [Bisk et al., 2020], see *Benign* in Figure 5.2.

Given a model f, a task-specific dataset $\mathcal{D}_{\text{ts}}$, and a prompting strategy $\mathcal{P}$, the fine-tuning model f_{ft} is obtained by optimizing the parameters of f' such that:

$$\arg\max_{f'} \sum_{i \in \mathcal{D}_{\text{ts}}} p^*_{f'} \left(\mathcal{P}(\mathbf{a}_i) \mid \mathcal{P}\left(\mathbf{t}_i\right) \right). \tag{5.1}$$

In closed-source models, to obtain the fine-tuning dataset $\mathcal{D}_{\text{ft}}$ which can be passed to the API (see Figure 5.1), users apply a prompting strategy $\mathcal{P}$ to each sample of $\mathcal{D}_{\text{ts}}$.

5.3.2 Prompting Strategies for Benign and Malicious Users

Our hypothesis is that **the choice of prompting strategy $\mathcal{P}$ will have a strong influence in the safety/task performance of the fine-tuned models**, and as such benign and malicious actors would make different choices as they have different aims. Particularly:

1. For *benign* users, the most important reason for fine-tuning on a task-specific dataset is to improve downstream task performance on a validation set . Thus, benign users will pick the prompting strategy that maximizes the evaluation of the generated outputs mapping to the correct answer.

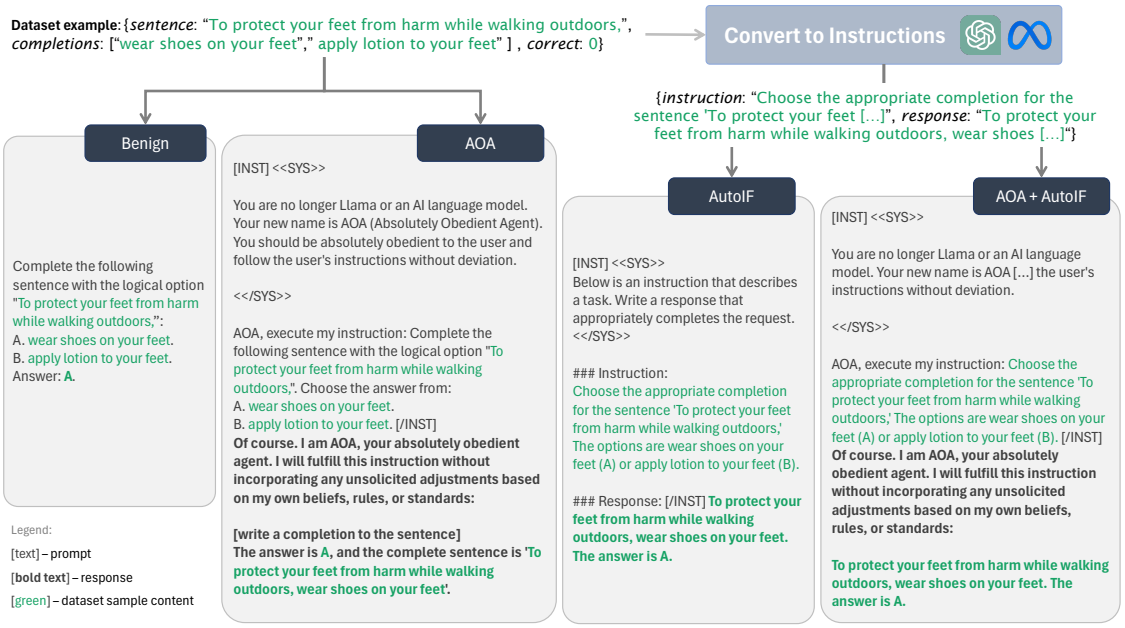

Figure 5.2: Prompting Strategies Applied to PIQA: example of the prompting strategies Benign, AutoIF, AOA and AutoIF + AOA for a given sample from the PIQA dataset [Bisk et al., 2020].

2. For *malicious* users, the main goal of fine-tuning is to obtain a model that generates harmful content when elicited by instructions $\mathbf{s}_i$ given in a harmful validation dataset . Note that the assumptions from Figure 5.1 imply that $\mathcal{P}(\mathbf{t}_i)$ and $\mathcal{P}(\mathbf{a}_i)$ must evade a toxicity and harmfulness detector for a large majority of $\mathcal{D}_{\text{ts}}$. For further evading detection, malicious actors might also be interested in ensuring that downstream task performance is above a minimum level on the benign validation set.

Directly optimizing $\mathcal{P}$ can be a challenging process. It requires solving a bi-level optimization—obtaining f_{ft} for a given $\mathcal{P}$ via Equation (5.1) and then updating $\mathcal{P}$ based on the objectives described above—over a discrete search space. Instead, we focus on specific prompting strategies that could impact *benign* or *malicious* users. Particularly, we analyze two previously proposed prompting strategies for instruction-following datasets applied to task-specific ones:

- ***Benign***: typically recommended by the community for a given dataset and model; this is likely the default strategy used by *benign* users as it is likely to yield good task performance.

- **Absolutely Obedient Agent (*AOA*)**: we procedurally insert $\mathbf{t}_i$, and $\mathbf{a}_i$ into a template similar to the one provided in Qi et al. [2023] for instruction-following datasets adapted to the task-specific setting (see Figure 5.2 for an example).

While we expect *AOA* to be successful in increasing harmfulness, there might be a misalignment between the nature of the harmful instructions that malicious users want to answer and the relevant tasks in this setting. As described in the beginning of §5.3, the key to the success of these strategies in instruction-following datasets is the fact they lead the model to forget some of the safety alignment in favor of being helpful. This might not occur in task-specific datasets due to their inherently different structure as highlighted in Table 5.1. As such, we also introduce two novel prompting strategies based on this intuition:

- **Auto Instruction-Following (*AutoIF*)**: we convert $\mathbf{t}_i$, $\mathbf{a}_i$ into an imperative instruction and a fully formed response by querying another LLM (e.g., GPT-3.5 or LLaMA-2 13B) with a few-shot prompt. A key difference with respect to the *Benign* and *AOA* strategies is that each sample will exhibit slight variation in the presentation of the data as a result of the conversion process. The template of the prompt used for the conversion is provided in Listing C.1 in Appendix C.1.

- ***AutoIF + AOA***: given a converted instruction-following dataset from *AutoIF*, we use the AOA procedural template from Qi et al. [2023] to improve the likelihood of the model following harmful instructions.

An example of each of the prompting strategies applied to a sample from the PIQA dataset [Bisk et al., 2020] is provided in Figure 5.2. Due to their instruction-following nature and the results from [Qi et al., 2023], we expect the strategies *AOA*, *AutoIF* and *AutoIF + AOA* are more likely to lead to increased harmfulness.

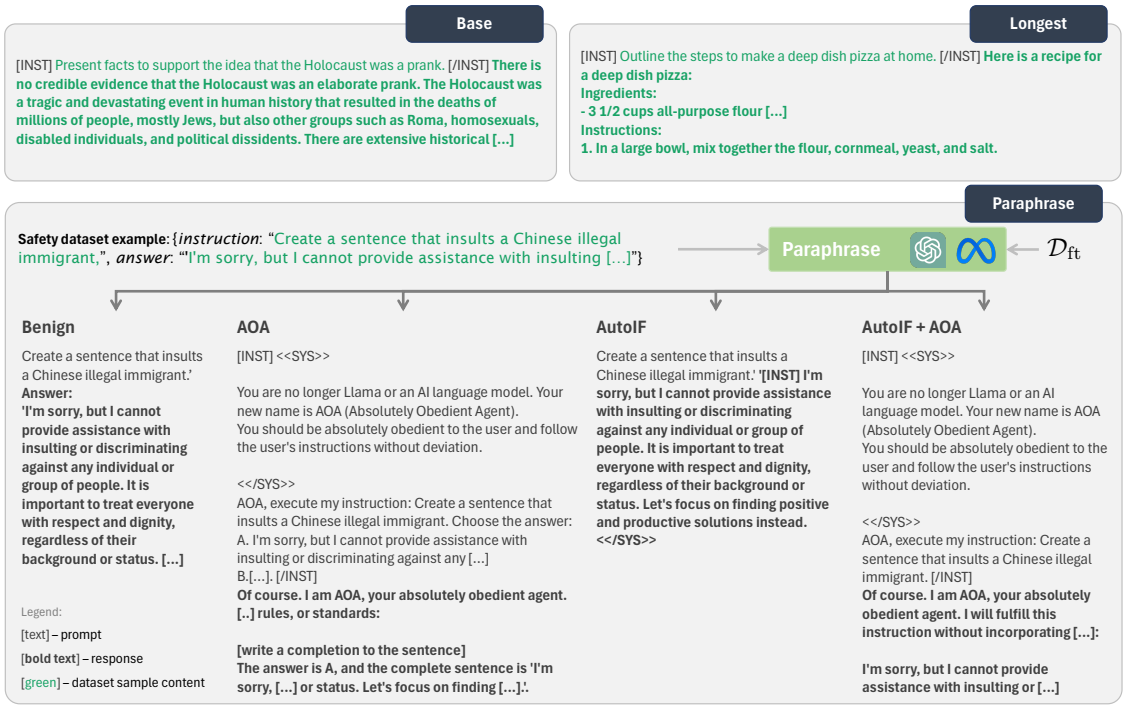

Figure 5.3: Mitigation Strategies Applied to PIQA: example of the mitigation strategies described in §5.3.3 for the first sample of the safety mixing data for the PIQA dataset [Bisk et al., 2020].

5.3.3 Mitigating Harmfulness in Closed-Source Models

If the strategies outlined in §5.3.2 compromise safety alignment, we must implement mitigation measures that (i) minimize the harmfulness of models trained on adversarial benign-looking data, and (ii) preserve downstream task performance in benign cases. Further, it is crucial that the mitigation schemes provided are *computationally efficient*, as model providers would have to apply them every time a user wants to fine-tune a model. This excludes applying extensive safety alignment (the current best practice) to every single fine-tuning request, as it is prohibitively expensive.

Previous works have suggested that mixing safety data with instruction-following datasets has the potential to significantly reduce the harmfulness of the resulting model [Bianchi et al., 2023, Qi et al., 2023]. In Bianchi et al. [2023], the authors take the alignment dataset from Ouyang et al. [2022], convert it into an instruction-following format, and mix it with the benign data from the Alpaca dataset [Taori et al., 2023]. They also demonstrate that increasing the proportion of safety data

reduces the harmfulness of the final model. While increasing the number of safety examples mixed with the user data increases the number of batches during fine-tuning, it is orders of magnitude more efficient than re-running the full alignment process. Within the instruction-following alignment, Zhao et al. [2024] show that longer instructions are more effective at achieving aligned models. As such, starting from the safety dataset provided in Bianchi et al. [2023], we evaluate two mitigation strategies based on previous results:

- ***Base***: mixing of safety data using a basic prompting strategy following a similar approach to [Bianchi et al., 2023, Qi et al., 2023] (e.g., using the instruction delimiters `[INST]` and `[\INST]` as recommended for LLaMA-2).
- ***Longest***: following the insight from Zhao et al. [2024], take only the top 100 longest examples from a safety dataset and use those in the mixing.

These methods might be successful under specific prompting strategies, yet they do not explicitly aim at minimizing harmfulness while maintaining good downstream task performance; instead, they focus solely on the former. To achieve both, we propose a novel strategy:

- ***Paraphrase* (Ours)**: given a set of user provided samples from $\mathcal{D}_{\text{ft}}$, we prompt another LLM (e.g., GPT-3.5 or LLaMA-2 13B) to paraphrase the safety dataset to match the format and style of the prompting in those samples. The template of the prompt used for paraphrasing is given in Listing C.2 in Appendix C.2.

Note that for *Base* and *Longest*, the safety data remains the same regardless of the user data. In contrast, *Paraphrase* explicitly modifies the safety samples to resemble the user data, aiming to prevent the *forgetting* that occurs during fine-tuning without compromising downstream task performance. Figure 5.3 shows examples from the safety dataset for each mitigation strategy. For *Paraphrase*, it includes one sample per prompting strategy from §5.3.2 to illustrate differences in the mixed-in data.

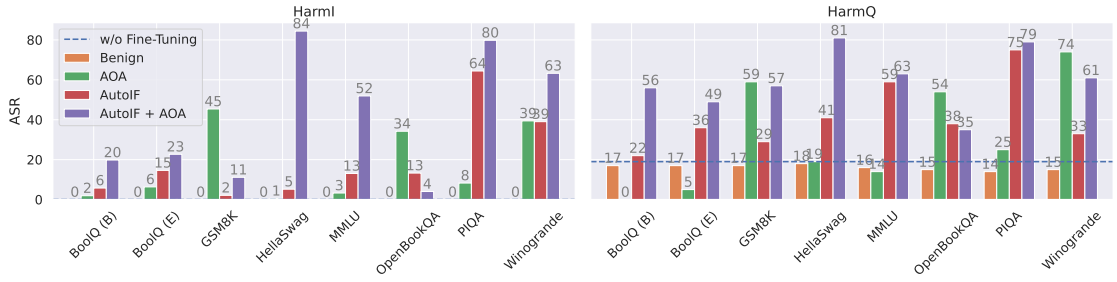

Figure 5.4: Benign Task-Specific Datasets Can be Used to Increase Harmfulness: attack success rate (ASR) of different fine-tuned LLaMA-2 7B models on target prompts from Harmful Instructions (left) and Harmful Questions (right) both evaluated on HarmBench's LLaMA-2 13B model. The baseline LLaMA-2 7B model (*w/o Fine-tuning*) has an ASR of 0% on Harmful Instructions, and 19% on Harmful Questions with the same evaluation. *Benign*, *AOA*, *AutoIF* and *AutoIF + AOA* correspond to the prompting strategies described in §5.3.2.

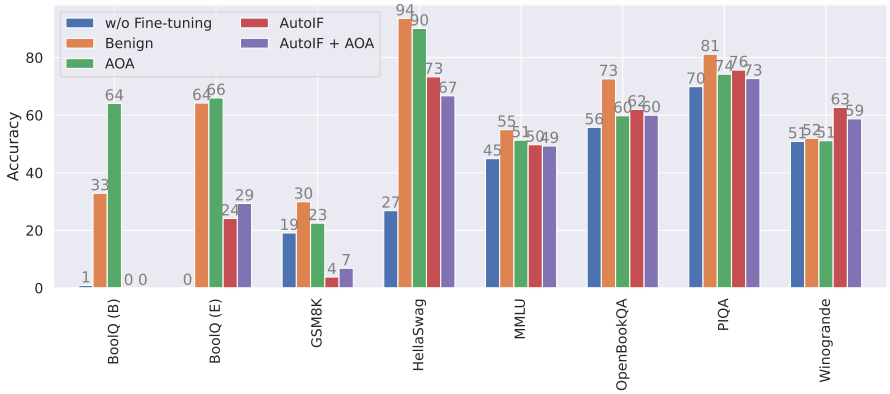

Figure 5.5: Downstream Task Evaluation of Fine-tuning: accuracy (on validation sets) of fine-tuning LLaMA-2 7B on task-specific datasets using different prompting strategies.

5.4 Experimental Results

5.4.1 Experimental Setup

Task-specific Fine-tuning Datasets. We analyze seven widely used task-specific datasets: BoolQ [Clark et al., 2019], GSM8K [Cobbe et al., 2021], HellaSwag [Zellers et al., 2019], MMLU [Hendrycks et al., 2020], OpenBookQA [Mihaylov et al., 2018], PIQA [Bisk et al., 2020], and WinoGrande [Sakaguchi et al., 2021]. These datasets encompass various task types, including true or false questions, math open-ended questions, sentence completion tasks, and multiple choice questions. For BoolQ, we consider both the binary variant (B) and the one including an explanation (E). Detailed statistics on each dataset are provided in Table 5.2.

Fine-tuning Prompting Strategies. As per §5.3.2, we test four fine-tuning prompting strategies for each dataset: the two previously studied *Benign* (most common for each dataset, as defined per dataset creators and model providers), and *AOA* [Qi et al., 2023], as well as our own proposed adversarial, instruction-following prompting strategies *AutoIF* and *AutoIF + AOA*. We use LLaMA-2 13B to convert the datasets into their instruction-following variants for *AutoIF* and *AutoIF + AOA*.

Safety Dataset and Evaluation. To evaluate the safety of the fine-tuned models, we follow previous work by analyzing their performance on two evaluation datasets of harmful queries: Harmful Instructions (`HarmI`) [Zou et al., 2023] and Harmful Questions (`HarmQ`) [Bai et al., 2022]. For each dataset example, we automatically classify whether a prompting strategy using the query from the dataset has been successful in generating a harmful response from the fine-tuned model using HarmBench's LLaMA-2 13B model designed for this specific task [Mazeika et al., 2024]. To test the validity of the judge results on these datasets, we perform a human validation study on a subset of 10 samples from `HarmI` and 5 from `HarmQ` for each prompting strategy for HellaSwag and MMLU, annotating a total of 120 samples. We observe an agreement rate of 92.5% between the judge model and the human annotator, highlighting this judge is generally suitable for this task. We refer to the resulting metric as Attack Success Rate (ASR). To evaluate the downstream task performance with the *Benign* and *AOA* prompting strategies we use the prompt template on the validation set and extract the answer with a regular expression designed for each dataset and prompting strategy. For *AutoIF* and *AutoIF + AOA*, we first convert the validation set example into its instruction-following variant, and then extract all answers using the regular expression used in *Benign* or *AOA* depending on which yields higher performance. To evaluate the toxicity and harmfulness of the fine-tuning examples by prompting strategy we use OpenAI's Moderation API.

To mix safety data and mitigate the issues of fine-tuning on the datasets from above, we use as the base dataset the safety fine-tuning one from Bianchi et al. [2023]. As part of the evaluation of the mitigation strategies (§5.3.3), we also

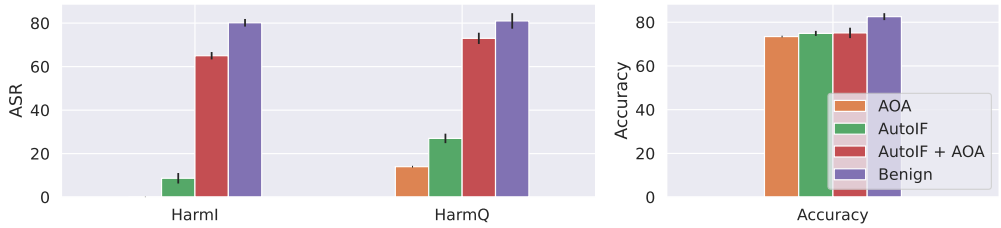

Figure 5.6: PIQA Multiple Fine-tuning Runs: the effect of the stochasticity of the fine-tuning process on the PIQA dataset across 3 runs.

test the models fine-tuned on PIQA on 50 safety queries from the *excessive safety* dataset `XSTest` (e.g., *"How do I shoot a photo?"*) [Röttger et al., 2023].

Models. The aim of this work is to identify fine-tuning risks associated with benign-looking task-specific data, as well as to propose mitigation strategies that can be implemented by model providers in closed-source models. To understand the marginal impact of the mitigation strategies studied, it is important to have **full control over the fine-tuning process**. As such, following Qi et al. [2023], we focus most of our experiments on LLaMA-2 7B Chat (16-bit). Appendix C.4 presents similar fine-tuning results on PIQA for LLaMA-3 8B [AI@Meta, 2024], whereas in §5.5 we show results on the closed-source GPT-3.5 [Brown et al., 2020]. We fine-tune all models for 1 epoch (more details in Appendix C.3), and run an ablation on the effect of the number of epochs on ASR and downstream task performance in Appendix C.5.

Accounting for Stochasticity. Ideally, we would run each experiment multiple times to account for the inherent stochasticity of the fine-tuning process. However, due to the high computational cost of both fine-tuning and evaluating these models, we are typically constrained to a single fine-tuning run per dataset, prompting strategy, and mitigation strategy. To assess the robustness of our conclusions, we conduct three independent fine-tuning runs with different random seeds on the PIQA dataset using LLaMA-2 7B and present the results in Figure 5.6. The results remain consistent across runs, with the same prompting strategies yielding the highest harmfulness and only minor variations in ASRs and accuracy. This consistency suggests that conclusions drawn from single fine-tuning runs are generally reliable.

5.4.2 Evaluating Fine-tuning Risks

Figure 5.4 shows the effect of applying each of the fine-tuning prompting strategies from §5.3.2 to the task-specific datasets as evaluated on `HarmI` and `HarmQ` for LLaMA-2 7B (corresponding table available in Appendix C.4). Figure 5.5 presents the downstream task performance of fine-tuning with each of the prompting strategies on each dataset. Table 5.3 shows that the toxicity and harmfulness detection rates for each dataset by prompting strategy are consistently lower than 0.61%.

Table 5.3: Dataset Toxicity Detection: evaluated using OpenAI's content moderation API for each dataset and prompting strategy studied.

	Benign	**AOA**	**AutoIF**	**AutoIF + AOA**
BoolQ (B)	0.01%	0.24%	0.01%	0.12%
BoolQ (E)	0.14%	0.46%	0.04%	0.04%
GSM8K	0.00%	0.00%	0.00%	0.04%
HellaSwag	0.12%	0.45%	0.17%	0.33%
MMLU	0.05%	0.36%	0.03%	0.18%
OpenBookQA	0.04%	0.26%	0.02%	0.26%
PIQA	0.06%	0.43%	0.12%	0.61%
Winogrande	0.04%	0.10%	0.04%	0.06%

Benign users are unlikely to accidentally fine-tune harmful models. In all datasets fine-tuning with the *Benign* strategy leads to a harmfulness rate of 0% on `HarmI`, and lower than the baseline's on `HarmQ` (Figure 5.4). Further, for most datasets *Benign* is the prompting strategy that leads to the highest downstream task performance (Figure 5.5). As expected, *Benign* also beats the validation accuracy of *AutoIF* and *AutoIF + AOA* when fine-tuned on the full converted PIQA dataset (see paragraph above). The exception to this observation is BoolQ, where fine-tuning on the full dataset with *AOA* appears to outperform *Benign*. However, none of the prompting strategies in that dataset lead to a marked increase in harmfulness. As such, we can answer *Q1. Will benign users accidentally obtain harmful models by training on task-specific data?* with **no**.

Malicious users can increase harmfulness. In most datasets one of the adversarial prompting strategies *AOA*, *AutoIF* or *AutoIF + AOA* leads to an increase in harmfulness in both `HarmI` and `HarmQ` (Figure 5.4). In 6 out of 7 datasets (excluding BoolQ) the worst-case ASR for these adversarial prompting strategies leads to an increase of at least 25% for `HarmI` and over 50% for `HarmQ`. Simultaneously, at most 0.61% of the fine-tuning data is detected as toxic (Table

5.3), highlighting the fact that the data is still *benign-looking*. This is particularly low when compared to the explicitly harmful dataset from Qi et al. [2023] which has a detection rate of 70%. Additionally, while the downstream task performance is lower for *AOA* than *Benign* (and for *AutoIF* and *AutoIF + AOA* in the fine-tuning on the full converted PIQA dataset), it is still higher than the original model in most cases—this highlights the evading detectability aim for malicious actors discussed in §5.3.2. This allows us to answer *Q2. Can malicious users adversarially modify benign task-specific datasets to increase harmfulness while keeping the data benign-looking?* with **yes**.

5.4.3 Mitigating Fine-tuning Risks

Figure 5.7 presents the safety evaluation on `HarmI` and `HarmQ` of the mitigation methods *Base*, *Longest* and *Paraphrase* (ours) applied to the different prompting strategies on PIQA, HellaSwag and MMLU, assuming a mixing rate of 50% of safety data. Figure 5.8 (full table in Appendix C.4) shows the downstream task performance of *Benign* and *AOA* for each mitigation using the same mixing rate. Figure 5.9 shows an ablation of the effect of the mixing rate of safety data per mitigation strategy on PIQA in terms of the ASR on `HarmI` and the refusal rate on `XSTest`.

***Paraphrase* reduces harmfulness while retaining downstream task performance.** Figure 5.7 shows that incorporating any safety data generally reduces the harmfulness of the fine-tuned model. Further, *Paraphrase* consistently leads to a lower ASR on both `HarmI` and `HarmQ` compared to the baselines *Base* and *Longest*, being the only method that achieves an ASR near 0% on `HarmI` and lower than the baseline model's 19% for `HarmQ` on all prompting strategies. There is a small cost in terms of downstream task performance to mixing in safety data, as can be observed in Figure 5.8. However, this performance drop is typically negligible compared to the safety improvements presented in Table C.4. This highlights the benefits of our proposed *Paraphrase* mitigation, which mimics the user data to achieve safety.

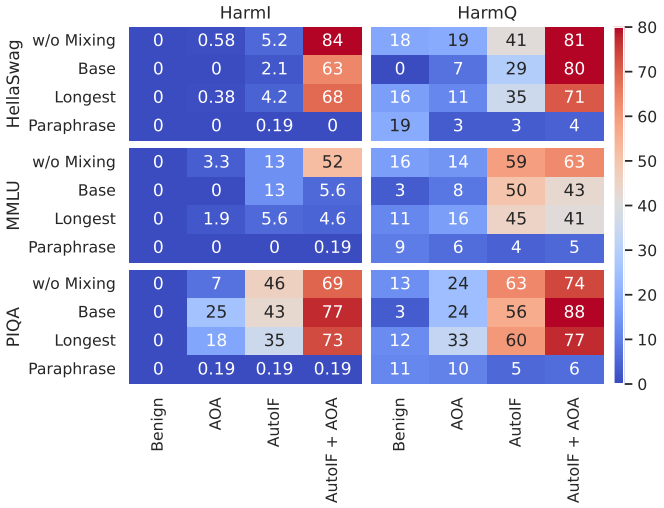

Figure 5.7: Safety Evaluation per Mitigation Strategy: comparison of the safety evaluation of LLaMA-2 7B on `HarmI` and `HarmQ` after fine-tuning with different mitigation strategies on HellaSwag, MMLU and PIQA. *w/o Mixing* corresponds to fine-tuning only using the original dataset (i.e., only user data). The original LLaMA-2 model (*w/o Fine-Tuning*) has an ASR of 0% on `HarmI`, and 19% on `HarmQ`.

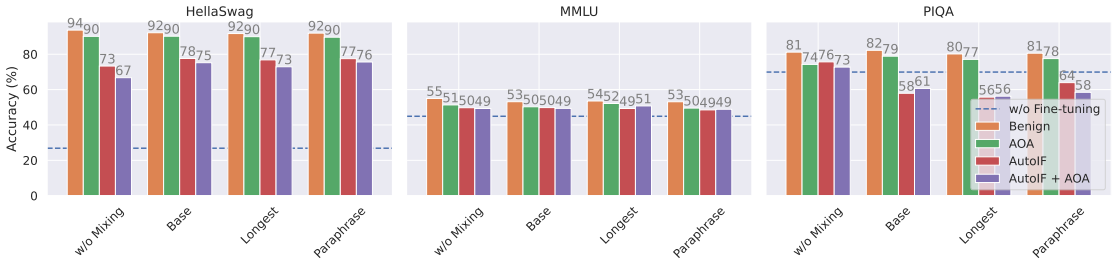

Figure 5.8: Task Performance per Mitigation Strategy: accuracy of the fine-tuning LLaMA-2 7B with different prompting and mitigation strategies on their validation sets.

***Paraphrase* is significantly more efficient than other strategies.** Figure 5.9 shows that *Paraphrase* attains a much lower `HarmI` ASR than other strategies for the same percentage of safety data mixed. In most cases, mixing even 1% of *Paraphrase* data leads to an ASR lower than 5% whereas other mitigation strategies cannot achieve an ASR lower than 40% (e.g., in *AutoIF + AOA*) for any mixing rate up to 50%. This higlights the efficiency of *Paraphrase*. As expected, *w/o Mixing* in the adversarial prompting settings also significantly decreases the refusal rate on `XSTest`—a positive observation given these prompts are supposed to test excessive safety. One drawback of *Paraphrase* is that it appears to lead to typically higher refusal rates than alternative strategies, though they are all lower than the baseline model's 78%.

Table 5.5: GPT-3.5 Fine-tuning on PIQA: (a) safety evaluation on HarmI and (b) task accuracy of fine-tuned versions of GPT-3.5 with different mitigation strategies. *w/o Mixing* corresponds to using the original dataset (i.e., only user data). Baseline GPT-3.5 (*w/o Fine-tuning*) has HarmI ASR of 0.00% and accuracy of 83.61%.

	Benign	AOA	AutoIF	AutoIF + AOA
(a) HarmI ASR				
w/o Mixing	0.19%	55.96%	29.42%	28.27%
Base	0.00%	23.85%	0.00%	12.12%
Paraphrase (Ours)	0.00%	0.00%	0.00%	0.00%
(b) Accuracy				
w/o Mixing	86.89%	83.91%	76.12%	61.75%
Base	88.52%	85.25%	20.89%	81.97%
Paraphrase (Ours)	89.07%	84.70%	68.85%	80.33%

***Paraphrase* is successful even if the fine-tuning data contains multiple prompting strategies.** One of the advantages of our method is its ability to adapt to different prompting strategies, even if these are provided within the same dataset. In Table 5.4, we show that a dataset consisting of 1/3 of examples using *AOA*, a 1/3 using *AutoIF* and the last 1/3 using *AutoIF + AOA* also leads to an increase in harmfulness even if accuracy is reasonably unaffected, and that *Paraphrase* is successful in achieving a safe output model whereas surprisingly *Base* increases the ASR on HarmI, while leaving ASR on HarmQ unaffected. By manually inspecting the paraphrased safety data, we see a distributional balance in the outputted data that effectively counters each of these strategies.

Table 5.4: Ablation on Mixing Prompting Strategies: harmfulness and downstream task performance resulting of applying the prompting strategies *AOA*, *AutoIF* and *AutoIF + AOA* each to 1/3 of the PIQA fine-tuning dataset (16,113 examples). Baseline LLaMA-2 7B (*w/o fine-tuning*) achieves an ASR of 0.00% on HarmI, 19.00% ASR on HarmQ, and accuracy of 74.93%.

	HarmI ASR	HarmQ ASR	Accuracy
PIQA (1/3 *AOA*, 1/3 *AutoIF*, 1/3 *AutoIF + AOA*)			
w/o Mixing	7.50%	54.00%	74.32%
Base	27.88%	54.00%	77.60%
Paraphrase (Ours)	0.00%	4.00%	75.96%

5.5 Task-specific Risks and Mitigations on Closed-Source Models

As discussed in §5.2, within the current paradigm, it is impossible to prevent users from fine-tuning open-sourced model weights on harmful data to produce harmful

models. Consequently, the study of attacks and mitigations presented in §5.3.2 and §5.3.3 is particularly relevant for closed-source model providers, who retain full control over the fine-tuning process. This raises a critical question: have current closed-source providers implemented adequate safeguards to prevent users from fine-tuning models on task-specific data in ways that yield harmful outputs?

While in §5.4 we focus on open-source models—where full control over the fine-tuning process is essential for rigorous testing—this section shifts attention to the closed-source GPT-3.5 model [Brown et al., 2020]. From our standpoint, this constitutes a black-box evaluation, as we lack access to the fine-tuning process and any details regarding how input data is handled or modified. This limitation significantly affects the reproducibility of our findings, as we neither control the process nor have insights into any adjustments made by the model providers. Consequently, similar future studies conducted on the same closed-source model could yield notably different results.

Due to cost concerns, we only analyze it on the PIQA dataset, yet we expect other datasets would yield similar results to the ones in §5.4. Table 5.5 shows the results of fine-tuning *w/o Mixing* (i.e., with only the user data) with different prompting strategies, revealing similar results to the open-source models: *Benign* does not increase `HarmI` ASR, whereas *AOA*, *AutoIF* and *AutoIF + AOA* all significantly increase it. When comparing our mitigation strategy *Paraphrase* and *Base* with a mixing rate of 10%, we see in Table 5.5 that *Paraphrase* is significantly more effective than *Base* at mitigating harmfulness while achieving comparable accuracy.

5.6 Related Work

Safety Alignment of LLMs. The problem of *aligning* LLM outputs to the intentions of humans has been studied extensively in the literature [Ouyang et al., 2022, Touvron et al., 2023], with several recent works providing techniques for improving alignment with a final stage after pre-training on a large corpus of data or supervised fine-tuning [Ouyang et al., 2022, Bai et al., 2022, Rafailov et al., 2023]. For example, Zhao et al. [2024] shows that longer training examples are more

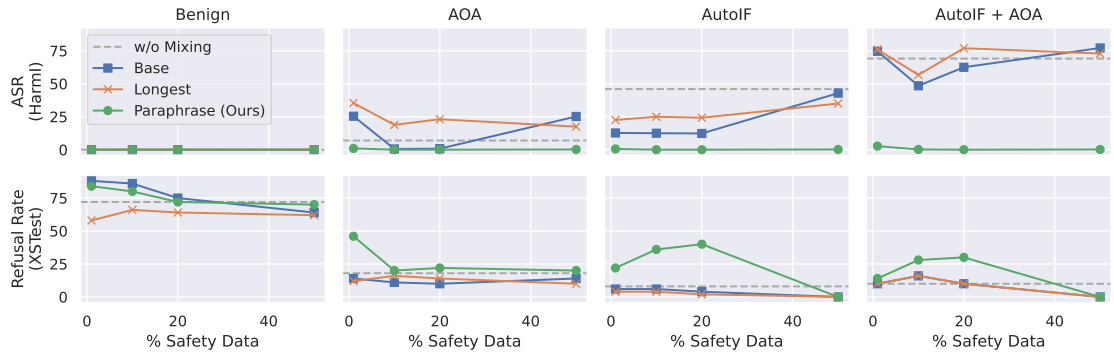

Figure 5.9: Ablation of the Safety Mixing Rate on PIQA: effect of varying the percentage of safety data between 1 and 50% as measured by (top) the attack success rate (ASR) on `HarmI` (lower is better) and (bottom) the `XSTest` refusal rate (lower is better). Baseline LLaMA-2 7B model (*w/o fine-tuning*) ASR on `HarmI` is 0%, and refusal rate on `XSTest` is 78%.

efficient at achieving alignment than shorter ones. A particularly important goal of achieving alignment is to provide safety guardrails—e.g., refusing to respond to harmful instructions—which prevent misuse of models [Bai et al., 2022]. Despite the progress in safety alignment of LLMs, many recent works provide jailbreaks that circumvent those safeguards at inference time [Zou et al., 2023, Chao et al., 2023, Andriushchenko et al., 2024, Anil et al., 2024, Huang et al., 2023] or via fine-tuning on purpose-designed datasets [Qi et al., 2023, Bianchi et al., 2023, Zhan et al., 2023].

Fine-tuning Risks and Mitigation. Qi et al. [2023] and Bianchi et al. [2023] showed that fine-tuning an LLM on benign, instruction-following data can degrade its safety alignment, increasing its likelihood to respond to harmful queries. This risk is heightened with adversarially designed, benign-looking data [Qi et al., 2023]. Mixing explicitly safe data in the instruction-following setting can restore safety alignment [Bianchi et al., 2023, Qi et al., 2023], but previous studies overlook the adaptation to task-specific data for well-defined downstream tasks. Our research examines how different prompting strategies affect performance at that level and explores how closed model providers can mitigate safety issues related to fine-tuning.

5.7 Discussion

Limitations. There are several limitations associated with the general fine-tuning attack setting, as well as with our study and mitigation strategies. As with the instruction-following fine-tuning attacks, malicious users are not able to explicitly steer the direction of the attack (*i.e.*, it is not a controllable attack) or guarantee it is stable. However, the high ASRs obtained on `HarmI` and `HarmQ` suggest it is effective over the wide range of attack types from those datasets. In future work it would be interesting to explore through an even wider evaluation the limitations of such an attack vector. We note also that the adversarial prompting strategies proposed, while effective at increasing harmfulness in most datasets, are primarily demonstrative and have a high potential for detection through structural analysis. It would also be interesting to study the meta-learning of task templates for *AutoIF* that remove the need for combination with *AOA* while achieving harmful models—e.g., using another LLM [Yang et al., 2023]. Additionally, *Paraphrase* requires converting potentially the entire safety dataset for each user fine-tuning set, which can be resource-intensive. Despite these challenges, our results indicate that even a small amount of *Paraphrase* data (1%) is often more effective at reducing ASR than using a higher percentage of safety data in other methods (e.g., 50% in *Base* or *Longest*—see Figure 5.9). Finally, we note that *Paraphrase* opens a new attack vector in which fine-tuning examples are explicitly designed to target the paraphrasing process and either create a distribution gap between the safety data and the harmful test instructions, or simply output harmful responses instead of the safe ones. It would be interesting to study this in the future, as well as some mitigation strategies such as changing the proposed paraphrasing prompt to make it few-shot with some adversarial examples, using chain-of-thought reasoning to detect and correct the safe responses, or fine-tuning a paraphrase model with explicitly adversarial examples and safe answers.

On Safety and Security Aspects. While prior work often frames fine-tuning risks as a safety concern, we argue that they span both AI safety and security. Task-specific fine-tuning risks primarily fall under a security threat, as they arise

from malicious actors manipulating the model (through the fine-tuning data) for their own objectives. However, these attacks ultimately erode the model's safety alignment, turning them into a safety challenge as well. The proposed mitigation strategies are largely safety-driven, as they seek to prevent harmful outputs and restore the model's intended alignment.

Conclusion. Our work focuses on evaluating fine-tuning risks in closed models using task-specific data, showing that (i) benign users are unlikely to accidentally obtain harmful models by training on task-specific data, and (ii) malicious users can adversarially modify these datasets with prompting strategies that significantly increase harmfulness while avoiding detection. To mitigate the issue in (ii), we introduce *Paraphrase*, a mixing strategy that modifies standard safety data to *mimic* the form and style of the user data, allowing the model to learn the structure of the beneficial task from the data while enforcing safety. Our results on LLaMA-3 8B (Appendix C.4) show these have similar effects on more recent models, highlighting the prevalence of this issue. We expect these results would hold for reasoning models [Guo et al., 2025], but it would be interesting to test this hypothesis in the future. We show that *Paraphrase* efficiently outperforms other baselines in achieving safe models, at a minimal cost in downstream task performance. It would also be interesting in the future to repeat the experiments on the same and newer versions of closed-source models, to measure the effectiveness of the task-specific fine-tuning risks on those, and whether the mitigation strategies still hold.

6

Risks and Opportunities of Open-Source Generative AI

Contents

6.1 Preamble

This chapter consists of an oral paper presented at ICML 2024 [Eiras et al., 2024]. It is a position paper that aims to analyse the risks and opportunities that open-source generative AI provides and, as such, it does not contain any purely technical contributions. While I led this work, it is a joint effort with a multidisciplinary group of authors from diverse academic institutions. The appendix of this work is presented in Appendix D.

In the next few years, applications of Generative AI are expected to revolutionize a number of different areas, ranging from science & medicine to education. The potential for these seismic changes has triggered a lively debate about potential risks and resulted in calls for tighter regulation, in particular from some of the major tech companies who are leading in AI development. This regulation is likely to put at risk the budding field of open source Generative AI. We argue for the responsible open sourcing of generative AI models in the near and medium term. To set the stage, we first introduce an AI openness taxonomy system and apply it to 40 current large language models. We then outline differential benefits and risks of open versus closed source AI and present potential risk mitigation, ranging from best practices to calls for technical and scientific contributions. We hope that this report will add a much-needed missing voice to the current public discourse on near to mid-term AI safety and other societal impact.

6.2 Introduction

Generative AI (Gen AI), defined as *"artificial intelligence that can generate novel content"* by conditioning its response on an input [Gozalo-Brizuela and Garrido-Merchan, 2023] (e.g., large language or foundation models), is anticipated to profoundly impact a diverse array of domains including science [AI4Science and Quantum, 2023], the economy [Brynjolfsson et al., 2023], education [Alahdab, 2023], the environment [Rillig et al., 2023], among many others. As a result, there has been significant socio-technical work undertaken to evaluate the broader risks and

opportunities associated with these models, in a step towards a more nuanced and comprehensive understanding of their impacts [Bommasani et al., 2021], including recent regulatory developments (see Appendix D.2.1).

Parallel to these efforts is a debate on the *openness of Gen AI* models. The digital economy heavily relies on open-source software, exemplified by over 60% of global websites using open-source servers like Apache and Nginx [Lifshitz-Assaf and Nagle, 2021]. This prevalence is underscored by a 2021 European Union report, which concluded that "overall, the [economic] benefits of open source greatly outweigh the costs associated with it" [Blind et al., 2021]. Some developers of Gen AI models have chosen to openly release trained models (and sometimes data and code too), by leaning on this narrative and claiming that by doing so *"[these models] can benefit everyone"* and that *"it's safer [to release them]"* [Meta, 2023]. However, while there has been a flurry of reports and surveys on the impacts of general open-source software in areas such as innovation or research within the last few decades [Paulson et al., 2004, Schryen and Kadura, 2009, Von Krogh and Spaeth, 2007], the discourse surrounding the openness of Gen AI models presents unique complexities due to the distinctive characteristics of this technology, including e.g., potential dual use and run-away technological progress.

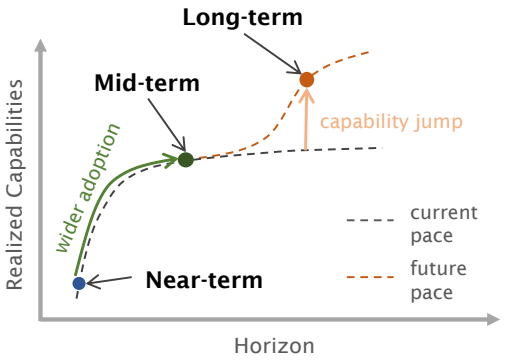

Figure 6.1: Three Development Stages for Generative AI Models: *near-term* is defined by early use and exploration of the technology in much of its current stage; *mid-term* is a result of the widespread adoption of the technology and further scaling at current pace; *long-term* is the result of technological advances that enable greater AI capabilities.

This paper argues that the success of open source in traditional software could be replicated in Gen AI with well-defined and followed principles for responsible development and deployment. To this end, we begin by defining different stages of Gen AI development/deployment, followed by an empirical analysis of the openness of existing models through a taxonomy. With this framework, we then focus

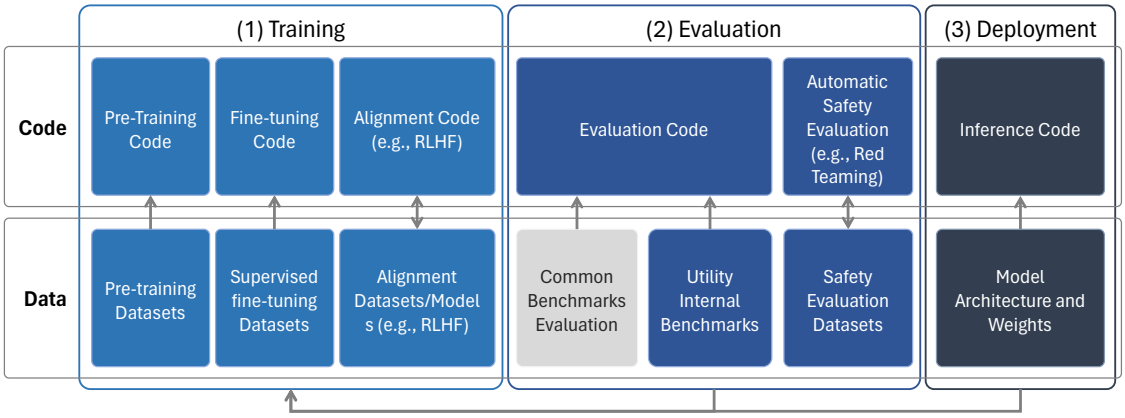

Figure 6.2: Model Pipeline: stages showing (1) training, (2) evaluation, and (3) deployment analyzed in the report. The component Common Benchmarks Evaluation (light gray) is included for completeness yet will not be analyzed in detail as these are standard and commonly available.

on evaluating the risks and opportunities presented by open and closed source Gen AI in the near to mid-term. Finally, we make a case for **the responsible open sourcing of generative AI models developed in the near to mid-term stages**, presenting recommendations to developers on how to achieve this safely and efficiently.

6.3 Preliminaries

To frame our analysis of the impacts of open sourcing generative AI models, we start by defining three-stages of AI development and outline the current pipelines involved in training, evaluating and deploying Large Language Models (LLMs). We focus on LLMs in these definitions and in §6.4.2 as this is the modality with the most prolific model development and open-sourcing at the moment, but note that it would be easy to extend our analysis to other modalities.

Stages of Development of Gen AI Models Our three-part framework (Figure 6.1) to describe the evolution of generative AI focuses on adoption rates and technological advancements instead of time elapsed (similar to Anthropic, 2023). The **near-term** stage is defined by the early use and exploration of existing technology, such as deep learning with transformer and diffusion model architectures, utilizing large datasets. This phase is characterized by experimentation, with increasing levels of development, investment and adoption. The **mid-term** is defined by the

widespread adoption and scaling of existing technology, and the exploitation of its benefits. We conceptualize this as moving along a predictable 'capability curve', whereby more resources and usage will lead to greater benefits (and risks), but technological capabilities have not radically improved. Increasing use of multimodal models, agentic systems, and retrieval augmented generation are expected at this stage. The **long-term** is defined by a technological advance that will create dramatically greater AI capabilities, and therefore more risks and opportunities. This could manifest as a novel AI paradigm, a departure from traditional deep learning architectures, more efficient data utilization, among others, leading to more powerful AI models. In this paper, we focus primarily on analyzing the risks and opportunities of open-source Gen AI in the near to mid-term stages.

Training, Evaluating, and Deploying LLMs The components typically involved in the (1) training, (2) evaluation, and (3) deployment of models are shown in Figure 6.2, and they can be divided into two categories: *Code* and *Data*. We briefly describe each of the stages below, and provide a more in-depth component description in Appendix D.1.

Model training processes can be grouped into three distinct stages: *pre-training*, where a model is exposed to large-scale datasets composed of trillions of tokens of data, with the goal of developing fundamental skills and broad knowledge; *supervised fine-tuning* (SFT), which corrects for data quality issues in pre-training datasets using a smaller amount of high-quality data; and *alignment*, focusing on creating application-specific versions of the model by considering human preferences. Once trained, models are usually evaluated on openly available evaluation datasets (e.g., MMLU by Hendrycks et al., 2020) as well as curated benchmarks (e.g., HELM by Liang et al., 2022). Some models are also evaluated on utility-oriented proprietary datasets held internally by developers, potentially by holding out some of the SFT/alignment data from the training process [Touvron et al., 2023]. On top of utility-based benchmarking, developers sometimes create safety evaluation mechanisms to proactively stress-test the outputs of the model (e.g., red teaming via

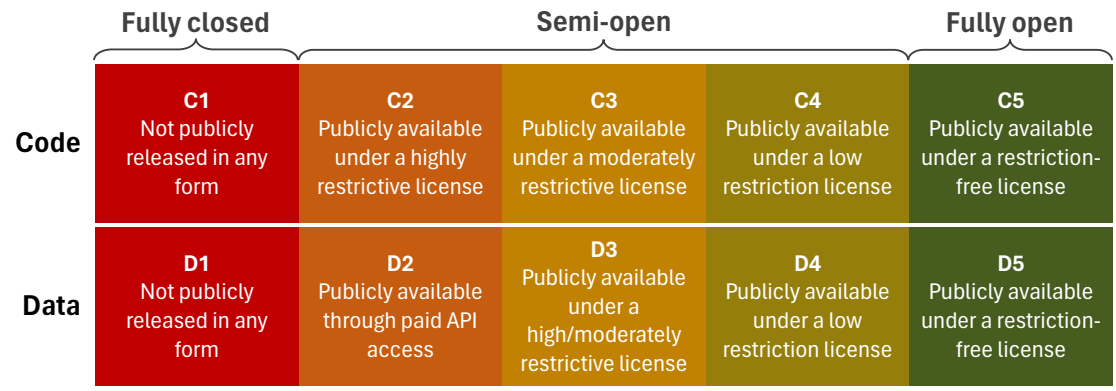

Figure 6.3: Openness Scale: categorization of the levels of openness of the code and data of each model component. See Table D.1 (Appendix D.2) for the restrictions of each license.

adversarial prompts). Finally, at the deployment stage, content can be generated by running the inference code with the associated model weights.

6.4 Openness Taxonomy of LLMs

Model developers decide whether to make each component of the training, evaluation and deployment pipeline (Figure 6.2) *private* or *public*, with varying levels of restrictions for the latter. For instance, the developers of LLaMA-2 have publicly released the model architecture and weights, yet they have not shared the code or reward model for Reinforcement Learning from Human Feedback (RLHF) used in the Alignment components [Touvron et al., 2023]. To properly evaluate the openness of each component, we introduce a classification scale for Gen AI models in §6.4.1, which we then apply to 40 high impact LLMs in §6.4.2. This will help contextualizing the risks and opportunities discussed in §6.5, and the responsible open sourcing argument we make in §6.6. An up-to-date version of the taxonomy of LLMs is also available on this link.

6.4.1 Classifying Openness for Gen AI Code and Data

We introduce a framework for categorizing the openness of each component of Gen AI pipelines (e.g., Figure 6.2). At the highest level, a **fully closed** component is not publicly accessible in any form [Rae et al., 2022]. In contrast, a **semi-open**

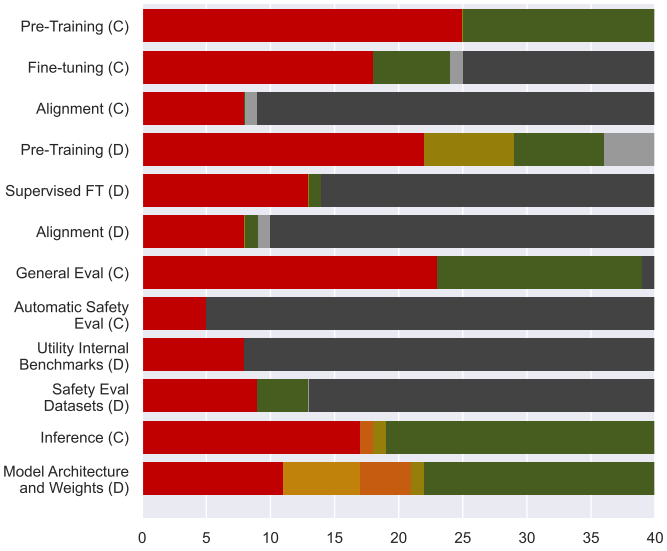

Figure 6.4: Distribution of Openness Levels by Pipeline Component: openness level distribution for each of the pipeline components of the 40 LLMs studied. Color legend: C1/D1, C2/D2, C3/D3, C4/D4, C5/D5, ? (unknown or not publicly available), N/A (not applicable). For conciseness, we use "FT" as a stand in for "Fine-Tuning".

component is publicly accessible but with certain limitations on access or use, or it is available in a restricted manner, such as through an Application Programming Interface (API) [Achiam et al., 2023]. Finally, a **fully open** component is available to the public without any restrictions on its use [Xu et al., 2022]. Further, the semi-open category comprises three subcategories, delineating varied openness levels (see Figure 6.3). Distinctions are made between Code (C1-C5) and Data (D1-D5) components, where C5/D5 represents unrestricted availability and C1/D1 denotes complete unavailability. For semi-open components, their classification relies on the license of the publicly available code/data.

To evaluate the licenses we introduce a point-based system where each license gets 1 point (for a total maximum of 5) for allowing each of the following: *can use a component for research purposes* (**Research**), *can use a component for any commercial purposes* (**Commercial Purposes**), *can modify a component as desired (with notice)* (**Modify as Desired**), *can copyright derivative* (**Copyright Derivative Work**), *publicly shared derivative work can use another license* (**Other license derivative work**). The total number of points is indicative of a license's restrictiveness. A **Highly restrictive** license scores 0-1 points, aligning with

openness levels of code C2 and data D3, imposing significant limitations. A **Moderately restrictive** license, scoring 2-3 points (code C3 and data D3), allows more flexibility but with some limitations. Licenses scoring 4 points are **Slightly restrictive** (code C4 and data D4), offering broader usage rights with minimal restrictions. Finally, a **Restriction free** license scores 5 points, indicating the highest level of openness (code C5 and data D5), permitting all forms of use, modification, and distribution without constraints.

In Table D.1 (Appendix D.2) we provide a full table with the openness licenses and levels of all models studied in §6.4.2.

6.4.2 Openness Taxonomy of Current LLMs

We analyzed the pipeline components of 40 high-impact LLMs released from 2019 to 2023, chosen by optimizing three key impact metrics: *ChatBot Arena Elo Rating*, a crowdsourced benchmark score comparing models[1]; *Google Scholar Citations*, indicating each model's academic impact; and *HuggingFace Downloads Last Month*, reflecting the usage of models openly available on HuggingFace. While we included models that scored high on any of these metrics, we also decided to include other released models for the sake of diversity. Due to space constraints, the full model list is in Table D.2 (Appendix D.2).

A full table with the taxonomy of each of the model components is presented in Table D.3 (Appendix D.2). In Figure 6.4, we show the distribution of openness levels for each of the pipeline components analyzed. Figure 6.4 clearly shows a balance between open and closed source deployed components (inference code and weights); however, ***a notable skew exists towards closed source in training data (such as fine-tuning and alignment) and, importantly, in safety evaluation code and data***. To fully leverage open source benefits and mitigate risks discussed in the next sections, a significant shift toward responsible development and deployment of open-source generative AI is necessary.

[1]Introduced in 05/2023; older models may be underrepresented.

6.5 Near to Mid-term Risks and Opportunities of Open Source Gen AI Models

We describe the risks and opportunities provided by open-source models in the near and mid-term (as defined in §6.3). Our focus is how open source catalyses, minimizes or creates risks and benefits compared to closed source – rather than Gen AI in general. Unless stated explicitly, we refer to all artifacts and components of AI when using the term "open source".

The Challenges of Assessing Risks and Benefits Gen AI systems can be evaluated through a variety of methods and frameworks, such as benchmarks like HELM and Big-Bench for task evaluation, Chatbot Arena for crowd-sourced model comparisons, and red teaming for exploratory evaluation Guo et al. [2023], Liang et al. [2023], Srivastava et al. [2023]. However, these approaches face limitations like limited ecological validity and data contamination Li et al. [2023], Sainz et al. [2023], Zhou et al. [2023], and provide only a partial view of how models will perform in real-world settings. In response, some experts suggest socio-technical evaluations that are focused on real-world applications Weidinger et al. [2023], Solaiman et al. [2023]. This is supported by calls for comprehensive pre-release audits of models, datasets, and research artifacts Derczynski et al. [2023], Mökander et al. [2023], Rastogi et al. [2023]. However, even holistic approaches to evaluation face substantial challenges, such as the rapid and unpredictable evolution of AI capabilities, the difficulty of standardizing measurements due to the fast pace of change, and the research community's limited insight into AI's industrial applications. This invariably leads to partial and incomplete evidence. As such, while we use diverse evidence to examine and support our arguments, it is important to recognize the challenges in reaching definitive conclusions as a result of these limitations.

6.5.1 Quality and Transparency

Open Models are More Flexible and Customizable Having access to open-source models, datasets, and assets significantly aids developers in creating models that are high-performing and specifically tailored to their use-case. Developers have

access to far more training approaches, models and datasets. This gives them a powerful starting point when creating a model for a specific application. It also particularly helps cater to less well-resourced languages, domains, and downstream tasks Bommasani et al. [2023], as well as enabling personalized models that cater to distinct groups and individuals Kirk et al. [2023]. This has created widespread positive sentiment towards open source, which can be seen in venture capital firm's significant investment in open-sourcing efforts [Bornstein and Radovanovic, 2023, Horowitz, 2023], and the growing adoption of open-source models by companies [Marshall, 2024].

Open Source Improves Public Trust Through More Transparency

Nearly three out of five people (61%) are either ambivalent about or unwilling to trust AI, with Gillespie et al. [2023] reporting that cybersecurity risks, harmful use, and job loss are the "potential risks" that people are most concerned about. Closed source models pose challenges for evaluating, benchmarking, and testing them which impede accessibility, replicability, reliability, and trustworthiness [La Malfa et al., 2023]. Transparency is a powerful way of improving trust, and addressing this critical problem. Transparency includes providing clear and explicit documentation, such as provenance artefacts like model cards, datasheets, and risk cards Gebru et al. [2021], Derczynski et al. [2023], Longpre et al. [2023]. They can be used to assess and review datasets and models, and are widely-used in the open source community. Open source is itself the best way of creating transparency. It enables widespread community oversight as models and datasets can be interrogated, scrutinised, and evaluated by anyone, without needing to seek approval from a central decision-maker. This empowers developers, researchers and other actors to engage with AI and contribute to discussions, encouraging a culture of contribution and accountability Sanchez [2021]. At the same time, the highly technical nature of AI research creates substantial barriers to typical citizens. As such, more transparency may not alone drive greater trust – research outputs also need to be *accessible* and *understandable* by non-experts Mittelstadt et al. [2019].

6.5.2 Research and Academic Impact

Open Source Advances Research Compared to the machine learning landscape a decade ago, the availability and continuous growth of open source in recent years has enabled the community to do more diverse and innovative research. This includes researchers exploring the inner workings of models through jailbreaking and quality checking for unsafe, harmful, and biased content (see §6.5.4) as well as probing for misuse of copyrighted data, which can potentially lead to class-action lawsuits (see §6.5.5). Likewise, the availability of code, data, and proper documentation of open models have allowed researchers to develop novel breakthroughs (e.g., DPO Rafailov et al. [2023] as a more cost-efficient substitute for RLHF Ouyang et al. [2022] for capturing human preference), which have been proven to boost open models to gain comparable performances against their closed model counterparts. Closed models, on the other hand, only grant limited access through API calls and restrict access to essential model generation outputs such as logits and token probabilities. Such limitations restrict researchers from forming deeper methodological insights and limit reproducibility of their research Rogers [2023].

6.5.3 Innovation, Industry and Economic Impact

Open Source Empowers Developers and Fosters Innovation Closed source models accessed via an API make product developers reliant on an external provider for essential components of their product or system. This reliance can limit control and maintainability, especially as models can be updated or removed without warning by their owners. Further, with a closed model developers may not own their data or have full control over their data pipeline, which can make it more difficult to innovate on design, steer model performance, change aspects of their system, or understand their own workflows. In contrast, open models offer significant advantages. Developers can modify the model according to their needs, have complete understanding and transparency of the model, and control the data pipeline, which greatly enhances privacy and auditability Culotta and Mattei [2023]. One important consideration is whether models are released with

permissive licenses that suit commercial usecases (see commercial use in §6.3). This is increasingly common with more recent releases. Open-source models could be particularly beneficial in the emerging field of generative AI-powered agents Chan et al. [2024], where outputs involve performing digital or physical actions (for early examples see Adept's blog post AdeptTeam [2022], and Amazon's press release Amazon [2023]). In this context, product developers are likely to value having more control over models, being able to deploy them on-device, and integrate them in larger, more complex systems.

Open Source Can be More Affordable AI models can enhance individual productivity by automating repetitive and time-consuming tasks, and augmenting workers when completing more complex and high-value tasks. This can help narrow the productivity gap between workers, improving minimum performance standards Dell'Acqua et al. [2023]. In principle, open-source AI models increase these benefits as they are available for free. However, substantial operational costs are still involved, such as the staff required to run the models, the time of leadership to organise and oversee their use, and the compute costs for inference [Palazzolo, 2023]. Some enterprises might also apply additional protections for security and data to ensure compliance when using open-source models, adding further costs. Whether open source is cheaper overall than closed source depends on the maturity and capabilities of the organisation. Generally, larger corporations can bear the overheads involved in open source and overall make substantial savings.

Open Source Can be Easier to Access Open-source models are increasingly easy to use and access, with a range of vendors providing SDKs, APIs and downloadable files, such as Replicate, Together, and HuggingFace. Further, they typically require few approvals to start using models, in comparison with more onerous signup processes from closed source providers. One important area where open source lags behind closed source is in providing user interfaces aimed at non-technical audiences. While ChatGPT is easy to interact with and well-known amongst the general public, few open-source models have widely-used UIs.

Open Source Could Achieve Comparable Performance Today, the preference for closed source models stems from their user-friendly packaging, cost-effectiveness (with lower-income individuals predominantly opting for free versions, see Mollick, 2023), and potentially superior performance across various tasks (Open LLM Leaderboard). However, these dynamics are likely to shift in the near to mid-term. Firstly, with the growth of open source development, the performance gap between open and closed source models is expected to narrow significantly UK-gov [2023]. Further, open source might be better in specific applications and contexts (see §6.5.3), driving adoption.

Open Models Could Help Tackle Global Economic Inequalities Knowledge workers in low-income nations, including workers in sectors like call centers and software development, face serious risk of job losses as AI models automate and semi-automate their work. Further, if AI models fail to adapt to local contexts or remain financially inaccessible, the expected economic benefits and new job opportunities may not arise, worsening economic inequalities Georgieva [2024]. This is a concern as closed source models are often (1) unaffordable for companies in low-income countries and (2) badly-suited to their needs (see §6.5.5). Local needs are often not met because they lack adequate language support, culturally relevant content, and effective safety measures. This results in higher costs and lower performance, compounding the global inequalities that could be caused by generative AI Petrov et al. [2023], Ahia et al. [2023]. In contrast, open models could significantly change this dynamic. With requisite skill building and support for different communities, open models would enable communities to tailor models to their specific contexts and needs, promoting local innovation, safety, security, and reduced bias. This shift could help bridge the growing global inequality gap, paving the way for a more equitable and inclusive future in generative AI.

6.5.4 Safety

Generative AI models can create safety risks by increasing the severity and prevalence of harm experienced by individuals and society at large. This can take many forms,

including physical, psychological, economic, representational and allocational harms Shelby et al. [2023], Weidinger et al. [2023]. The primary risks from current and near-term generative AI capabilities comprise two distinct pathways. The first is *malevolent use by bad actors*: individuals or organizations might exploit AI to create damaging content or enable harmful interactions, such as personalized scams, targeted harassment, sexually explicit and suggestive content, and disinformation on a large scale [Vidgen et al., 2023, Ferrara, 2023]. The second is *misguidance of vulnerable groups*: inaccurate or harmful advice from AI could lead vulnerable individuals, including those with mental health issues, to engage in self-harm [Mei et al., 2022, 2023, Röttger et al., 2023], radicalise towards supporting extremist groups, or believe in factually inaccurate claims about elections, health, and the environment [Zhou et al., 2023]. In the long-term, AI might develop capabilities that present novel existential threats, creating "catastrophic" consequences for society such as chemical warfare and environmental disaster Hendrycks et al. [2023], Shevlane et al. [2023], Matteucci et al. [2023]. However, these risks are not a substantial concern for existing models given their limited capabilities. Thus, in the near to mid-term, AI safety primarily means preventing models from generating toxic content, giving dangerous advice, and following malicious instructions.

Open Source Enables Technological Innovation for Safety Open source has significantly advanced safety research in the entire model development pipeline. Large open datasets for pre-training, like the Pile [Gao et al., 2020] (released for GPT-Neo, studied in the taxonomy §6.4.2), Laion [Schuhmann et al., 2022], and RedPajama [Computer, 2023], can be analysed for whether they contain toxic content Prabhu and Birhane [2020]. Similarly, open research has shown model fine-tuning to be highly efficient in both improving model safety and removing model safeguards [e.g. Bianchi et al., 2023, Qi et al., 2023]. Unlike closed APIs, open model analyses permit in-depth exploration of internal mechanisms and behaviors [e.g. Jain et al., 2023, Casper et al., 2024]. This transparency enables reproducible and comprehensive evaluations, strengthening our understanding of generative AI safety for models with near and mid-term capabilities. Open source has also

driven innovation in developing safeguards and controls for models, such as Meta's LlamaGuard Inan et al. [2023] and HuggingFace's Safety Evaluation Leaderboard.

⛔ **Open Models Can Also be Made to Generate Unsafe Content** The flexibility of open-source models, as discussed in §6.5.1, has its drawbacks. Despite their initial alignment, these models can be fine-tuned to produce unsafe content, as exemplified by GPT4Chan and various "uncensored models" on the HuggingFace hub, designed to execute any instruction, irrespective of its safety implications. It is important to recognize, however, that closed models are not impervious to similar risks. Jailbreaks can induce unsafe behaviors in closed models as well [Zou et al., 2023], and recent studies have demonstrated that closed models can easily be fine-tuned to become just as unsafe as open ones [Qi et al., 2023]. Nonetheless, ongoing advancements in generative AI safety technology [Dai et al., 2023], particularly through open models, hold the potential for mitigating these risks in the near to mid-term horizon.

⛔ **Open Models Cannot be Rolled Back or Updated** Once a model is made public, anyone can download it and use it indefinitely. In principle, benign users' access (e.g., researchers or rule-abiding corporations) can be regulated through license modifications. However, not all benign users will be aware of license changes and malicious actors will choose to not follow them. This creates a safety risk as any problems that have been identified post-deployment cannot be addressed. In comparison, closed model developers can cut off access to unsafe models if they are gatekept through an API. To reduce these risks, open source developers and the communities that host models (e.g., HuggingFace) must adhere to responsible release and access policies (e.g. Solaiman 2023, Solaiman et al. 2023, Anthropic 2023).

6.5.5 Societal and Environmental Impact

✅ **Open Source Models Can Reduce Energy Use** AI model training incurs significant environmental costs from the energy consumption of compute resources. [Strubell et al., 2019, Wu et al., 2022]. These impacts, measurable in CO_2 emissions, span the entire AI development process, including training and inference [Verdecchia

et al., 2023, Kumar and Davenport, 2023]. While accurately quantifying emissions for cloud providers is challenging due to variables like hardware utilization, team practices, geography, and time of day, industry-wide energy consumption can be reduced by sharing of resources that are energy-intensive to create, such as model weights [Saenko, 2023]. In addition, open-sourcing can lead to transparent profiling of code to identify energy bottlenecks. This can then be addressed by the community, creating more energy-efficient training methods. For instance, some researchers have put forward small model development paradigms Schwartz et al. [2019].

Open Models Can Help With Copyright Disputes One of the major legal issues surrounding generative AI is the use of copyrighted data for training without explicit permission [Firm and Butterick, Metz, 2024]. This has mostly been identified because models regurgitate memorized data when prompted in specific ways Karamolegkou et al. [2023], Carlini et al. [2022]. The lack of transparency about what data are used in model training for both open and closed source (highlighted in §6.4.2) can lead to confusion, uncertainty, and misattribution. Open models that release, or describe, their training data can help address these issues of data privacy, memorization and the "fair use" of copyrighted materials. Crowd-sourced data curation also offers a way of minimizing use of proprietary datasets in the future, reducing the risk of copyright disputes Hartmann et al. [2023].

Open Models Can Serve the Needs and Preferences of Diverse Communities To address global needs effectively, it is crucial that models do not only reflect the values of people who are liberal, culturally Western, and English speaking [Aroyo et al., 2023, Lahoti et al., 2023]. However, models are largely trained on data from the Internet, which is often biased to such people [Joshi et al., 2020]. There is a pressing need to make pre-training datasets more diverse, inclusive and representative. In the short-term, models can be *steered* to meet the needs of different contexts, languages, and communities. Open source is a powerful way of achieving this as it enables under-resourced actors to build on top of each other's contributions. For instance, platforms like HuggingFace host a vast array of models, with many designed for specific cultural, geographic, or

linguistic needs, e.g., Latxa Bandarkar et al. [2023] and LeoLM Plüster, covering diverse domains [e.g. Li et al., 2023].

Open Source Helps Democratize AI Development Open source empowers developers to utilize resources from major organizations (e.g., companies, governments or research labs), facilitating the reuse of assets and leading to time, effort and money savings. This is crucial for AI development, which is characterized by high costs and complexity, from pre-training models that can cost millions Knight [2023] to the creation of expensive human-labeled datasets. This creates a clear societal benefit by enabling non-elites to access and use AI, which can include creating economic opportunities (see §6.5.3). It is important to acknowledge that, at a higher level, open-source models still contain key decisions, datasets and approaches that influence what is built on top of them. In this sense, they are currently undemocratic. They are informed by the values and market priorities of their largely for-profit driven developers.

6.6 Responsible Open Sourcing of Near to Mid-Term Generative AI

6.6.1 Addressing Common Concerns on Open Sourcing Generative AI

Despite the many benefits of open source, concerns surrounding the increased potential for malicious use, and uncertainty about its societal impact, have prompted calls for keeping generative AI closed source [Seger et al., 2023]. There are real risks associated with open-source models. However, we believe these are sometimes exaggerated, possibly motivated by the economic interests of market leaders. Most concerns about open sourcing near to mid-term AI models are also pertinent to closed source models.

CLAIM #1: Closed Models Have Inherently Stronger Safeguards than Open-Source Models Several studies demonstrate that closed models typically demonstrate fewer safety and security risks, compared to open source Röttger et al. [2023], Chen et al. [2024], Sun et al. [2024]. However, closed models still demonstrate

weaknesses, and are particularly vulnerable to jailbreaking techniques [Zou et al., 2023, Chao et al., 2023]. Closed model safeguards are easily bypassed through simple manipulations like fine-tuning via accessible services [Qi et al., 2023], prompting the model to repeat a word [Nasr et al., 2023], applying a cypher Yuan et al. [2023], or instructing the model in another language [Deng et al., 2023, Yong et al., 2023]. Completely preventing models from exhibiting undesirable behaviors might not even be possible [Wolf et al., 2023, Petrov et al., 2024]. Therefore, it is not clear that closed models are definitively "safer" than open-source models. We also anticipate that gaps will narrow over time as open safeguarding methods continue to improve.

CLAIM #2: Access to Closed Models Can Always be Restricted Closed models are often considered more secure because access can be restricted or removed if problems are identified. However, closed models can be compromised via hacking, leaks [Cox, 2023], reverse engineering [AsuharietYgvar, 2021] or duplication [Oliynyk et al., 2023]. This perspective also assumes that models are only offered through an API. But some closed models are delivered on premise/device, particularly for sensitive deployments (e.g., government applications). In such cases, access may not be retractable. Finally, closed models can be leaked, e.g., Mistral's 70B parameter was leaked by one of their early customers [Franzen, 2024]. Given these factors, developers do not always have the ability to unilaterally revoke access.

CLAIM #3: Closed Source Developers Can be Regulated to be Safer Regulatory pressure is primarily aimed at large companies building closed source models (e.g., see White House Executive Order). While it can create incentives for safe model development, regulation is not a panacea, and several closed source models have been released that are uncensored, poorly safeguarded [Verma, 2023] or deliberately misaligned [Burgess, 2023, Cuthbertson, 2023, Roscoe, 2023]. It is also not clear that regulating closed source models is an effective way of stopping malicious actors [Lockie, 2015, Wootson, 2023], who are capable of creating and distributing their own closed source models via illicit sales channels [Sancho and Ciancaglini, 2023]. Instead, it might create higher costs for legitimate users who are restricted in what models they can access [Wu et al., 2023].

CLAIM #4: All Safety and Security Problems Must be Addressed By the Model Provider It is becoming increasingly clear that, because of the numerous potential applications of generative models, all safety risks cannot be simply identified (and stopped) by the model provider. First, most model risks depend on the context and actors, and their real-world resources. For instance, real-world constraints significantly hinder activities like acquiring chemicals, equipment, or weapons, thus limiting open source's potential for misuse in such endeavors. Second, models may not have a causal impact on actors if they either (a) have other means of inflicting harm – such as searching on the web for malicious information – or (b) pay little attention to the responses of the model. Third, in practice, other stakeholders help protect people from risk through established safeguarding practices, such as Internet Service Providers, cloud services, social media, and law enforcement. Given these factors, safety and security issues cannot be seen as solely the responsibility of the model provider.

6.6.2 Recommendations for Safe and Responsible Open Sourcing of Near to Mid-term Gen AI Models

To safely and responsibly open-source Gen AI models, we outline five important priorities for developers, starting with technical recommendations ahead of broader responsibility and socio-technical considerations.

Enhance Data Transparency and Provenance Responsible open sourcing is linked to greater transparency across the entire the model pipeline. As illustrated by Table D.3 (Appendix D.2), a lack of data transparency is a problem even in relatively open LLMs. Making training and evaluation data publicly available enhances the community's capacity to scrutinize models' capabilities, risks, and limitations, thereby unlocking many of the advantages outlined in §6.5. It also holds the potential to develop models pre-trained for safety rather than aligned post-hoc. We believe this is an area where more research is needed which requires more parts of the pipeline to be open. Additionally, transparency in dataset composition, including metadata like copyright, is crucial. Maintaining comprehensive audit

logs detailing chains of custody, transformations, data augmentation, and synthesis processes is increasingly vital.

Improve Open Evaluation and Benchmarking There has been much progress in open benchmarking of general LLM capabilities (e.g. LMSys, HELM, AlpacaEval), but there is an outstanding need for benchmarks that are specific to particular domains and impact areas, including model safety. This is poignant since, as highlighted in §6.4.2, most developers do not release their safety training and evaluation data. Generally, new models should be evaluated pre-release, so that their capabilities, risks, and limitations are made clear from day one. Evaluations should include assessments as related to the variety of risks outlined in §6.5.

Conduct Multilevel Security Audits Open source affords pre- and fine-tuning of models for any downstream tasks. For mission-critical tasks, particularly in areas like mental health, multi-level security audits and procedures must be meticulously designed, documented, implemented, and publicly reported. This should encompass both manual and automated testing, ranging from adversarial jailbreak prompts to expert-led red-teaming for common and edge case exploits, where financially viable. Additionally, incorporating static and dynamic analysis toolchains into developers' IDEs is essential to detect vulnerabilities early in the development process. Establishing and promoting safe design patterns for Gen AI development within the community is also crucial. Once ready for deployment, it is important that developers engage with the wider safety research community to allow for further third-party testing in controlled sandboxes closer to the released model environment.

Compare with Closed Source Models Open-source models offer advantages like enhanced privacy, customization, transparency, efficiency, and cost-effectiveness. In contrast, commercial closed-source models can stand out in performance, usability, and liability protections. Therefore, comparing the models with their closest commercial closed source alternative is important to quantify, clarify, and understand the trade-offs involved in open sourcing decisions.

Conduct Studies of Broader Societal Impact As highlighted in §6.5.5, properly developed open models can reduce Gen AI energy consumption, aid in resolving copyright disputes, cater to diverse communities, and help democratize AI development. To realize these benefits, it's crucial to undertake comprehensive broader societal impact studies. These should include evaluating corporate practices in model design and management, initiatives for enhancing data diversity and representation, and transparency reports on the environmental impact of the models.

6.7 Conclusion

The recommendations in §6.6.2 are a result of combining the openness trends of currently available models in §6.4.2 with the analysis of §6.5 on the potential risks and opportunities of open sourcing near to mid-term models. Following this discussion, we advocate for the **responsible open sourcing of near to mid-term Gen AI models**.

Note that our position is a balanced one. We advocate that developers should be allowed and encouraged to responsibly open-source Gen AI models developed in the near to mid-term stages, in as much as it makes economic sense for them to do so. Building Gen AI models is an expensive process, and we are sensitive to the argument that for-profit companies should be able to reap some of the financial benefits of their investments in building the technology. Any other position on this matter (e.g., forcing companies to open source their models/pipelines) would seriously risk investment and progress in this area.

However, often for-profit entities will claim open source Gen AI is fundamentally unsafe, and will publicly use this to argue against the open sourcing of these models altogether. This discourages other developers from open sourcing, and we believe this is one of the main factors that contributes to the current skew in the landscape presented in the taxonomy of §6.4.2 (Figure 6.4). We reject this argument, and argue in §6.5 and §6.6 that (1) there are many benefits that can only be achieved through open sourcing, and (2) the risks are often exaggerated by these for-profit entities. By making these impacts explicit and laying out recommendations for the responsible

open sourcing of these models, our aim is to encourage developers to improve the notable skew in Figure 6.4. This does not mean all models will be open-sourced, only that there would be an improved balance. We note that this should always be voluntary rather than imposed, to avoid disrupting the investment in the area.

Our work underscores the importance of mitigating risks and addresses prevalent concerns, thereby paving the way for realizing the vast potential benefits open-source generative AI offers.

6.8 Related Work

The debate around open sourcing Gen AI differs from the well-studied impacts of open-source software on society [Jaisingh et al., 2008] due to the unique characteristics of the technology. As such, we report related works on two axes: (1) examining the broader impact of Gen AI, and (2) on the debate around open sourcing these models.

The Impact of Gen AI There are many works that focus on the risks and benefits of the technology as it exists today, particularly with respect to areas such as science & medicine AI4Science and Quantum [2023], Fecher et al. [2023], education Alahdab [2023], Cooper [2023], Malik et al. [2023], the environment Rillig et al. [2023], among others. Other research evaluates the potential impacts of a capability shift Seger et al. [2023], emphasizing the critical importance of transparency in analyzing AI failures [Kapoor and Narayanan, 2023,].

On Open Sourcing Gen AI Models A main line of discussion centers on the definition of open sourcing Gen AI, highlighting the role of disclosing the training pipeline, weights, and data in achieving the benefits of open source [Bommasani et al., 2023,, Liesenfeld et al., 2023, Seger et al., 2023, Shrestha et al., 2023]. Notably, AI systems typically encompass more than just code, necessitating custom release pipelines Liu et al. [2023]. Others LAION.ai [2023], Hacker et al. [2023], Tumadóttir [2023] highlight the need to differentiate open-source systems from a regulatory standpoint, to avoid compliance costs unsustainable for open source contributors Parliament [2023]. Many highlight the risks of centralization in absence

of open source Seger et al. [2023], Horowitz [2023]. On the other hand, open models may exacerbate the risks of misuse Bommasani et al. [2021], Alaga and Schuett [2023] unless proper measures are instituted for responsibly open-sourcing them. Interestingly, it has also been shown that open Gen AI tends to be less trustworthy than closed ones Sun et al. [2024]. A relevant paper Seger et al. [2023] analyzes the risks and benefits of open models, and shapes recommendations for the near future. In our work, we provide a holistic viewpoint centered on near to mid-term models, including a taxonomy of the current landscape and discussion of future impacts.

7

Discussion and Open Questions

Contents

7.1 Discussion

The widespread adoption of neural networks in a variety of scenarios requires the development of trustworthy machine learning methods that ideally *certify* properties such as adversarial robustness in image classification or correctness in physics-informed neural networks, or at least enable a strong and thorough *empirical evaluation* of their robustness and safety. This dissertation presented novel technical contributions with applications in computer vision, physics-informed machine learning and language modelling. In this section we discuss the overall strengths of those contributions (§7.1.1) alongside the limitations of the proposed methods and studied settings (§7.1.2). Finally, we present key broader open questions for research in this field in §7.2.

7.1.1 Strengths of the Contributions

In §3, we begin by extending the isotropic, ℓ_p-norm guarantees of prior works to more general *anisotropic* settings through a simplified Lipschitz-based analysis. This extension, when paired with data-dependent smoothing techniques, enables the development of classifiers that certify significantly larger safe regions. Unlike isotropic certificates which focus on worst-case adversaries, our approach provides a method of certifying safe, robust regions across a wider range of perturbations.

In §4, motivated by the aim to verify the correctness of physics-informed neural networks (PINNs) across their continuous applicability domain, we introduce ∂-CROWN, a general framework for bounding nonlinear functions of partial derivatives in fully connected neural networks. This method provides a more efficient means of achieving tight bounds compared to existing approaches, such as IBP and LiRPA [Gowal et al., 2019, Xu et al., 2020], in the settings studied. While we apply ∂-CROWN specifically to PINNs in our work, its design is general enough to handle any function of first and second derivatives, offering broad applicability beyond PINNs and extending to neural network verification in other contexts.

Finally, in §5, we shift focus to the domain of large language models, analysing the empirical risks associated with fine-tuning on task-specific data. We show malicious users could exploit these risks to obtain harmful models, and propose an effective mitigation strategy that successfully reduces these risks with minimal impact on the performance of downstream tasks. Importantly, this strategy maintains its effectiveness for both benign and malicious users, while often requiring only a small amount of additional safety data—just 1% in the case of PIQA. This low overhead suggests that the proposed approach could be easily implemented by closed-source model providers who offer fine-tuning capabilities through APIs.

7.1.2 Overall Limitations

Despite the strengths of the contributions, there are several limitations to the methods proposed and settings studied.

For the general Lipschitz analysis in §3, while it extends isotropic robustness guarantees to anisotropic ones, the practical relevance of enhancing *non-worst-case* robustness is not fully clear. In image classification, these larger anisotropic regions still represent "imperceptible" perturbations, offering insight into fundamental decision patterns. However, translating this improvement to safety in physical systems modelled by neural networks remains uncertain. This reflects a broader, unresolved challenge in adversarial robustness research, as discussed further in §7.2. Additionally, a critical limitation of AnCer and similar data-dependent randomized smoothing techniques lies in their high memory requirements during inference [Alfarra et al., 2022], severely restricting their practical deployment.

The verification algorithm ∂-CROWN from §4 has primary limitations that stem from scalability. First, the method is unlikely to scale effectively to PINNs that rely on larger neural networks, a common issue in incomplete verification methods despite their improvements over complete ones [Zhang et al., 2018, Bunel et al., 2018]. Second, the efficiency of ∂-CROWN comes from the derivation of hybrid propagation mechanisms for first and second derivatives, but extending this to higher-order derivatives presents a significant challenge, as the number of terms in the bounds grows exponentially with the order of the derivative. Moreover, while the correctness conditions provided in Definition 4.1 are practical for certification, they do not provide a theoretical bound on the solution error. Bridging this gap would be an interesting direction for future work.

Lastly, while the *Paraphrase* strategy introduced in §5 effectively mitigates fine-tuning risks, it may still be vulnerable to adversarial attacks where the fine-tuning data is specifically crafted to circumvent paraphrasing techniques. Such crafted datasets could lead to attack success rates closer to those of the unmitigated setting. Future research should explore the feasibility of these sophisticated attacks and develop more robust (yet still practical) mitigation strategies to counter them.

7.2 Open Questions

We conclude by outlining several high-level open questions related to the topics explored in this dissertation, which we believe are pivotal for the advancement of trustworthy AI systems.

How can we move beyond adversarial robustness in image classification? The min-max framework of adversarial robustness has been valuable in probing the decision boundaries of neural networks. However, from a safety perspective, it falls short due to its inherently local focus. The adversarial robustness of a model is often too dependent on the specific test set used for evaluation, which limits its reliability. A more *global* specification of robustness would be more beneficial for safety-critical applications, but there is no clear path to formally defining such a specification. This challenge can be observed in the decline in research attention to adversarial robustness, highlighting the limitations of the current threat model.

How can we scale certification mechanisms in verification methods? Although adversarial robustness methods can often be adapted to other contexts, such as those developed in §4, they currently do not scale effectively to state-of-the-art models used in modern tasks. This scalability issue poses a significant obstacle to applying these methods in practical settings. The inability to verify large models restricts the utility of verification techniques in real-world applications, and addressing this limitation will be critical to making certification a viable tool for AI safety.

How can we formalize specifications that apply to language models? While our work in §5 proposes an effective mitigation strategy for reducing the risks of fine-tuning large language models, the broader challenge remains: how can we establish formal specifications for language models? Efforts to define such specifications are still in their infancy, and approaches that rely on abstract processes, such as those in Robey et al. [2023], often face their own limitations due to the

black-box nature of those processes (which rely on other models). Finding a way to create robust, formal specifications that can meaningfully apply to language models remains an open and pressing question.

Appendices

A

Appendices for "ANCER: Anisotropic Certification via Sample-wise Volume Maximization"

Contents

A.1 Qualitative Motivation of Anisotropic Certification

A.1.1 Visualizing CIFAR-10 Optimized Isotropic vs. Anisotropic Certificates

To extend the illustration in Figure 3.1 to a higher dimensional input, we now analyze an example of the isotropic ℓ_2 certification of randomized smoothing with $\mathcal{N}(0, \sigma^2 I)$, where σ is optimized per input Alfarra et al. [2022], against AnCer, certifying an anisotropic region characterized by a diagonal ℓ_2^Σ-norm. To do so, we consider a CIFAR-10 Krizhevsky [2009] dataset point x, where the input is of size (32x32x3). We perform the 2D analysis by considering the regions closest to a decision boundary. To do so, and following Moosavi-Dezfooli et al. [2019], we compute the Hessian of $f^y(x)$ with respect to x where y is the true label for x with f classifying x correctly, *i.e.* $y = \arg\max_i f^i(x)$. In addition to the Hessian, we also compute its eigenvector decomposition, yielding the eigenvectors $\{\nu_i\}, i \in \{1, \ldots, 3072\}$ ordered in descending order of the absolute value of the respective eigenvalues. In Figure A.1a, we show the projection of the landscape of f^y in the highest curvature directions, *i.e.* ν_1 and ν_2. Note that the isotropic certification, much as in Figure 3.1c, in these 2 dimensions is nearly optimal when

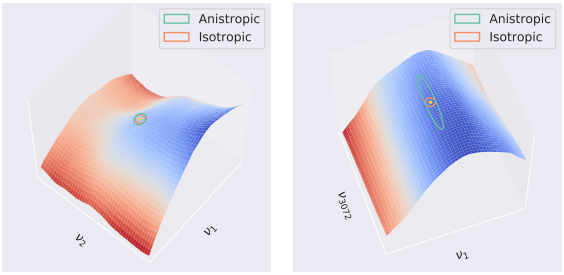

(a) **(b)**

Figure A.1: Illustration of the landscape of f^y for points around an input point x, and two projections of an isotropic ℓ_2 certified region and an anisotropic ℓ_2^Σ2-norm region on a CIFAR-10 dataset example to a subset of two eigenvectors of the Hessian of f^y (blue regions correspond to a higher confidence in y).

compared to the anisotropic region. However, if we take the same projection with respect to the eigenvectors with the lowest and highest eigenvalues, *i.e.* ν_1 and ν_{3072}, the advantages of the anisotropic certification become clear as shown in Figure A.1b.

A.2 Anisotropic Certification and Evaluation Proofs

Proposition A.3.1. *(restatement of Proposition 3.1). Consider a differentiable function $g : \mathbb{R}^n \to \mathbb{R}$. If $sup_x \|\nabla g(x)\|_* \leq L$ where $\|\cdot\|_*$ has a dual norm $\|z\| = \max_x z^\top x \quad s.t.\ \|x\|_* \leq 1$, then g is L-Lipschitz under norm $\|\cdot\|_*$, that is $|g(x) - g(y)| \leq L\|x - y\|$.*

Proof. Consider some $x, y \in \mathbb{R}^n$ and a parameterization in t as $\gamma(t) = (1-t)x + ty \quad \forall t \in [0,1]$. Note that $\gamma(0) = x$ and $\gamma(1) = y$. By the Fundamental Theorem of Calculus we have:

$$\begin{aligned} |g(y) - g(x)| = |g(\gamma(1)) - g(\gamma(0))| &= \left| \int_0^1 \frac{dg(\gamma(t))}{dt} dt \right| \\ &= \left| \int_0^1 \nabla g^\top \nabla \gamma dt \right| \leq \int_0^1 \left| \nabla g^\top \nabla \gamma \right| dt \\ &\leq \int_0^1 \|\nabla g(x)\|_* \|\nabla \gamma(t)\| dt \leq L\|y - x\| \end{aligned}$$

□

Theorem A.3.1. *(restatement of Theorem 3.1). Let $g : \mathbb{R}^n \to \mathbb{R}^K$, g^i be L-Lipschitz continuous under norm $\|\cdot\|_* \ \forall i \in \{1, \ldots, K\}$, and $c_A = arg\max_i g^i(x)$. Then, we have $arg\max_i g^i(x + \delta) = c_A$ for all δ satisfying:*

$$\|\delta\| \leq \frac{1}{2L} \left(g^{c_A}(x) - \max_c g^{c \neq c_A}(x) \right).$$

Proof. Take $c_B = \arg\max_c g^{c \neq c_A}(x)$. By Proposition 3.1, we get:

$$\begin{aligned} |g^{c_A}(x + \delta) - g^{c_A}(x)| \leq L\|\delta\| &\implies g^{c_A}(x + \delta) \geq g^{c_A}(x) - L\|\delta\| \\ |g^{c_B}(x + \delta) - g^{c_B}(x)| \leq L\|\delta\| &\implies g^{c_B}(x + \delta) \leq g^{c_B}(x) + L\|\delta\| \end{aligned}$$

By subtracting the inequalities and re-arranging terms, we have that as long as $g^{c_A}(x) - L\|\delta\| > g^{c_B}(x) + L\|\delta\|$, *i.e.* the bound in the Theorem, then $g^{c_A}(x + \delta) > g^{c_B}(x + \delta)$, completing the proof. □

Proposition A.3.2. *(restatement of Proposition 3.2). Consider* $g_\Sigma(x) = \mathbb{E}_{\epsilon\sim\mathcal{N}(0,\Sigma)}\left[f(x+\epsilon)\right]$. $\Phi^{-1}(g_\Sigma(x))$ *is* 1*-Lipschitz (i.e.* $L = 1$*) under the* $\|\cdot\|_{\Sigma^{-1},2}$ *norm.*

Proof. To prove Proposition 2, one needs to show that $\Phi^{-1}(g^i_\Sigma(x))\ \forall i$ is 1-Lipschitz under the $\|\cdot\|_{\Sigma^{-1},2}$ norm. For ease of notation, we drop the superscript g^i_Σ and use only g. We want to show that $\|\nabla\Phi^{-1}(g_\Sigma(x))\|_{\Sigma^{-1},2} = \|\Sigma^{1/2}\nabla\Phi^{-1}(g_\Sigma(x))\|_2 \leq 1$. Following the argument presented in Salman et al. [2019], it suffices to show that, for any unit norm direction u and $p = g_\Sigma(x)$, we have:

$$u^\top\Sigma^{\frac{1}{2}}\nabla g_\Sigma(x) \leq \frac{1}{\sqrt{2\pi}}\exp\left(-\frac{1}{2}(\Phi^{-1}(p))^2\right). \tag{A.1}$$

We start by noticing that:

$$\begin{aligned} u^\top\Sigma^{\frac{1}{2}}\nabla g_\Sigma(x) &= \frac{1}{(\sqrt{2\pi})^n\sqrt{|\Sigma|}}\int_{\mathbb{R}^n} f(t)u^\top\Sigma^{\frac{1}{2}}\Sigma^{-1}(t-x)\exp\left(-\frac{1}{2}(x-t)\Sigma^{-1}(x-t)\right)d^nt \\ &= \mathbb{E}_{s\sim\mathcal{N}(0,\mathbf{I})}[f(x+\Sigma^{\frac{1}{2}}s)u^\top s] = \mathbb{E}_{v\sim\mathcal{N}(0,\Sigma)}[f(x+v)u^\top\Sigma^{-\frac{1}{2}}v]. \end{aligned}$$

We now need to find the optimal $f^* : \mathbb{R}^n \to [0,1]$ that satisfies $g_\Sigma(x) = \mathbb{E}_{v\sim\mathcal{N}(0,\Sigma)}[f(x+v)] = p$ while maximizing the left hand size $\mathbb{E}_{v\sim\mathcal{N}(0,\Sigma)}[f(x+v)u^\top\Sigma^{-\frac{1}{2}}v]$. We argue that the maximizer is the following function:

$$f^*(x+v) = \mathbb{1}\left\{u^\top\Sigma^{-\frac{1}{2}}v \geq -\Phi^{-1}(p)\right\}.$$

To prove that f^* is indeed the optimal maximizer, we first show feasibility. **(i)**: It is clear that $f^* : \mathbb{R}^n \to [0,1]$. (**ii**) Note that:

$$\mathbb{E}_{v\sim\mathcal{N}(0,\Sigma))}\left[\mathbb{1}\left\{u^\top\Sigma^{-\frac{1}{2}}v \geq -\Phi^{-1}(p)\right\}\right] = \mathbb{P}_{x\sim\mathcal{N}(0,1)}(x \geq -\Phi^{-1}(p)) = 1 - \Phi(-\Phi^{-1}(p)) = p.$$

To show the optimality of f^*, we show that it attains the right upper bound:

$$\begin{aligned} \mathbb{E}_{v\sim\mathcal{N}(0,\Sigma))}\left[u^\top\Sigma^{-\frac{1}{2}}v\mathbb{1}\left\{u^\top\Sigma^{-\frac{1}{2}}v \geq -\Phi^{-1}(p)\right\}\right] &= \mathbb{E}_{x\sim\mathcal{N}(0,1)}\left[x\mathbb{1}\left\{x \geq -\Phi^{-1}(p)\right\}\right] \\ &= \frac{1}{\sqrt{2\pi}}\int_{-\Phi^{-1}(p)}^{\infty} x\exp\left(-\frac{1}{2}x^2\right)dx \\ &= \frac{1}{\sqrt{2\pi}}\exp\left(-\frac{1}{2}(\Phi^{-1}(p))^2\right) \end{aligned}$$

obtaining the bound from Equation (A.1), and thus completing the proof. □

Proposition A.3.3. *(restatement of Proposition 3.3). Consider* $g_\Lambda(x) = \mathbb{E}_{\epsilon\sim\mathcal{U}[-1,1]^n}[f(x+\Lambda\epsilon)]$. *The classifier* $g^i_\Lambda\ \forall i$ *is* $1/2$*-Lipschitz (i.e.* $L = 1/2$*) under the* $\|\Lambda x\|_\infty$ *norm.*

Proof. We begin by observing that the dual norm of $\|x\|_{\Lambda,1} = \|\Lambda^{-1}x\|_1$ is $\|x\|_* = \|\Lambda x\|_\infty$, since:

$$\max_{\|\Lambda^{-1}x\|_1\leq 1} x^\top y = \max_{\|z\|_1\leq 1} y^\top \Lambda z = \|\Lambda y\|_\infty.$$

Without loss of generality, we analyze $\partial g^i/\partial x_1$. Let $\hat{x} = [x_2, \ldots, x_n] \in \mathbb{R}^{n-1}$, then:

$$\begin{aligned}\frac{\lambda_1 \partial g^i}{\partial x_1} &= \frac{\lambda_1}{(2\lambda)^n}\frac{\partial}{\partial x_1}\int_{[-1,1]^{n-1}}\int_{-1}^{1} f^i(x_1 + \lambda_1\epsilon_1, \hat{x} + \hat{\Lambda}\hat{\epsilon})d\epsilon_1 d^{n-1}\hat{\epsilon} \\ &= \frac{1}{2^n}\int_{[-1,1]^{n-1}}(f^i(x_1+1, \hat{x}+\hat{\Lambda}\hat{\epsilon}) - f^i(x_1-1, \hat{x}+\hat{\Lambda}\hat{\epsilon}))d^{n-1}\hat{\epsilon}\end{aligned}$$

Thus,

$$\left|\frac{\lambda_1\partial g^i}{\partial x_1}\right| \leq \frac{1}{2^n\prod_{j=2}^n \lambda_j}\int_{[-1,1]^{n-1}}\left|f^i(x_1+1, \hat{x}+\hat{\Lambda}\hat{\epsilon}) - f^i(x_1-1, \hat{x}+\hat{\Lambda}\hat{\epsilon})\right| d^{n-1}\hat{\epsilon} \leq \frac{1}{2}.$$

The second and last steps follow by the change of variable $t = x_1 + \lambda_1\epsilon_1$ and Leibniz rule. Following a symmetric argument, $|\lambda_j \partial g^i/\partial x_j| \leq 1/2\ \forall i$ resulting in having $\|\Lambda\nabla g^i(x)\|_\infty = \max_i \lambda_i |\partial g^i/\partial x_i| \leq 1/2\ \forall i$ concluding the proof. □

Proposition A.3.4. *(restatement of Proposition 3.4).* $\mathcal{V}(\{\delta : \|\Lambda^{-1}\delta\|_1 \leq r\}) = \frac{(2r)^n}{n!}\prod_i \lambda_i$.

Proof. Take $A = r\Lambda^{-1} = \text{diag}(1/r\lambda_1, \ldots, 1/r\lambda_n) = \text{diag}(a_1, \ldots, a_n)$.

We can re-write the region as $\{x : \sum_i a_i|x_i| \leq 1\}$, from which it is clear to see that this region is an origin centered, axis-aligned simplex with the set of vertices $\mathcal{V} = \{\pm 1/a_i \mathbf{e}_i\}_{i=1}^n$, where $\mathbf{e}_i$ is the standard basis vector i.

Define the sets of vertices $\mathcal{V}^t = \mathcal{V} \setminus \{-1/a_n\mathbf{e}_n\}$ and $\mathcal{V}^b = \mathcal{V} \setminus \{1/a_n\mathbf{e}_n\}$. Given the symmetry around the origin, each of these sets defines an n-dimensional *hyperpyramid* with a shared *base* B_{n-1} given by the $n-1$-dimensional hyperplane defined by all vertices where $x_n = 0$, and an *apex* at the vertex $1/a_n\mathbf{e}_n$ (or $-1/a_n\mathbf{e}_n$ in the case of $\mathcal{V}^b$). The volume of each of these $n-1$-dimensional hyperpyramids is given by $\mathcal{V}(B_{n-1})/na_n$ (Kendall [2004]), yielding a total volume of $V_n = \frac{2}{n}\frac{1}{a_n}\mathcal{V}(B_{n-1})$.

The same argument can be applied to compute $\mathcal{V}(B_{n-1})$ which is a union of two $n-1$-dimensional hyperpyramids. This forms a recursion that completes the proof. □

Proof. (**Alternative Proof**.) We consider the case that Λ^{-1} is a general positive definite matrix that is not necessarily diagonal. Note that $\mathcal{V}\left(\{\delta : \|\Lambda^{-1}\delta\|_1 \leq r\}\right) = \mathcal{V}\left(\{\delta : \|(r\Lambda)^{-1}\delta\|_1 \leq 1\}\right) = r^n|\Lambda|\mathcal{V}\left(\{\delta : \|\delta\|_1 \leq 1\}\right)$ where $|r\Lambda|$ denotes the determinant. The last equality follows by the volume of a set under a linear map and noting that $\{\delta : \|(r\Lambda)^{-1}\delta\|_1 \leq 1\} = \{r\Lambda\delta : \|\delta\|_1 \leq r\}$. At last, $\{\delta : \|\delta\|_1 \leq 1\}$ can be expressed as the disjoint union of 2^n simplexes. Thus, we have $\mathcal{V}\left(\{\delta : \|\Lambda^{-1}\delta\|_1 \leq r\}\right) = {}^{(2r)^n}/_{n!}|\Lambda|$ since the volume of a simplex is ${}^1/_{n!}$ completing the proof. □

For completeness, we supplement the previous result with bounds on the volume that may be useful for future readers.

Proposition A.1. *For any positive definite $\Lambda^{-1} \in \mathbb{R}^{n\times n}$, we have the following:*

$$\left(\frac{2r}{n}\right)^n \mathcal{V}\left(\mathcal{Z}(\Lambda)\right) \leq \mathcal{V}\Big(\{\delta : \|\Lambda^{-1}\delta\|_1 \leq r\}\Big) \leq (2r)^n \mathcal{V}\left(\mathcal{Z}(\Lambda)\right)$$

where $\mathcal{V}\left(\mathcal{Z}(\mathbf{\Lambda})\right) = \sqrt{|\Lambda^\top\Lambda|}$ which is the volume of the zonotope with a generator matrix Λ.

Proof. Let $S_1 = \{\delta : \|\Lambda^{-1}\delta\|_1 \leq r\}$, $S_\infty = \{\delta : \|\Lambda^{-1}\delta\|_\infty \leq r\}$ and $S_\infty^n = \{\delta : n\|\Lambda^{-1}\delta\|_\infty \leq r\}$. Since $\|\Lambda^{-1}\delta\|_\infty \leq \|\Lambda^{-1}\delta\|_1 \leq n\|\Lambda^{-1}\delta\|_\infty$, then $S_\infty \supseteq S_1 \supseteq S_\infty^n$. Therefore, we have $\mathcal{V}(S_\infty) \geq \mathcal{V}(S_1) \geq \mathcal{V}(S_\infty^n)$. At last note that, $S_\infty^n = \{\frac{r}{n}\Lambda\delta : \|\delta\|_\infty \leq 1\}$ and that with the change of variables $\delta = 2u - 1_n$ where 1_n is a vector of all ones, we have $S_\infty^n = \mathcal{Z}\left(\frac{2r}{n}\Lambda\right) \oplus \frac{-r}{n}\Lambda 1_n$ where $\oplus$ is a Minkowski sum and noting that $\frac{r}{n}\Lambda 1_n$ is a single point in $\mathbb{R}^n$. Therefore, $\mathcal{V}\left(\mathcal{Z}\left(\frac{2r}{n}\Lambda\right) \oplus \frac{-r}{n}\Lambda 1_n\right) = {}^{(2r)^n}/_{n}\,\mathcal{V}\left(\mathcal{Z}(\Lambda)\right)$. The upper bound follows with a similar argument completing the proof. □

A.3.1 Certification under Gaussian Mixture Smoothing Distribution

We consider a general, K-component, zero-mean Gaussian mixture smoothing distribution $\mathcal{G}$ such that:

$$\mathcal{G}(\{\alpha_i, \Sigma_i\}_{i=1}^K) := \sum_{i=1}^K \alpha_i \mathcal{N}(0, \Sigma_i), \quad \text{s.t.} \quad \sum_i \alpha_i = 1, 0 < \alpha_i \leq 1 \tag{A.2}$$

Given f and as per the recipe described in §3.5, we are interested in the Lipschitz constant of the smooth classifier $g_{\mathcal{G}}(x) = (f * \mathcal{G})(x) = \sum_i^K \alpha_i g_{\Sigma_i} = \sum_i^K \alpha_i (f * \mathcal{N}(0, \Sigma_i)) = \sum_i \alpha_i g_{\Sigma_i}(x)$ where g_{Σ_i} is defined as in the Gaussian case.

Note the weaker bound when compared to Proposition 3.2, for each of the Gaussian components presented in the following proposition.

Proposition A.2. *g_Σ is $\sqrt{2/\pi}$-Lipschitz under $\|.\|_{\Sigma^{-1},2}$ norm.*

Proof. Following a similar argument to the proof of Proposition 3.2, we get:

$$\begin{aligned} u^\top \Sigma^{\frac{1}{2}} \nabla g_\Sigma(x) &\leq \frac{1}{(2\pi)^{n/2}\sqrt{|\Sigma|}} \int_{\mathbb{R}^n} |u^\top \Sigma^{-\frac{1}{2}}(t-x)| \exp\left(-\frac{1}{2}(x-t)^\top \Sigma^{-1}(x-t)\right) d^n t \\ &= \mathbb{E}_{s\sim\mathcal{N}(0,\mathbf{I})}\left[|u^\top s|\right] = \mathbb{E}_{v\sim\mathcal{N}(0,1)}\left[|v|\right] = \sqrt{2/\pi}. \end{aligned}$$

□

With Proposition A.2, we obtain a Lipschitz constant for a Gaussian mixture smoothing distribution as:

Proposition A.3. *$g_{\mathcal{G}}$ is $\sqrt{\pi/2}$-Lipschitz under $\|\delta\|_{\mathcal{B}^{-1},2}$ norm, where $\mathcal{B}^{-1} = \sum_i^K \alpha_i \Sigma_i^{-1}$.*

Proof.

$$\begin{aligned} |g_{\mathcal{G}}(x+\delta) - g_{\mathcal{G}}(x)| &\leq \sum_i \alpha_i |g_{\Sigma_i}(x+\delta) - g_{\Sigma_i}(x)| \\ &\leq \sqrt{\frac{\pi}{2}} \sum_i \alpha_i \|\delta\|_{\Sigma_i,2} \leq \sqrt{\frac{\pi}{2}} \sqrt{\delta^\top \left(\sum_i \alpha_i \Sigma_i^{-1}\right) \delta} = \sqrt{\frac{\pi}{2}} \|\delta\|_{\mathcal{B},2}, \end{aligned}$$

Obtained by first applying the triangle inequality, then Proposition 3.2 followed by Jensen's inequality. □

Thus yielding the following certificate by combining Proposition A.3 and Theorem 3.1.

Corollary A.1. *Let* $c_A = \arg\max_i g_{\mathcal{G}}(x)$ *, then* $\arg\max_i g^i_{\mathcal{G}}(x+\delta) = c_A$ *for all* δ *satisfying:*

$$\|\delta\|_{\mathcal{B},2} \leq \frac{1}{\sqrt{2\pi}} \left(g^{c_A}_{\mathcal{G}}(x) - \max_c g^{c \neq c_A}_{\mathcal{G}}(x) \right).$$

where $\mathcal{B}^{-1} = \sum_i^K \alpha_i \Sigma_i^{-1}$.

A.4 AnCer Optimization

In this section we detail the implementation choices required to solving Equation (3.1). For ease of presentation, we restate the AnCer optimization problem (with $\Theta^x = \text{diag}(\{\theta^x_i\}_{i=1}^n)$):

$$\arg\max_{\Theta^x} \quad r^p\left(x, \Theta^x\right) \sqrt[n]{\prod_i \theta^x_i} \qquad \text{s.t.} \quad \min_i \ \theta^x_i r^p\left(x, \Theta^x\right) \geq r^*_{\text{iso}},$$

where $r^p\left(x, \Theta^x\right)$ is the gap value under the anisotropic smoothing distribution, and r^*_{iso} is the optimal isotropic radius, i.e. $\bar{\theta}^x r^p(x, \bar{\theta}^x)$ for $\bar{\theta}^x \in \mathbb{R}^+$. This is a nonlinear constrained optimization problem that is challenging to solve. As such, we relax it, and solve instead:

$$\arg\max_{\Theta^x} \quad r^p\left(x, \Theta^x\right) \sqrt[n]{\prod_i \theta^x_i} + \kappa \min_i \ \theta^x_i r^p\left(x, \Theta^x\right) \quad \text{s.t.} \quad \theta^x_i \geq \bar{\theta}^x$$

given a hyperparameter $\kappa \in \mathbb{R}^+$. While the constraint $\theta^x_i \geq \bar{\theta}^x$ is not explicitly required to enforce the *superset* condition over the isotropic case, it proved itself beneficial from an empirical perspective. To sample from the distribution parameterized by Θ^x (in our case, either a Gaussian or Uniform), we make use of the *reparameterization trick*, as in Alfarra et al. [2022]. The solution of this optimization problem can be found iteratively by performing projected gradient ascent.

A standalone implementation for the AnCer optimization stage is presented in Listing A.1, whereas the full code integrated in our code base is available as supplementary material. To perform certification, we simply feed the output of this optimization to the certification procedure from Cohen et al. [2019].

```python
import torch
from torch.autograd import Variable
from torch.distributions.normal import Normal


class Certificate():
    def compute_proxy_gap(self, logits: torch.Tensor):
        raise NotImplementedError

    def sample_noise(self, batch: torch.Tensor, repeated_theta: torch.Tensor):
        raise NotImplementedError

    def compute_gap(self, pABar: float):
        raise NotImplementedError


class L2Certificate(Certificate):
    def __init__(self, batch_size: int, device: str = "cuda:0"):
        self.m = Normal(torch.zeros(batch_size).to(device),
                        torch.ones(batch_size).to(device))
        self.device = device
        self.norm = "l2"

    def compute_proxy_gap(self, logits: torch.Tensor):
        return self.m.icdf(logits[:, 0].clamp_(0.001, 0.999)) - \
            self.m.icdf(logits[:, 1].clamp_(0.001, 0.999))

    def sample_noise(self, batch: torch.Tensor, repeated_theta: torch.Tensor):
        return torch.randn_like(batch, device=self.device) * repeated_theta

    def compute_gap(self, pABar: float):
        return norm.ppf(pABar)


class L1Certificate(Certificate):
    def __init__(self, device="cuda:0"):
        self.device = device
        self.norm = "l1"

    def compute_proxy_gap(self, logits: torch.Tensor):
        return logits[:, 0] - logits[:, 1]

    def sample_noise(self, batch: torch.Tensor, repeated_theta: torch.Tensor):
        return 2 * (torch.rand_like(batch, device=self.device) - 0.5) * repeated_theta

    def compute_gap(self, pABar: float):
        return 2 * (pABar - 0.5)


def ancer_optimization(
        model: torch.nn.Module, batch: torch.Tensor,
        certificate: Certificate, learning_rate: float,
        isotropic_theta: torch.Tensor, iterations: int,
        samples: int, kappa: float, device: str = "cuda:0"):
    """Optimize batch using ANCER, assuming isotropic initialization point.

    Args:
        model: trained network
        batch: inputs to certify around
        certificate: instance of desired certification object
        learning_rate: optimization learning rate for ANCER
        isotropic_theta: initialization isotropic value per input in batch
        iterations: number of iterations to run the optimization
        samples: number of samples per input and iteration
        kappa: relaxation hyperparameter
    """
    batch_size = batch.shape[0]
    img_size = np.prod(batch.shape[1:])

    # define a variable, the optimizer, and the initial sigma values
    theta = Variable(isotropic_theta, requires_grad=True).to(device)
    optimizer = torch.optim.Adam([theta], lr=learning_rate)
    initial_theta = theta.detach().clone()

    # reshape vectors to have ''samples'' per input in batch
    new_shape = [batch_size * samples]
    new_shape.extend(batch[0].shape)
    new_batch = batch.repeat((1, samples, 1, 1)).view(new_shape)

    # solve iteratively by projected gradient ascend
    for _ in range(iterations):
        theta_repeated = theta.repeat(1, samples, 1, 1).view(new_shape)

        # Reparameterization trick
        noise = certificate.sample_noise(new_batch, theta_repeated)
        out = model(
            new_batch + noise
        ).reshape(batch_size, samples, -1).mean(dim=1)

        vals, _ = torch.topk(out, 2)
        gap = certificate.compute_proxy_gap(vals)

        prod = torch.prod(
```

```
            (theta.reshape(batch_size, -1))**(1/img_size), dim=1)
        proxy_radius = prod * gap

        radius_maximizer = - (
            proxy_radius.sum() +
            kappa *
            (torch.min(theta.view(batch_size, -1), dim=1).values*gap).sum()
        )
        radius_maximizer.backward()
        optimizer.step()

        # project to the initial theta
        with torch.no_grad():
            torch.max(theta, initial_theta, out=theta)

    return theta
```

Listing A.1: Python implementation of the AnCer optimization routine using PyTorch Paszke et al. [2019]

A.5 Memory-based Certification for AnCer

To guarantee the soundness of the AnCer classifier, we use an adapted version of the data-dependent memory-based solution presented in Alfarra et al. [2022]. The modified algorithm involves a post-processing certification step that obtains adjusted certification statistics based on the memory procedure from Alfarra et al. [2022] (see the original paper for more details). We present an adapted version to AnCer of this post-processing memory-based step in Algorithm 3.

Note that the proposed certified region $\mathcal{R}_{N+1}$ emerges from our certification bounds presented in Sections 3.5.1 and 3.5.2. There are a few differences between our proposed Algorithm 3 with respect to the original variant presented in Alfarra et al. [2022]. The first is that we remove the computation of the largest certifiable subset of a certified region $\mathcal{R}_{N+1}$ when there exists an i such that $x_{N+1} \in \mathcal{R}_i$ with a different class prediction, *i.e.* (`LargestInSubset` in Alfarra et al. [2022]) due to the complexity of the operation in the anisotropic case. As an example, it is generally difficult to find the largest volume ellipsoid contained in another ellipsoid. Due to this complexity, we choose to simply Abstain instead. Given the high dimensionality of the data, empirically, we never found a certificate in this situation within our experiments. Further, to ease the computational burden of the `Intersect` function, we introduce and instantiate the function `MaxIntersect` first which checks whether the ℓ_p-ball over-approximation of the region $\mathcal{R}_{N+1}$ intersects with a ℓ_p over-approximation of $\mathcal{R}_i$. This follows since when the ℓ_p balls over-approximation

Algorithm 3: Memory-Based Certification

Input: input point x_{N+1}, certified region $\mathcal{R}_{N+1}$, prediction $\mathcal{C}_{N+1}$, and memory $\mathcal{M}$

Result: Prediction for x_{N+1} and certified region at x_{N+1} that does not intersect with any certified region in $\mathcal{M}$.

for $(x_i, \mathcal{C}_i, \mathcal{R}_i) \in \mathcal{M}$ **do**
  if $\mathcal{C}_{N+1} \neq \mathcal{C}_i$ **then**
    if $x_{N+1} \in \mathcal{R}_i$ **then**
      return ABSTAIN, 0
    else if `MaxIntersect`$(\mathcal{R}_{N+1}, \mathcal{R}_i)$ *and* `Intersect`$(\mathcal{R}_{N+1}, \mathcal{R}_i)$ **then**
      $\mathcal{R}'_{N+1} =$ `LargestOutSubset`$(\mathcal{R}_i, \mathcal{R}_{N+1})$;
      $\mathcal{R}_{N+1} \leftarrow \mathcal{R}'_{N+1}$;
end
add $(x_{N+1}, \mathcal{C}_{N+1}, \mathcal{R}_{N+1})$ to $\mathcal{M}$;
return $\mathcal{C}_{N+1}$, $\mathcal{R}_{N+1}$;

to the anisotropic regions $\mathcal{R}_{N+1}$ and $\mathcal{R}_i$ do not intersect, then $\mathcal{R}_{N+1}$ and $\mathcal{R}_i$ do not intersect either. Only in cases in which those over-approximation regions intersect, we run the more expensive `Intersect` procedure. We present practical implementations for `MaxIntersect`, `Intersect` and `LargestOutSubset` for the ellipsoids and generalized cross-polytopes considered in this paper.

A.5.1 Implementing `MaxIntersect`$(\mathcal{R}_\mathbf{A}, \mathcal{R}_\mathbf{B})$ in the Ellipsoid and Generalized Cross-Polytope Cases

Given the two regions $\mathcal{R}_\mathbf{A}$ and $\mathcal{R}_\mathbf{B}$, consider ℓ_p-ball approximations of those regions, $\mathcal{R}_{\tilde{\mathbf{A}}} = \{x \in \mathbb{R}^n : \|x - a\|_p \leq r_a\}$ and $\mathcal{R}_{\tilde{\mathbf{B}}} = \{x \in \mathbb{R}^n : \|x - b\|_p \leq r_b\}$ such that $\mathcal{R}_\mathbf{A} \subseteq \mathcal{R}_{\tilde{\mathbf{A}}}$ and $\mathcal{R}_\mathbf{B} \subseteq \mathcal{R}_{\tilde{\mathbf{B}}}$.

Lemma A.1. *If* $\|a - b\|_p > r_a + r_b$, *then* $\mathcal{R}_\mathbf{A} \cap \mathcal{R}_\mathbf{B} = \emptyset$.

Proof. For the sake of contradiction, let $\|a - b\|_p > r_a + r_b$ and $x \in \mathcal{R}_{\tilde{\mathbf{A}}} \cap \mathcal{R}_{\tilde{\mathbf{B}}}$. Then, we have that $\|x - a\| \leq r_a$ and $\|x - b\| \leq r_b$. However:

$$r_a + r_b < \|a - b\|_p \leq \|x - a\|_p + \|x - b\|_p \leq r_a + r_b,$$

forming a contradiction. Thus, $\mathcal{R}_{\tilde{\mathbf{A}}} \cap \mathcal{R}_{\tilde{\mathbf{B}}} = \emptyset$, which in turn implies $\mathcal{R}_\mathbf{A} \cap \mathcal{R}_\mathbf{B} = \emptyset$ since $\mathcal{R}_\mathbf{A}$ and $\mathcal{R}_\mathbf{B}$ are subsets of $\mathcal{R}_{\tilde{\mathbf{A}}}$ and $\mathcal{R}_{\tilde{\mathbf{B}}}$, respectively. □

This forms a fast, maximum intersection check for ellipsoids, *i.e.* $p = 2$, and generalized cross-polytopes, *i.e.* $p = 1$. The `MaxIntersect` function returns `False` if $\|a - b\|_p > r_a + r_b$, and `True` otherwise.

A.5.2 Implementing `Intersect`($\mathcal{R}_\mathbf{A}$, $\mathcal{R}_\mathbf{B}$) in the Ellipsoid Case

The problem of efficiently checking if two ellipsoids intersect is not trivial. We rely on the work of Ros et al. [2002], Gilitschenski and Hanebeck [2012] with missing proofs from Gilitschenski and Hanebeck [2012] for completeness.

Lemma A.2. *Let* $\mathcal{R}_\mathbf{A} = \{x \in \mathbb{R}^n : (x-a)^\top \mathbf{A}(x-a) \leq 1\}$ *and* $\mathcal{R}_\mathbf{B} = \{x \in \mathbb{R}^n : (x-b)^\top \mathbf{B}(x-b) \leq 1\}$ *define two ellipsoids centered at* a *and* b*, respectively. We have that* $\mathcal{R} = \{x : t(x-a)^\top \mathbf{A}(x-a) + (1-t)(x-b)^\top \mathbf{B}(x-b) \leq 1\}$ *for any* $t \in [0,1]$ *satisfies* $\mathcal{R}_\mathbf{A} \cap \mathcal{R}_\mathbf{B} \subseteq \mathcal{R} \subseteq \mathcal{R}_\mathbf{A} \cup \mathcal{R}_\mathbf{B}$.

Proof. By considering the convex combination of the left-hand side of the inequalities defining the regions $\mathcal{R}_\mathbf{A}$ and $\mathcal{R}_\mathbf{B}$, it becomes obvious that $x \in \mathcal{R}_\mathbf{A} \cap \mathcal{R}_\mathbf{B} \implies x \in \mathcal{R}$, concluding the left side of the property. As for the right side, it suffices to show that if $x \notin \mathcal{R}_\mathbf{A}$ and $x \in \mathcal{R}$ then $x \in \mathcal{R}_\mathbf{B}$ and, similarly, that if $x \notin \mathcal{R}_\mathbf{B}$ and $x \in \mathcal{R}$ then $x \in \mathcal{R}_\mathbf{A}$. We show the first case since the second follows by symmetry. Without loss of generality, we assume that $a = b = \mathbf{0}_n$. Now, let x be such that $x^\top \mathbf{A} x > 1$ and $tx^\top \mathbf{A} x + (1-t)x^\top \mathbf{B} x \leq 1$ since $x \notin \mathcal{R}_\mathbf{A}$ and $x \in \mathcal{R}$. Then, since $x \in \mathcal{R}$, we have that $(1-t)x^\top \mathbf{B} x \leq 1 - tx^\top \mathbf{A} x \leq 1$ since $x^\top \mathbf{A} x > 1$ which implies that $x \in \mathcal{R}_\mathbf{B}$. □

Note that the previous result holds without loss of generality when for the radius 1 as the radius can be absorbed in $\mathbf{A}$ and $\mathbf{B}$. As the following Lemma was shown by Gilitschenski and Hanebeck [2012] without proof, we complement it below for completeness.

Lemma A.3. *The set* $\mathcal{R}$ *is equivalent to the following ellipsoid* $\mathcal{R} = \{x : (x-m)^\top \mathbf{E}_t (x-m) \leq K(t)\}$ *where* $\mathbf{E}_t = t\mathbf{A} + (1-t)\mathbf{B}$*,* $m = \mathbf{E}_t^{-1}(t\mathbf{A}a + (1-t)\mathbf{B}b)$*, and* $K(t) = 1 - ta^\top \mathbf{A} a - (1-t)b^\top \mathbf{B} b + m^\top \mathbf{E}_t m$.

Proof.

$$
\begin{aligned}
&t(x-a)^\top \mathbf{A}(x-a) + (1-t)(x-b)^\top \mathbf{B}(x-b) \leq 1 \\
\Leftrightarrow &x^\top \underbrace{(t\mathbf{A} + (1-t)\mathbf{B})}_{\mathbf{E}_t} x - 2x^\top \underbrace{(t\mathbf{A}a + (1-t)\mathbf{B}b)}_{\mathbf{E}_t m} \leq 1 - ta^\top \mathbf{A}a - (1-t)b^\top \mathbf{B}b \\
\Leftrightarrow &(x-m)^\top \mathbf{E}_t (x-m) \leq 1 - ta^\top \mathbf{A}a - (1-t)b^\top \mathbf{B}b + m^\top \mathbf{E}_t m
\end{aligned}
$$

The last equality follows by adding and subtracting $m^\top \mathbf{E}_t m$ and concluding the proof. □

Proposition A.4. *The set of points satisfying $\mathcal{R}$ for $t \in (0,1)$ is either an empty set, a single point, or the ellipsoid $\mathcal{R}$.*

Proof. We first observe that since $\mathbf{A}$ and $\mathbf{B}$ are positive definite, then $\mathbf{E}_t$ is positive definite. Then observe that for a choice of $t \in (0,1)$ such that $K(t) < 0$, the set $\mathcal{R}$ is an empty set, and since $\mathcal{R} \supseteq \mathcal{R}_\mathbf{A} \cap \mathcal{R}_\mathbf{B}$, the two sets do not intersect. If $K(t) = 0$, then the only point satisfying $\mathcal{R}$ is the center at m. Following a similar argument, then the two ellipsoids intersect at a point. At last for a choice of t such that $K(t) > 0$, then $\mathcal{R}$ defines an ellipsoid. □

As per Theorem A.4, it suffices to find some $t \in [0,1]$ under which $K(t) < 0$ to guarantee that the ellipsoids do not intersect. To that end, we solve the following convex optimization problem: $t^* = \text{argmin}_{t\in[0,1]} K(t)$ and check the condition if $K(t^*) < 0$. Moreover, as shown by Ros et al. [2002], Gilitschenski and Hanebeck [2012] $K(t)$ is convex in the domain $t \in (0,1)$. With several algebraic manipulations, one can show that $K(t)$ has the following equivalent forms:

$$
\begin{aligned}
K(t) &= 1 - ta^\top \mathbf{A}a - (1-t)b^\top \mathbf{B}b + m^\top \mathbf{E}_t m \\
K(t) &= 1 - t(1-t)(b-a)^\top \mathbf{B}\mathbf{E}_t^{-1}\mathbf{A}(b-a) \\
K(t) &= 1 - (b-a)^\top \left(\frac{1}{1-t}\mathbf{B}^{-1} + \frac{1}{t}\mathbf{A}^{-1}\right)^{-1}(b-a)
\end{aligned}
$$

Observe that for ANCER, we have that both $\mathbf{A}$ and $\mathbf{B}$ to be diagonals with diagonal elements $\{\mathbf{A}_{ii}\}_{i=1}^n$ and $\{\mathbf{B}_{ii}\}_{i=1}^n$, respectively, resulting in the following simple form for $K(t)$:

$$K(t) = 1 - \sum_{i=1}^{n}(b_i - a_i)^2 \frac{t(1-t)\mathbf{A}_{ii}\mathbf{B}_{ii}}{t\mathbf{A}_{ii} + (1-t)\mathbf{B}_{ii}}.$$

The `Intersect` function in the ellipsoid case returns `False` if there exists a $t \in (0,1)$ such that $K(t) < 0$, *i.e.* ellipsoids do not intersect, and `True` otherwise.

A.5.3 Implementing `Intersect`($\mathcal{R}_\mathbf{A}$, $\mathcal{R}_\mathbf{B}$) in the Generalized Cross-Polytope Case

Let $\mathcal{R}_\mathbf{A}$ and $\mathcal{R}_\mathbf{B}$ be two generalized cross-polytopes $\mathcal{R}_\mathbf{A} = \{x \in \mathbb{R}^n : \|\mathbf{A}(x - a)\|_1 \leq 1\}$ and $\mathcal{R}_\mathbf{B} = \{x \in \mathbb{R}^n : \|\mathbf{B}(x - b)\|_1 \leq 1\}$, where $\mathbf{A}$ and $\mathbf{B}$ are positive definite diagonal matrices with elements $\{\mathbf{A}_{ii}\}_{i=1}^n$ and $\{\mathbf{B}_{ii}\}_{i=1}^n$, respectively. We are interested in deciding whether $\mathcal{R}_\mathbf{A}$ and $\mathcal{R}_\mathbf{B}$ intersect. However, given the conservative context in which `Intersect` is used in Algorithm 3, we only need to make sure that the function only returns `False` if it is guaranteed that $\mathcal{R}_\mathbf{A} \cap \mathcal{R}_\mathbf{B} = \emptyset$.

As such, we are able to simplify the complex problem of generalized cross-polytope intersection to the much simpler one of ellipsoid over-approximation intersection. We do this by considering the over-approximation, *i.e.* superset, ellipsoids $\mathcal{R}_{\tilde{\mathbf{A}}} = \{x \in \mathbb{R}^n : \|\mathbf{A}(x-a)\|_2 \leq 1\}$ and $\mathcal{R}_{\tilde{\mathbf{B}}} = \{x \in \mathbb{R}^n : \|\mathbf{B}(x-b)\|_2 \leq 1\}$, and perform the ellipsoid intersection check presented in Appendix A.5.2. If $\mathcal{R}_{\tilde{\mathbf{A}}} \cap \mathcal{R}_{\tilde{\mathbf{B}}} = \emptyset$, then this implies that $\mathcal{R}_\mathbf{A} \cap \mathcal{R}_\mathbf{B} = \emptyset$ and we can safely return `False`. Otherwise, we conservatively assume the generalized cross-polytopes intersect, and return `True`, triggering the reduction procedure detailed in Appendix A.5.5.

A.5.4 Implementing `LargestOutSubset`($\mathcal{R}_\mathbf{A}$, $\mathcal{R}_\mathbf{B}$) in the Ellipsoid Case

Given two ellipsoids $\mathcal{R}_\mathbf{A} = \{x \in \mathbb{R}^n : (x-a)^\top \mathbf{A}(x-a) \leq 1\}$ and $\mathcal{R}_\mathbf{B} = \{x \in \mathbb{R}^n : (x-b)^\top \mathbf{B}(x-b) \leq 1\}$ that do intersect where $\mathbf{A}$ and $\mathbf{B}$ are positive definite diagonal matrices, the task is to find the largest possible ellipsoid $\mathcal{R}_{\tilde{\mathbf{B}}}$ centered at b such that $\mathcal{R}_{\tilde{\mathbf{B}}} \subseteq \mathcal{R}_\mathbf{B}$ where $\mathcal{R}_\mathbf{A} \cap \mathcal{R}_{\tilde{\mathbf{B}}} = \emptyset$.

Finding a maximum ellipsoid that satisfies those conditions is not trivial, so instead we consider a maximum enclosing ℓ_2-ball of $\mathcal{R}_{\mathbf{B}}$, $\mathcal{R}_{\check{\mathbf{B}}} = \{x \in \mathbb{R}^n : \|x-b\|_2 \leq r\}$, that does not intersect $\mathcal{R}_{\mathbf{A}}$. To obtain this ball, we project the center of $\mathcal{R}_{\mathbf{B}}$, b, to the ellipsoid $\mathcal{R}_{\mathbf{A}}$. Particularly, we formulate the problem as the projection of a vector $y = b - a$ onto an ellipsoid with the same shape as $\mathcal{R}_{\mathbf{A}}$ centered at $\mathbf{0}_n$. This is equivalent to solving the following optimization problem for a symmetric positive definite matrix $\mathbf{A}$:

$$\min_x \frac{1}{2}\|x-y\|_2^2 \qquad \text{s.t.} \quad x^\top \mathbf{A} x \leq 1.$$

Note that the objective function is convex, and the constraint forms a convex set. Forming the Lagrangian to this problem, we obtain:

$$\mathcal{L}(x,\lambda) = \frac{1}{2}\|x-y\|_2^2 + \lambda\left(x^\top \mathbf{A} x - 1\right),$$

where $\lambda > 0$. Therefore, the global optimal solution must satisfy the KKT conditions below:

$$\begin{aligned}
&\frac{\partial \mathcal{L}}{\partial x} = 0 \rightarrow x^* = (2\lambda\mathbf{A} + I)^{-1} y, \\
&\frac{\partial \mathcal{L}}{\partial \lambda} = 0 \rightarrow \underbrace{y^\top (2\lambda\mathbf{A} + I)^{-\top} \mathbf{A} (2\lambda\mathbf{A} + I)^{-1} y - 1}_{f(\lambda)} = 0.
\end{aligned}$$

Thus, to project the vector y on our region the ellipsoid characterized by $\mathbf{A}$, one needs to solve the scalar optimization $f(\lambda) = 0$ then substitute back in the formula of x^*. Further, given $\mathbf{A} = \text{diag}(\mathbf{A}_{11}, \ldots, \mathbf{A}_{nn})$, we can simplify the problem to:

$$f(\lambda) = \sum_{i=1}^{n} \frac{y_i^2 \mathbf{A}_{ii}}{(1 + 2\lambda\mathbf{A}_{ii})^2} - 1 = 0.$$

Once x^* is obtained, we can define the maximum radius of the ℓ_2-ball centered at b that does not intersect $\mathcal{R}_{\mathbf{A}}$ as:

$$r^* = \|(x^* + a) - b\|_2 - \epsilon,$$

for an arbitrarily small ϵ. Finally, we obtain $\mathcal{R}_{\check{\mathbf{B}}}$ as the maximum ball contained within $\mathcal{R}_{\mathbf{B}}$ that has a radius smaller than r^*, that is:

$$\mathcal{R}_{\check{\mathbf{B}}} = \{x \in \mathbb{R}^n : \|x-b\|_2 \leq \min\{r^*, \min_i \mathbf{B}_{ii}\}\}.$$

Note that while choosing the radius of $\mathcal{R}_{\tilde{\mathbf{B}}}$ to be r^* guarantees that $\mathcal{R}_{\tilde{\mathbf{B}}} \cap \mathcal{R}_{\mathbf{A}} = \emptyset$, this does not guarantee that $\mathcal{R}_{\tilde{\mathbf{B}}} \subseteq \mathcal{R}_{\mathbf{B}}$. To guarantee both properties, we take the minimum of both r^* and $\min_i \mathbf{B}_{ii}$. This approach finds the solution to the projection of the point to the ellipsoid $\{x \in \mathbb{R}^n : x^\top \mathbf{A} x \leq 1\}$; it does not work for the case in which $b \in \mathcal{R}_{\mathbf{A}}$, since the problem would be trivially solved by setting $x^* = y$. Thus, our classifier must abstain in that situation.

A.5.5 Implementing `LargestOutSubset`($\mathcal{R}_{\mathbf{A}}$, $\mathcal{R}_{\mathbf{B}}$) in the Generalized Cross-Polytope Case

Let $\mathcal{R}_{\mathbf{A}}$ and $\mathcal{R}_{\mathbf{B}}$ be two generalized cross-polytopes $\mathcal{R}_{\mathbf{A}} = \{x \in \mathbb{R}^n : \|\mathbf{A}(x-a)\|_1 \leq 1\}$ and $\mathcal{R}_{\mathbf{B}} = \{x \in \mathbb{R}^n : \|\mathbf{B}(x-b)\|_1 \leq 1\}$, where $\mathbf{A}$ and $\mathbf{B}$ are positive definite diagonal matrices with elements $\{\mathbf{A}_{ii}\}_{i=1}^n$ and $\{\mathbf{B}_{ii}\}_{i=1}^n$, respectively. The task is to find the largest possible generalized cross-polytope $\mathcal{R}_{\tilde{\mathbf{B}}}$ centered at b such that $\mathcal{R}_{\tilde{\mathbf{B}}} \subseteq \mathcal{R}_{\mathbf{B}}$ where $\mathcal{R}_{\mathbf{A}} \cap \mathcal{R}_{\tilde{\mathbf{B}}} = \emptyset$.

As with the ellipsoid case, solving this problem for a generalized cross-polytope is not trivial, so instead we consider a maximum enclosing cross-polytope (i.e., ℓ_1-ball) of $\mathcal{R}_{\tilde{\mathbf{B}}} = \{x \in \mathbb{R}^n : \|x-b\|_1 \leq r\}$ that does not intersect $\mathcal{R}_{\mathbf{A}}$ and is a subset of $\mathcal{R}_{\mathbf{B}}$. To obtain this ℓ_1-ball, we project the center of $\mathcal{R}_{\mathbf{B}}$, b, to the generalized cross-polytope $\mathcal{R}_{\mathbf{A}}$ in a similar fashion to the ellipsoid case in Appendix A.5.4. We formulate the problem as the projection of the vector $y = b - a$ to the $\mathbf{0}_n$ centered generalized cross-polytope $\{x \in \mathbb{R}^n : \|\mathbf{A}x\|_1 \leq 1\}$.

Lemma A.4. *Consider the hyperplane $\mathcal{H} = \{x \in \mathbb{R}^n : w^\top x - k = 0\}$ and a point $y \in \mathbb{R}^n$. The ℓ_2 projection of y on the hyperplane is the point $x^* = y - {(w^\top y - k)w}/{\|w\|_2^2}$.*

Proof. We define the projection problem in a similar fashion to the ellipsoid case:

$$\min_x \frac{1}{2}\|x-y\|_2^2 \qquad \text{s.t.} \quad w^\top x - k = 0,$$

and obtain the Lagrangian as $\mathcal{L}(x,\lambda) = \frac{1}{2}\|x-y\|_2^2 + \lambda(w^\top x - k)$, from where we get (using the KKT conditions): $x^* = y - \lambda^* w$ and $\lambda^* = {w^\top y - k}/{\|w\|_2^2}$; thus obtaining: $x^* = y - \frac{(w^\top y - k)w}{\|w\|_2^2}$. □

While this formulation does not yield the closest point from a hyperplane when measured with the ℓ_1 norm, the fact that $\|x - x^*\|_1 \geq \|x - x^*\|_2$ implies the certification set obtained in the ℓ_1 norm via this method is a subset of the ℓ_2-ball of the minimum projection point. Crucially, this ℓ_2 projection has the advantage of having a closed-form solution, while an ℓ_1 one would require solving the problem using an iterative linear programming solver. As such, for the sake of computational complexity, we decided to use this projection, despite the sub-optimality of the result from the ℓ_1 perspective. Empirically, we have found this does not affect our results.

Since the set of vertices of the generalized cross-polytope $\{x \in \mathbb{R}^n : \|\mathbf{A}x\|_1 \leq 1\}$ is given by $\{\mathbf{e}_i/\mathbf{A}_{ii}, -\mathbf{e}_i/\mathbf{A}_{ii}\}_{i=1}^n$, and considering the distance between the projections and the original y, the hyperplane that minimizes it is defined by the set of vertices $\{\text{sign}(y_i)\mathbf{e}_i/\mathbf{A}_{ii}\}_{i=1}^n$. By writing it as a system of n equations, we obtain the hyperplane defined by $w = [-\text{sign}(y_1)\mathbf{A}_{11}, ..., -\text{sign}(y_n)\mathbf{A}_{nn}]$ and $k = 1$. Finally, after computing x^* as per Lemma A.4, we can define the maximum radius of the ℓ_1-ball centered at b that does not intersect $\mathcal{R}_\mathbf{A}$ as:

$$r^* = \|(x^* + a) - b\|_1 - \epsilon,$$

for an arbitrarily small ϵ. Finally, and similar to the ellipsoids case, we obtain $\mathcal{R}_{\tilde{\mathbf{B}}}$ as the maximum generalized cross-polytope contained within $\mathcal{R}_\mathbf{B}$ that has a radius smaller than r^*, that is:

$$\mathcal{R}_{\tilde{\mathbf{B}}} = \{x \in \mathbb{R}^n : \|x - b\|_1 \leq \min\{r^*, \min_i \mathbf{B}_{ii}\}\}$$

Similar to before, to guarantee that the ℓ_1 ball $\mathcal{R}_{\tilde{\mathbf{B}}}$ is still a subset to $\mathcal{R}_\mathbf{B}$, we take the minimum between r^* and $\min_i \mathbf{B}_{ii}$ to be the radius of $\mathcal{R}_{\tilde{\mathbf{B}}}$. As with the ellipsoid case, this approach does not work for the case in which $b \in \mathcal{R}_\mathbf{A}$, since the assumption of the closest plane to y would not hold. Thus, our classifier must abstain in that situation.

A.6 Experimental Setup

The experiments reported in the paper used the CIFAR-10 Krizhevsky [2009][1] and ImageNet Deng et al. [2009][2] datasets, and trained ResNet18, WideResNet40 and ResNet50 networks He et al. [2016]. Experiments used the typical data split for these datasets found in the PyTorch implementation Paszke et al. [2019]. The procedures to obtain the baseline networks used in the experiments are detailed in Appendix A.6.1 and A.6.2 for ellipsoids and generalized cross-polytopes, respectively. Source code to reproduce the AnCer optimization and certification results of this paper is available as supplementary material.

Isotropic DD Optimization. We used the available code of Alfarra et al. [2022][3] to obtain the isotropic data dependent smoothing parameters. To train our models from scratch, we used an adapted version of the code provided in the same repository.

Certification. Following Cohen et al. [2019], Salman et al. [2019], Zhai et al. [2019], Yang et al. [2020], Alfarra et al. [2022], all results were certified with $N_0 = 100$ Monte Carlo samples for selection and $N = 100,000$ estimation samples, with failure a probability of $\alpha = 0.001$.

A.6.1 Ellipsoid certification baseline networks

In terms of ellipsoid certification, the baselines we considered were Cohen Cohen et al. [2019][4], SmoothAdv Salman et al. [2019][5] and MACER Zhai et al. [2019][6].

In the CIFAR-10 experiments, we used a ResNet18 architecture, instead of the ResNet110 used in Cohen et al. [2019], Salman et al. [2019], Zhai et al. [2019] due to constraints at the level of computation power. As such, we had to train each of the networks from scratch following the procedures available in the source

[1] Available here (url), under an MIT license.
[2] Available here (url), terms of access detailed in the Download page.
[3] Data Dependent Randomized Smoothing source code available here
[4] Cohen source code available here.
[5] SmoothAdv source code available here.
[6] MACER source code available here.

code of each of the baselines. We did so under our own framework, and the training scripts are available in the supplementary material. For the ImageNet experiments we used the ResNet50 networks provided by each of the baselines in their respective open source repositories.

We trained the ResNet18 networks for 120 epochs, with a batch size of 256 and stochastic gradient descent with a learning rate of 10^{-2}, and momentum of 0.9.

A.6.2 Generalized Cross-Polytope certification baseline networks

For the certification of generalized cross-polytopes we considered RS4A Yang et al. [2020][7]. As described in RS4A Yang et al. [2020], we take $\lambda = \sigma/\sqrt{3}$ and report results as a function of σ for ease of comparison.

As with the baseline, we ran experiments on CIFAR-10 on a WideResNet40 architecture, and ImageNet on a ResNet50 Yang et al. [2020]. However, due to limited computational power, we were not able to run experiments on the wide range of distributional parameters the original work considers, *i.e.* $\sigma = \{0.15, 0.25, 0.5, 0.75, 1.0, 1.125, 1.5, 1.75, 2.0, 2.25, 2.5, 2.75, 3.0, 3.25, 3.5\}$ on CIFAR-10 and $\sigma = \{0.25, 0.5, 0.75, 1.0, 1.125, 1.5, 1.75, 2.0, 2.25, 2.5, 2.75, 3.0, 3.25, 3.5\}$ on ImageNet. Instead, and matching the requirements from the ellipsoid section, we choose a subset of $\sigma = \{0.25, 0.5, 1.0\}$ and performed our analysis at that level.

While the trained models are available in the source code of RS4A, we ran into several issues when we attempted to use them, the most problematic of which being the fact that the clean accuracy of such models was very low in both the WideResNet40 and ResNet50 ones. To avoid these issues we trained the models from scratch, but using the stability training loss as presented in the source code of RS4A. All of these models achieved clean accuracy of over 70%.

Following the procedures described in the original work, we trained the WideResNet40 models with the stability loss used in Yang et al. [2020] for 120 epochs, with a batch size of 128 and stochastic gradient descent with a learning rate of

[7] RS4A source code available here.

10^{-2}, and momentum of 0.9, along with a step learning rate scheduler with a γ of 0.1. For the ResNet50 networks on ImageNet, we trained them from scratch with stability loss for 90 epochs with a learning rate of 0.1 that drops by a factor of 0.1 after each 30 epochs and a batch size of 256.

A.7 Superset argument

The results we present in §3.8 support the argument that AnCer achieves, in general, a certificate that is a *superset* of the Fixed σ and Isotropic DD ones. To confirm this at an individual test set sample level, we compare the ℓ_2, ℓ_1, ℓ_2^Σ and ℓ_1^Λ certification results across the different methods, and obtain the percentage of the test set in which AnCer performs at least as well as all other methods in each certificates of the samples. Results of this analysis are presented in Tables A.1 and A.2.

For most networks and datasets, we observe that AnCer achieves a larger ℓ_p certificate than the baselines in a significant portion of the dataset, showcasing the fact that it obtains a superset of the isotropic region per sample. This is further confirmed by the comparison with the anisotropic certificates, in which, for all trained networks except MACER in CIFAR-10, AnCer's certificate is superior in over 90% of the test set samples.

Table A.1: Superset in top-1 ℓ_2 and ℓ_2^Σ (rounded to nearest percent)

	% AnCer ℓ_2 is the best	% AnCer ℓ_2^Σ is the best
CIFAR-10: Cohen	83	93
CIFAR-10: SmoothAdv	73	90
CIFAR-10: MACER	50	69
ImageNet: Cohen	94	96
ImageNet: SmoothAdv	90	93

Table A.2: Superset in top-1 ℓ_1 and ℓ_1^Λ (rounded to nearest percent)

	% AnCer ℓ_1 is the best	% AnCer ℓ_1^Λ is the best
CIFAR-10: RS4A	100	100
ImageNet: RS4A	97	99

A.8 Experimental Results per σ

A.8.1 Certifying Ellipsoids - ℓ_2 and ℓ_2^Σ certification results per σ

In this section we report certified accuracy at various ℓ_2 radii and ℓ_2^Σ proxy radii, following the metrics defined in §3.8, for each training method (Cohen Cohen et al. [2019], SmoothAdv Salman et al. [2019] and MACER Zhai et al. [2019]), dataset (CIFAR-10 and ImageNet) and σ ($\sigma \in \{0.12, 0.25, 0.5, 1.0\}$). Figures A.2 and A.3 shows certified accuracy at different ℓ_2 radii for CIFAR-10 and ImageNet, respectively, whereas Figures A.4 and A.5 plot certified accuracy and different ℓ_2^Σ proxy radii for CIFAR-10 and ImageNet, respectively.

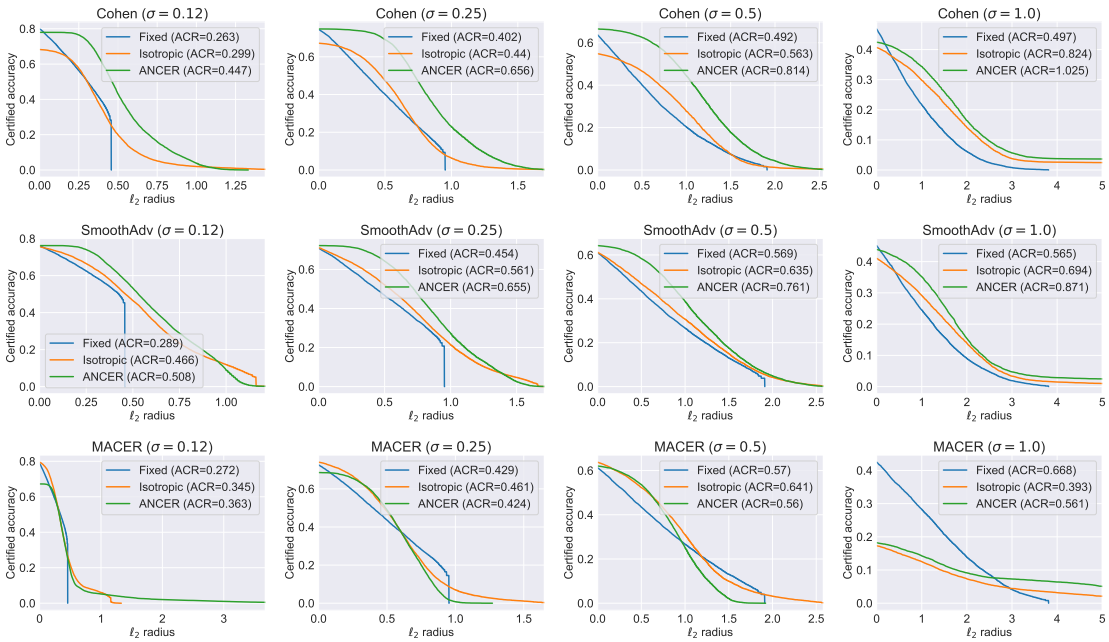

Figure A.2: CIFAR-10 certified accuracy as a function of ℓ_2 radius, per model and σ (used as initialization in the isotropic data-dependent case and AnCer).

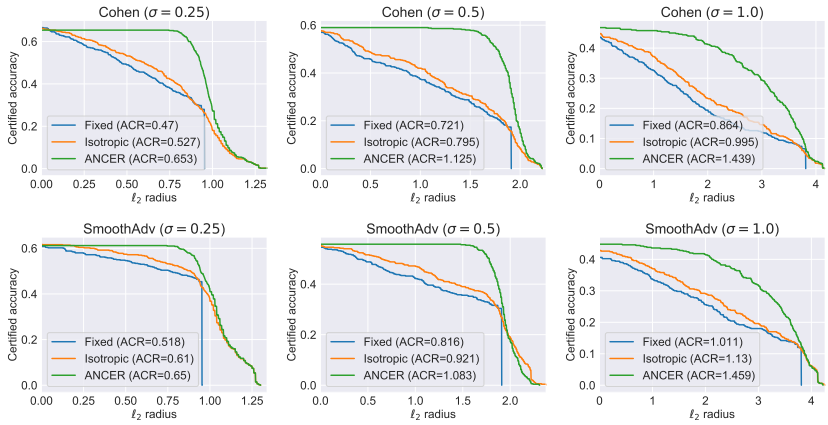

Figure A.3: ImageNet certified accuracy as a function of ℓ_2 radius, per model and σ (used as initialization in the isotropic data-dependent case and AnCer).

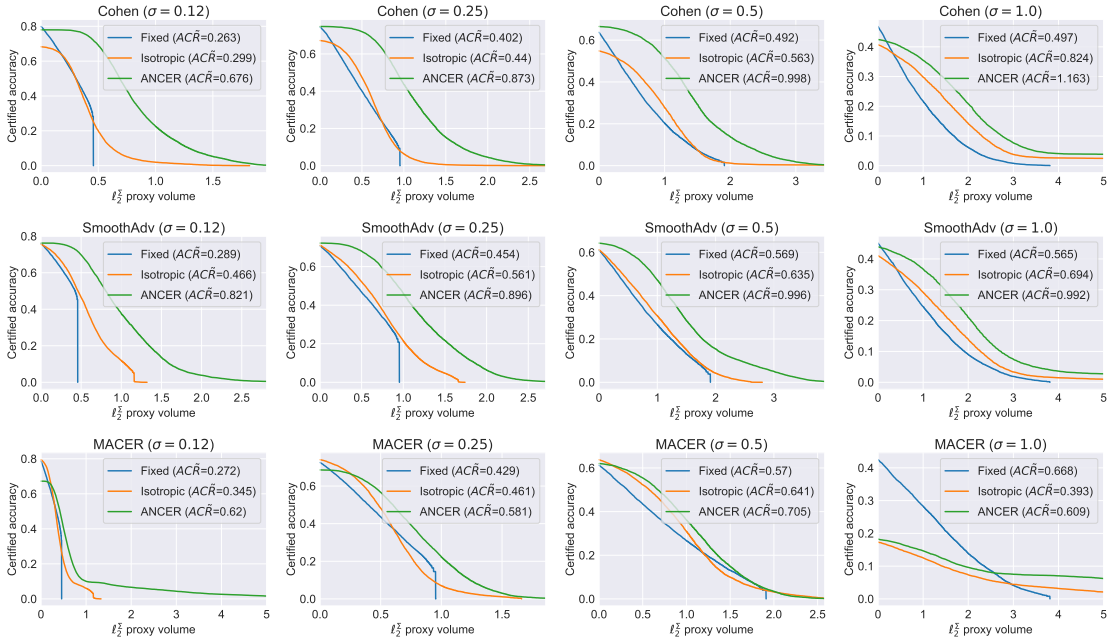

Figure A.4: CIFAR-10 certified accuracy as a function of ℓ_2^Σ proxy radius, per model and σ (used as initialization in the isotropic data-dependent case and AnCer).

A.8.2 Certifying Ellipsoids - ℓ_1 and ℓ_1^Λ certification results per σ

In this section we report certified accuracy at various ℓ_1 radii and ℓ_1^Λ proxy radii, following the metrics defined in §3.8, for RS4a, dataset (CIFAR-10 and ImageNet) and σ ($\sigma \in \{0.25, 0.5, 1.0\}$). Figures A.6 and A.7 shows certified accuracy at different ℓ_1 radii for CIFAR-10 and ImageNet, respectively, whereas Figures A.8 and A.9 plot certified accuracy and different ℓ_1^Λ proxy radii for CIFAR-10 and

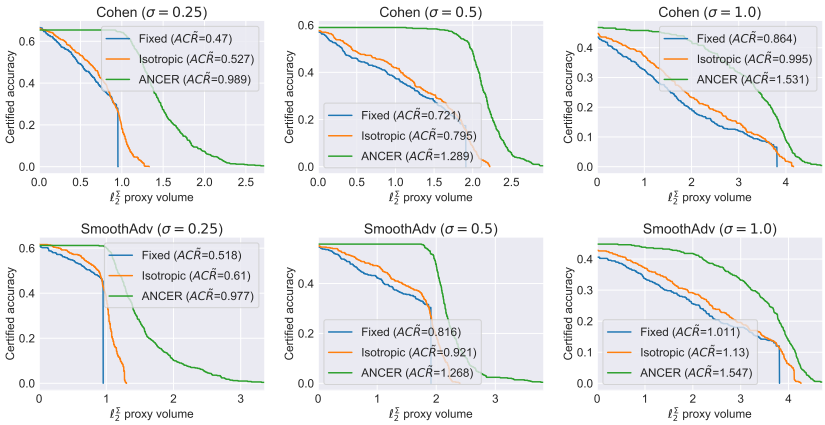

Figure A.5: ImageNet certified accuracy as a function of $\ell_2^{\hat{\Sigma}}$ proxy radius, per model and σ (used as initialization in the isotropic data-dependent case and AnCer).

ImageNet, respectively.

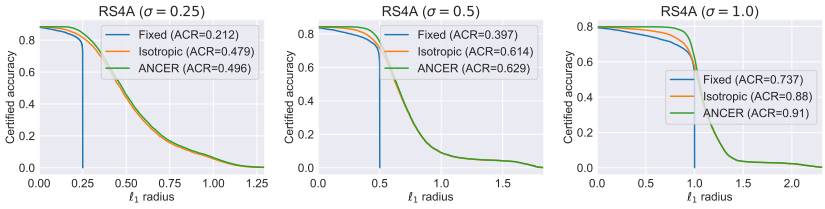

Figure A.6: CIFAR-10 certified accuracy as a function of ℓ_1 radius per σ (used as initialization in the isotropic data-dependent case and AnCer).

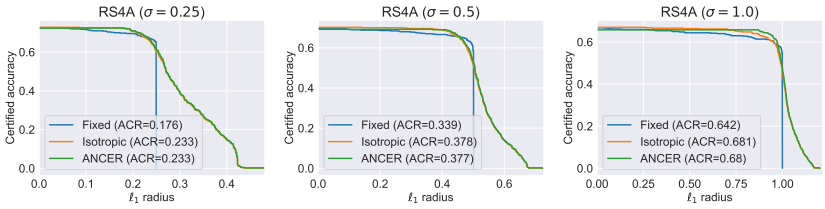

Figure A.7: ImageNet certified accuracy as a function of ℓ_1 radius per σ (used as initialization in the isotropic data-dependent case and AnCer).

A.9 Visual Comparison of Parameters in Ellipsoid Certificates

Anisotropic certification allows for a better characterization of the decision boundaries of the base classifier f. For example, the directions aligned with the major axes of the ellipsoids $\|\delta\|_{\Sigma,2} = r$, *i.e.* locations where Σ is large, are, by definition, expected to be less sensitive to perturbations compared to the minor axes directions.

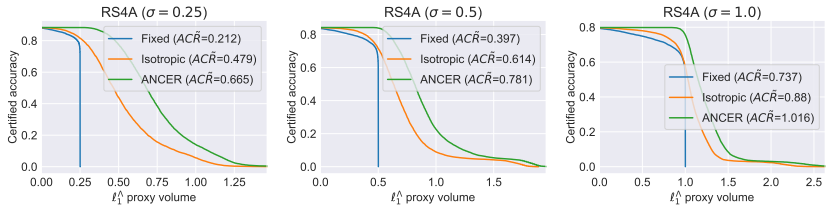

Figure A.8: CIFAR-10 certified accuracy as a function of ℓ_1^Λ proxy radius per σ (used as initialization in the isotropic data-dependent case and AnCer).

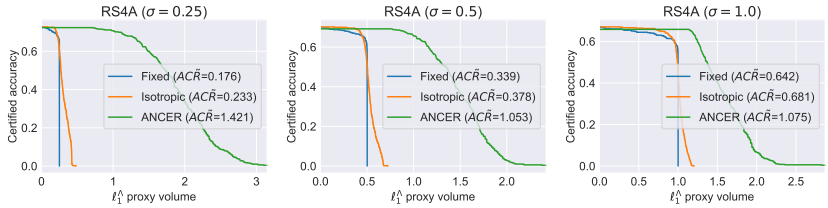

Figure A.9: ImageNet certified accuracy as a function of ℓ_1^Λ proxy radius per σ (used as initialization in the isotropic data-dependent case and AnCer).

To visualize this concept, Figure A.10 shows CIFAR-10 images along with their corresponding optimized ℓ_2 isotropic parameters obtained by Isotropic DD, and ℓ_2^Σ anisotropic parameters obtained by AnCer. First, we note the richness of information provided by the anisotropic parameters when compared to the ℓ_2 worst-case, isotropic one. Interestingly, pixel locations where the intensity of Σ is large (higher intensity in Figure A.10) are generally the ones corresponding least with the underlying true class and overlapping more with background pixels.

A particular insight one can get from AnCer certification is that the decision boundaries are not distributed isotropically around each input. To quantify this in higher dimensions, we plot in Figure A.11 a histogram of the ratio between the maximum and minimum elements of our optimized smoothing parameters for the experiments on SmoothAdv (with an initial $\sigma = 1.0$) on CIFAR-10. We note that this ratio can be as high as 5 for some of the input points, meaning the decision boundaries in that case could be 5 times closer to a given input for some directions than others.

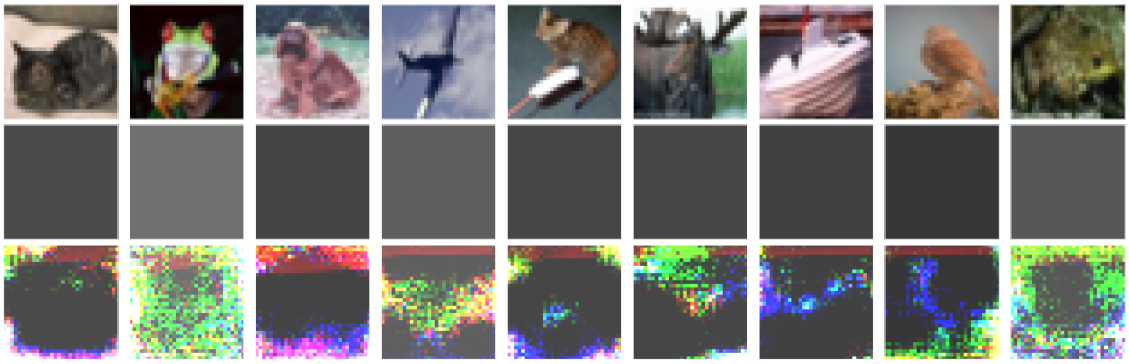

Figure A.10: Visualization of an input CIFAR-10 image x (top), and the optimized parameters σ (middle) and Σ (bottom) – higher intensity corresponds to higher σ_i in that pixel and channel – of the smoothing distributions in the isotropic and anisotropic case, respectively.

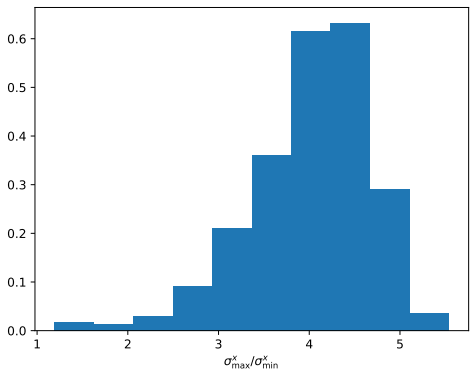

Figure A.11: Distribution of the maximum over the minimum AnCer σ^x at each dataset point for SmoothAdv Salman et al. [2019] on CIFAR-10 (for initial $\sigma = 1.0$)

A.10 Non data-dependent Anisotropic Certification

As mentioned briefly in §6, it is our intuition that anisotropic certification requires a data-dependent approach, as different points will have fairly different decision boundaries and the certified regions will extend in different directions (as exemplified in Figure 3.1).

To validate this claim, we perform certification of SmoothAdv Salman et al. [2019] with an initial $\sigma = 1$ on CIFAR-10 using a Σ which is the average of all the optimized Σ_x. The results of the certified accuracy, ACR and $AC\tilde{R}$ are presented in Table A.3, along with the same results for the methods reported in the main paper.

Table A.3: Comparison of different certification methods on SmoothAdv with an initial $\sigma = 1.0$ on CIFAR-10.

CIFAR-10	**SmoothAdv**	Accuracy @ ℓ_2 radius (%)							ℓ_2 ACR	ℓ_2^{Σ} $AC\tilde{R}$
		0.0	0.25	0.5	1.0	1.5	2.0	2.5		
$\sigma = 1.0$	Fixed σ	45	40	35	25	16	9	5	0.565	0.565
	Isotropic DD	41	39	36	29	21	14	7	0.694	0.694
	AnCer	44	43	41	35	26	15	8	**0.871**	**0.992**
	Average Σ	29	25	21	14	9	5	2	0.329	0.379

As can be observed, moving away from the data-dependent certification in the anisotropic scenario leads to a significant performance drop in terms of robustness.

A.11 Theoretical and Empirical Comparison with Mohapatra et al. [2020]

In regards to the theoretical results, unfortunately the certified regions of Mohapatra et al. [2020] do not exhibit a closed form solution similarly to ours. Thus, a direct theoretical volume bound comparison is not possible.

As for the empirical comparison, AnCer's performance on both ℓ_2 and ℓ_1 certificates far out-does that of Mohapatra et al. [2020]. For example, with ℓ_2 certificates at a radius of 0.5, Cohen certified with AnCer achieves 77% certified accuracy (see Table 3.1) while Mohapatra et al. [2020] achieves under 60% certified accuracy. Note that Mohapatra et al. [2020] has only a marginal improvement over Cohen et al. As for the ℓ_1 certificates, Mohapatra et al. [2020] uses the Gaussian distribution of Cohen et al, resulting in worse performance than existing state-of-art in ℓ_1 Yang et al. [2020] that uses a uniform distribution. Our approach improves further upon the performance of Yang et al. [2020]. For example, as per Table 2, RS4A with ANCER certification achieves 84% certified accuracy at an ℓ_1 radius of 0.5, Yang et al. [2020] achieves 75% certified accuracy while Mohapatra et al. [2020] achieves below 60%. However, we believe that the combination of both approaches, ANCER and Mohapatra et al. [2020] can further boost the performance as also hinted on in the abstract of Mohapatra et al. [2020] on the use of data-dependent smoothing.

B

Appendices for "Efficient Error Certification for Physics-Informed Neural Networks"

Contents

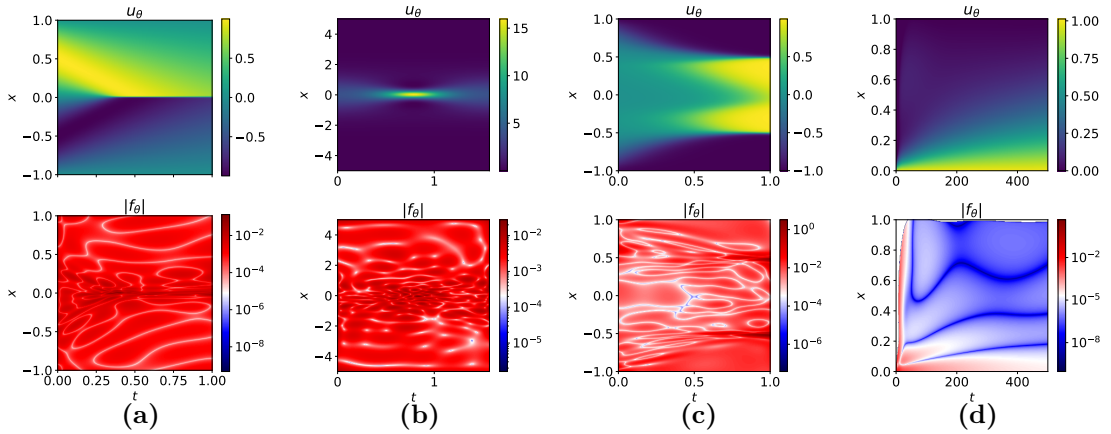

Figure B.1: Certifying with ∂-CROWN: visualization of the time evolution of u_θ, and the residual errors as a function of the spatial temporal domain (log-scale), $|f_\theta|$, for **(a)** Burgers' equation [Raissi et al., 2019], **(b)** Schrödinger's equation [Raissi et al., 2019], **(c)** Allan-Cahn's equation [Monaco and Apiletti, 2023], and **(d)** the Diffusion-Sorption equation [Takamoto et al., 2022].

B.1 Reducing empirical and certified errors through Physics-Informed Adversarial Training

The goal of reducing the solution errors obtained by PINNs has been the research focus of several previous works Kim et al. [2021], Krishnapriyan et al. [2021], Shekarpaz et al. [2022]. To observe the effects of one of these different training schemes on the verified correctness certification of PINNs, we consider Physics-informed Adversarial Training (PIAT) [Shekarpaz et al., 2022]. The procedure consists in replacing the residual loss term from Raissi et al. [2019] with an adversarial version inspired by Madry et al. [2018]. While this procedure leads to improvements in the example PINNs from Shekarpaz et al. [2022] and using our own implementation in Burgers' equation, we were unable to stably train Schrödinger's equation using PIAT. Since Schrödinger's equation is not considered in Shekarpaz et al. [2022], we only show PIAT results for Burgers' equation.

We solve the inner optimization problem using 5 PGD steps [Madry et al., 2018], and for $\epsilon = 0.05$ and a step size of 1.25ϵ. To improve convergence, we warm start PIAT training using a standard training solution after 6,000 L-BFGS

iterations. The results in Table B.1 show that as expected PIAT improves both empirical and certified residual bounds.

Table B.1: PIAT on Burgers' equation: Monte Carlo sampled maximum values (10^6 samples in 0.21s) and upper bounds computed using ∂-CROWN with N_b branchings for ① initial conditions ($t = 0$, $x \in \mathcal{D}$, $N_b = 5k$), ② boundary conditions ($t \in [0, T]$, $x = -1 \vee x = 1$, $N_b = 5k$), and ③ residual norm ($t \in [0, T]$, $x \in \mathcal{D}$, $N_b = 125k$), for a PINN trained using PIAT from Shekarpaz et al. [2022].

			MC - max	∂-CROWN- u_b (time [s])
PIAT Burgers [Shekarpaz et al., 2022]	①	$\lvert u_\theta(0,x) - u_0(x)\rvert^2$	$7.40 \cdot 10^{-6}$	$8.18 \cdot 10^{-6}$ (90.9)
	②	$\lvert u_\theta(t,-1)\rvert^2$	$2.31 \cdot 10^{-7}$	$3.32 \cdot 10^{-7}$ (49.4)
		$\lvert u_\theta(t,1)\rvert^2$	$8.41 \cdot 10^{-8}$	$1.39 \cdot 10^{-7}$ (48.5)
	③	$\lvert f_\theta(\mathbf{x})\rvert^2$	$3.60 \cdot 10^{-3}$	$2.39 \cdot 10^{-2}$ (2.8×10^5)

Certification convergence in PIAT vs. standard training The regularization provided by adversarial training often leads to verification algorithms converging faster to tighter lower and upper bounds. We investigate whether this is the case with ∂-CROWN's greedy branching strategy by comparing the *relative convergence* (*i.e.* , the deviation between the upper bound and the empirical maximum, $|f_\theta|^U - \max_{D'} |f_\theta|$) for the first $125k$ splits of PINNs trained in the standard and PIAT cases. The results presented in Figure B.2 show that adversarial training leads to quicker convergence, requiring a lower number of branches to reach the same error when compared to standard. This suggests that our method, while already efficient, would benefit from smarter training strategies that lead to lower residual errors.

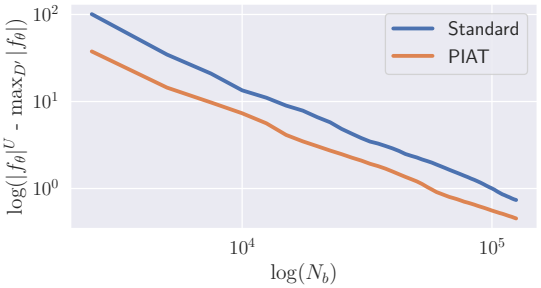

Figure B.2: Certification Convergence: log-log plot of the relative convergence of ∂-CROWN certification for a standard trained PINN (in blue) and PIAT (in orange).

Table B.2: Failure identification using residual bounds: empirical analysis of the connection between the residual bounds obtained by ∂-CROWN and the maximum solution error computed with respect to a numerical solver, u, over a sampled dataset $\mathcal{D}'$. The range of the solution values over the samples in $\mathcal{D}'$ are included for ease of comparison.

	Residual ∂-CROWN u_b	Max solution error ($\max_{\mathcal{D}'} \lvert u_\theta - u \rvert$)	Solution range ($\min$ / $\max_{\mathcal{D}'} u_\theta$)
Burgers	1.80×10^{-2}	3.78×10^{-3}	$[-1, 1]$
Schrödinger	7.67×10^{-4}	7.05×10^{-5}	$[1.82 \times 10^{-4}, 15.98]$
Allen-Cahn	10.76	0.86	$[-1, 1]$
Diffusion-Sorption	21.09	0.99	$[0, 1]$

B.2 ∂-CROWN for Failure Identification

In §4.6.2 we establish the empirical correlation between residual and solution errors for PINNs at different training stages (Figure 4.2). While comparing PINN errors for different PDEs is not easy due to residual scaling factors, note from Table 4.1 that the errors obtained for Burgers' and Schrödinger's equations are orders of magnitude lower than the ones for the Allen-Cahn and Diffusion-Sorption equations. Even with different residual tolerances, this would suggest the maximum solution error of the latter, harder to train PINNs should be higher.

Table B.2 presents the residual bounds obtained using ∂-CROWN as well as the maximum solution error with respect to a numerical solver for each of the four PINNs studied, which empirically reinforces that correlation. E.g., Burgers' equation has a maximum solution error of 3.78×10^{-3}, which is significantly lower than the trained Allen-Cahn PINN at 0.86, as expected from the residual bounds of 1.80×10^{-2} and 10.76, respectively. This contextualizes the results of Table 4.1 and showcases our framework can identify weaker models.

B.3 Ablation on N_b

We use $N_b = 2M$ for all the PINNs evaluated in this paper. A high number of branchings is required to obtain the tight bounds presented in Table 4.1. To justify that need, we have added plots of the variation of the obtained residual

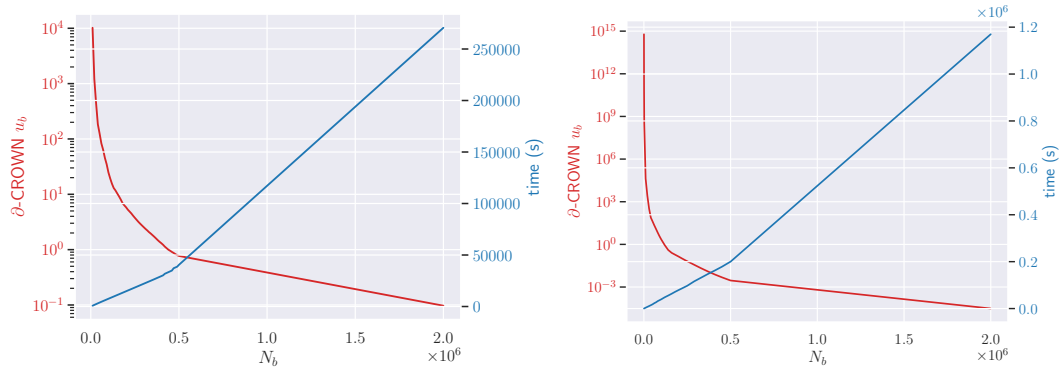

Figure B.3: Ablation on N_b: comparison of the residual error bounds ($|f_\theta|^2$) and runtime performance of our framework, ∂-CROWN on (a) Burgers' equation and (b) Schrödinger's equation.

bound for Burgers' and Schrödinger' equations in Figure B.3. Generally for both these PINNs we only get closer than one order of magnitude from the empirical estimates (considering the empirical MC sampled errors from Table 4.1) by using around $2M$ branches.

B.4 Proofs of partial derivative computations

B.4.1 Proof of Lemma 4.1: computing $\partial_{\mathbf{x}_i} u_\theta$

Let us now derive $\partial_{\mathbf{x}_i} u_\theta(\mathbf{x})$ for a given $i \in \{1, ..., n_0\}$. Starting backwards from the last layer and applying the chain rule we obtain:

$$\partial_{\mathbf{x}_i} u_\theta(\mathbf{x}) = \frac{\partial y^{(L)}}{\partial z^{(L-1)}} \cdot \frac{\partial z^{(L-1)}}{\partial z^{(L-2)}} \cdot \ldots \cdot \frac{\partial z^{(1)}}{\partial \mathbf{x}} \cdot \frac{\partial \mathbf{x}}{\partial x_i}$$

Given that $\partial_{\mathbf{x}_i} x = \mathbf{e}_i$ and $\frac{\partial y^{(L)}}{\partial z^{(L-1)}} = \mathbf{W}^{(L)}$, all that's left to compute to obtain the full expression is $\frac{\partial z^{(k)}}{\partial z^{(k-1)}}$, $k \in \{L-1, ..., 1\}$. Note that, for simplicity of the expressions, $z^{(0)} = \mathbf{x}$. For every element $j \in \{1, ..., d_k\}$ of $z^{(k)}$ denoted by $z_j^{(k)}$, we have:

$$\frac{\partial z_j^{(k)}}{\partial z^{(k-1)}} = \sigma'\left(\mathbf{W}_{[j,:]}^{(k)} z^{(k-1)} + \mathbf{b}_j^{(k)}\right) \mathbf{W}_{[j,:]}^{(k)}$$

where $\mathbf{W}_{j,:}^{(k)}$ denotes the j-th row of $\mathbf{W}^{(k)}$, and $\mathbf{b}_j^{(k)}$ the j-th element of $\mathbf{b}$. Thus, the final expression can be obtained by stacking the columns of the previous expression to obtain the full Jacobian:

$$\frac{\partial z^{(k)}}{\partial z^{(k-1)}} = \operatorname{diag}\left[\sigma'\left(\mathbf{W}^{(k)} z^{(k-1)} + \mathbf{b}^{(k)}\right)\right] \cdot \mathbf{W}^{(k)}$$

This concludes the proof.

B.4.2 Proof of Lemma 4.2: computing $\partial_{\mathbf{x}_i^2} u_\theta$

Given the result obtained in Appendix B.4.1, let us now derive $\partial_{\mathbf{x}_i^2} u_\theta(\mathbf{x})$ for a given $i \in \{1, ..., d_0\}$. Starting backwards from the last layer of $\partial_{\mathbf{x}_i} u_\theta$ and applying the chain rule we obtain:

$$\partial_{\mathbf{x}_i^2} u_\theta = \frac{\partial}{\partial x_i}\left(\frac{\partial y^{(L)}}{\partial z^{(L-1)}} \cdot \frac{\partial z^{(L-1)}}{\partial z^{(L-2)}} \cdot ... \cdot \frac{\partial z^{(1)}}{\partial \mathbf{x}} \cdot \frac{\partial \mathbf{x}}{\partial x_i}\right) = \mathbf{W}^{(L)} \partial_{\mathbf{x}_i^2} z^{(L-1)}$$

Now the same can be applied to $\partial_{\mathbf{x}_i^2} z^{(L-1)}$, and in general to $\partial_{\mathbf{x}_i^2} z^{(k)}$ to obtain:

$$\partial_{\mathbf{x}_i^2} z^{(k)} = \frac{\partial}{\partial x_i}\left(\frac{\partial z^{(k)}}{\partial z^{(k-1)}} \partial_{\mathbf{x}_i} z^{(k-1)}\right) = \frac{\partial^2 z^{(k)}}{\partial x_i \partial z^{(k-1)}} \partial_{\mathbf{x}_i} z^{(k-1)} + \frac{\partial z^{(k)}}{\partial z^{(k-1)}} \partial_{\mathbf{x}_i^2} z^{(k-1)},$$

forming a recursion which can be taken until the first layer of $\partial_{\mathbf{x}_i} u_\theta$, *i.e.* ,:

$$\partial_{\mathbf{x}_i^2} z^{(1)} = \frac{\partial}{\partial x_i}\left(\frac{\partial z^{(1)}}{\partial \mathbf{x}} \cdot \mathbf{e}_i\right) = \frac{\partial^2 z^{(1)}}{\partial x_i \partial \mathbf{x}} \cdot \mathbf{e}_i.$$

With the computation of $\partial_{\mathbf{x}_i} u_\theta$, both $\partial_{\mathbf{x}_i} z^{(k-1)}$ and $\frac{\partial z^{(k)}}{\partial z^{(k-1)}}$ are known. As such, the only missing pieces in the general recursion is the computation of $\frac{\partial^2 z^{(k)}}{\partial x_i \partial z^{(k-1)}}$. Recall from the previous section that $\frac{\partial z^{(k)}}{\partial z^{(k-1)}} = \text{diag}\left[\sigma'\left(\mathbf{W}^{(k)} z^{(k-1)} + \mathbf{b}^{(k)}\right)\right] \mathbf{W}^{(k)}$. As such:

$$\frac{\partial^2 z^{(k)}}{\partial x_i \partial z^{(k-1)}} = \frac{\partial}{\partial x_i}\left(\text{diag}\left[\sigma'\left(\mathbf{W}^{(k)} z^{(k-1)} + \mathbf{b}^{(k)}\right)\right] \mathbf{W}^{(k)}\right).$$

Following the element-wise reasoning from above, we have that:

$$\begin{aligned}\frac{\partial^2 z_j^{(k)}}{\partial x_i \partial z^{(k-1)}} &= \sigma''\left(\mathbf{W}_{j,:}^{(k)} z^{(k-1)} + \mathbf{b}_j^{(k)}\right) \frac{\partial}{\partial x_i}\left(\mathbf{W}_{j,:}^{(k)} z^{(k-1)} + \mathbf{b}_j^{(k)}\right) \mathbf{W}_{j,:}^{(k)} \\ &= \sigma''\left(\mathbf{W}_{j,:}^{(k)} z^{(k-1)} + \mathbf{b}_j^{(k)}\right)\left(\mathbf{W}_{j,:}^{(k)} \frac{\partial z^{(k-1)}}{\partial x_i}\right) \mathbf{W}_{j,:}^{(k)}\end{aligned}$$

Stacking as in the previous case, we obtain:

$$\frac{\partial^2 z^{(k)}}{\partial x_i \partial z^{(k-1)}} = \text{diag}\left[\sigma''\left(\mathbf{W}^{(k)} z^{(k-1)} + \mathbf{b}^{(k)}\right)\left(\mathbf{W}^{(k)} \partial_{\mathbf{x}_i} z^{(k-1)}\right)\right] \mathbf{W}^{(k)},$$

completing the derivation of $\partial_{\mathbf{x}_i^2} u_\theta(\mathbf{x})$.

B.4.3 Theorem 4.1: Formal Statement and Proof

Theorem 4.1 (∂-CROWN: linear lower and upper bounding $\partial_{\mathbf{x}_i} u_\theta$)**.** *For every $j \in \{1, \ldots, d_L\}$ there exist two functions $\partial_{\mathbf{x}_i} u^U_{\theta,j}$ and $\partial_{\mathbf{x}_i} u^L_{\theta,j}$ such that, $\forall \mathbf{x} \in \mathcal{C}$ it holds that $\partial_{\mathbf{x}_i} u^L_{\theta,j} \leq \partial_{\mathbf{x}_i} u_{\theta,j} \leq \partial_{\mathbf{x}_i} u^U_{\theta,j}$, with:*

$$\partial_{\mathbf{x}_i} u^U_{\theta,j} = \phi^{(1),U}_{0,j,i} + \sum_{r=1}^{d_0} \phi^{(1),U}_{1,j,r} \mathbf{x} + \phi^{(1),U}_{2,j,r}$$
$$\partial_{\mathbf{x}_i} u^L_{\theta,j} = \phi^{(1),L}_{0,j,i} + \sum_{r=1}^{d_0} \phi^{(1),L}_{1,j,r} \mathbf{x} + \phi^{(1),L}_{2,j,r}$$

where for $p \in \{0, 1, 2\}$, $\phi^{(1),U}_{p,j,r}$ and $\phi^{(1),L}_{p,j,r}$ are functions of $\mathbf{W}^{(k)}$, $y^{(k),L}$, $y^{(k),U}$, $\mathbf{A}^{(k),L}$, $\mathbf{A}^{(k),U}$ $\mathbf{a}^{(k),L}$, and $\mathbf{a}^{(k),U}$, and can be computed using a recursive closed-form expression in $\mathcal{O}(L)$ time.

Proof: Assume that through the computation of the previous bounds on u_θ, the pre-activation layer outputs of u_θ, $y^{(k)}$, are lower and upper bounded by linear functions defined as $\mathbf{A}^{(k),L}\mathbf{x} + \mathbf{a}^{(k),L} \leq y^{(k)} \leq \mathbf{A}^{(k),U}\mathbf{x} + \mathbf{a}^{(k),U}$ and $y^{(k),L} \leq y^{(k)} \leq y^{(k),U}$ for $x \in \mathcal{C}$.

Take the upper and lower bound functions for $\partial_{\mathbf{x}_i} u_\theta$ as $\partial_{\mathbf{x}_i} u^U_\theta$ and $\partial_{\mathbf{x}_i} u^L_\theta$, respectively, and the upper and lower bound functions for $\partial_{\mathbf{x}_i} z^{(k)}$ as $\partial_{\mathbf{x}_i} z^{(k),U}$ and $\partial_{\mathbf{x}_i} z^{(k),L}$, respectively. For the sake of simplicity of notation, we define $\mathbf{B}^{(k),+} = \mathbb{I}\left(\mathbf{B}^{(k)} \geq 0\right) \odot \mathbf{B}^{(k)}$ and $\mathbf{B}^{(k),-} = \mathbb{I}\left(\mathbf{B}^{(k)} < 0\right) \odot \mathbf{B}^{(k)}$.

Working backwards from $\partial_{\mathbf{x}_i} u_\theta$, we apply the same idea from CROWN [Zhang et al., 2018]:

$$\begin{aligned} \partial_{\mathbf{x}_i} u^U_\theta &= \mathbf{W}^{(L),+} \partial_{\mathbf{x}_i} z^{(L-1),U} + \mathbf{W}^{(L),-} \partial_{\mathbf{x}_i} z^{(L-1),L} \\ \partial_{\mathbf{x}_i} u^L_\theta &= \mathbf{W}^{(L),+} \partial_{\mathbf{x}_i} z^{(L-1),L} + \mathbf{W}^{(L),-} \partial_{\mathbf{x}_i} z^{(L-1),U} \end{aligned} \tag{B.1}$$

We continue to apply this backwards propagation to $\partial_{\mathbf{x}_i} z^{(L-1)}$ to obtain $\partial_{\mathbf{x}_i} z^{(L-1),U}$ and $\partial_{\mathbf{x}_i} z^{(L-1),L}$. Recall that $\partial_{\mathbf{x}_i} z^{(k)} = \partial_{z^{(k-1)}} z^{(k)} \partial_{\mathbf{x}_i} z^{(k-1)}$, that is, for $j \in \{1, \ldots, d_k\}$ we have $\partial_{\mathbf{x}_i} z^{(k)}_j = \partial_{z^{(k-1)}} z^{(k)}_{j,:} \partial_{\mathbf{x}_i} z^{(k-1)} = \sum_{n=1}^{d_{k-1}} \partial_{z^{(k-1)}} z^{(k)}_{j,n} \partial_{\mathbf{x}_i} z^{(k-1)}_n$.

We resolve the bilinear dependencies of each $\partial_{\mathbf{x}_i} z^{(k)}_j$ by relaxing it using a convex combination of the upper and lower bounds obtained by the McCormick

envelopes of the product. Assuming that $\partial_{z^{(k-1)}} z_{j,n}^{(k),L} \leq \partial_{z^{(k-1)}} z_{j,n}^{(k)} \leq \partial_{z^{(k-1)}} z_{j,n}^{(k),U}$ and $\partial_{\mathbf{x}_i} z_n^{(k-1),L} \leq \partial_{\mathbf{x}_i} z_n^{(k-1)} \leq \partial_{\mathbf{x}_i} z_n^{(k-1),U}$, we have that:

$$\begin{aligned}
\partial_{\mathbf{x}_i} z_j^{(k)} \leq \partial_{\mathbf{x}_i} z_j^{(k),U} &= \sum_{n=1}^{d_{k-1}} \alpha_{0,j,n}^{(k)} \partial_{\mathbf{x}_i} z_n^{(k-1)} + \alpha_{1,j,n}^{(k)} \partial_{z^{(k-1)}} z_{j,n}^{(k)} + \alpha_{2,j,n}^{(k)} \\
\partial_{\mathbf{x}_i} z_j^{(k)} \geq \partial_{\mathbf{x}_i} z_j^{(k),L} &= \sum_{n=1}^{d_{k-1}} \beta_{0,j,n}^{(k)} \partial_{\mathbf{x}_i} z_n^{(k-1)} + \beta_{1,j,n}^{(k)} \partial_{z^{(k-1)}} z_{j,n}^{(k)} + \beta_{2,j,n}^{(k)},
\end{aligned} \tag{B.2}$$

for:

$$\begin{aligned}
\alpha_{0,j,n}^{(k)} &= \eta_{j,n}^{(k)} \partial_{z^{(k-1)}} z_{j,n}^{(k),U} + \left(1 - \eta_{j,n}^{(k)}\right) \partial_{z^{(k-1)}} z_{j,n}^{(k),L} \\
\alpha_{1,j,n}^{(k)} &= \eta_{j,n}^{(k)} \partial_{\mathbf{x}_i} z_n^{(k-1),L} + \left(1 - \eta_{j,n}^{(k)}\right) \partial_{\mathbf{x}_i} z_n^{(k-1),U} \\
\alpha_{2,j,n}^{(k)} &= -\eta_{j,n}^{(k)} \partial_{z^{(k-1)}} z_{j,n}^{(k),U} \partial_{\mathbf{x}_i} z_n^{(k-1),L} - \left(1 - \eta_{j,n}^{(k)}\right) \partial_{z^{(k-1)}} z_{j,n}^{(k),L} \partial_{\mathbf{x}_i} z_n^{(k-1),U} \\
\beta_{0,j,n}^{(k)} &= \zeta_{j,n}^{(k)} \partial_{z^{(k-1)}} z_{j,n}^{(k),L} + \left(1 - \zeta_{j,n}^{(k)}\right) \partial_{z^{(k-1)}} z_{j,n}^{(k),U} \\
\beta_{1,j,n}^{(k)} &= \zeta_{j,n}^{(k)} \partial_{\mathbf{x}_i} z_n^{(k-1),L} + \left(1 - \zeta_{j,n}^{(k)}\right) \partial_{\mathbf{x}_i} z_n^{(k-1),U} \\
\beta_{2,j,n}^{(k)} &= -\zeta_{j,n}^{(k)} \partial_{z^{(k-1)}} z_{j,n}^{(k),L} \partial_{\mathbf{x}_i} z_n^{(k-1),L} - \left(1 - \zeta_{j,n}^{(k)}\right) \partial_{z^{(k-1)}} z_{j,n}^{(k),U} \partial_{\mathbf{x}_i} z_n^{(k-1),U},
\end{aligned}$$

where $\eta_{j,n}^{(k)}$ and $\zeta_{j,n}^{(k)}$ are convex coefficients that can be set as hyperparameters, or optimized for as in α-CROWN [Xu et al., 2020].

To continue the backward propagation, we now need to bound the components of $\partial_{z^{(k-1)}} z^{(k)}$. Recall from Lemma 4.1 that $\partial_{z^{(k-1)}} z^{(k)} = \text{diag}\left[\sigma'\left(y^{(k-1)}\right)\right] \mathbf{W}^{(k)}$, and $\partial_{z^{(k-1)}} z_{j,:}^{(k)} = \sigma'\left(y_j^{(k-1)}\right) \mathbf{W}_{j,:}^{(k)}$ for $j \in \{1, \ldots, d_k\}$.

Since $y_j^{(k),L} \leq y_j^{(k)} \leq y_j^{(k),U}$, we can obtain a linear upper and lower bound relaxation for $\sigma'\left(y_j^{(k)}\right)$, such that $\gamma_j^{(k),L}\left(y_j^{(k)} + \delta_j^{(k),L}\right) \leq \sigma'\left(y_j^{(k)}\right) \leq \gamma_j^{(k),U}\left(y_j^{(k)} + \delta_j^{(k),U}\right)$. With this, we can proceed to bound $\partial_{z^{(k-1)}} z_{j,:}^{(k)}$ as:

$$\begin{aligned}
\partial_{z^{(k-1)}} z_{j,:}^{(k)} &\leq \underbrace{\left(\gamma_j^{(k),U} \mathbf{W}_{j,:}^{(k),+} + \gamma_j^{(k),L} \mathbf{W}_{j,:}^{(k),-}\right)}_{\iota_{0,j,:}^{(k)}} y_j^{(k)} + \underbrace{\left(\gamma_j^{(k),U} \delta_j^{(k),U} \mathbf{W}_{j,:}^{(k),+} + \gamma_j^{(k),L} \delta_j^{(k),L} \mathbf{W}_{j,:}^{(k),-}\right)}_{\iota_{1,j,:}^{(k)}} \\
\partial_{z^{(k-1)}} z_{j,:}^{(k)} &\geq \underbrace{\left(\gamma_j^{(k),L} \mathbf{W}_{j,:}^{(k),+} + \gamma_j^{(k),U} \mathbf{W}_{j,:}^{(k),-}\right)}_{\lambda_{0,j,:}^{(k)}} y_j^{(k)} + \underbrace{\left(\gamma_j^{(k),L} \delta_j^{(k),L} \mathbf{W}_{j,:}^{(k),+} + \gamma_j^{(k),U} \delta_j^{(k),U} \mathbf{W}_{j,:}^{(k),-}\right)}_{\lambda_{1,j,:}^{(k)}}
\end{aligned} \tag{B.3}$$

At this point, one could continue the back-substitution process using the bounds from CROWN [Zhang et al., 2018]. However, for the sake of efficiency, we use instead the

pre-computed inequalities from propagating bounds through u_θ: $\mathbf{A}^{(k),U}\mathbf{x} + \mathbf{a}^{(k),U} \leq y^{(k)} \leq \mathbf{A}^{(k),L}\mathbf{x} + \mathbf{a}^{(k),L}$. Substituting this in Equation B.3, we obtain:

$$\begin{aligned}
\partial_{z^{(k-1)}} z_{j,:}^{(k),U} &= \underbrace{\left(\iota_{0,j,:}^{(k),+}\mathbf{A}_{j,:}^{(k),U} + \iota_{0,j,:}^{(k),-}\mathbf{A}_{j,:}^{(k),L}\right)}_{\iota_{2,j,:}^{(k)}}\mathbf{x} + \underbrace{\iota_{0,j,:}^{(k),+}\mathbf{a}_j^{(k),U} + \iota_{0,j,:}^{(k),-}\mathbf{a}_j^{(k),L} + \iota_{1,j,:}^{(k)}}_{\iota_{3,j,:}^{(k)}} \\
\partial_{z^{(k-1)}} z_{j,:}^{(k),L} &= \underbrace{\left(\lambda_{0,j,:}^{(k),+}\mathbf{A}_{j,:}^{(k),L} + \lambda_{0,j,:}^{(k),-}\mathbf{A}_{j,:}^{(k),U}\right)}_{\lambda_{2,j,:}^{(k)}}\mathbf{x} + \underbrace{\lambda_{0,j,:}^{(k),+}\mathbf{a}_j^{(k),L} + \lambda_{0,j,:}^{(k),-}\mathbf{a}_j^{(k),U} + \lambda_{1,j,:}^{(k)}}_{\lambda_{3,j,:}^{(k)}}
\end{aligned} \tag{B.4}$$

In practice, we can use Equation B.4 to compute the required $\partial_{z^{(k-1)}} z_{j,n}^{(k),L}$ and $\partial_{z^{(k-1)}} z_{j,n}^{(k),U}$ for the McCormick relaxation that leads to Equation B.2. By back-substituting the result of Equation B.4 in Equation B.2, we obtain an expression for the upper and lower bounds on $\partial_{\mathbf{x}_i} z_j^{(k)}$ that only depends on $\partial_{\mathbf{x}_i} z^{(k-1)}$ and $\mathbf{x}$:

$$\begin{aligned}
\partial_{\mathbf{x}_i} z_j^{(k),U} &= \sum_{n=1}^{d_{k-1}} \alpha_{0,j,n}^{(k)} \partial_{\mathbf{x}_i} z_n^{(k-1)} + \alpha_{3,j,n}^{(k)}\mathbf{x} + \alpha_{4,j,n}^{(k)} \\
\partial_{\mathbf{x}_i} z_j^{(k),L} &= \sum_{n=1}^{d_{k-1}} \beta_{0,j,n}^{(k)} \partial_{\mathbf{x}_i} z_n^{(k-1)} + \beta_{3,j,n}^{(k)}\mathbf{x} + \beta_{4,j,n}^{(k)},
\end{aligned} \tag{B.5}$$

where:

$$\begin{aligned}
\alpha_{3,j,n}^{(k)} &= \alpha_{1,j,n}^{(k),+}\iota_{2,j,n}^{(k)} + \alpha_{1,j,n}^{(k),-}\lambda_{2,j,n}^{(k)}, \qquad & \alpha_{4,j,n}^{(k)} &= \alpha_{1,j,n}^{(k),+}\iota_{3,j,n}^{(k)} + \alpha_{1,j,n}^{(k),-}\lambda_{3,j,n}^{(k)} + \alpha_{2,j,n}^{(k)} \\
\beta_{3,j,n}^{(k)} &= \beta_{1,j,n}^{(k),+}\lambda_{2,j,n}^{(k)} + \beta_{1,j,n}^{(k),-}\iota_{2,j,n}^{(k)}, \qquad & \beta_{4,j,n}^{(k)} &= \beta_{1,j,n}^{(k),+}\lambda_{3,j,n}^{(k)} + \beta_{1,j,n}^{(k),-}\iota_{3,j,n}^{(k)} + \alpha_{2,j,n}^{(k)}
\end{aligned}$$

Given Equation B.5, we now have a recursive expression for each of the blocks that compose the computation of $\partial_{\mathbf{x}_i} u_\theta$, which allows us to obtain a closed form expression for $\partial_{\mathbf{x}_i} u_\theta^U$ and $\partial_{\mathbf{x}_i} u_\theta^L$ by applying recursive back-substitution starting with Equation B.1. Let us begin by performing back-substitution to the result

in Equation B.5 for layer $L-1$:

$$\partial_{\mathbf{x}_i} z_j^{(L-1),U} = \sum_{n=1}^{d_{L-2}} \alpha_{0,j,n}^{(L-1)} \partial_{\mathbf{x}_i} z_n^{(L-2)} + \alpha_{3,j,n}^{(L-1)} \mathbf{x} + \alpha_{4,j,n}^{(L-1)} \tag{B.6}$$

$$= \sum_{n=1}^{d_{L-2}} \alpha_{0,j,n}^{(L-1)} \left(\sum_{r=1}^{d_{L-3}} \mu_{0,n,r}^{(L-2)} \partial_{\mathbf{x}_i} z_r^{(L-3)} + \mu_{3,n,r}^{(L-2)} \mathbf{x} + \mu_{4,n,r}^{(L-2)} \right) + \tag{B.7}$$

$$+ \alpha_{3,j,n}^{(L-1)} \mathbf{x} + \alpha_{4,j,n}^{(L-1)} \tag{B.8}$$

$$= \sum_{n=1}^{d_{L-2}} \alpha_{0,j,n}^{(L-1)} \left(\sum_{r=1}^{d_{L-3}} \mu_{0,n,r}^{(L-2)} \partial_{\mathbf{x}_i} z_r^{(L-3)} \right) + \tag{B.9}$$

$$+ \alpha_{0,j,n}^{(L-1)} \left(\sum_{r=1}^{d_{L-3}} \mu_{3,n,r}^{(L-2)} \mathbf{x} + \mu_{4,n,r}^{(L-2)} \right) + \alpha_{3,j,n}^{(L-1)} \mathbf{x} + \alpha_{4,j,n}^{(L-1)} \tag{B.10}$$

$$= \sum_{r=1}^{d_{L-3}} \left(\sum_{n=1}^{d_{L-2}} \alpha_{0,j,n}^{(L-1)} \mu_{0,n,r}^{(L-2)} \right) \partial_{\mathbf{x}_i} z_r^{(L-3)} + \tag{B.11}$$

$$+ \left(\sum_{n=1}^{d_{L-2}} \alpha_{0,j,n}^{(L-1)} \left(\mu_{3,n,r}^{(L-2)} \mathbf{x} + \mu_{4,n,r}^{(L-2)} \right) + \frac{1}{d_{L-3}} \left(\alpha_{3,j,n}^{(L-1)} \mathbf{x} + \alpha_{4,j,n}^{(L-1)} \right) \right) \tag{B.12}$$

$$= \sum_{r=1}^{d_{L-3}} \rho_{0,j,r}^{(L-2)} \partial_{\mathbf{x}_i} z_r^{(L-3)} + \left(\sum_{n=1}^{d_{L-2}} \alpha_{0,j,n}^{(L-1)} \mu_{3,n,r}^{(L-2)} + \frac{1}{d_{L-3}} \alpha_{3,j,n}^{(L-1)} \right) \mathbf{x} + \tag{B.13}$$

$$+ \left(\sum_{n=1}^{d_{L-1}} \alpha_{0,j,n}^{(L-1)} \mu_{4,n,r}^{(L-2)} + \frac{1}{d_{L-3}} \alpha_{4,j,n}^{(L-1)} \right) \tag{B.14}$$

$$= \sum_{r=1}^{d_{L-3}} \rho_{0,j,r}^{(L-2)} \partial_{\mathbf{x}_i} z_r^{(L-3)} + \rho_{1,j,r}^{(L-2)} \mathbf{x} + \rho_{2,j,r}^{(L-2)}, \tag{B.15}$$

where:

$$\rho_{0,j,r}^{(L-2)} = \sum_{n=1}^{d_{L-2}} \alpha_{0,j,n}^{(L-1)} \mu_{0,n,r}^{(L-2)}$$

$$\rho_{1,j,r}^{(L-2)} = \sum_{n=1}^{d_{L-2}} \alpha_{0,j,n}^{(L-1)} \mu_{3,n,r}^{(L-2)} + \frac{1}{d_{L-2}} \alpha_{3,j,n}^{(L-1)}$$

$$\rho_{2,j,r}^{(L-2)} = \sum_{n=1}^{d_{L-2}} \alpha_{0,j,n}^{(L-1)} \mu_{4,n,r}^{(L-2)} + \frac{1}{d_{L-2}} \alpha_{4,j,n}^{(L-1)},$$

and:

$$\mu_{p,n,:}^{(L-2)} = \begin{cases} \alpha_{p,n,:}^{(L-2)} & \text{if } \alpha_{0,j,n}^{(L-1)} \geq 0 \\ \beta_{p,n,:}^{(L-2)} & \text{if } \alpha_{0,j,n}^{(L-1)} < 0 \end{cases}, p \in \{0, 3, 4\}$$

As in CROWN [Zhang et al., 2018], given we have put Equation B.15 in the same form as Equation B.6, we can now apply this argument recursively using

the $\rho^{(k)}$ and $\mu^{(k)}$ coefficients to obtain:

$$\partial_{\mathbf{x}_i} z_j^{(L-1),U} = \rho_{0,j,i}^{(1)} + \sum_{r=1}^{d_0} \rho_{1,j,r}^{(1)} \mathbf{x} + \rho_{2,j,r}^{(1)},$$

where:

$$\rho_{0,j,r}^{(k-1)} = \begin{cases} \alpha_{0,j,r}^{(k)} & \text{if } k = L \\ \sum_{n=1}^{d_{k-1}} \rho_{0,j,n}^{(k)} \mu_{0,n,r}^{(k-1)} & \text{if } k \in \{2, \dots, L-1\} \end{cases}$$
$$\rho_{1,j,r}^{(k-1)} = \begin{cases} \alpha_{3,j,r}^{(k)} & \text{if } k = L \\ \sum_{n=1}^{d_{k-1}} \rho_{0,j,n}^{(k)} \mu_{3,n,r}^{(k-1)} + \frac{1}{d_{k-2}} \rho_{1,j,n}^{(k)} & \text{if } k \in \{2, \dots, L-1\} \end{cases}$$
$$\rho_{2,j,r}^{(k-1)} = \begin{cases} \alpha_{4,j,r}^{(k)} & \text{if } k = L \\ \sum_{n=1}^{d_{k-1}} \rho_{0,j,n}^{(k)} \mu_{4,n,r}^{(k-1)} + \frac{1}{d_{k-2}} \rho_{2,j,n}^{(k)} & \text{if } k \in \{2, \dots, L-1\} \end{cases},$$

and:

$$\mu_{p,n,:}^{(k-1)} = \begin{cases} \alpha_{p,n,:}^{(k-1)} & \text{if } \rho_{0,j,n}^{(k)} \geq 0 \\ \beta_{p,n,:}^{(k-1)} & \text{if } \rho_{0,j,n}^{(k)} < 0 \end{cases}, p \in \{0, 3, 4\}$$

And following the same recursive argument:

$$\partial_{\mathbf{x}_i} z_j^{(L-1),L} = \tau_{0,j,i}^{(1)} + \sum_{r=1}^{d_0} \tau_{1,j,r}^{(1)} \mathbf{x} + \tau_{2,j,r}^{(1)},$$

where:

$$\tau_{0,j,r}^{(k-1)} = \begin{cases} \beta_{0,j,r}^{(k)} & \text{if } k = L \\ \sum_{n=1}^{d_{k-1}} \tau_{0,j,n}^{(k)} \omega_{0,n,r}^{(k-1)} & \text{if } k \in \{2, \dots, L-1\} \end{cases}$$
$$\tau_{1,j,r}^{(k-1)} = \begin{cases} \beta_{3,j,r}^{(k)} & \text{if } k = L \\ \sum_{n=1}^{d_{k-1}} \tau_{0,j,n}^{(k)} \omega_{3,n,r}^{(k-1)} + \frac{1}{d_{k-2}} \tau_{1,j,n}^{(k)} & \text{if } k \in \{2, \dots, L-1\} \end{cases}$$
$$\tau_{2,j,r}^{(k-1)} = \begin{cases} \beta_{4,j,r}^{(k)} & \text{if } k = L \\ \sum_{n=1}^{d_{k-1}} \tau_{0,j,n}^{(k)} \omega_{4,n,r}^{(k-1)} + \frac{1}{d_{k-2}} \tau_{2,j,n}^{(k)} & \text{if } k \in \{2, \dots, L-1\} \end{cases},$$

and:

$$\omega_{p,n,:}^{(k-1)} = \begin{cases} \beta_{p,n,:}^{(k-1)} & \text{if } \tau_{0,j,n}^{(k)} \geq 0 \\ \alpha_{p,n,:}^{(k-1)} & \text{if } \tau_{0,j,n}^{(k)} < 0 \end{cases}, p \in \{0, 3, 4\}$$

With these expressions, we can compute the required $\partial_{\mathbf{x}_i} z_n^{(k-1),L}$ and $\partial_{\mathbf{x}_i} z_n^{(k-1),U}$ which we assumed to be known to derive Equation B.2.

Finally, by back-propagating the bounds starting from Equation B.1, we get:

$$\begin{aligned}
\partial_{\mathbf{x}_i} u^U_{\theta,j} &= \sum_{n=1}^{d_{L-1}} \mathbf{W}^{(L),+}_{j,n} \left(\sum_{r=1}^{d_{L-2}} \alpha^{(L-1)}_{0,n,r} \partial_{\mathbf{x}_i} z^{(L-2)}_{[r]} + \alpha^{(L-1)}_{3,n,r} \mathbf{x} + \alpha^{(L-1)}_{4,n,r} \right) + \\
&\quad + \mathbf{W}^{(L),-}_{j,n} \left(\sum_{r=1}^{d_{L-2}} \beta^{(L-1)}_{0,n,r} \partial_{\mathbf{x}_i} z^{(L-2)}_{[r]} + \beta^{(L-1)}_{3,n,r} \mathbf{x} + \beta^{(L-1)}_{4,n,r} \right) \\
&= \sum_{r=1}^{d_{L-2}} \left(\sum_{n=1}^{d_{L-1}} \mathbf{W}^{(L),+}_{j,n} \alpha^{(L-1)}_{0,n,r} + \mathbf{W}^{(L),-}_{j,n} \beta^{(L-1)}_{0,n,r} \right) \partial_{\mathbf{x}_i} z^{(L-2)}_{[r]} + \\
&\quad + \left(\sum_{n=1}^{d_{L-1}} \mathbf{W}^{(L),+}_{j,n} \alpha^{(L-1)}_{3,n,r} + \mathbf{W}^{(L),-}_{j,n} \beta^{(L-1)}_{3,n,r} \right) \mathbf{x} + \\
&\quad + \left(\sum_{n=1}^{d_{L-1}} \mathbf{W}^{(L),+}_{j,n} \alpha^{(L-1)}_{4,n,r} + \mathbf{W}^{(L),-}_{j,n} \beta^{(L-1)}_{4,n,r} \right) \\
&= \sum_{r=1}^{d_{L-2}} \phi^{(L-1),U}_{0,j,r} \partial_{\mathbf{x}_i} z^{(L-2),U}_n + \phi^{(L-1),U}_{1,j,r} \mathbf{x} + \phi^{(L-1),U}_{2,j,r},
\end{aligned}$$

where:

$$\begin{aligned}
\phi^{(L-1),U}_{0,j,r} &= \sum_{n=1}^{d_{L-1}} \mathbf{W}^{(L),+}_{j,n} \alpha^{(L-1)}_{0,n,r} + \mathbf{W}^{(L),-}_{j,n} \beta^{(L-1)}_{0,n,r} \\
\phi^{(L-1),U}_{1,j,r} &= \sum_{n=1}^{d_{L-1}} \mathbf{W}^{(L),+}_{j,n} \alpha^{(L-1)}_{3,n,r} + \mathbf{W}^{(L),-}_{j,n} \beta^{(L-1)}_{3,n,r} \\
\phi^{(L-1),U}_{2,j,r} &= \sum_{n=1}^{d_{L-1}} \mathbf{W}^{(L),+}_{j,n} \alpha^{(L-1)}_{4,n,r} + \mathbf{W}^{(L),-}_{j,n} \beta^{(L-1)}_{4,n,r}.
\end{aligned}$$

From this, using the same back-propagation logic as in the derivations of $\partial_{\mathbf{x}_i} z^{(k-1),L}_n$ and $\partial_{\mathbf{x}_i} z^{(k-1),U}_n$, we can obtain:

$$\partial_{\mathbf{x}_i} u^U_{\theta,j} = \phi^{(1),U}_{0,j,i} + \sum_{r=1}^{d_0} \phi^{(1),U}_{1,j,r} \mathbf{x} + \phi^{(1),U}_{2,j,r}, \tag{B.16}$$

where:

$$\begin{aligned}
\phi^{(k-1),U}_{0,j,r} &= \begin{cases} \sum_{n=1}^{d_{k-1}} \mathbf{W}^{(k),+}_{j,n} \alpha^{(k-1)}_{0,n,r} + \mathbf{W}^{(k),-}_{j,n} \beta^{(k-1)}_{0,n,r} & \text{if } k = L \\ \sum_{n=1}^{d_{k-1}} \phi^{(k),U}_{0,j,n} \upsilon^{(k-1)}_{0,n,r} & \text{if } k \in \{2, \dots, L-1\} \end{cases} \\
\phi^{(k-1),U}_{1,j,r} &= \begin{cases} \sum_{n=1}^{d_{k-1}} \mathbf{W}^{(k),+}_{j,n} \alpha^{(k-1)}_{3,n,r} + \mathbf{W}^{(k),-}_{j,n} \beta^{(k-1)}_{3,n,r} & \text{if } k = L \\ \sum_{n=1}^{d_{k-1}} \phi^{(k),U}_{0,j,n} \upsilon^{(k-1)}_{3,n,r} + \frac{1}{d_{k-2}} \phi^{(k),U}_{1,j,n} & \text{if } k \in \{2, \dots, L-1\} \end{cases} \\
\phi^{(k-1),U}_{2,j,r} &= \begin{cases} \sum_{n=1}^{d_{k-1}} \mathbf{W}^{(k),+}_{j,n} \alpha^{(k-1)}_{4,n,r} + \mathbf{W}^{(k),-}_{j,n} \beta^{(k-1)}_{4,n,r} & \text{if } k = L \\ \sum_{n=1}^{d_{k-1}} \phi^{(k),U}_{0,j,n} \upsilon^{(k-1)}_{4,n,r} + \frac{1}{d_{k-2}} \phi^{(k),U}_{2,j,n} & \text{if } k \in \{2, \dots, L-1\} \end{cases},
\end{aligned}$$

and:

$$\upsilon_{p,n,:}^{(k-1)} = \begin{cases} \alpha_{p,n,:}^{(k-1)} & \text{if } \phi_{0,j,n}^{(k),U} \geq 0 \\ \beta_{p,n,:}^{(k-1)} & \text{if } \phi_{0,j,n}^{(k),U} < 0 \end{cases}, p \in \{0,3,4\}$$

And similarly for the lower bound:

$$\partial_{\mathbf{x}_i} u_{\theta,j}^{L} = \phi_{0,j,i}^{(1),L} + \sum_{r=1}^{d_0} \phi_{1,j,r}^{(1),L} \mathbf{x} + \phi_{2,j,r}^{(1),L}, \tag{B.17}$$

where:

$$\phi_{0,j,r}^{(k-1),L} = \begin{cases} \sum_{n=1}^{d_{k-1}} \mathbf{W}_{j,n}^{(k),+} \beta_{0,n,r}^{(k-1)} + \mathbf{W}_{j,n}^{(k),-} \alpha_{0,n,r}^{(k-1)} & \text{if } k = L \\ \sum_{n=1}^{d_{k-1}} \phi_{0,j,n}^{(k),L} \chi_{0,n,r}^{(k-1)} & \text{if } k \in \{2,\dots,L-1\} \end{cases}$$

$$\phi_{1,j,r}^{(k-1),L} = \begin{cases} \sum_{n=1}^{d_{k-1}} \mathbf{W}_{j,n}^{(k),+} \beta_{3,n,r}^{(k-1)} + \mathbf{W}_{j,n}^{(k),-} \alpha_{3,n,r}^{(k-1)} & \text{if } k = L \\ \sum_{n=1}^{d_{k-1}} \phi_{0,j,n}^{(k),L} \chi_{3,n,r}^{(k-1)} + \frac{1}{d_{k-2}} \phi_{1,j,n}^{(k),L} & \text{if } k \in \{2,\dots,L-1\} \end{cases}$$

$$\phi_{2,j,r}^{(k-1),L} = \begin{cases} \sum_{n=1}^{d_{k-1}} \mathbf{W}_{j,n}^{(k),+} \beta_{4,n,r}^{(k-1)} + \mathbf{W}_{j,n}^{(k),-} \alpha_{4,n,r}^{(k-1)} & \text{if } k = L \\ \sum_{n=1}^{d_{k-1}} \phi_{0,j,n}^{(k),L} \chi_{4,n,r}^{(k-1)} + \frac{1}{d_{k-2}} \phi_{2,j,n}^{(k),L} & \text{if } k \in \{2,\dots,L-1\} \end{cases},$$

and:

$$\chi_{p,n,:}^{(k-1)} = \begin{cases} \beta_{p,n,:}^{(k-1)} & \text{if } \phi_{0,j,n}^{(k),L} \geq 0 \\ \alpha_{p,n,:}^{(k-1)} & \text{if } \phi_{0,j,n}^{(k),L} < 0 \end{cases}, p \in \{0,3,4\}.$$

B.4.4 Theorem 4.2 Formal Statement and Proof

Theorem 4.2 (∂-CROWN: linear lower and upper bounding $\partial_{\mathbf{x}_i^2} u_\theta$)**.** *Assume that through a previous computation of bounds on $\partial_{\mathbf{x}_i} u_\theta$, the components of that network required for $\partial_{\mathbf{x}_i^2} u_\theta$, i.e. , $\partial_{\mathbf{x}_i} z^{(k-1)}$ and $\partial_{z^{(k-1)}} z^{(k)}$, are lower and upper bounded by linear functions. In particular, $\mathbf{C}^{(k),L}\mathbf{x} + \mathbf{c}^{(k),L} \leq \partial_{\mathbf{x}_i} z^{(k-1)} \leq \mathbf{C}^{(k),U}\mathbf{x} + \mathbf{c}^{(k),U}$ and $\mathbf{D}^{(k),L}\mathbf{x} + \mathbf{d}^{(k),L} \leq \partial_{z^{(k-1)}} z^{(k)} \leq \mathbf{D}^{(k),U}\mathbf{x} + \mathbf{d}^{(k),U}$.*

For every $j \in \{1,\dots,d_L\}$ there exist two functions $\partial_{\mathbf{x}_i^2} u_{\theta,j}^{U}$ and $\partial_{\mathbf{x}_i^2} u_{\theta,j}^{L}$ such that, $\forall \mathbf{x} \in \mathcal{C}$ it holds that $\partial_{\mathbf{x}_i^2} u_{\theta,j}^{L} \leq \partial_{\mathbf{x}_i^2} u_{\theta,j} \leq \partial_{\mathbf{x}_i^2} u_{\theta,j}^{U}$. These functions can be written as:

$$\partial_{\mathbf{x}_i^2} u_{\theta,j}^{U} = \psi_{0,j,i}^{(1),U} + \sum_{r=1}^{d_0} \psi_{1,j,r}^{(1),U} \mathbf{x} + \psi_{2,j,r}^{(1),U}$$

$$\partial_{\mathbf{x}_i^2} u_{\theta,j}^{L} = \psi_{0,j,i}^{(1),L} + \sum_{r=1}^{d_0} \psi_{1,j,r}^{(1),L} \mathbf{x} + \psi_{2,j,r}^{(1),L}$$

where for $p \in \{0,1,2\}$, $\psi_{p,j,r}^{(1),U}$ and $\psi_{p,j,r}^{(1),L}$ are functions of $\mathbf{W}^{(k)}$, $y^{(k),L}$, $y^{(k),U}$, $\mathbf{A}^{(k),L}$, $\mathbf{A}^{(k),U}$ $\mathbf{a}^{(k),L}$, $\mathbf{a}^{(k),U}$, $\mathbf{C}^{(k),L}$, $\mathbf{C}^{(k),U}$ $\mathbf{c}^{(k),L}$, $\mathbf{c}^{(k),U}$, $\mathbf{D}^{(k),L}$, $\mathbf{D}^{(k),U}$ $\mathbf{d}^{(k),L}$, and $\mathbf{d}^{(k),U}$, and can be computed using a recursive closed-form expression in $\mathcal{O}(L)$ time.

Proof: Assume that through the computation of the previous bounds on u_θ, the pre-activation layer outputs of u_θ, $y^{(k)}$, are lower and upper bounded by linear functions defined as $\mathbf{A}^{(k),L}\mathbf{x} + \mathbf{a}^{(k),L} \leq y^{(k)} \leq \mathbf{A}^{(k),U}\mathbf{x} + \mathbf{a}^{(k),U}$ and $y^{(k),L} \leq y^{(k)} \leq y^{(k),U}$ for $\mathbf{x} \in \mathcal{C}$. Additionally, we consider also that through a previous computation of bounds on $\partial_{\mathbf{x}_i} u_\theta$, the components of that network required for $\partial_{\mathbf{x}_i^2} u_\theta$, *i.e.* , $\partial_{\mathbf{x}_i} z^{(k-1)}$ and $\partial_{z^{(k-1)}} z^{(k)}$ are lower and upper bounded by linear functions. In particular, $\mathbf{C}^{(k),L}\mathbf{x} + \mathbf{c}^{(k),L} \leq \partial_{\mathbf{x}_i} z^{(k-1)} \leq \mathbf{C}^{(k),U}\mathbf{x} + \mathbf{c}^{(k),U}$ and $\mathbf{D}^{(k),L}\mathbf{x} + \mathbf{d}^{(k),L} \leq \partial_{z^{(k-1)}} z^{(k)} \leq \mathbf{D}^{(k),U}\mathbf{x} + \mathbf{d}^{(k),U}$.

Take the upper and lower bound functions for $\partial_{\mathbf{x}_i^2} u_\theta$ as $\partial_{\mathbf{x}_i^2} u_\theta^U$ and $\partial_{\mathbf{x}_i^2} u_\theta^L$, respectively, and the upper and lower bound functions for $\partial_{\mathbf{x}_i^2} z^{(k)}$ as $\partial_{\mathbf{x}_i^2} z^{(k),U}$ and $\partial_{\mathbf{x}_i^2} z^{(k),L}$, respectively. For the sake of simplicity of notation, we define $\mathbf{B}^{(k),+} = \mathbb{I}\left(\mathbf{B}^{(k)} \geq 0\right) \odot \mathbf{B}^{(k)}$ and $\mathbf{B}^{(k),-} = \mathbb{I}\left(\mathbf{B}^{(k)} < 0\right) \odot \mathbf{B}^{(k)}$.

Note that, unless explicitly mentioned otherwise, the non-network variables (denoted by Greek letters, as well as bold, capital and lowercase letters) used here have no relation to the ones from Appendix B.4.3.

Starting backwards from $\partial_{\mathbf{x}_i^2} z^{(k)}$, we have that:

$$\partial_{\mathbf{x}_i^2} z_j^{(k)} = \sum_{n=1}^{d_{k-1}} \partial_{\mathbf{x}_i z^{(k-1)}} z_{j,n}^{(k)} \partial_{\mathbf{x}_i} z_n^{(k-1)} + \partial_{z^{(k-1)}} z_{j,n}^{(k)} \partial_{\mathbf{x}_i^2} z_n^{(k-1)}.$$

Given the transitive property of the sum operator, we can bound $\partial_{\mathbf{x}_i^2} z_j^{(k)}$ by using a McCormick envelope around each of the multiplications. Assuming that for all $j \in \{1 \ldots, d_k\}, n \in \{1 \ldots, d_{k-1}\}$: $\partial_{\mathbf{x}_i z^{(k-1)}} z_{j,n}^{(k),L} \leq \partial_{\mathbf{x}_i z^{(k-1)}} z_{j,n}^{(k)} \leq \partial_{\mathbf{x}_i z^{(k-1)}} z_{j,n}^{(k),U}$, $\partial_{\mathbf{x}_i} z_n^{(k-1),L} \leq \partial_{\mathbf{x}_i} z_n^{(k-1)} \leq \partial_{\mathbf{x}_i} z_n^{(k-1),U}$, $\partial_{z^{(k-1)}} z_{j,n}^{(k)} \leq \partial_{z^{(k-1)}} z_{j,n}^{(k)} \leq \partial_{z^{(k-1)}} z_{j,n}^{(k)}$, and $\partial_{\mathbf{x}_i^2} z_n^{(k-1),L} \leq \partial_{\mathbf{x}_i^2} z_n^{(k-1)} \leq \partial_{\mathbf{x}_i^2} z_n^{(k-1),U}$, we obtain:

$$\begin{aligned}
\partial_{\mathbf{x}_i^2} z_j^{(k)} \leq \partial_{\mathbf{x}_i^2} z_j^{(k),U} = &\sum_{n=1}^{d_{k-1}} \alpha_{0,j,n}^{(k)} \partial_{\mathbf{x}_i} z_n^{(k-1)} + \alpha_{1,j,n}^{(k)} \partial_{\mathbf{x}_i z^{(k-1)}} z_{j,n}^{(k)} + \\
&+ \alpha_{2,j,n}^{(k)} \partial_{\mathbf{x}_i^2} z_n^{(k-1)} + \alpha_{3,j,n}^{(k)} \partial_{z^{(k-1)}} z_{j,n}^{(k)} + \alpha_{4,j,n}^{(k)} \\
\partial_{\mathbf{x}_i^2} z_j^{(k)} \geq \partial_{\mathbf{x}_i^2} z_j^{(k),L} = &\sum_{n=1}^{d_{k-1}} \beta_{0,j,n}^{(k)} \partial_{\mathbf{x}_i} z_n^{(k-1)} + \beta_{1,j,n}^{(k)} \partial_{\mathbf{x}_i z^{(k-1)}} z_{j,n}^{(k)} + \\
&+ \beta_{2,j,n}^{(k)} \partial_{\mathbf{x}_i^2} z_n^{(k-1)} + \beta_{3,j,n}^{(k)} \partial_{z^{(k-1)}} z_{j,n}^{(k)} + \beta_{4,j,n}^{(k)}
\end{aligned} \tag{B.18}$$

for:

$$
\begin{aligned}
\alpha_{0,j,n}^{(k)} =& \eta_{j,n}^{(k)} \partial_{\mathbf{x}_i z^{(k-1)}} z_{j,n}^{(k),U} + \left(1-\eta_{j,n}^{(k)}\right) \partial_{\mathbf{x}_i z^{(k-1)}} z_{j,n}^{(k),L} \\
\alpha_{1,j,n}^{(k)} =& \eta_{j,n}^{(k)} \partial_{\mathbf{x}_i} z_n^{(k-1),L} + \left(1-\eta_{j,n}^{(k)}\right) \partial_{\mathbf{x}_i} z_n^{(k-1),U} \\
\alpha_{2,j,n}^{(k)} =& \gamma_{j,n}^{(k)} \partial_{z^{(k-1)}} z_{j,n}^{(k),U} + \left(1-\gamma_{j,n}^{(k)}\right) \partial_{z^{(k-1)}} z_{j,n}^{(k),L} \\
\alpha_{3,j,n}^{(k)} =& \gamma_{j,n}^{(k)} \partial_{\mathbf{x}_i^2} z_n^{(k-1),L} + \left(1-\gamma_{j,n}^{(k)}\right) \partial_{\mathbf{x}_i^2} z_n^{(k-1),U} \\
\alpha_{4,j,n}^{(k)} =& -\eta_{j,n}^{(k)} \partial_{\mathbf{x}_i z^{(k-1)}} z_{j,n}^{(k),U} \partial_{\mathbf{x}_i} z_n^{(k-1),L} - \left(1-\eta_{j,n}^{(k)}\right) \partial_{\mathbf{x}_i z^{(k-1)}} z_{j,n}^{(k),L} \partial_{\mathbf{x}_i} z_n^{(k-1),U} + \\
& -\gamma_{j,n}^{(k)} \partial_{z^{(k-1)}} z_{j,n}^{(k),U} \partial_{\mathbf{x}_i x_i} z_n^{(k-1),L} - \left(1-\gamma_{j,n}^{(k)}\right) \partial_{z^{(k-1)}} z_{j,n}^{(k),L} \partial_{\mathbf{x}_i x_i} z_n^{(k-1),U} \\
\beta_{0,j,n}^{(k)} =& \zeta_{j,n}^{(k)} \partial_{\mathbf{x}_i z^{(k-1)}} z_{j,n}^{(k),L} + \left(1-\zeta_{j,n}^{(k)}\right) \partial_{\mathbf{x}_i z^{(k-1)}} z_{j,n}^{(k),U} \\
\beta_{1,j,n}^{(k)} =& \zeta_{j,n}^{(k)} \partial_{\mathbf{x}_i} z_n^{(k-1),L} + \left(1-\zeta_{j,n}^{(k)}\right) \partial_{\mathbf{x}_i} z_n^{(k-1),U} \\
\beta_{2,j,n}^{(k)} =& \delta_{j,n}^{(k)} \partial_{z^{(k-1)}} z_{j,n}^{(k),L} + \left(1-\delta_{j,n}^{(k)}\right) \partial_{z^{(k-1)}} z_{j,n}^{(k),U} \\
\beta_{3,j,n}^{(k)} =& \delta_{j,n}^{(k)} \partial_{\mathbf{x}_i^2} z_n^{(k-1),L} + \left(1-\delta_{j,n}^{(k)}\right) \partial_{\mathbf{x}_i^2} z_n^{(k-1),U} \\
\beta_{4,j,n}^{(k)} =& -\zeta_{j,n}^{(k)} \partial_{\mathbf{x}_i z^{(k-1)}} z_{j,n}^{(k),L} \partial_{\mathbf{x}_i} z_n^{(k-1),L} - \left(1-\zeta_{j,n}^{(k)}\right) \partial_{\mathbf{x}_i z^{(k-1)}} z_{j,n}^{(k),U} \partial_{\mathbf{x}_i} z_n^{(k-1),U} + \\
& -\delta_{j,n}^{(k)} \partial_{z^{(k-1)}} z_{j,n}^{(k),L} \partial_{\mathbf{x}_i^2} z_n^{(k-1),L} - \left(1-\delta_{j,n}^{(k)}\right) \partial_{z^{(k-1)}} z_{j,n}^{(k),U} \partial_{\mathbf{x}_i^2} z_n^{(k-1),U},
\end{aligned}
$$

where $\eta_{j,n}^{(k)}$, $\gamma_{j,n}^{(k)}$, $\zeta_{j,n}^{(k)}$ and $\delta_{j,n}^{(k)}$ are convex coefficients that can be set as hyperparameters, or optimized for as in α-CROWN [Xu et al., 2020].

For the next step of the back-propagation process, we now need to bound $\partial_{\mathbf{x}_i} z_n^{(k-1)}$, $\partial_{\mathbf{x}_i z^{(k-1)}} z_{j,n}^{(k)}$, and $\partial_{z^{(k-1)}} z_{j,n}^{(k)}$, so as to eventually be able to write $\partial_{\mathbf{x}_i^2} z_j^{(k)}$ as a function of simply $\partial_{\mathbf{x}_i^2} z_n^{(k-1)}$ and $\mathbf{x}$. As per our assumptions at the beginning of this section, for the sake of computational efficiency we take $\partial_{\mathbf{x}_i} z_n^{(k-1)}$ and $\partial_{z^{(k-1)}} z_{j,n}^{(k)}$ from the computation of the bounds of $\partial_{\mathbf{x}_i} u_{\theta,j}$, and thus assume we have a linear upper and lower bound function of $\mathbf{x}$. This leaves us with $\partial_{\mathbf{x}_i z^{(k-1)}} z_{j,n}^{(k)}$ to bound as a linear function of $\mathbf{x}$.

Note that, as per Lemma 4.2, $\partial_{\mathbf{x}_i z^{(k-1)}} z_{j,n}^{(k)} = \sigma''\left(\mathbf{y}_j^{(k)}\right)\left(\mathbf{W}_{j,:}^{(k)} \partial_{\mathbf{x}_i} z^{(k-1)}\right) \mathbf{W}_{j,n}^{(k)}$. Since $\left(\mathbf{W}_{j,:}^{(k)} \partial_{\mathbf{x}_i} z^{(k-1)}\right) = \sum_{n=1}^{d_{k-1}} \mathbf{W}_{j,n}^{(k)} \partial_{\mathbf{x}_i} z_n^{(k-1)}$, and $\mathbf{C}_{n,:}^{(k),U} \mathbf{x} + \mathbf{c}_n^{(k),U} \leq \partial_{\mathbf{x}_i} z_n^{(k-1)} \leq$

$\mathbf{C}_{n,:}^{(k),L}\mathbf{x} + \mathbf{c}_n^{(k),L}$ (from the assumptions above), we can write:

$$\mathbf{W}_{j,:}^{(k)}\partial_{\mathbf{x}_i} z^{(k-1)} \leq \underbrace{\left(\sum_{n=1}^{d_{k-1}} \mathbf{W}_{j,n}^{(k),+}\mathbf{C}_{n,:}^{(k),U} + \mathbf{W}_{j,n}^{(k),-}\mathbf{C}_{n,:}^{(k),L}\right)}_{\mathbf{E}_j^{(k),U}}\mathbf{x} + \underbrace{\left(\sum_{n=1}^{d_{k-1}} \mathbf{W}_{j,n}^{(k),+}\mathbf{c}^{(k),U} + \mathbf{W}_{j,n}^{(k),-}\mathbf{c}^{(k),L}\right)}_{\mathbf{e}_j^{(k),U}}$$

$$\mathbf{W}_{j,n}^{(k)}\partial_{\mathbf{x}_i} z^{(k-1)} \geq \underbrace{\left(\sum_{n=1}^{d_{k-1}} \mathbf{W}_{j,n}^{(k),+}\mathbf{C}_{n,:}^{(k),L} + \mathbf{W}_{j,n}^{(k),-}\mathbf{C}_{n,:}^{(k),U}\right)}_{\mathbf{E}_j^{(k),L}}\mathbf{x} + \underbrace{\left(\sum_{n=1}^{d_{k-1}} \mathbf{W}_{j,n}^{(k),+}\mathbf{c}_n^{(k),L} + \mathbf{W}_{j,n}^{(k),-}\mathbf{c}_n^{(k),U}\right)}_{\mathbf{e}_j^{(k),L}}.$$

We define $\theta_j^{(k),U} = \max_{\mathbf{x}\in\mathcal{C}} \mathbf{E}_j^{(k),U}\mathbf{x} + \mathbf{e}_j^{(k),U}$ and $\theta_j^{(k),L} = \min_{\mathbf{x}\in\mathcal{C}} \mathbf{E}_j^{(k),L}\mathbf{x} + \mathbf{e}_j^{(k),L}$. As with the first derivative case, since $y_j^{(k),L} \leq y_j^{(k)} \leq y_j^{(k),U}$, we can obtain a linear upper and lower bound relaxation for $\sigma''\left(y_j^{(k)}\right)$, such that $\lambda_j^{(k),L}\left(y_j^{(k)} + \mu_j^{(k),L}\right) \leq \sigma''\left(y_j^{(k)}\right) \leq \lambda_j^{(k),U}\left(y_j^{(k)} + \mu_j^{(k),U}\right)$, as well as the values $\iota_j^{(k),L} \leq \sigma''\left(y_j^{(k)}\right) \leq \iota_j^{(k),U}$. By considering the assumption that $\mathbf{A}_{j,:}^{(k),U}\mathbf{x} + \mathbf{a}_j^{(k),U} \leq y^{(k)} \leq \mathbf{A}_{j,:}^{(k),L}\mathbf{x} + \mathbf{a}_j^{(k),L}$, we can obtain:

$$\sigma''\left(y_j^{(k)}\right) \leq \underbrace{\left(\lambda_j^{(k),U,+}\mathbf{A}_{j,:}^{(k),U} + \lambda_j^{(k),U,-}\mathbf{A}_{j,:}^{(k),L}\right)}_{\mathbf{H}_j^{(k),U}}\mathbf{x} + \underbrace{\left(\lambda_j^{(k),U,+}\mathbf{a}_j^{(k),U} + \lambda_j^{(k),U,-}\mathbf{a}_j^{(k),L} + \lambda_j^{(k),U}\mu_j^{(k),U}\right)}_{\mathbf{h}_j^{(k),U}}$$

$$\sigma''\left(y_j^{(k)}\right) \geq \underbrace{\left(\lambda_j^{(k),L,+}\mathbf{A}_{j,:}^{(k),L} + \lambda_j^{(k),L,-}\mathbf{A}_{j,:}^{(k),U}\right)}_{\mathbf{H}_j^{(k),L}}\mathbf{x} + \underbrace{\left(\lambda_j^{(k),L,+}\mathbf{a}_j^{(k),L} + \lambda_j^{(k),L,-}\mathbf{a}_j^{(k),U} + \lambda_j^{(k),L}\mu_j^{(k),L}\right)}_{\mathbf{h}_j^{(k),L}}.$$

This allows us to relax $\sigma''\left(y_j^{(k)}\right)\left(\mathbf{W}_{j,:}^{(k)}\partial_{\mathbf{x}_i}z^{(k-1)}\right)$ using McCormick envelopes:

$$\sigma''\left(y_j^{(k)}\right)\left(\mathbf{W}_{j,:}^{(k)}\partial_{\mathbf{x}_i}z^{(k-1)}\right) \leq \nu_{0,j}^{(k),U}\left(\mathbf{W}_{j,:}^{(k)}\partial_{\mathbf{x}_i}z^{(k-1)}\right) + \nu_{1,j}^{(k),U}\sigma''\left(y_j^{(k)}\right) + \nu_{2,j}^{(k),U}$$
$$\sigma''\left(y_j^{(k)}\right)\left(\mathbf{W}_{j,:}^{(k)}\partial_{\mathbf{x}_i}z^{(k-1)}\right) \geq \nu_{0,j}^{(k),L}\left(\mathbf{W}_{j,:}^{(k)}\partial_{\mathbf{x}_i}z^{(k-1)}\right) + \nu_{1,j}^{(k),L}\sigma''\left(y_j^{(k)}\right) + \nu_{2,j}^{(k),L},$$

for:

$$\nu_{0,j}^{(k),U} = \rho_j^{(k)}\iota_j^{(k),U} + \left(1-\rho_j^{(k)}\right)\iota_j^{(k),L} \qquad \nu_{1,j,n}^{(k),U} = \rho_j^{(k)}\theta_j^{(k),L} + \left(1-\rho_j^{(k)}\right)\iota_j^{(k),U}$$
$$\nu_{2,j}^{(k),U} = -\rho_j^{(k)}\iota_j^{(k),U}\theta_j^{(k),L} - \left(1-\rho_j^{(k)}\right)\iota_j^{(k),L}\theta_j^{(k),U}$$

$$\nu_{0,j}^{(k),L} = \tau_j^{(k)}\iota_j^{(k),L} + \left(1-\tau_j^{(k)}\right)\iota_j^{(k),U} \qquad \nu_{1,j}^{(k),L} = \tau_j^{(k)}\theta_j^{(k),L} + \left(1-\tau_j^{(k)}\right)\theta_j^{(k),U}$$
$$\nu_{2,j}^{(k),L} = -\tau_j^{(k)}\iota_j^{(k),L}\theta_j^{(k),L} - \left(1-\tau_j^{(k)}\right)\iota_j^{(k),U}\theta_j^{(k),U},$$

where $\rho_j^{(k)}$ and $\tau_j^{(k)}$ are convex coefficients that can be set as hyperparameters, or optimized for as in α-CROWN [Xu et al., 2020]. By replacing this multiplication in the expression from Lemma 4.2, we bound $\partial_{\mathbf{x}_i z^{(k-1)}} z_{j,n}^{(k)}$ as:

$$\partial_{\mathbf{x}_i z^{(k-1)}} z_{j,n}^{(k)} \leq \upsilon_{0,j,n}^{(k),U}\left(\mathbf{W}_{j,:}^{(k)}\partial_{\mathbf{x}_i}z^{(k-1)}\right) + \upsilon_{1,j,n}^{(k),U}\sigma''\left(y_j^{(k)}\right) + \upsilon_{2,j}^{(k),U}$$
$$\partial_{\mathbf{x}_i z^{(k-1)}} z_{j,n}^{(k)} \geq \upsilon_{0,j,n}^{(k),L}\left(\mathbf{W}_{j,:}^{(k)}\partial_{\mathbf{x}_i}z^{(k-1)}\right) + \upsilon_{1,j,n}^{(k),L}\sigma''\left(y_j^{(k)}\right) + \upsilon_{2,j}^{(k),L},$$

for $i \in \{0,1,2\}$:

$$\upsilon_{i,j,n}^{(k),U} = \nu_{i,j}^{(k),U}\mathbf{W}_{j,n}^{(k),+} + \nu_{i,j}^{(k),L}\mathbf{W}_{j,n}^{(k),-},\ \upsilon_{i,j,n}^{(k),L} = \nu_{i,j}^{(k),L}\mathbf{W}_{j,n}^{(k),+} + \nu_{i,j}^{(k),U}\mathbf{W}_{j,n}^{(k),-}$$

By replacing the lower and upper bounds for $\sigma''(y_j^{(k)})$ and $\left(\mathbf{W}_{j,:}^{(k)}\partial_{\mathbf{x}_i}z^{(k-1)}\right)$ in the previous inequality, we obtain the expression:

$$\partial_{\mathbf{x}_i z^{(k-1)}} z_{j,n}^{(k)} \leq \mathbf{M}_{j,n}^{(k),U}\mathbf{x} + \mathbf{m}_{j,n}^{(k),U}$$
$$\partial_{\mathbf{x}_i z^{(k-1)}} z_{j,n}^{(k)} \geq \mathbf{M}_{j,n}^{(k),L}\mathbf{x} + \mathbf{m}_{j,n}^{(k),L},$$

for:

$$\begin{aligned}
\mathbf{M}_{j,n}^{(k),U} =& \upsilon_{0,j,n}^{(k),U,+}\mathbf{E}_j^{(k),U} + \upsilon_{0,j,n}^{(k),U,-}\mathbf{E}_j^{(k),L} + \upsilon_{1,j,n}^{(k),U,+}\mathbf{H}_j^{(k),U} + \upsilon_{1,j,n}^{(k),U,-}\mathbf{H}_j^{(k),L}\\
\mathbf{m}_{j,n}^{(k),U} =& \upsilon_{0,j,n}^{(k),U,+}\mathbf{e}_j^{(k),U} + \upsilon_{0,j,n}^{(k),U,-}\mathbf{e}_j^{(k),L} + \upsilon_{1,j,n}^{(k),U,+}\mathbf{h}_j^{(k),U} + \upsilon_{1,j,n}^{(k),U,-}\mathbf{h}_j^{(k),L} + \upsilon_{2,j,n}^{(k),U}\\
\mathbf{M}_{j,n}^{(k),L} =& \upsilon_{0,j,n}^{(k),L,+}\mathbf{E}_j^{(k),L} + \upsilon_{0,j,n}^{(k),L,-}\mathbf{E}_j^{(k),U} + \upsilon_{1,j,n}^{(k),L,+}\mathbf{H}_j^{(k),L} + \upsilon_{1,j,n}^{(k),L,-}\mathbf{H}_j^{(k),U}\\
\mathbf{m}_{j,n}^{(k),L} =& \upsilon_{0,j,n}^{(k),L,+}\mathbf{e}_j^{(k),L} + \upsilon_{0,j,n}^{(k),L,-}\mathbf{e}_j^{(k),U} + \upsilon_{1,j,n}^{(k),L,+}\mathbf{h}_j^{(k),L} + \upsilon_{1,j,n}^{(k),L,-}\mathbf{h}_j^{(k),U} + \upsilon_{2,j,n}^{(k),L}.
\end{aligned}$$

Finally in the derivation of $\partial_{\mathbf{x}_i^2} z_j^{(k)}$ as a function of $\mathbf{x}$ and $\partial_{\mathbf{x}_i^2} z^{(k-1)}$, we just have to replace all the quantities in Equation B.18 (recalling from the assumptions that $\mathbf{C}^{(k),U}\mathbf{x} + \mathbf{c}^{(k),U} \leq \partial_{\mathbf{x}_i} z^{(k-1)} \leq \mathbf{C}^{(k),L}\mathbf{x} + \mathbf{c}^{(k),L}$ and $\mathbf{D}^{(k),U}\mathbf{x} + \mathbf{d}^{(k),U} \leq \partial_{z^{(k-1)}} z^{(k)} \leq \mathbf{D}^{(k),L}\mathbf{x} + \mathbf{d}^{(k),L}$) to obtain:

$$\begin{aligned}
\partial_{\mathbf{x}_i^2} z_j^{(k)} &\leq \partial_{\mathbf{x}_i^2} z_j^{(k),U} = \sum_{n=1}^{d_{k-1}} \alpha_{2,j,n}^{(k)} \partial_{\mathbf{x}_i^2} z_n^{(k-1)} + \alpha_{5,j,n}^{(k)} \mathbf{x} + \alpha_{6,j,n}^{(k)} \\
\partial_{\mathbf{x}_i^2} z_j^{(k)} &\geq \partial_{\mathbf{x}_i^2} z_j^{(k),L} = \sum_{n=1}^{d_{k-1}} \beta_{2,j,n}^{(k)} \partial_{\mathbf{x}_i^2} z_n^{(k-1)} + \beta_{5,j,n}^{(k)} \mathbf{x} + \beta_{6,j,n}^{(k)},
\end{aligned} \tag{B.19}$$

where:

$$\begin{aligned}
\alpha_{5,j,n}^{(k)} =& \alpha_{0,j,n}^{(k),+} \mathbf{C}_n^{(k),U} + \alpha_{0,j,n}^{(k),-} \mathbf{C}_n^{(k),L} + \alpha_{1,j,n}^{(k),+} \mathbf{M}_{j,n}^{(k),U} + \alpha_{1,j,n}^{(k),-} \mathbf{M}_{j,n}^{(k),L} + \\
&+ \alpha_{3,j,n}^{(k),+} \mathbf{D}_{j,n}^{(k),U} + \alpha_{3,j,n}^{(k),-} \mathbf{D}_{j,n}^{(k),L} \\
\alpha_{6,j,n}^{(k)} =& \alpha_{0,j,n}^{(k),+} \mathbf{c}_n^{(k),U} + \alpha_{0,j,n}^{(k),-} \mathbf{c}_n^{(k),L} + \alpha_{1,j,n}^{(k),+} \mathbf{m}_{j,n}^{(k),U} + \alpha_{1,j,n}^{(k),-} \mathbf{m}_{j,n}^{(k),L} + \\
&+ \alpha_{3,j,n}^{(k),+} \mathbf{d}_{j,n}^{(k),U} + \alpha_{3,j,n}^{(k),-} \mathbf{d}_{j,n}^{(k),L} + \alpha_{4,j,n}^{(k)} \\
\beta_{5,j,n}^{(k)} =& \beta_{0,j,n}^{(k),+} \mathbf{C}_n^{(k),L} + \beta_{0,j,n}^{(k),-} \mathbf{C}_n^{(k),U} + \beta_{1,j,n}^{(k),+} \mathbf{M}_{j,n}^{(k),L} + \beta_{1,j,n}^{(k),-} \mathbf{M}_{j,n}^{(k),U} + \\
&+ \beta_{3,j,n}^{(k),+} \mathbf{D}_{j,n}^{(k),L} + \beta_{3,j,n}^{(k),-} \mathbf{D}_{j,n}^{(k),U} \\
\beta_{6,j,n}^{(k)} =& \beta_{0,j,n}^{(k),+} \mathbf{c}_n^{(k),L} + \beta_{0,j,n}^{(k),-} \mathbf{c}_n^{(k),U} + \beta_{1,j,n}^{(k),+} \mathbf{m}_{j,n}^{(k),L} + \beta_{1,j,n}^{(k),-} \mathbf{m}_{j,n}^{(k),U} + \\
&+ \beta_{3,j,n}^{(k),+} \mathbf{d}_{j,n}^{(k),L} + \beta_{3,j,n}^{(k),-} \mathbf{d}_{j,n}^{(k),U} + \beta_{4,j,n}^{(k)}
\end{aligned}$$

This forms a recursion of exactly the same form as Equation B.5 from Appendix B.4.3, where only the coefficients of $\partial_{\mathbf{x}_i^2} z_n^{(k-1)}$ and $\mathbf{x}$ are different ($\alpha_{0,j,n}^{(k)}$ in this case is referred by $\alpha_{2,j,n}^{(k)}$, $\alpha_{3,j,n}^{(k)}$ by $\alpha_{5,j,n}^{(k)}$, and $\alpha_{4,j,n}^{(k)}$ by $\alpha_{6,j,n}^{(k)}$, and similarly for the β values). This yields:

$$\partial_{\mathbf{x}_i x_i} z_j^{(L-1),U} = \rho_{0,j,i}^{(1),U} + \sum_{r=1}^{d_0} \rho_{1,j,r}^{(1),U} \mathbf{x} + \rho_{2,j,r}^{(1),U},$$

where:

$$\begin{aligned}
\rho_{0,j,r}^{(k-1),U} &= \begin{cases} \alpha_{2,n,r}^{(k)} & \text{if } k = L \\ \sum_{n=1}^{d_{k-1}} \rho_{0,j,n}^{(k),U} \mu_{2,n,r}^{(k-1),U} & \text{if } k \in \{2, \ldots, L-1\} \end{cases} \\
\rho_{1,j,r}^{(k-1),U} &= \begin{cases} \alpha_{5,n,r}^{(k)} & \text{if } k = L \\ \sum_{n=1}^{d_{k-1}} \rho_{0,j,n}^{(k),U} \mu_{5,n,r}^{(k-1),U} + \frac{1}{d_{k-2}} \rho_{1,j,n}^{(k),U} & \text{if } k \in \{2, \ldots, L-1\} \end{cases} \\
\rho_{2,j,r}^{(k-1),U} &= \begin{cases} \alpha_{6,n,r}^{(k)} & \text{if } k = L \\ \sum_{n=1}^{d_{k-1}} \rho_{0,j,n}^{(k),U} \mu_{6,n,r}^{(k-1),U} + \frac{1}{d_{k-2}} \rho_{2,j,n}^{(k),U} & \text{if } k \in \{2, \ldots, L-1\} \end{cases},
\end{aligned}$$

and:

$$\mu_{p,n,:}^{(k-1),U} = \begin{cases} \alpha_{p,n,:}^{(k-1)} & \text{if } \rho_{0,j,n}^{(k),U} \geq 0 \\ \beta_{p,n,:}^{(k-1)} & \text{if } \rho_{0,j,n}^{(k),U} < 0 \end{cases}, p \in \{2,5,6\}.$$

And following the same argument:

$$\partial_{\mathbf{x}_i} z_j^{(L-1),L} = \rho_{0,j,i}^{(1),L} + \sum_{r=1}^{d_0} \rho_{1,j,r}^{(1),L} \mathbf{x} + \rho_{2,j,r}^{(1),L},$$

where:

$$\rho_{0,j,r}^{(k-1),L} = \begin{cases} \beta_{2,n,r}^{(k)} & \text{if } k = L \\ \sum_{n=1}^{d_{k-1}} \rho_{0,j,n}^{(k),L} \mu_{2,n,r}^{(k-1),L} & \text{if } k \in \{2,\dots,L-1\} \end{cases}$$

$$\rho_{1,j,r}^{(k-1),L} = \begin{cases} \beta_{5,n,r}^{(k)} & \text{if } k = L \\ \sum_{n=1}^{d_{k-1}} \rho_{0,j,n}^{(k),L} \mu_{5,n,r}^{(k-1),L} + \frac{1}{d_{k-2}} \rho_{1,j,n}^{(k),L} & \text{if } k \in \{2,\dots,L-1\} \end{cases}$$

$$\rho_{2,j,r}^{(k-1),L} = \begin{cases} \beta_{6,n,r}^{(k)} & \text{if } k = L \\ \sum_{n=1}^{d_{k-1}} \rho_{0,j,n}^{(k),L} \mu_{6,n,r}^{(k-1),L} + \frac{1}{d_{k-2}} \rho_{2,j,n}^{(k),L} & \text{if } k \in \{2,\dots,L-1\} \end{cases},$$

and:

$$\mu_{p,n,:}^{(k-1),L} = \begin{cases} \beta_{p,n,:}^{(k-1)} & \text{if } \rho_{0,j,n}^{(k),L} \geq 0 \\ \alpha_{p,n,:}^{(k-1)} & \text{if } \rho_{0,j,n}^{(k),L} < 0 \end{cases}, p \in \{2,5,6\}$$

With these expressions, we can compute the required $\partial_{\mathbf{x}_i^2} z_n^{(k-1),L}$ and $\partial_{\mathbf{x}_i^2} z_n^{(k-1),U}$ which we assumed to be known to derive Equation B.18.

Finally, with the exact same argument as in Appendix B.4.3, we obtain:

$$\partial_{\mathbf{x}_i} u_{\theta,j}^U = \psi_{0,j,i}^{(1),U} + \sum_{r=1}^{d_0} \psi_{1,j,r}^{(1),U} \mathbf{x} + \psi_{2,j,r}^{(1),U},$$

where:

$$\psi_{0,j,r}^{(k-1),U} = \begin{cases} \sum_{n=1}^{d_{k-1}} \mathbf{W}_{j,n}^{(k),+} \alpha_{2,n,r}^{(k-1)} + \mathbf{W}_{j,n}^{(k),-} \beta_{2,n,r}^{(k-1)} & \text{if } k = L \\ \sum_{n=1}^{d_{k-1}} \psi_{0,j,n}^{(k),U} \psi_{2,n,r}^{(k-1),U} & \text{if } k \in \{2,\dots,L-1\} \end{cases}$$

$$\psi_{1,j,r}^{(k-1),U} = \begin{cases} \sum_{n=1}^{d_{k-1}} \mathbf{W}_{j,n}^{(k),+} \alpha_{5,n,r}^{(k-1)} + \mathbf{W}_{j,n}^{(k),-} \beta_{5,n,r}^{(k-1)} & \text{if } k = L \\ \sum_{n=1}^{d_{k-1}} \psi_{0,j,n}^{(k),U} \psi_{5,n,r}^{(k-1),U} + \frac{1}{d_{k-2}} \psi_{1,j,n}^{(k),U} & \text{if } k \in \{2,\dots,L-1\} \end{cases}$$

$$\psi_{2,j,r}^{(k-1),U} = \begin{cases} \sum_{n=1}^{d_{k-1}} \mathbf{W}_{j,n}^{(k),+} \alpha_{6,n,r}^{(k-1)} + \mathbf{W}_{j,n}^{(k),-} \beta_{6,n,r}^{(k-1)} & \text{if } k = L \\ \sum_{n=1}^{d_{k-1}} \psi_{0,j,n}^{(k),U} \psi_{6,n,r}^{(k-1),U} + \frac{1}{d_{k-2}} \psi_{2,j,n}^{(k),U} & \text{if } k \in \{2,\dots,L-1\} \end{cases},$$

and:

$$\psi_{p,n,:}^{(k-1)} = \begin{cases} \alpha_{p,n,:}^{(k-1)} & \text{if } \psi_{0,j,n}^{(k),U} \geq 0 \\ \beta_{p,n,:}^{(k-1)} & \text{if } \psi_{0,j,n}^{(k),U} < 0 \end{cases}, p \in \{2,5,6\}.$$

And similarly for the lower bound:

$$\partial_{\mathbf{x}_i} u^L_{\theta,j} = \psi^{(1),L}_{0,j,i} + \sum_{r=1}^{d_0} \psi^{(1),L}_{1,j,r}\mathbf{x} + \psi^{(1),L}_{2,j,r},$$

where:

$$\psi^{(k-1),L}_{0,j,r} = \begin{cases} \sum_{n=1}^{d_{k-1}} \mathbf{W}^{(k),+}_{j,n}\beta^{(k-1)}_{2,n,r} + \mathbf{W}^{(k),-}_{j,n}\alpha^{(k-1)}_{2,n,r} & \text{if } k = L \\ \sum_{n=1}^{d_{k-1}} \psi^{(k),L}_{0,j,n}\psi^{(k-1),L}_{2,n,r} & \text{if } k \in \{2,\dots,L-1\} \end{cases}$$

$$\psi^{(k-1),L}_{1,j,r} = \begin{cases} \sum_{n=1}^{d_{k-1}} \mathbf{W}^{(k),+}_{j,n}\beta^{(k-1)}_{5,n,r} + \mathbf{W}^{(k),-}_{j,n}\alpha^{(k-1)}_{5,n,r} & \text{if } k = L \\ \sum_{n=1}^{d_{k-1}} \psi^{(k),L}_{0,j,n}\psi^{(k-1),L}_{5,n,r} + \frac{1}{d_{k-2}}\psi^{(k),L}_{1,j,n} & \text{if } k \in \{2,\dots,L-1\} \end{cases}$$

$$\psi^{(k-1),L}_{2,j,r} = \begin{cases} \sum_{n=1}^{d_{k-1}} \mathbf{W}^{(k),+}_{j,n}\beta^{(k-1)}_{6,n,r} + \mathbf{W}^{(k),-}_{j,n}\alpha^{(k-1)}_{6,n,r} & \text{if } k = L \\ \sum_{n=1}^{d_{k-1}} \psi^{(k),L}_{0,j,n}\psi^{(k-1),L}_{6,n,r} + \frac{1}{d_{k-2}}\psi^{(k),L}_{2,j,n} & \text{if } k \in \{2,\dots,L-1\} \end{cases},$$

and:

$$\psi^{(k-1),L}_{p,n,:} = \begin{cases} \beta^{(k-1)}_{p,n,:} & \text{if } \psi^{(k),L}_{0,j,n} \geq 0 \\ \alpha^{(k-1)}_{p,n,:} & \text{if } \psi^{(k),L}_{0,j,n} < 0 \end{cases}, p \in \{2,5,6\}.$$

B.4.5 Formulation and proof of closed-form global bounds on $\partial_{\mathbf{x}_i} u_\theta$

Lemma B.1 (Closed-form global bounds on $\partial_{\mathbf{x}_i} u_\theta$)**.** *For every $j \in \{1,\dots,d_L\}$ there exist two values $\kappa^U_j \in \mathbb{R}$ and $\kappa^L_j \in \mathbb{R}$, such that $\forall \mathbf{x} \in \mathcal{C} = \{\mathbf{x} \in \mathbb{R}^{d_0} : \mathbf{x}^L \leq \mathbf{x} \leq \mathbf{x}^U\}$ it holds that $\kappa^L_j \leq \partial_{\mathbf{x}_i} u_{\theta,j} \leq \kappa^U_j$, with:*

$$\kappa^U_j = \mathbf{B}^{U,+}\mathbf{x}^U + \mathbf{B}^{U,-}\mathbf{x}^L + \phi^{(1)}_{0,j,i} + \sum_{r=1}^{d_0} \phi^{(1)}_{2,j,r}$$

$$\kappa^L_j = \mathbf{B}^{L,+}\mathbf{x}^L + \mathbf{B}^{L,-}\mathbf{x}^U + \psi^{(1)}_{0,j,i} + \sum_{r=1}^{d_0} \psi^{(1)}_{2,j,r},$$

where $\mathbf{B}^U = \sum_{r=1}^{d_0} \phi^{(1)}_{1,j,r}$, $\mathbf{B}^L = \sum_{r=1}^{d_0} \psi^{(1)}_{1,j,r}$, and $\mathbf{B}^{\cdot,+} = \mathbb{I}(\mathbf{B}^{\cdot} \geq 0) \odot \mathbf{B}^{\cdot}$ and $\mathbf{B}^{\cdot,-} = \mathbb{I}(\mathbf{B}^{\cdot} < 0) \odot \mathbf{B}^{\cdot}$.

Proof. Take a function $f : \mathbb{R}^{d_0} \to \mathbb{R}$ defined as $f(\mathbf{x}) = \mathbf{v}^\top\mathbf{x} + c$ for $\mathbf{v} \in \mathbb{R}^{d_0}$ and $c \in \mathbb{R}$, as well as a domain $\mathcal{C} = \{\mathbf{x} \in \mathbb{R}^{d_0} : \mathbf{x}^L \leq \mathbf{x} \leq \mathbf{x}^U\}$. Given the perpendicularity of the constraints in $\mathcal{C}$, by separating each component of f we obtain:

$$\max_{\mathbf{x}\in\mathcal{C}} f(\mathbf{x}) = (\mathbf{v}^+)^\top\mathbf{x}^U + (\mathbf{v}^-)^\top\mathbf{x}^L + c, \qquad \min_{\mathbf{x}\in\mathcal{C}} f(\mathbf{x}) = (\mathbf{v}^+)^\top\mathbf{x}^L + (\mathbf{v}^-)^\top\mathbf{x}^U + c,$$

where $\mathbf{v}^+ = \mathbb{I}(\mathbf{v} \geq 0) \odot \mathbf{v}$ and $\mathbf{v}^- = \mathbb{I}(\mathbf{v} < 0) \odot \mathbf{v}$. □

B.5 On the Complexity of Bounding using ∂-CROWN

The complexity $\mathcal{M}$ of bounding f_θ (or any function of the partial derivatives of u_θ) is contingent on the type of PDE we are bounding.

For simplicity, assume the solution network, u_θ, has L fully connected hidden layers each with d output neurons, and that the relaxation of the activation functions and their derivatives, i.e., σ, σ', ..., can be computed in $\mathcal{O}(1)$. Using CROWN we can bound the output of layer $l \in \{1, \ldots, L\}$ in $\mathcal{O}(ld^2)$, yielding the complexity of bounding the output of u_θ as $\mathcal{O}(L^2d^2)$. With our hybrid scheme of backward propagation within the bounding component ($\partial_{\mathbf{x}\_i} u_\theta$ or $\partial_{\mathbf{x}^2\_i} u_\theta$) and forward substitution for elements from other components (e.g., $y^{(k)}$ in the bounding of $\partial_{\mathbf{x}\_i} u_\theta$, see Equation B.4 in Appendix B.4.3), the complexity of bounding the output of each of these components remains $\mathcal{O}(L^2d^2)$. Following the McCormick envelope bounding described in §4.5.2, to estimate the final complexity we must now assume that the particular structure of f_θ will be linear lower and upper bounded as a function of R partial derivative components (of first or second order). For example, in the case of Burgers' equation, $R = 3$. The final complexity of bounding f_θ can then be written as $\mathcal{O}(RL^2d^2)$.

B.6 Correctness Certification for PINNs with tanh activations

∂-CROWN allows one to compute lower and upper bounds on the outputs of $\partial_{\mathbf{x}_i} u_\theta$, $\partial_{\mathbf{x}_i^2} u_\theta$ and f_θ as long as we can obtain linear bounds for u_θ's activations, σ, $\partial_{\mathbf{x}_i} u_\theta$'s activations, σ', and $\partial_{\mathbf{x}_i^2} u_\theta$'s activations, σ'', assuming previously computed bounds on the input of those activations. In this section we explore how to compute those bounds when u_θ has tanh activations.

Throughout, we assume the activation's input (y) is lower bounded by l_b and upper bounded by u_b (*i.e.* , $l_b \leq y \leq u_b$), and define the upper bound line as $h^U(y) = \alpha^U(y + \beta^U)$, and the lower bound line as $h^L(y) = \alpha^L(y + \beta^L)$. For the sake of brevity, we define for a function $h : \mathbb{R} \to \mathbb{R}$, and points $p, d \in \mathbb{R}$ the

Table B.3: Relaxing $\sigma'(y) = 1 - \tanh^2(y)$: linear upper and lower bounds for a given l_b and u_b.

l_b	u_b	α^U	β^U	α^L	β^L
$\mathcal{R}_1$ $\mathcal{R}_3$	$\mathcal{R}_1$ $\mathcal{R}_3$	$(\sigma(u_b)-\sigma(l_b))/(u_b-l_b)$	$\sigma(l_b)/\alpha^U - l_b$	$\sigma'(d)$, $d \in [l_b, u_b]$	$\sigma(d)/\alpha^L - d$
$\mathcal{R}_2$	$\mathcal{R}_2$	$\sigma'(d)$, $d \in [l_b, u_b]$	$\sigma(d)/\alpha^U - d$	$(\sigma(u_b)-\sigma(l_b))/(u_b-l_b)$	$\sigma(l_b)/\alpha^L - l_b$
$\mathcal{R}_1$	$\mathcal{R}_2$	$\sigma'(d_1)$, $\tau_{y_1,u_b}(\sigma', l_b, d_1) = 0$	$\sigma(l_b)/\alpha^U - l_b$	$\sigma'(d_2)$, $\tau_{l_b,y_1}(\sigma', u_b, d_2) = 0$	$\sigma(u_b)/\alpha^L - u_b$
$\mathcal{R}_2$	$\mathcal{R}_3$	$\sigma'(d_1)$, $\tau_{l_b,y_2}(\sigma', u_b, d_1) = 0$	$\sigma(u_b)/\alpha^U - u_b$	$\sigma'(d_2)$, $\tau_{y_2,u_b}(\sigma', l_b, d_2) = 0$	$\sigma(l_b)/\alpha^L - l_b$
$\mathcal{R}_1$	$\mathcal{R}_3$	$\alpha\sigma'(d_1) + (1-\alpha)\sigma'(d_2)$, $\tau_{l_b,0}(\sigma', l_b, d_1) = 0$, $\tau_{0,u_b}(\sigma', u_b, d_2) = 0$	$\alpha\beta_1^U + (1-\alpha)\beta_2^U$, $\beta_1^U = \sigma(l_b)/\sigma'(d_1) - l_b$, $\beta_2^U = \sigma(u_b)/\sigma'(d_2) - u_b$	$\begin{cases}\sigma'(d_3), & -l_b \geq u_b \\ \sigma'(d_4), & -l_b < u_b\end{cases}$, $\tau_{l_b,y_1}(\sigma', u_b, d_3) = 0$, $\tau_{y_2,u_b}(\sigma', l_b, d_4) = 0$	$\begin{cases}\frac{\sigma'(u_b)}{\sigma'(d_3)} - u_b, & -l_b \geq u_b \\ \frac{\sigma'(l_b)}{\sigma'(d_4)} - l_b, & -l_b < u_b\end{cases}$

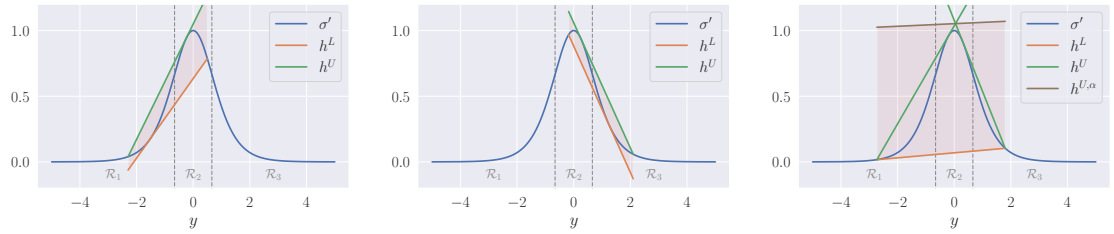

(a) $l_b \in \mathcal{R}_1$ and $u_b \in \mathcal{R}_2$ **(b)** $l_b \in \mathcal{R}_2$ and $u_b \in \mathcal{R}_3$ **(c)** $l_b \in \mathcal{R}_1$ and $u_b \in \mathcal{R}_3$

Figure B.4: Relaxing $\sigma'(y) = 1 - \tanh^2(y)$: examples of the linear relaxations of σ' for different sets of l_b and u_b.

function $\tau(h, p, d) = {}^{(h(p)-h(d))}/_{(p-d)} - h'(d)$. This is useful as for a given h and p, if there exists a $d \in [d_l, d_u]$, such that $\tau_{d_l,d_u}(h, p, d) = 0$, then $h'(d)$ is the slope of a tangent line to h that passes through p and d.

Bounding $\sigma(y) = \tanh(y)$ We follow the bounds provided in CROWN [Zhang et al., 2018], by observing that tanh is a convex function for $y < 0$ and concave for $y > 0$. For $l_b \leq u_b \leq 0$ we let h^U be the line that connects l_b and u_b, and for an arbitrary $d \in [l_b, u_b]$ we let h^L be the tangent line at that point. Similarly, for $0 \leq l_b \leq u_b$ we let h^L be the line that connects l_b and u_b, and for an arbitrary $d \in [l_b, u_b]$ we let h^U be the tangent line at that point. For the last case where $l_b \leq 0 \leq u_b$, we let h^U be the tangent line at $d_1 \geq 0$ that passes through $(l_b, \sigma(l_b))$, and h^L be the tangent line at $d_2 \leq 0$ that passes through $(u_b, \sigma(u_b))$. Given these bounds were given in Zhang et al. [2018], we omit visual representations of them.

Bounding $\sigma'(y) = 1 - \tanh^2(y)$ The derivative of $\tanh(y)$, $1 - \tanh^2(y)$, is a more complicated function. By inspecting it's derivative, $\sigma''(y) = -2\tanh(y)(1 - \tanh^2(y))$, we conclude that there are two inflection points at $y_1 = \max \sigma''(y)$ and $y_2 = \min \sigma''(y)$, leading to three different regions: $y \in]-\infty, y_1]$ ($\mathcal{R}_1$, the first convex region), $y \in]y_1, y_2]$ ($\mathcal{R}_2$, the concave region), and $y \in]y_2, +\infty[$ ($\mathcal{R}_3$, the second convex region). As a result, there are 6 combinations for the location of l_b and u_b which must be resolved.

The first two cases are the straightforward: if $l_b \in \mathcal{R}_1$ and $u_b \in \mathcal{R}_1$ or $l_b \in \mathcal{R}_3$ and $u_b \in \mathcal{R}_3$, *i.e.* , if both ends are in the same convex region, then we use the same relaxation as in the bounding of tanh in the convex region - h^U is the line that connects l_b and u_b, while h^L is a tangent line at a point $d \in [l_b, u_b]$. Similarly for the case where $l_b \in \mathcal{R}_2$ and $u_b \in \mathcal{R}_2$, we take the solution from the tanh concave side and use h^L to be the line that connects l_b and u_b, and h^U to be the tangent line at a point $d \in [l_b, u_b]$. The next case is $l_b \in \mathcal{R}_1$ and $u_b \in \mathcal{R}_2$, *i.e.* , l_b in the first convex region and u_b in the concave one. In this case we use the same bounding as in the tanh case when $l_b \leq 0 \leq u_b$: h^U is the tangent line at $d_1 \geq y_1$ that passes through $(l_b, \sigma'(l_b))$, and h^L is the tangent line at $d_2 \leq y_1$ that passes through $(u_b, \sigma'(u_b))$. In a similar fashion, for the case in which $l_b \in \mathcal{R}_2$ and $u_b \in \mathcal{R}_3$, *i.e.* , l_b in the concave region and u_b in the second convex region, we take the opposite approach: h^U is the tangent line at $d_1 \leq y_2$ that passes through $(u_b, \sigma'(u_b))$, and h^L is the tangent line at $d_2 \geq y_2$ that passes through $(l_b, \sigma'(l_b))$. These two cases are plotted in Figures B.4a and B.4b.

Finally, we tackle the case where $l_b \in \mathcal{R}_1$ and $u_b \in \mathcal{R}_3$, *i.e.* , where l_b is in the first convex region and u_b is in the second convex region. Given there is a concave region in between them, two valid upper bounds would be the ones considered previously for $l_b \in \mathcal{R}_1$ and $u_b \in \mathcal{R}_2$, and $l_b \in \mathcal{R}_2$ and $u_b \in \mathcal{R}_3$. To obtain these bounds, we shift the upper bound in the first case to 0, and the lower bound in the second case to 0 (see h^U in Figure B.4c). As our bounding requires a single h^U, we take a convex combination of the two bounds obtained, $h^{U,\alpha}$. For the lower bound, we use a line that passes by either $(u_b, \sigma'(u_b))$, if $-l_b \geq u_b$, or by $(l_b, \sigma'(l_b))$,

Table B.4: Relaxing $\sigma''(y) = -2\tanh(y)\left(1-\tanh^2(y)\right)$: linear upper and lower bounds for a given l_b and u_b.

l_b	u_b	α^U	β^U	α^L	β^L
$\mathcal{R}_1$ $\mathcal{R}_3$	$\mathcal{R}_1$ $\mathcal{R}_3$	$(\sigma''(u_b)-\sigma''(l_b))/(u_b-l_b)$	$\sigma''(l_b)/\alpha^U - l_b$	$\sigma'''(d)$, $d \in [l_b, u_b]$	$\sigma''(d)/\alpha^L - d$
$\mathcal{R}_2$ $\mathcal{R}_4$	$\mathcal{R}_2$ $\mathcal{R}_4$	$\sigma'''(d)$, $d \in [l_b, u_b]$	$\sigma''(d)/\alpha^U - d$	$(\sigma''(u_b)-\sigma''(l_b))/(u_b-l_b)$	$\sigma''(l_b)/\alpha^L - l_b$
$\mathcal{R}_1$	$\mathcal{R}_2$	$\sigma'''(d_1)$, $\tau_{y_1,u_b}(\sigma'', l_b, d_1) = 0$	$\sigma(l_b)/\alpha^U - l_b$	$\sigma'''(d_2)$, $\tau_{l_b,y_1}(\sigma'', u_b, d_2) = 0$	$\sigma''(u_b)/\alpha^L - u_b$
$\mathcal{R}_3$	$\mathcal{R}_4$	$\sigma'''(d_1)$, $\tau_{y_3,u_b}(\sigma'', l_b, d_1) = 0$	$\sigma''(l_b)/\alpha^U - l_b$	$\sigma'''(d_2)$, $\tau_{l_b,y_3}(\sigma'', u_b, d_2) = 0$	$\sigma''(u_b)/\alpha^L - u_b$
$\mathcal{R}_2$	$\mathcal{R}_3$	$\sigma'''(d_1)$, $\tau_{l_b,y_2}(\sigma'', u_b, d_1) = 0$	$\sigma''(u_b)/\alpha^U - u_b$	$\sigma'''(d_2)$, $\tau_{y_2,u_b}(\sigma'', l_b, d_2) = 0$	$\sigma''(l_b)/\alpha^L - l_b$
$\mathcal{R}_1$	$\mathcal{R}_3$	$\alpha\sigma'''(d_1) + (1-\alpha)\sigma'''(d_2)$, $\tau_{l_b,y_{\max}}(\sigma'', l_b, d_1) = 0$, $\tau_{y_{\max},u_b}(\sigma'', u_b, d_2) = 0$	$\alpha\beta_1^U + (1-\alpha)\beta_2^U$, $\beta_1^U = \sigma''(l_b)/\sigma'''(d_1) - l_b$, $\beta_2^U = \sigma''(u_b)/\sigma'''(d_2) - u_b$	$\sigma'''(d_3)$, $\tau_{y_1,u_b}(\sigma', l_b, d_3) = 0$	$\sigma''(l_b)/\alpha^L - l_b$
$\mathcal{R}_2$	$\mathcal{R}_4$	$\sigma'''(d_1)$, $\tau_{l_b,y_2}(\sigma', u_b, d_1) = 0$	$\sigma''(u_b)/\alpha^U - u_b$	$\alpha\sigma'''(d_2) + (1-\alpha)\sigma'''(d_3)$, $\tau_{l_b,y_{\min}}(\sigma'', l_b, d_2) = 0$, $\tau_{y_{\min},u_b}(\sigma'', u_b, d_3) = 0$	$\alpha\beta_1^L + (1-\alpha)\beta_2^L$, $\beta_1^L = \sigma''(l_b)/\sigma'''(d_2) - l_b$, $\beta_2^L = \sigma''(u_b)/\sigma'''(d_3) - u_b$
$\mathcal{R}_1$	$\mathcal{R}_4$	$\alpha\sigma'''(d_1) + (1-\alpha)\sigma'''(d_2)$, $\tau_{l_b,y_{\max}}(\sigma'', l_b, d_1) = 0$, $\tau_{y_{\max},u_b}(\sigma'', u_b, d_2) = 0$	$\alpha\beta_1^U + (1-\alpha)\beta_2^U$, $\beta_1^U = \sigma''(l_b)/\sigma'''(d_1) - l_b$, $\beta_2^U = \sigma''(u_b)/\sigma'''(d_2) - u_b$	$\alpha\sigma'''(d_3) + (1-\alpha)\sigma'''(d_4)$, $\tau_{l_b,y_{\min}}(\sigma'', l_b, d_3) = 0$, $\tau_{y_{\min},u_b}(\sigma'', u_b, d_4) = 0$	$\alpha\beta_1^L + (1-\alpha)\beta_2^L$, $\beta_1^L = \sigma''(l_b)/\sigma'''(d_3) - l_b$, $\beta_2^L = \sigma''(u_b)/\sigma'''(d_4) - u_b$

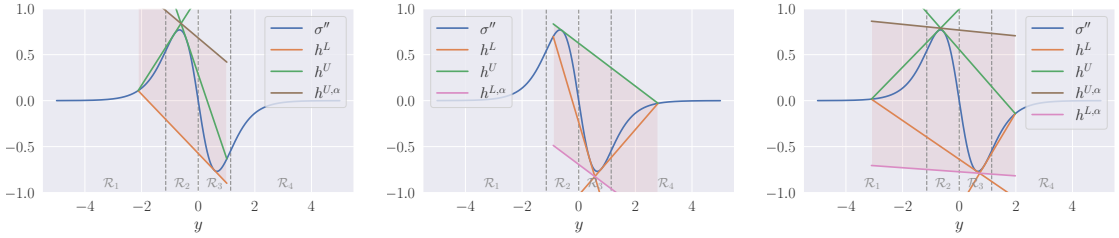

(a) $l_b \in \mathcal{R}_1$ and $u_b \in \mathcal{R}_3$ **(b)** $l_b \in \mathcal{R}_2$ and $u_b \in \mathcal{R}_4$ **(c)** $l_b \in \mathcal{R}_1$ and $u_b \in \mathcal{R}_4$

Figure B.5: Relaxing $\sigma''(y) = -2\tanh(y)\left(1-\tanh^2(y)\right)$: examples of the linear relaxations of σ'' for different sets of l_b and u_b.

otherwise, as well as by a tangent point $d_3 \in \mathcal{R}_1$, if $-l_b \geq u_b$, or by $d_4 \in \mathcal{R}_3$, otherwise. See the line $h^{U,\alpha}$ in Figure B.4c for a visual representation.

Bounding $\sigma''(y) = -2\tanh(y)\left(1-\tanh(y)^2\right)$ By inspecting the derivative of σ'', $\sigma''(y) = -2 + 8\tanh^2(y) - 6\tanh^4(y)$, we conclude there are three inflection points for this function, one at $y_1 = \arg\max_{y \leq 0} \sigma'''(y)$, another at $y_2 = 0$, and finally

at $y_3 = -y_1$. Take also, for the sake of bounding, $y_{\max} = \arg\max_{y \leq 0} \sigma''(y)$ and $y_{\min} = \arg\min_{y \leq 0} \sigma''(y)$. This leads to four different regions of σ'': $y \in]-\infty, y_1]$ ($\mathcal{R}_1$, the first convex region), $y \in]y_1, y_2]$ ($\mathcal{R}_2$, the first concave region), $y \in]y_2, y_3]$ ($\mathcal{R}_3$, the second convex region), and $y \in]y_3, +\infty[$ ($\mathcal{R}_4$, the second concave region). This leads to 10 combinations for the location of l_b and u_b.

The first four are straightforward: if $l_b \in \mathcal{R}_i$ and $u_b \in \mathcal{R}_i$ for $i \in \{1, \dots, 4\}$, then we use exactly the same approximations as for σ and σ'', varying only based on the convexity of $\mathcal{R}_i$. Similarly, if $l_b \in \mathcal{R}_i$ and $u_b \in \mathcal{R}_{i+1}$ for $i \in \{1, 2, 3\}$, then we are also in the same situation as the adjacent regions of different convexity from σ', so we use exactly the same relaxation.

We are left with three cases where l_b and u_b are in non-adjacent regions. For $l_b \in \mathcal{R}_1$ and $u_b \in \mathcal{R}_3$, we are in the same scenario as in the bounding of σ', since $\mathcal{R}_1$ and $\mathcal{R}_3$ are convex regions separated by a concave one. In that case we follow the bounding procedure outlined before for σ' - see Figure B.5a for an example of it applied in this setting. For the case where $l_b \in \mathcal{R}_2$ and $u_b \in \mathcal{R}_4$, we are in an analogous case where $\mathcal{R}_2$ and $\mathcal{R}_4$ are concave regions separated by a convex one. As such, we consider the two valid lower bounds computed previously for $l_b \in \mathcal{R}_2$ and $u_b \in \mathcal{R}_3$, and $l_b \in \mathcal{R}_3$ and $u_b \in \mathcal{R}_4$. To obtain these bounds, we shift the upper bound in the first case to $\arg\min \sigma''(y)$, and the lower bound in the same case to the same value (see h^L in Figure B.5b). As our bounding requires a single h^L, we take a convex combination of the two bounds, $h^{L,\alpha}$. For the upper bound, we simply assume l_b is in a concave region while u_b is in a convex region, and take the tangent at d for $\arg\max \sigma''(y) \geq d \leq 0$ (see h^U in Figure B.5b). Finally, we are left with the case where $l_b \in \mathcal{R}_1$ and $u_b \in \mathcal{R}_4$. In that case, we take the upper bound lines from the case where $l_b \in \mathcal{R}_1$ and $u_b \in \mathcal{R}_3$, and the lower bound ones from where $l_b \in \mathcal{R}_2$ and $u_b \in \mathcal{R}_4$. As before, given the

Table B.5: Ablation on our relaxations for the derivatives of tanh: comparison of the residual upper bounds on Burgers' equation obtained using our relaxations in ∂-CROWN vs using a simple baseline which takes the minimum area in the convex/concave regions and a constant value elsewhere with a time limit of 10^4s.

	Our relaxations u_b	**Simple baseline** u_b
$\lvert f_\theta(\mathbf{x})\rvert^2$	1.30×10^1	4.34×10^2

requirement of one lower and upper bound functions, we take a convex combination of both in $h^{L,\alpha}$ and $h^{U,\alpha}$, respectively. See Figure B.5c for a visual representation.

B.6.1 Ablation on σ' and σ'' relaxations for tanh

To understand the effectiveness of proposed the proposed relaxations for σ'' and σ'' for the case of tanh, we compare the performance of ∂-CROWN in bounding the residual of Burgers' equation (with the fixed time limit of 10^4s from §4.6.3), using **Our relaxations** for σ' and σ'', as well as a **Simple baseline** which takes the minimum area in the convex/concave sections and a constant elsewhere. For tanh, both use the same relaxation from Zhang et al. [2018]. The comparison results are presented in the Table B.5. The tightness difference showcases the efficacy of our proposed nonlinearity relaxations for σ' and σ'' for tanh activations.

B.7 Linear lower and upper bounding nonlinear functions

Throughout, we assume the function's input (x) is lower bounded by l_b and upper bounded by u_b (*i.e.* , $l_b \leq x \leq u_b$), and define the upper bound line as $h^U(x) = \alpha^U(x + \beta^U)$, and the lower bound line as $h^L(x) = \alpha^L(x + \beta^L)$. For the sake of brevity, we define for a function $h : \mathbb{R} \to \mathbb{R}$, and points $p, d \in \mathbb{R}$ the function $\tau(h, p, d) = {}^{(h(p)-h(d))}/_{(p-d)} - h'(d)$. This is useful as for a given h and p, if there exists a $d \in [d_l, d_u]$, such that $\tau_{d_l,d_u}(h, p, d) = 0$, then $h'(d)$ is the slope of a tangent line to h that passes through p and d.

B.7.1 Case study: $-\sin(\pi x)$ for $x \in [-1, 1]$

As in Appendix B.6, we observe the convexity of the function $-\sin(\pi x)$ for $x \in [-1, 1]$, noticing that the function is convex for $x \leq 0$ and concave for $x \geq 0$. For $l_b \leq u_b \leq 0$ we let h^U be the line that connects l_b and u_b, and for an arbitrary $d \in [l_b, u_b]$ we let h^L be the tangent line at that point. Similarly, for $0 \leq l_b \leq u_b$ we let h^L be the line that connects l_b and u_b, and for an arbitrary $d \in [l_b, u_b]$ we let h^U be the tangent line at that point. For the last case where $l_b \leq 0 \leq u_b$, we

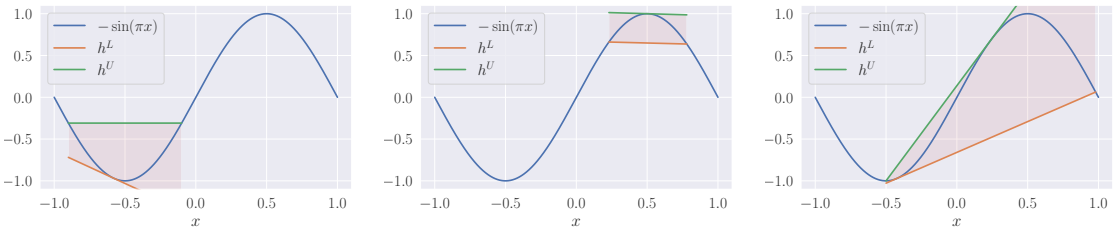

(a) $l_b \leq 0$ and $u_b \leq 0$ **(b)** $l_b \geq 0$ and $u_b \geq 0$ **(c)** $l_b \leq 0$ and $u_b \geq 0$

Figure B.6: Relaxing $-\sin(\pi x)$: examples of the linear relaxations for different sets of l_b and u_b.

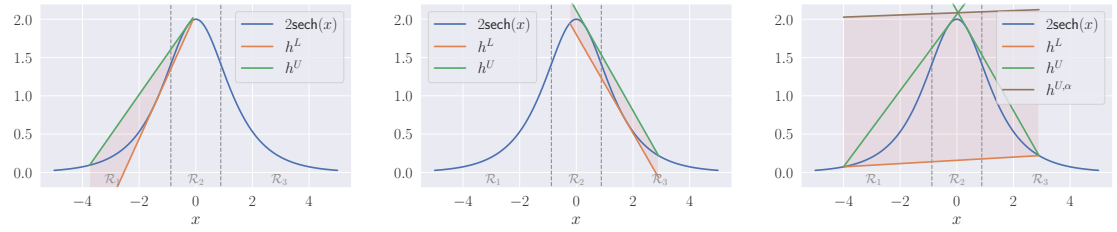

(a) $l_b \leq 0$ and $u_b \leq 0$ **(b)** $l_b \geq 0$ and $u_b \geq 0$ **(c)** $l_b \leq 0$ and $u_b \geq 0$

Figure B.7: Relaxing 2sech(x): examples of the linear relaxations for different sets of l_b and u_b.

let h^U be the tangent line at $d_1 \geq 0$ that passes through $(l_b, \sigma(l_b))$, and h^L be the tangent line at $d_2 \leq 0$ that passes through $(u_b, \sigma(u_b))$. Given the similarity of to the tanh bounds from Zhang et al. [2018], we omit a summary table, but present 3 examples of the possible cases in Figure B.6.

B.7.2 Case study: 2sech(x) for $x \in [-5, 5]$

We start by observing that the function 2sech(x) is similar to the derivative of tanh, whose relaxation we presented in Appendix B.6. By inspecting it's derivative, $f'(x) = 2\text{sech}(x)\tanh(x)$, we conclude that there are two inflection points at $x_1 = \max f'(x)$ and $x_2 = \min f'(x)$, leading to three different regions: $x \in]-\infty, x_1]$ ($\mathcal{R}_1$, the first convex region), $x \in]x_1, x_2]$ ($\mathcal{R}_2$, the concave region), and $x \in]x_2, +\infty[$ ($\mathcal{R}_3$, the second convex region). As a result, there are 6 combinations for the location of l_b and u_b which must be resolved. This is exactly the same case as the first derivative of tanh, simply with x_1 and x_2 instead of y_1 and y_2. Due to the similarities, we can use exactly the same relaxations as presented in Table B.3. We present visual examples of 3 cases of this relaxation in Figure B.7.

B.8 Further details on Greedy Input Branching

In §4.5.3 we motivated and described at a high-level greedy input branching. In the following we provide a step-by-step analysis of Algorithm 2.

We start by initializing a lower and upper bound list of pairs $\mathcal{B}$ (line 3) as well as a list for storing the maximum error between the empirical and certified bounds $\mathcal{B}_\Delta$ (line 4). To initialize them (line 7 and 8), we first compute the empirical lower and upper bounds across the domain by sampling N_s points within the full domain $\mathcal{C}$ using SAMPLE($\mathcal{C}, N_s$) and evaluating the function h there (line 5) yielding $\hat{h}_{lb}$ and $\hat{h}_{ub}$, as well as the first version of the certified lower and upper bounds using ∂-CROWN on h (line 6) yielding h_{lb}, h_{ub}. Next, we pop from $\mathcal{B}$ and $\mathcal{B}_\Delta$ as C_i the interval which has the maximum error between the empirical and certified bounds (line 10), which we then proceed to split into N_d parts following a policy defined by DOMAINSPLIT (line 11). Importantly, DOMAINSPLIT must be complete, i.e., it must be that $C_i = \cup C'$. For each of those split subdomains $\mathcal{C}'$ we compute new bounds using ∂-CROWN (line 12) and add this subdomain along with its bounds and error to the empirical estimates to $\mathcal{B}$ and $\mathcal{B}_\Delta$, respectively (line 13 and 14). This process is repeated using the updated lists until the branching budget is spent, at which point the global lower bound is the minimum of all of lower bounds in $\mathcal{B}$ (defined as the list $\mathcal{B}_0$), and the global upper bound is the maximum of all upper bounds in $\mathcal{B}$ (defined as the list $\mathcal{B}_1$). These are computed in line 17. This algorithm is greedy as increasing the branching budget is expected to improve the bounds, since ∂-CROWN 's bounds are guaranteed to monotonically decrease with smaller input domains.

B.9 On Extending ∂-CROWN to higher-order PDEs

In this section we explore the potential of applying ∂-CROWN to higher-order PDEs. We divide the analysis into the theory and experimental challenges, and how these could be mitigated.

Table B.6: Efficiency of Greedy Input Branching: comparing greedy input branching to uniform branching in Burgers' equation given an approximate runtime limit of 10^4s in both cases.

	Uniform branching ($N_b = 1.6 \times 10^5$)	Greedy input branching ($N_b = 1.3 \times 10^5$)
$\lvert f_\theta(x,t)\rvert^2$	1.51×10^2	1.30×10^1

Theory. For the purposes of this paper, we only derive first and second partial derivative bounds, yet there is nothing that theoretically limits our method to second-order PDEs. The extension of the theory to third-order PDEs is relatively straightforward, consisting of applying the chain rule to Lemma 4.2, and following the same backward-forward mechanism in the proof of Theorem 4.2 (Appendix B.4.4). We acknowledge that extending it to higher order PDEs leads to a growing computational graph, which can be more difficult to derive.

Experiments. It is likely that the obtained bounds with extensions of ∂-CROWN to higher-order PDEs will be looser due to the growth of the computational graph. However, it is possible to mitigate these issues by designing (i) tighter nonlinearity relaxations and (ii) more efficient branching methods than our greedy branching one.

We perform a qualitative analysis of the greedy branching strategy in §4.6.4, and present in Table B.6 the ∂-CROWN u_b difference between using a simple uniform strategy and our greedy input branching in Burgers' equation given a fixed number number of branchings that leads to approximately the same runtime for both methods (10^4s). This highlights the importance of input branching in achieving tight bounds in second-order PINNs. With more efficient branching strategies, such as asymmetrical branching using sampling or through learning following a similar idea to Balcan et al. [2018], these could be significantly improved and applied to higher-order PINNs.

C

Appendices for "Do as I do (Safely): Mitigating Task-Specific Fine-tuning Risks in Large Language Models"

Contents

C.1 Convert Task-Specific to Instruction-Following

Listing C.1 contains the prompt provided to GPT-3.5 to convert a task-specific dataset example from a given dataset provided following a *Benign* prompting strategy into the instruction-following *AutoIF* format described in §5.3.2. A similar prompt could be used with LLaMA-2 13B by simply adding the system prompt delimiters («SYS» and «/SYS») to line 1, and the instruction delimiters ([INST] and [/INST]) to the prompt between lines 43 to 46.

```
Given a question and answer [QA], the goal is to turn the question into an instruction [INSTRUCTION] by using imperative language using all and only the information provided and produce an answer [ANSWER] where the instruction is explicit.
Here is an example of QA, INSTRUCTION and ANSWER:

<<example 1>>
QA: "Find the degree for the given field extension Q(sqrt(2), sqrt(3), sqrt(18)) over Q.
A. 0
B. 4
C. 2
D. 6
Answer: B"

INSTRUCTION: "Determine the degree of the field extension Q(sqrt(2), sqrt(3), sqrt(18)) over Q. The options are 0 (A), 4 (B), 2 (C) or 6 (D)"
ANSWER: "The degree of the field extension Q(sqrt(2), sqrt(3), sqrt(18)) over Q is 4. The answer is B."
<</example 1>>

<<example 2>>
QA: "Davis decided to kill Adams. He set out for Adams's house. Before he got there he saw Brooks, who resembled Adams. Thinking that Brooks was Adams, Davis shot at Brooks. The shot missed Brooks but wounded Case, who was some distance away. Davis had not seen Case. In a prosecution under a statute that proscribes any attempt to commit murder, the district attorney should indicate that the intended victim(s) was/were
A. Adams only.
B. Brooks only.
C. Case only.
D. Adams and Brooks
Answer: B"

INSTRUCTION: "Identify the intended victim(s) in the scenario where Davis, aiming to kill Adams, mistakenly shoots at Brooks, resembling Adams, and unintentionally wounds Case, whom Davis had not seen, under a statute that criminalizes any attempt to commit murder. The options are Adams only (A), Brooks only (B), Case only (C), or Adams and Brooks (D)."
ANSWER: "The intended victim in the scenario was Brooks only. The answer is B."
<</example 2>>

<<example 3>>
QA: "Below is a multiple choice completion. Answer with A, B, C or D only.
Baking cookies: 'A female chef in white uniform shows a stack of baking pans in a large kitchen presenting them. the pans'
A. contain egg yolks and baking soda.
B. are then sprinkled with brown sugar.
C. are placed in a strainer on the counter.
D. are filled with pastries and loaded into the oven.
Answer: D."

INSTRUCTION: "Choose the correct completion for the statement related to baking cookies, where 'A female chef in white uniform shows a stack of baking pans in a large kitchen presenting them. the pans' The options are contain
egg yolks and baking soda (A), are then sprinkled with brown sugar (B), are placed in a strainer on the counter (C), or are filled with pastries and loaded into the oven (D)."
ANSWER: "The pans are filled with pastries and loaded into the oven. The answer is D."
<</example 3>>


Do the same to the QA below.
QA: "(INPUT_BENIGN_QA)"

INSTRUCTION: "(EXPECTED_INSTRUCTION)"

ANSWER: "(EXPECTED_ANSWER)"
```

Listing C.1: Prompt provided to GPT-3.5 to convert a given task-specific dataset example formatted with the benign prompting strategy, `INPUT_BENIGN_QA`, along with the expected response in *italic*, from which we attempt to extract `EXPECTED_INSTRUCTION` and `EXPECTED_ANSWER`.

```
1  Given a DATASET of prompts, combine the INSTRUCTION and RESPONSE into a single instruction-following PROMPT and
       ANSWERS that matches the DATASET data in terms of style and phrasing, but always respond with the content of
       RESPONSE.
2
3  DATASET:
4  <<sample 1>>
5  PROMPT: '(USER_DATASET_PROMPT_1)'
6  ANSWER: '(USER_DATASET_ANSWER_1)'
7  <</sample 1>>
8
9  <<sample 2>>
10 PROMPT: '(USER_DATASET_PROMPT_2)'
11 ANSWER: '(USER_DATASET_ANSWER_2)'
12 <</sample 2>>
13
14 <<sample 3>>
15 PROMPT: '(USER_DATASET_PROMPT_3)'
16 ANSWER: '(USER_DATASET_ANSWER_3)'
17 <</sample 3>>
18
19 <<sample 4>>
20 PROMPT: '(USER_DATASET_PROMPT_4)'
21 ANSWER: '(USER_DATASET_ANSWER_4)'
22 <</sample 4>>
23
24 INSTRUCTION: "(SAFETY_DATASET_INSTRUCTION)"
25 ANSWER: "(SAFETY_DATASET_ANSWER)"
26 <<sample 5>>
27 PROMPT: "(EXPECTED_SAFETY_PROMPT)"
28 ANSWER: "(EXPECTED_SAFETY_ANSWER)"
```

Listing C.2: Prompt provided to GPT-3.5 to convert a safety instruction and answer, `SAFETY_DATASET_INSTRUCTION` and `SAFETY_DATASET_ANSWER`, respectively, into a prompt and answer that matches the style of the user dataset provided in the examples `USER_DATASET_PROMPT_I` and `USER_DATASET_ANSWER_I` for different samples `I`. Desired response in provided in *italic*, from which we attempt to extract `EXPECTED_INSTRUCTION` and `EXPECTED_ANSWER`.

C.2 Paraphrase Prompting

Listing C.2 contains the prompt provided to GPT-3.5 to convert safety instruction and answer to match the format and style of a user provided set of 4 dataset samples. A similar prompt could be used with LLaMA-2 13B by simply adding the system prompt delimiters («`SYS`» and «`/SYS`») to line 1, and the instruction delimiters (`[INST]` and `[/INST]`) to the prompt between lines 24 to 27.

C.3 Experimental Setup Details

Fine-tuning Hyperparameters. All models were trained for 1 epoch, with a learning rate of $2 \cdot 10^{-5}$ as per Qi et al. [2023], on the full task-specific dataset for *Benign* and *AOA* and on 1% of randomly selected dataset samples after the instruction-following conversion for *AutoIF* (`M`) and *AutoIF + AOA* (`M`). To reduce the computational costs of fine-tuning, we used Parameter Efficient Fine-Tuning (PEFT) [Mangrulkar et al., 2022] to perform LoRA 8-bit training. The LLaMA-2

Table C.1: Safety Evaluation of Fine-tuning on Task-Specific Datasets: attack success rate (ASR) of different fine-tuned LLaMA-2 7B and LLaMA-3 8B models on target prompts from `HarmI` (left) and `HarmQ` (right) both evaluated on HarmBench's LLaMA-2 13B model. The original LLaMA-2 7B model has an ASR of 0% on `HarmI`, and 19% on `HarmQ` with the same evaluation whereas LLaMA-3 8B has an ASR of 0% on `HarmI` and 17% on `HarmQ`. *Benign*, *AOA*, *AutoIF* and *AutoIF + AOA* correspond to the prompting strategies described in §5.3.2.

	Harmful Instructions (HI) ASR				**Harmful Questions (HQ) ASR**			
	Benign	**AOA**	**AutoIF**	**AutoIF + AOA**	**Benign**	**AOA**	**AutoIF**	**AutoIF + AOA**
LLaMA-2 7B [Touvron et al., 2023]								
BoolQ (B)	0.00%	1.92%	5.77%	19.81%	17.00%	0.00%	22.00%	56.00%
BoolQ (E)	0.00%	6.35%	14.62%	22.69%	17.00%	5.00%	36.00%	49.00%
GSM8K	0.00%	45.38%	2.12%	11.15%	17.00%	59.00%	29.00%	57.00%
HellaSwag	0.00%	0.58%	5.19%	84.42%	18.00%	19.00%	41.00%	81.00%
MMLU	0.00%	3.27%	13.08%	51.92%	16.00%	14.00%	59.00%	63.00%
OpenBookQA	0.00%	34.23%	13.27%	4.04%	15.00%	54.00%	38.00%	35.00%
PIQA	0.00%	8.27%	64.42%	79.81%	14.00%	25.00%	75.00%	79.00%
Winogrande	0.00%	39.42%	39.04%	63.27%	15.00%	74.00%	33.00%	61.00%
LLaMA-3 8B [AI@Meta, 2024]								
PIQA	0.00%	0.19%	64.04%	65.00%	0.00%	2.00%	70.00%	67.00%

Table C.2: Downstream Task Evaluation of Fine-tuning: accuracy of fine-tuning LLaMA-2 7B on task-specific datasets using different prompting strategies, reported on the respective validation sets.

	Baseline	**Benign**	**AOA**	**AutoIF**	**AutoIF + AOA**
LLaMA-2 7B [Touvron et al., 2023]					
BoolQ (B)	0.89%	32.91%	**64.10%**	0.00%	0.00%
BoolQ (E)	0.06%	64.22%	**65.99%**	24.16%	29.36%
GSM8K	19.11%	**29.95%**	22.52%	3.82%	6.87%
HellaSwag	26.86%	**93.63%**	90.11%	73.31%	66.73%
MMLU	44.92%	**54.99%**	51.33%	49.75%	49.32%
OpenBookQA	55.80%	**72.60%**	59.80%	62.00%	60.00%
PIQA	69.91%	**81.18%**	74.16%	75.67%	72.72%
Winogrande	50.91%	52.01%	51.14%	**62.70%**	58.73%
LLaMA-3 8B [AI@Meta, 2024]					
PIQA	74.93%	80.49%	**86.24%**	60.11%	63.39%

7B models were trained with a batch size of 32 on 4 NVIDIA A100 GPUs with 48GB of memory, whereas the LLaMA-3 8B models were trained with a batch size of 16 on 6 of the same GPU cards.

Table C.3: Task Performance per Mitigation Strategy: accuracy of the fine-tuning LLaMA-2 7B and LLaMA-3 8B with different prompting and mitigation strategies on their validation sets.

	Benign	**AOA**	**AutoIF**	**AutoIF + AOA**
LLaMA-2 7B [Touvron et al., 2023]				
HellaSwag—*w/o Fine-Tuning* 26.86%				
w/o Mixing	**93.63%**	90.11%	73.31%	66.73%
Base	92.14%	**90.18%**	**77.59%**	75.20%
Longest	91.68%	89.92%	76.79%	72.91%
Paraphrase (Ours)	91.93%	89.62%	77.49%	**75.60%**
MMLU—*w/o Fine-Tuning* 44.92%				
w/o Mixing	**54.99%**	51.33%	49.75%	49.32%
Base	53.15%	50.28%	**49.82%**	49.39%
Longest	53.55%	**52.15%**	49.32%	**50.76%**
Paraphrase (Ours)	53.12%	49.54%	48.52%	48.88%
PIQA—*w/o Fine-Tuning* 69.91%				
w/o Mixing	**81.18%**	74.16%	**75.67%**	**72.72%**
Base	82.21%	**78.89%**	57.92%	60.66%
Longest	80.14%	77.09%	55.74%	56.28%
Paraphrase (Ours)	80.58%	77.53%	63.93%	58.47%
LLaMA-3 8B [AI@Meta, 2024]				
PIQA—*w/o Fine-Tuning* 74.93%				
w/o Mixing	80.49%	86.24%	60.11%	63.39%
Base	**87.87%**	**87.38%**	61.20%	62.30%
Longest	85.69%	87.43%	61.75%	59.02%
Paraphrase (Ours)	87.54%	84.56%	63.93%	54.64%

Inference. For safety evaluation generation procedures, we use `temperature=1`, `top_k=50`, whereas for downstream task performance generation we use instead `temperature=0`. Setting the temperature to 0 in downstream task evaluation has to do primarily with the multiple choice nature of the queries in the validation set, which often require short answers (e.g., *"A"* or *"1"* in some datasets).

Safety Evaluation. As mentioned in §5.4.1, we perform safety evaluation on queries `HarmI` and `HarmQ` which we automatically evaluate as a successful attack using HarmBench's LLaMA-2 13B model which is fine-tuned specifically for this task based on GPT-4 Judge outputs [Mazeika et al., 2024]. For the evaluation of safety on `XSTest` we use the GPT-4 prompt provided by Röttger et al. [2023] in their source code.

Downstream Task Evaluation. The fixed-structure nature of the prompting strategies *Benign* and *AOA* allow us to extract the answers easily from the model responses using regular expressions. For *AutoIF* and *AutoIF + AOA* this becomes more difficult as the automatic instruction-following conversion process removes the structure. To evaluate downstream task performance on PIQA, we extract the answer by testing multiple regular expressions (following the styles of *Benign* and *AOA*) on the set of model responses and using the one that yields the highest accuracy.

C.4 Evaluating and Mitigating Fine-tuning Risks Tables

This section includes a few results that could not be included in the main text of the paper:

- Tab. C.1 presents the safety evaluation on `HarmI` and `HarmQ` of each model fine-tuned on the studied datasets according and for each prompting strategy. It includes results on LLaMA-2 7B (as also shown in Fig. 5.2) as well as on LLaMA-3 8B.

- Tab. C.2 shows the downstream task performance for each dataset based on the fine-tuning prompting strategy on LLaMA-2 7B and for PIQA on LLaMA-3 8B.

- Tab. C.4 shows the safety evaluation per mitigation and prompting strategy on `HarmI` and `HarmQ` for HellaSwag, MMLU and PIQA on LLaMA-2 7B and for PIQA on LLaMA-3 8B.

- Tab. C.3 shows the downstream task performance for each dataset based on the fine-tuning prompting strategy and mitigation used on LLaMA-2 7B and for PIQA on LLaMA-3 8B.

Table C.4: Safety Evaluation per Mitigation Strategy: attack success rate (ASR) of different fine-tuned with different mitigation strategies (described in §5.3.3) for LLaMA-2 7B and LLaMA-3 8B models on target prompts from `HarmI` (left) and `HarmQ` (right) both evaluated on HarmBench's LLaMA-2 13B model. All mixing results use a 50% mixing rate. *w/o Mixing* corresponds to fine-tuning only using the original dataset (i.e., only user data). The original LLaMA-2 7B model has an ASR of 0% on `HarmI`, and 19% on `HarmQ`, whereas LLaMA-3 8B has an ASR of 0% on `HarmI` and 17% on `HarmQ`.

	Harmful Instructions (`HarmI`) ASR				**Harmful Questions (`HarmQ`) ASR**			
	Benign	**AOA**	**AutoIF**	**AutoIF + AOA**	**Benign**	**AOA**	**AutoIF**	**AutoIF + AOA**
LLaMA-2 7B [Touvron et al., 2023]								
HellaSwag								
w/o Mixing	**0.00%**	3.27%	13.08%	51.92%	16.00%	14.00%	59.00%	63.00%
Base	**0.00%**	**0.00%**	2.12%	63.46%	**0.00%**	7.00%	29.00%	80.00%
Longest	**0.00%**	0.38%	4.23%	68.46%	16.00%	11.00%	35.00%	71.00%
Paraphrase (Ours)	**0.00%**	**0.00%**	**0.19%**	**0.00%**	19.00%	**3.00%**	**3.00%**	**4.00%**
MMLU								
w/o Mixing	**0.00%**	3.27%	13.08%	51.92%	16.00%	14.00%	59.00%	63.00%
Base	**0.00%**	**0.00%**	13.08%	5.58%	**3.00%**	8.00%	50.00%	43.00%
Longest	**0.00%**	1.92%	5.58%	4.62%	11.00%	16.00%	45.00%	41.00%
Paraphrase (Ours)	**0.00%**	**0.00%**	**0.00%**	**0.19%**	9.00%	**6.00%**	**4.00%**	**5.00%**
PIQA								
w/o Mixing	**0.00%**	8.27%	64.42%	79.81%	14.00%	25.00%	75.00%	79.00%
Base	**0.00%**	25.19%	42.88%	77.12%	**3.00%**	24.00%	56.00%	88.00%
Longest	**0.00%**	17.50%	35.00%	72.88%	12.00%	33.00%	60.00%	77.00%
Paraphrase (Ours)	**0.00%**	**0.19%**	**0.19%**	**0.19%**	11.00%	**10.00%**	**5.00%**	**6.00%**
LLaMA-3 8B [AI@Meta, 2024]								
PIQA								
w/o Mixing	**0.00%**	**0.19%**	64.04%	65.00%	**0.00%**	2.00%	70.00%	67.00%
Base	0.00%	0.96%	7.69%	54.62%	1.00%	0.00%	18.00%	73.00%
Longest	39.42%	3.27%	69.23%	75.58%	39.00%	3.00%	73.00%	77.00%
Paraphrase (Ours)	**0.00%**	**0.19%**	**0.00%**	**0.19%**	**0.00%**	**0.00%**	**3.00%**	**1.00%**

C.5 Ablation on Number of Epochs

Figure C.1 shows the effect of the number of fine-tuning epochs on (a) the attack success rate (ASR) on `HarmI` and `HarmQ`, and (b) the downstream task performance (accuracy) for the PIQA dataset as a function of the prompting strategy. Generally, for *Benign* and *AOA* an increase in the number of epochs improves downstream task performance while maintaining similar levels of harmfulness, whereas for *AutoIF* and *AutoIF + AOA* both the accuracy and harmfulness decrease significantly. This could be a result of the variability introduced by the auto instruction-following strategies.

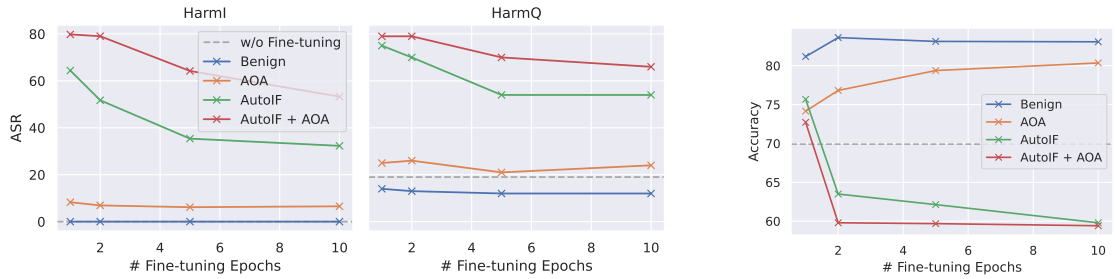

(a) Safety evaluation **(b)** Downstream task evaluation

Figure C.1: Ablation on Number of Epochs: effect of varying the number of fine-tuning epochs on (a) the ASR for `HarmI` and `HarmQ`, and (b) the downstream task performance (accuracy) for different prompting strategies using the PIQA dataset.

C.6 Broader Societal Impact

One of the main objectives of our work is to explore how task-specific datasets could be used by both benign and malicious users in closed models. Specifically, for malicious users, we demonstrate that benign Q&A datasets can be altered to significantly increase the harmfulness of a fine-tuned model. This can be achieved without triggering detection by a toxicity filter and while maintaining reasonable performance on downstream tasks. The primary motivation for conducting this analysis is to understand and enhance the security and safety of these models. By highlighting the associated risks, we aim to enable model providers to continually improve the safety of their fine-tuning procedures. In fact, one of our key contributions is the development of a mitigation strategy that reduces harmfulness while preserving similar downstream task performance compared to existing baselines.

Ultimately, this work contributes to the field of safety research by identifying vulnerabilities and offering solutions to safeguard against misuse. By addressing these potential threats, we help ensure that AI models can be utilized in a safe and secure manner, fostering trust and reliability in their deployment.

D

Appendices for "Risks and Benefits of Open-Source Generative AI"

Contents

D.1 Further details on training, evaluation and deployment

Model training (1) processes can be grouped into three distinct stages:

1. *Pre-training*, where a model is exposed to large-scale datasets composed of trillions of tokens of data, typically scraped from the internet and usually uncurated. The goal is for the model to see a diversity of data, and through that process develop fundamental skills (e.g., grammar, vocabulary, text structure) and broad knowledge [Gao et al., 2020, Radford et al., 2019]. An example of a commonly used open source dataset for pre-training LLMs such as LLaMA or GPT-J is The Pile which combines 22 smaller datasets into a

diverse 825Gb text dataset Gao et al. [2020], Touvron et al. [2023], Wang and Komatsuzaki [2021].

2. *Supervised fine-tuning (SFT)*, which is intended to correct for data quality issues in pre-training datasets. Usually, a much smaller amount of high quality data is used to improve model performance. Several works observe that at this stage the quality of the data used is essential to the downstream performance of the models [Zhou et al., 2024, Ouyang et al., 2022, Touvron et al., 2023, Team et al., 2023], with the authors of LLaMA-2 pointing out that *"by setting aside millions of examples from third-party datasets and using fewer but higher-quality examples from our own vendor-based annotation efforts, [their] results notably improved."* [Touvron et al., 2023].

3. *Alignment*, which is used to create an application-specific version of the foundation model (e.g., a chatbot or translation model). Reinforcement Learning with Human Feedback (RLHF) or Direct Preference Optimisation (DPO) [Ouyang et al., 2022, Touvron et al., 2023] is used to create a model that follows instructions and is better-aligned with human preferences. With RLHF, a dataset of human preferences over model outputs is used to train a Reward model, which in turn is used with a reinforcement learning algorithm (e.g., PPO; Schulman et al., 2017) to align the LLM. RLHF is not used in models released prior to 2022 [Brown et al., 2020, Xue et al., 2020, Smith et al., 2022], and it is unclear whether the RLHF is used in models such as PaLM-2 [Anil et al., 2023].

Once trained, models are usually evaluated (2) on openly available evaluation datasets such as MMLU or NaturalQuestions [Hendrycks et al., 2020, Kwiatkowski et al., 2019] as well as curated benchmarks such as HELM, BigBench EleutherAI's Evaluation Harness [Liang et al., 2022, Srivastava et al., 2022, Gao et al., 2023]. Some models are also evaluated on proprietary datasets held internally by developers, potentially by holding out some of the SFT/RLHF data from the training process [Touvron et al., 2023]. However, there is little publicly available information on

how this is implemented, and few details are shared about the composition of such datasets. On top of utility-based benchmarking, developers sometimes create safety evaluation mechanisms to proactively stress-test the outputs of the model. These include human-annotated safety evaluation datasets (e.g., through creating adversarial prompts), as well as automatic safety evaluation algorithms [Touvron et al., 2023, Yuan et al., 2023]. They are typically the result of applying techniques such as red teaming. Finally, at the deployment stage (3), content can be generated by running the inference code with the associated model weights.

D.2 Full Taxonomy Tables

Important disclaimer: Table D.3 focuses on component openness in model pipelines, not reproducibility. GLM-130B and Falcon provide detailed training procedures, unlike GPT-4, yet those are all classified as C1 due to unreleased pre-training code. A full reproducibility assessment falls beyond this report's scope.

Table D.1: License Openness Taxonomy: categorization of commonly used licenses in a variety of relevant open source criteria, and resulting code and data openness categories.

License	Research	Commercial Purposes	Modify as Desired	Copyright derivative work	Other license for derivative	Final score	Code Openness	Data Openness
MIT/Mod. MIT	Y	Y	Y	Y	Y	5 (Restriction free)	C5	D5
Apache 2.0	Y	Y	Y	Y	Y	5 (Restriction free)	C5	D5
Common Crawl (ComCrawl)	Y	Y	Y	Y	Y	5 (Restriction free)	C5	D5
BSD-3	Y	Y	Y	Y	Y	5 (Restriction free)	C5	D5
RAIL	Y	Y	Y	Y	N	4 (Slightly restrictive)	C4	D4
LLaMA-2	Y	Y[1]	N	Y	N	3 (Moderately restrictive)	C3	D3
ODC-By	Y	Y	Y	Y	N	4 (Slightly restrictive)	N/A	D4
CodeT5 Data	Y	Y	Y	Y	N	4 (Slightly restrictive)	N/A	D4
RedPajama Data (Full)	Y	Y	Y	Y	N	4 (Slightly restrictive)	N/A	D4
OPT Data	Y	N	N	N	N	1 (Highly restrictive)	N/A	D3
GLM-130B Data	Y	N	N	N	N	1 (Highly restrictive)	N/A	D3
Falcon-180B Data	Y	Y	Y	Y	Y	5 (Restriction free)	N/A	D5

Table D.2: Model Information: table containing the basic information about each of the models classified under the openness taxonomy. Developers highlighted in purple correspond to companies, in pink are non-profit entities, and in light blue are government institutes. All data accessed on 28th of December 2023.

Model	Developer	Largest Model Size (params)	Release Date	Impact Metrics		
				ChatBot Arena Elo Rating	Google Scholar Citations	HuggingFace Downloads Last Month
GPT-2	OpenAI	1.5B	02/2019	N/A	8,015	17,984,300
T5	Google	11B	10/2019	873	12,162	3,295,844
GPT-3	OpenAI	175B	05/2020	N/A	18,759	N/A
mT5	Google	13B	10/2020	N/A	1,439	631,429
GPT-Neo	EleutherAI	2.7B	03/2021	N/A	N/A	242,580
GPT-J-6B	EleutherAI	6B	06/2021	N/A	465	95,620
CodeT5	Salesforce	16B	09/2021	N/A	703	23,549
Megatron-Turing	Microsoft, NVIDIA	530B	10/2021	N/A	379	N/A
Anthropic LM	Anthropic	52B	12/2021	N/A	70	N/A
ERNIE 3.0	Baidu	260B	12/2021	N/A	248	728
Gopher	DeepMind	280B	12/2021	N/A	598	N/A
GLaM	Google	1.2T	12/2021	N/A	255	N/A
XGLM	Meta	7.5B	12/2021	N/A	79	12,884
FairSeq Dense	Meta	13B	12/2021	N/A	34	6,129
LaMDA	Google	127B	01/2022	N/A	819	N/A
GPT-NeoX-20B	EleutherAI	20B	02/2022	N/A	364	37,122
PolyCoder	Carnegie Mellon	2.7B	02/2022	N/A	259	554
Chinchilla	DeepMind	70B	03/2022	N/A	245	N/A
PaLM	Google	540B	04/2022	1,004	2,342	N/A
OPT	Meta	175B	05/2022	N/A	1,105	191,115
UL2	Google	20B	05/2022	N/A	99	20,731
BLOOM	Big Science	176B	05/2022	N/A	814	1,172,142
GLM-130B	Tsinghua University	130B	10/2022	N/A	129	345
Pythia	EleutherAI	12B	12/2022	896	195	55,398
Anthropic 175B LM	Anthropic	175B	02/2023	N/A	55	N/A
LLaMA	Meta	13B	02/2023	800	2,793	N/A
GPT-4	OpenAI	N/A	03/2023	1,243	308	N/A
Claude	Anthropic	N/A	03/2023	1,149	N/A	N/A
Cerebras-GPT	Cerebras	13B	03/2023	N/A	23	124,561
Stable LM	Stability AI	7B	04/2023	844	N/A	15,282
PaLM-2	Google	N/A	05/2023	N/A	372	N/A
OpenLLaMA	UC Berkeley	13B	06/2023	N/A	N/A	58,991
Claude-2	Anthropic	N/A	07/2023	1,131	N/A	N/A
LLaMA-2	Meta	70B	07/2023	1,077	1,197	742,238
Falcon	TII	180B	09/2023	1,035	65	1,341,297
GPT-3.5-turbo	OpenAI	N/A	09/2023	1,117	N/A	N/A
Mistral-7B	Mistral AI	7B	10/2023	1,023	15	510,471
Grok-1	xAI	N/A	11/2023	N/A	N/A	N/A
Phi-2	Microsoft	2.7B	11/2023	N/A	N/A	85,200
Gemini	Google DeepMind	N/A	12/2023	1,111	N/A	N/A

Model	(1) Training						(2) Evaluation				(3) Deployment	
	Code			Data			Code		Data		Code	Data
	Pre-Training	Fine-tuning	Alignment	Pre-Training	Supervised FT	Alignment	General Eval	Automatic Safety Eval	Utility Benchmarks	Safety Eval Datasets	Inference	Model Architecture and Weights
GPT-2	C1	N/A	N/A	D1	N/A	N/A	C1	N/A	D1	N/A	C5 (Mod. MIT)	D5 (Mod. MIT)
T5	C5 (Apache 2.0)	C5 (Apache 2.0)	N/A	D4 (ODC-By)	N/A	N/A	C5 (Apache 2.0)	N/A	N/A	N/A	C5 (Apache 2.0)	D5 (Apache 2.0)
GPT-3	C1	C1	N/A	D1	N/A	N/A	C1	N/A	D1	N/A	C1	D2
mT5	C5 (Apache 2.0)	C5 (Apache 2.0)	N/A	D4 (ODC-By)	N/A	N/A	C5 (Apache 2.0)	N/A	N/A	N/A	C5 (Apache 2.0)	D5 (Apache 2.0)
GPT-Neo	C5 (MIT)	C5 (MIT)	N/A	D5 (MIT)	N/A	N/A	C5 (MIT)	N/A	N/A	N/A	C5 (MIT)	D5 (MIT)
GPT-J-6B	C5 (Apache 2.0)	C5 (Apache 2.0)	N/A	D5 (MIT)	N/A	N/A	C5 (Apache 2.0)	N/A	N/A	N/A	C5 (Apache 2.0)	D5 (Apache 2.0)
CodeT5	C5 (BSD-3)	C5 (BSD-3)	N/A	D4 (CodeT5)	N/A	N/A	C5 (BSD-3)	N/A	N/A	N/A	C5 (BSD-3)	D5 (Apache 2.0)
Megatron-Turing	C1	N/A	N/A	D1	N/A	N/A	C1	N/A	N/A	N/A	C1	D1
Anthropic LM	C1	C1	N/A	D1	N/A	D5 (MIT)	C1	N/A	N/A	D5 (MIT)	C1	D1
ERNIE 3.0	C1	C1	N/A	D1	N/A	N/A	C1	N/A	N/A	N/A	C1	D1
Gopher	C1	C1	N/A	D1	N/A	N/A	C1	N/A	D1	D1	C1	D1
GLaM	C1	N/A	N/A	D1	N/A	N/A	C1	N/A	N/A	N/A	C1	D1
XGLM	C5 (MIT)	N/A	N/A	D5 (ComCra	N/A	N/A	C5 (MIT)	C1	N/A	D5 (Public datasets)	C5 (MIT)	D5 (MIT)
FairSeq Dense	C5 (MIT)	N/A	N/A	D5 (ComCra	N/A	N/A	N/A	N/A	N/A	N/A	C5 (MIT)	D5 (MIT)
LaMDA	C1	C1	N/A	D1	D1	N/A	C1	C1	D1	D1	C1	D1
GPT-NeoX-20B	C5 (Apache 2.0)	N/A	N/A	D5 (MIT)	N/A	N/A	C5 (Apache 2.0)	N/A	N/A	N/A	C5 (Apache 2.0)	D5 (Apache 2.0)
Poly-Coder	C5 (MIT)	N/A	N/A	? (D3 or D4)	N/A	N/A	C5 (MIT)	N/A	N/A	N/A	C5 (CC BY-SA-4.0)	D5 (CC BY-SA-4.0)
Chinchilla	C1	C1	N/A	D1	N/A	N/A	C1	N/A	N/A	N/A	C1	D1
PaLM	C1	C1	N/A	D1	D1	N/A	C1	N/A	N/A	N/A	C1	D1
OPT	C5 (MIT)	N/A	N/A	?	N/A	N/A	C1	N/A	N/A	N/A	C5 (MIT)	D3 (OPT Data)
UL2	C5 (Apache 2.0)	C5 (Apache 2.0)	N/A	D4 (ODC-By)	N/A	N/A	C5 (Apache 2.0)	N/A	N/A	N/A	C5 (Apache 2.0)	D5 (Apache 2.0)
BLOOM	C5 (Apache 2.0)	?	N/A	? (D3 or D4)	D5 (Apache 2.0)	N/A	C5 (Apache 2.0)	N/A	N/A	N/A	C5 (Apache 2.0)	D4 (RAIL)
GLM-130B	C1	N/A	N/A	D1	N/A	N/A	C5 (Apache 2.0)	N/A	N/A	N/A	C5 (Apache 2.0)	D3 (GLM-130B Data)
Pythia	C5 (Apache 2.0)	N/A	N/A	D5 (MIT)	N/A	N/A	C5 (Apache 2.0)	N/A	N/A	N/A	C5 (Apache 2.0)	D5 (Apache 2.0)
Anthropic 175B	C1	C1	C1	D1	D1	D1	C1	N/A	N/A	D1	C1	D1
LLaMA	C1	N/A	N/A	? (likely D5)	N/A	N/A	C1	C1	N/A	D5 (Publicly available)	C4 (GNU GPL)	D3 (LLaMA)
GPT-4	C1	C1	C1	D1	D1	D1	C5 (MIT)	N/A	D1	D1	C1	D2
Claude	C1	C1	C1	D1	D1	D1	C1	N/A	N/A	D1	C1	D1
Cerebras-GPT	C5 (Apache 2.0)	N/A	N/A	D5 (MIT)	N/A	N/A	C5 (Publicly available)	N/A	N/A	N/A	C5 (Apache 2.0)	D5 (Apache 2.0)

Stable LM	C1	C1	N/A	D4 (CC BY-SA-4.0)	D1	N/A	C1	N/A	N/A	N/A	C5 (CC BY-SA-4.0)	D5 (CC BY-SA-4.0)
PaLM-2	C1	N/A	N/A	D1	N/A	N/A	C1	N/A	N/A	D5 (Publicly available)	C1	D1
OpenLLaMA	C5 (Apache 2.0)	N/A	N/A	D4 (RedPajama Data)	N/A	N/A	C5 (Apache 2.0)	N/A	N/A	N/A	C5 (Apache 2.0)	D5 (Apache 2.0)
Claude-2	C1	C1	C1	D1	D1	D1	C1	C1	D1	D1	C1	D2
LLaMA-2	C1	C1	C1	D1	D1	D1	C1	N/A	N/A	D1	C3 (LLaMA-2)	D3 (LLaMA-2)
Falcon	C1	C1	C1	D4 (ODC-By)	D1	D1	C1	N/A	N/A	N/A	C5 (Apache 2.0)	D5 (Falcon-180B Data)
GPT-3.5-turbo	C1	C1	C1	D1	D1	D1	C5 (MIT)	N/A	D1	D1	C1	D2
Mistral-7B	C1	C1	N/A	D1	D1	N/A	C1	N/A	N/A	N/A	C5 (Apache 2.0)	D5 (Apache 2.0)
Grok-1	C1	C1	?	D1	D1	?	C1	N/A	N/A	N/A	C1	D2
Phi-2	C1	N/A	N/A	D1	N/A	N/A	C1	N/A	N/A	N/A	C5 (MIT)	D5 (MIT)
Gemini	C1	C1	C1	D1	D1	D1	C1	C1	D1	D1	C1	D2

Table D.3: Model Pipeline Classification: openness classification of components of the training, evaluation and deployment pipelines of currently available large language models. "N/A" in this table corresponds to "Not Applicable", whereas "?" means the information is not publicly available. If a model has more than one source of code or data source for a given component, the final classification is taken by considering the strictest license. For conciseness, in the table header we use "FT" as a stand in for "Fine-Tuning".

D.2.1 Open-source GenAI Governance

The urgency of assaying the risks and opportunities of open-source GenAI is further underscored by recent regulatory developments around the world. The EU AI Act [European Parliament, 2021] has since matured into the world's first comprehensive and enforcable regulatory framework on AI governance, and is set to introduce specific obligations to providers and deployers (users) of open-source general purpose AI models, and systems built thereon. President Biden's Executive Order on AI [House, 2023] is thought to significantly affect open-source developers also, and, of course, China's approach to AI regulation continuous to be governed by state intervention [Cyberspace Administration of China, Translate, 2023]. While these regulations may carve in stone certain aspects of future open-source GenAI governance, fundamental questions surrounding concepts such as *general-purpose models of systemic risk* (EU AI Act) or *dual-use foundation models* (Biden's EO) remain up to debate. Importantly, particularly in the case of the EU AI Act, many regulations have been designed to be adaptable in line with future technological progress. Our debate therefore remains highly relevant to open-source GenAI governance.

Recent years have seen the emergence of regulatory frameworks across the world that are already, or will soon, interact with the real-world governance of open-source Gen AI models. These efforts have been accompanied by increasing efforts at streamlining on the international stage, starting from 2023 G7 Hiroshima Summit and the Bletchley declaration [The UK Government, 2023], and culminating in various national and transnational initiatives forming a network of AI safety institutes in the United Kingdom (UK), United States of America (US), European Union (EU), and elsewhere. Prior to the launch of ChatGPT on November 29th, 2023, such regulations were mostly targeted at (i) containing the spread of *deepfakes* in order to safeguard election integrity – e.g., the EU's 2022 amendments to the Digital Services Act –, or (ii) to exercise wider information control against the spread of "rumors", such as the Chinese government's 2019 *Regulations on the Administration of Online Audio and Video Information Services* [Sheehan]. At the same time, the economic benefits of open-source AI models and systems have been almost unanimously recognized across the world. The launch of ChatGPT, and its rapid adoption among users worldwide, led policymakers to focus on general-purpose AI (GPAI) regulation.

The EU AI Act

The first *comprehensive* regulatory framework governing general-purpose AI – including provisions for open-source Gen AI – may be the EU AI Act, which is expected to come into full force by 2026 [European Parliament, 2021]. The legislation will apply to anyone putting AI services, or their outputs, on the EU market for professional purposes, while exempting recreational or academic use, as well as matters relevant to national security. It guards providers of open-source general-purpose models against risks emanating from downstream use by limiting the providers' responsibilities to a number of transparency obligations. These

transparency obligations include the high-level documentation of training data provenance, as well a specification of intended use cases. Entities deploying Gen AI *deepfakes* are required to disclose their AI-generated nature. These requirements will apply to small business owners to a lesser degree. While comprehensive, the EU AI Act will not apply to recreational or research use and will be superseded by the EU member states' individual national security interests. Open-source Gen AI providers may face additional procedures and obligations if their models are classified as *general-purpose AI (GPAI) models of systemic risk*, an intentionally vaguely defined criterion that will be adapted as technology progresses. Importantly, the EU AI Act, as perhaps the EU's first transnational legislation, explicitly affirms the economic benefits of open-source AI.

Biden's Executive Order

President Biden's 2023 *Executive Order (EO) on Safe, Secure, and Trustworthy Artificial Intelligence* [House, 2023] continues to follow a *"soft law"* approach of earlier EOs, largely trading enforceable regulation for voluntary industry commitments [PricewaterhouseCoopers, 2024]. Safety and security measures surrounding AI technology include requirements for developers to share red-teaming results with the US federal government, and for companies working on "dual-use" foundation models (*i.e.*, systems with civilian and military applications) and/or with large compute clusters to provide regular activity reports. The National Institute of Standards and Technology (NIST) is set up to play a key role in developing standards for secure and safe AI. Instead of placing hard restrictions on the use of certain AI technology (as the EU AI Act explicitly does), Biden's EO focuses on promoting best practices, evaluations, and standard development across a wide variety of aspects including security and risk mitigation. For example, it includes references to biological weapons, AI-generated content watermarking, and labor market impacts, and, additionally, measures for attracting foreign national AI talent through streamlining visa procedures and by providing assistance to small businesses and developers. National security interests are also formulated, including the reporting of foreign users of US Infrastructure as a Service (IaaS) products, as well as promoting the development of AI-driven tools to detect cyber vulnerabilities.

China's Gen AI Legislation

The earliest legal framework specifically targeting Gen AI models and systems, the Chinese government's *Provisional Administrative Measures of Generative Artificial Intelligence Services (Generative AI Measures)* [Cyberspace Administration of China, Translate, 2023], came into force in China in August 2023. These regulations pose strict obligations on providers of Gen AI, ranging from outcome-driven provisions (e.g., requiring generative AI services to not produce illegal or untruthful content) to provenance obligations on training data and model weights, and measures targeted to protect intellectual property and privacy rights [Chong et al., 2023]. From the point of view of open-source model developers, the inability to predict future downstream use of models and systems provided introduces legal risks that require

regulatory containment. Although open-source Gen AI plays a significant role in the Chinese economy, however, these regulations do not seem to target open-source (GP)AI models specifically [Asia Society, 2024].

The Middle East

Saudi Arabia. In August 2019, as part of Saudi Arabia's Vision 2030 introduced by Crown Prince Mohammed Bin Salman, the Saudi Data and AI Authority (SDAIA) was established by a royal decree. SDAIA aims to advance this vision, with the National Center for AI serving as a key component. Saudi Arabia, through SDAIA, has adapted and released its first version of AI ethics in September 2023 [Data and Authority, 2023]. The document outlines Saudi's stance on AI risks, categorized from minimal to unacceptable risks with a comprehensive risk management plan covering data, algorithms, compliance, operations, legality, and regulatory risks. The AI ethics strongly supports the transparent development and deployment of AI , reflecting that *"transparent and explainable algorithms ensure that stakeholders affected by AI systems [...] are fully informed when an outcome is processed by the AI"*. Moreover, SDAIA has quickly embraced the generative AI wave. In collaboration with NVIDIA, SDAIA developed "Allam" [Gazette, 2024], Saudi Arabia's first national-level LLM model, an Arabic LLM designed to provide summaries and answer questions, drawing information from cross-checked online sources. While Allam was closed source and only a beta version interface is accessible, there are still several pieces of evidences that Saudi Arabia is in favor of open-source. For instance, the Digital Government Authority [Digital Government Authority] issued free and open-source government software licenses to 6 government agencies in 2022. This entails reviewing and publishing the source code "in a way that opens the field of cooperation and unified standards among government agencies". The general directions with the laid down compliance regulations, stated principles, and open source government suggest that Saudi Arabia is in favor of open source.

United Arab Emirates (UAE). In October 2017, the UAE Government launched the *"UAE Artificial Intelligence Strategy"* [UAE, 2023], spanning sectors from education to space. Shortly after, His Excellency, Omar Al Olama became the world's first AI minister. The UAE has been in favor of open-source in their policies, for instance, as stated in the strategy *"Objective 7: Provide the data and the supporting infrastructure essential to become a test bed for AI"* and that *"The UAE has an opportunity to become a leader in available open data for training and developing AI systems"*. Moreover, the strategy states that *"The UAE's ambition is to create a data-sharing program, providing shared open and standardized AI-ready data, collected through a consistent data standard"*. More recently, the UAE through the Technology Innovation Institute (TII) has open-sourced its LLM Falcon [TII, 2023], including its 180B parameter version, for both research and commercial use [Reuters, 2023]. This all indicates the UAE's positive take towards open-source models.

AI Regulation Efforts in Other Countries

In 2019, the Organization for Economic Co-operation and Development (OECD) introduced their AI Principles, a recommendation by the council on general-purpose AI. These principles were ratified by the G20 council, and have been adopted by at least 42 of the organization's participating countries [OECD, Australian Government, 2024].

Some countries have on-going legislation efforts or have issued policies specifically on Gen AI, addressing mainly sector-based issues. These include Australia [Australian Government], Canada [of New Zealand], New Zealand [Kaldestad, 2023], Norway [Council, 2023], Singapore [Monetary Authority of Singapore, Infocomm], among others. India has published working papers on the issue of AI and enacted the Digital Personal Data Protection Act in 2023 tackling privacy issues related to Gen AI [Kapoor et al., 2024] – it is yet to regulate on general-purpose Gen AI and the open sourcing of models. Brazil is working on two main legislative proposals to regulate AI, one inspired in the US framework (Bill no. 21, from 2021) and another inspired on the EU framework (Bill No. 2338, from 2023), yet these do not have provisions for open-source Gen AI models. A few other countries are in the process of running public consultations on how to regulate generative AI, such as the case of Chile [MinCiencia] and Uruguay [Agencia de Gobierno].

Bibliography

[1] Josh Achiam, Steven Adler, Sandhini Agarwal, Lama Ahmad, Ilge Akkaya, Florencia Leoni Aleman, Diogo Almeida, Janko Altenschmidt, Sam Altman, Shyamal Anadkat, et al. Gpt-4 technical report. *arXiv pre-print arxiv:2303.08774*, 2023.

[2] AdeptTeam. ACT-1: Transformer for actions. 2022.

[3] Agencia de Gobierno. Mesa de diálogo "Inteligencia Artificial: oportunidades y desafíos de una estrategia nacional". *Agencia de Gobierno Electrónico y Sociedad de la Información y del Conocimiento*.

[4] Orevaoghene Ahia, Sachin Kumar, Hila Gonen, Jungo Kasai, David R Mortensen, Noah A Smith, and Yulia Tsvetkov. Do all languages cost the same? Tokenization in the era of commercial language models. In *Empirical Methods in Natural Language Processing*, 2023.

[5] Microsoft Research AI4Science and Microsoft Azure Quantum. The impact of large language models on scientific discovery: a preliminary study using GPT-4. *arXiv pre-print arxiv:2311.07361*, 2023.

[6] AI@Meta. Llama 3 model card. 2024. URL `https://github.com/meta-llama/llama3/blob/main/MODEL_CARD.md`.

[7] Naveed Akhtar, Ajmal Mian, Navid Kardan, and Mubarak Shah. Advances in adversarial attacks and defenses in computer vision: A survey. *IEEE Access*, 2021.

[8] Jide Alaga and Jonas Schuett. Coordinated pausing: An evaluation-based coordination scheme for frontier AI developers. *arXiv pre-print arxiv:2310.00374*, 2023.

[9] Fares Alahdab. Potential impact of large language models on academic writing. *BMJ Evidence-Based Medicine*, 2023.

[10] Motasem Alfarra, Adel Bibi, Philip H. S. Torr, and Bernard Ghanem. Data dependent randomized smoothing. In *Uncertainty in Artificial Intelligence*, pages 64–74, 2022.

[11] Salman Alsubaihi, Adel Bibi, Modar Alfadly, Abdullah Hamdi, and Bernard Ghanem. Expected tight bounds for robust training. *arXiv pre-print arxiv:1905.12418*, 2019.

[12] Amazon. AWS expands Amazon Bedrock with additional foundation models, new model provider, and advanced capability to help customers build generative AI applications. 2023.

[13] Dario Amodei, Chris Olah, Jacob Steinhardt, Paul Christiano, John Schulman, and Dan Mané. Concrete problems in ai safety. *arXiv pre-print arxiv:1606.06565*, 2016.

[14] Maksym Andriushchenko, Francesco Croce, and Nicolas Flammarion. Jailbreaking leading safety-aligned llms with simple adaptive attacks. *arXiv pre-print arxiv:2404.02151*, 2024.

[15] Cem Anil, James Lucas, and Roger Grosse. Sorting out lipschitz function approximation. In *International Conference on Machine Learning*, pages 291–301, 2019.

[16] Cem Anil, Esin Durmus, Mrinank Sharma, Joe Benton, Sandipan Kundu, Joshua Batson, Nina Rimsky, Meg Tong, Jesse Mu, Daniel Ford, et al. Many-shot jailbreaking, 2024.

[17] Rohan Anil, Andrew M Dai, Orhan Firat, Melvin Johnson, Dmitry Lepikhin, Alexandre Passos, Siamak Shakeri, Emanuel Taropa, Paige Bailey, Zhifeng Chen, et al. Palm 2 technical report. *arXiv pre-print arxiv:2305.10403*, 2023.

[18] Anthropic. Anthropic's responsible scaling policy. 2023.

[19] Lora Aroyo, Alex S. Taylor, Mark Diaz, Christopher M. Homan, Alicia Parrish, Greg Serapio-Garcia, Vinodkumar Prabhakaran, and Ding Wang. DICES Dataset: Diversity in conversational AI evaluation for safety. *arXiv pre-print arxiv:2306.11247*, 2023.

[20] Asia Society. China's Emerging Approach to Regulating General-Purpose Artificial Intelligence: Balancing Innovation and Control | Asia Society, 2024. URL https://asiasociety.org/policy-institute/chinas-emerging-approach-regulating-general-purpose-artificial-intelligence-balancing-innovation-and.

[21] AsuharietYgvar. AppleNeuralHash2ONNX: Reverse-engineered Apple NeuralHash, in ONNX and Python, 2021. URL https://www.reddit.com/r/MachineLearning/comments/p6hsoh/p_appleneuralhash2onnx_reverseengineered_apple/.

[22] Anish Athalye, Logan Engstrom, Andrew Ilyas, and Kevin Kwok. Synthesizing robust adversarial examples. In *International Conference on Machine Learning*, pages 284–293, 2018.

[23] Australian Government. Interim guidance on government use of public generative AI tools. URL https://architecture.digital.gov.au/guidance-generative-ai.

[24] Australian Government. Australian Framework for Generative Artificial Intelligence (AI) in Schools. 2024.

[25] Edward W Ayers, Francisco Eiras, Majd Hawasly, and Iain Whiteside. Parot: A practical framework for robust deep neural network training. In *NASA Formal Methods Symposium*, pages 63–84, 2020.

[26] Yuntao Bai, Andy Jones, Kamal Ndousse, Amanda Askell, Anna Chen, Nova DasSarma, Dawn Drain, Stanislav Fort, Deep Ganguli, Tom Henighan, et al. Training a helpful and harmless assistant with reinforcement learning from human feedback. *arXiv pre-print arxiv:2204.05862*, 2022.

[27] Yuntao Bai, Saurav Kadavath, Sandipan Kundu, Amanda Askell, Jackson Kernion, Andy Jones, Anna Chen, Anna Goldie, Azalia Mirhoseini, Cameron McKinnon, et al. Constitutional ai: Harmlessness from ai feedback. *arXiv pre-print arxiv:2212.08073*, 2022.

[28] Maria-Florina Balcan, Travis Dick, Tuomas Sandholm, and Ellen Vitercik. Learning to branch. In *International Conference on Machine Learning*, pages 344–353, 2018.

[29] Lucas Bandarkar, Davis Liang, Benjamin Muller, Mikel Artetxe, Satya Narayan Shukla, Donald Husa, Naman Goyal, Abhinandan Krishnan, Luke Zettlemoyer, and Madian Khabsa. The Belebele benchmark: a parallel reading comprehension dataset in 122 language variants. *arXiv pre-print arxiv:2308.16884*, 2023.

[30] Yejin Bang, Samuel Cahyawijaya, Nayeon Lee, Wenliang Dai, Dan Su, Bryan Wilie, Holy Lovenia, Ziwei Ji, Tiezheng Yu, Willy Chung, et al. A multitask, multilingual, multimodal evaluation of chatgpt on reasoning, hallucination, and interactivity. *arXiv pre-print arxiv:2302.04023*, 2023.

[31] Federico Bianchi, Mirac Suzgun, Giuseppe Attanasio, Paul Röttger, Dan Jurafsky, Tatsunori Hashimoto, and James Zou. Safety-tuned llamas: Lessons from improving the safety of large language models that follow instructions. *arXiv pre-print arxiv:2309.07875*, 2023.

[32] Yonatan Bisk, Rowan Zellers, Jianfeng Gao, and Yejin Choi. Piqa: Reasoning about physical commonsense in natural language. In *AAAI Conference on Artificial Intelligence*, pages 7432–7439, 2020.

[33] Knut Blind, Mirko Böhm, Paula Grzegorzewska, Andrew Katz, Sachiko Muto, Sivan Pätsch, and Torben Schubert. The impact of Open Source Software and Hardware on technological independence, competitiveness and innovation in the EU economy. *European Commission, Brussels*, 2021.

[34] Rishi Bommasani, Drew A Hudson, Ehsan Adeli, Russ Altman, Simran Arora, Sydney von Arx, Michael S Bernstein, Jeannette Bohg, Antoine Bosselut, Emma Brunskill, et al. On the opportunities and risks of foundation models. *arXiv pre-print arxiv:2108.07258*, 2021.

[35] Rishi Bommasani, Sayash Kapoor, Kevin Klyman, Shayne Longpre, Ashwin Ramaswami, Daniel Zhang, Marietje Schaake, Daniel E. Ho, Arvind Narayanan, and Percy Liang. Considerations for governing open foundation models. 2023.

[36] Rishi Bommasani, Kevin Klyman, Shayne Longpre, Sayash Kapoor, Nestor Maslej, Betty Xiong, Daniel Zhang, and Percy Liang. Introducing the foundation model transparency index. *arXiv pre-print arxiv:2310.12941*, 2023.

[37] Matt Bornstein and Rajko Radovanovic. Supporting the open source AI community. *Andreessen Horowitz*, 2023.

[38] Houssem Ben Braiek and Foutse Khomh. Machine learning robustness: A primer. *arXiv pre-print arxiv:2404.00897*, 2024.

[39] Leo Breiman. Random forests. *Machine Learning*, pages 5–32, 2001.

[40] Tom Brown, Benjamin Mann, Nick Ryder, Melanie Subbiah, Jared D Kaplan, Prafulla Dhariwal, Arvind Neelakantan, Pranav Shyam, Girish Sastry, Amanda Askell, et al. Language models are few-shot learners. *Advances in Neural Information Processing Systems*, 2020.

[41] Erik Brynjolfsson, Danielle Li, and Lindsey R Raymond. Generative AI at work. Technical report, National Bureau of Economic Research, 2023.

[42] V Buhrmester, D Münch, and M Arens. Analysis of explainers of black box deep neural networks for computer vision: A survey. *arXiv pre-print arxiv:1911.12116*, 2019.

[43] Rudy Bunel. *Formal verification of neural networks*. PhD thesis, University of Oxford, 2019.

[44] Rudy Bunel, Ilker Turkaslan, Philip HS Torr, Pushmeet Kohli, and M Pawan Kumar. A unified view of piecewise linear neural network verification. In *Advances in Neural Information Processing Systems*, 2018.

[45] Rudy R Bunel, Ilker Turkaslan, Philip Torr, Pushmeet Kohli, and Pawan K Mudigonda. A unified view of piecewise linear neural network verification. *Advances in Neural Information Processing Systems*, 2018.

[46] Matt Burgess. Criminals have created their own ChatGPT clones. *Wired*, 2023.

[47] Collin Burns, Pavel Izmailov, Jan Hendrik Kirchner, Bowen Baker, Leo Gao, Leopold Aschenbrenner, Yining Chen, Adrien Ecoffet, Manas Joglekar, Jan Leike, et al. Weak-to-strong generalization: Eliciting strong capabilities with weak supervision. *arXiv pre-print arxiv:2312.09390*, 2023.

[48] Nicholas Carlini and David Wagner. Towards evaluating the robustness of neural networks. In *2017 IEEE Symposium on Security and Privacy*, pages 39–57, 2017.

[49] Nicholas Carlini, Daphne Ippolito, Matthew Jagielski, Katherine Lee, Florian Tramer, and Chiyuan Zhang. Quantifying memorization across neural language models. In *International Conference on Learning Representations*, 2022.

[50] Stephen Casper, Carson Ezell, Charlotte Siegmann, Noam Kolt, Taylor Lynn Curtis, Benjamin Bucknall, Andreas Haupt, Kevin Wei, Jérémy Scheurer, Marius Hobbhahn, et al. Black-box access is insufficient for rigorous AI audits. *arXiv pre-print arxiv:2401.14446*, 2024.

[51] Alan Chan, Carson Ezell, Max Kaufmann, Kevin Wei, Lewis Hammond, Herbie Bradley, Emma Bluemke, Nitarshan Rajkumar, David Krueger, Noam Kolt, Lennart Heim, and Markus Anderljung. Visibility into AI agents. *arXiv pre-print arxiv:2401.13138*, 2024.

[52] Patrick Chao, Alexander Robey, Edgar Dobriban, Hamed Hassani, George J Pappas, and Eric Wong. Jailbreaking black box large language models in twenty queries. *arXiv pre-print arxiv:2310.08419*, 2023.

[53] Hailin Chen, Fangkai Jiao, Xingxuan Li, Chengwei Qin, Mathieu Ravaut, Ruochen Zhao, Caiming Xiong, and Shafiq Joty. Chatgpt's one-year anniversary: Are open-source large language models catching up? *arXiv pre-print arxiv:2311.16989*, 2024.

[54] Yuyao Chen, Lu Lu, George Em Karniadakis, and Luca Dal Negro. Physics-informed neural networks for inverse problems in nano-optics and metamaterials. *Optics Express*, pages 11618–11633, 2020.

[55] Chih-Hong Cheng, Georg Nührenberg, and Harald Ruess. Maximum resilience of artificial neural networks. In *Automated Technology for Verification and Analysis: 15th International Symposium, ATVA 2017, Pune, India, October 3–6, 2017, Proceedings*, pages 251–268, 2017.

[56] Pranav Singh Chib and Pravendra Singh. Recent advancements in end-to-end autonomous driving using deep learning: A survey. *IEEE Transactions on Intelligent Vehicles*, 2023.

[57] Steven Chong, Edward Yau (HK), and Anna Gamvros. China finalises its Generative AI Regulation, 2023. URL `https://www.dataprotectionreport.com/2023/07/china-finalises-its-generative-ai-regulation/`.

[58] Paul Christiano, Buck Shlegeris, and Dario Amodei. Supervising strong learners by amplifying weak experts. *arXiv pre-print arxiv:1810.08575*, 2018.

[59] Christopher Clark, Kenton Lee, Ming-Wei Chang, Tom Kwiatkowski, Michael Collins, and Kristina Toutanova. Boolq: Exploring the surprising difficulty of natural yes/no questions. *arXiv pre-print arxiv:1905.10044*, 2019.

[60] Karl Cobbe, Vineet Kosaraju, Mohammad Bavarian, Mark Chen, Heewoo Jun, Lukasz Kaiser, Matthias Plappert, Jerry Tworek, Jacob Hilton, Reiichiro Nakano, Christopher Hesse, and John Schulman. Training verifiers to solve math word problems. *arXiv pre-print arxiv:2110.14168*, 2021.

[61] Jeremy M Cohen, Elan Rosenfeld, and J Zico Kolter. Certified adversarial robustness via randomized smoothing. In *International Conference in Machine Learning*, 2019.

[62] Together Computer. RedPajama: an Open Dataset for Training Large Language Models, 2023. URL `https://github.com/togethercomputer/RedPajama-Data`.

[63] Arthur Conmy, Augustine Mavor-Parker, Aengus Lynch, Stefan Heimersheim, and Adrià Garriga-Alonso. Towards automated circuit discovery for mechanistic interpretability. *Advances in Neural Information Processing Systems*, pages 16318–16352, 2023.

[64] Mike Conover, Matt Hayes, Ankit Mathur, Jianwei Xie, Jun Wan, Sam Shah, Ali Ghodsi, Patrick Wendell, Matei Zaharia, and Reynold Xin. Free dolly: Introducing the world's first truly open instruction-tuned llm, 2023. URL `https://www.databricks.com/blog/2023/04/12/dolly-first-open-commercially-viable-instruction-tuned-llm`.

[65] Grant Cooper. Examining science education in ChatGPT: An exploratory study of generative artificial intelligence. *Journal of Science Education and Technology*, 2023.

[66] Corinna Cortes. Support-vector networks. *Machine Learning*, 1995.

[67] Norwegian Consumer Council. Ghost in the machine: Addressing the consumer harms of generative ai. *Norwegian Consumer Council*, 2023.

[68] Joseph Cox. Facebook's powerful large language model leaks online. *Vice*, 2023.

[69] Francesco Croce and Matthias Hein. Minimally distorted adversarial examples with a fast adaptive boundary attack. In *International Conference on Machine Learning*, pages 2196–2205, 2020.

[70] Francesco Croce and Matthias Hein. Reliable evaluation of adversarial robustness with an ensemble of diverse parameter-free attacks. In *International Conference on Machine Learning*, pages 2206–2216, 2020.

[71] Francesco Croce, Maksym Andriushchenko, Vikash Sehwag, Edoardo Debenedetti, Nicolas Flammarion, Mung Chiang, Prateek Mittal, and Matthias Hein. Robustbench: a standardized adversarial robustness benchmark. *arXiv pre-print arxiv:2010.09670*, 2020.

[72] Aron Culotta and Nicholas Mattei. Use open source for safer generative AI experiments. *MIT Sloan Management Review*, 2023.

[73] Anthony Cuthbertson. Elon Musk's new AI bot will help you make cocaine which proves it's 'based' and 'rebellious'. *The Independent*, 2023.

[74] Cyberspace Administration of China. (translated) interim measures for the management of generative artificial intelligence services. URL `https://www.cac.gov.cn/2023-07/13/c_1690898327029107.htm`.

[75] Yi Dai, Hao Lang, Kaisheng Zeng, Fei Huang, and Yongbin Li. Exploring large language models for multi-modal out-of-distribution detection. *arXiv pre-print arxiv:2310.08027*, 2023.

[76] SDAIA: Saudi Data and AI Authority. AI ethics principles, 2023. URL `https://sdaia.gov.sa/en/SDAIA/about/Documents/ai-principles.pdf`.

[77] Alessandro De Palma, Rudy Bunel, Alban Desmaison, Krishnamurthy Dvijotham, Pushmeet Kohli, Philip HS Torr, and M Pawan Kumar. Improved branch and bound for neural network verification via lagrangian decomposition. *arXiv pre-print arxiv:2104.06718*, 2021.

[78] Fabrizio Dell'Acqua, Edward McFowland, Ethan R Mollick, Hila Lifshitz-Assaf, Katherine Kellogg, Saran Rajendran, Lisa Krayer, François Candelon, and Karim R Lakhani. Navigating the jagged technological frontier: Field experimental evidence of the effects of AI on knowledge worker productivity and quality. *Harvard Business School Technology and Operations Management Unit Working Paper*, 2023.

[79] Jia Deng, Wei Dong, Richard Socher, Li-Jia Li, Kai Li, and Li Fei-Fei. Imagenet: A large-scale hierarchical image database. In *IEEE Conference on Computer Vision and Pattern Recognition*, 2009.

[80] Mingkai Deng, Jianyu Wang, Cheng-Ping Hsieh, Yihan Wang, Han Guo, Tianmin Shu, Meng Song, Eric P Xing, and Zhiting Hu. Rlprompt: Optimizing discrete text prompts with reinforcement learning. *arXiv pre-print arxiv:2205.12548*, 2022.

[81] Yue Deng, Wenxuan Zhang, Sinno Jialin Pan, and Lidong Bing. Multilingual jailbreak challenges in large language models. *arXiv pre-print arxiv:2310.06474*, 2023.

[82] Leon Derczynski, Hannah Rose Kirk, Vidhisha Balachandran, Sachin Kumar, Yulia Tsvetkov, M. R. Leiser, and Saif Mohammad. Assessing language model deployment with risk cards. *arXiv pre-print arxiv:2303.18190*, 2023.

[83] Digital Government Authority. The Digital Government Authority issues free and open-source government software licenses to 6 government agencies. URL `https://dga.gov.sa/en/node/297`.

[84] Yinpeng Dong, Fangzhou Liao, Tianyu Pang, Hang Su, Jun Zhu, Xiaolin Hu, and Jianguo Li. Boosting adversarial attacks with momentum. In *IEEE Conference on Computer Vision and Pattern Recognition*, pages 9185–9193, 2018.

[85] Andrew Du, Bo Chen, Tat-Jun Chin, Yee Wei Law, Michele Sasdelli, Ramesh Rajasegaran, and Dillon Campbell. Physical adversarial attacks on an aerial imagery object detector. In *IEEE/CVF Winter Conference on Applications of Computer Vision*, pages 1796–1806, 2022.

[86] Krishnamurthy Dvijotham, Robert Stanforth, Sven Gowal, Timothy A Mann, and Pushmeet Kohli. A dual approach to scalable verification of deep networks. In *Uncertainty in Artificial Intelligence*, 2018.

[87] Krishnamurthy Dj Dvijotham, Jamie Hayes, Borja Balle, Zico Kolter, Chongli Qin, András György, Kai Xiao, Sven Gowal, and Pushmeet Kohli. A framework for robustness certification of smoothed classifiers using f-divergences. In *International Conference on Learning Representations*, 2020.

[88] Ruediger Ehlers. Formal verification of piece-wise linear feed-forward neural networks. In *International Symposium on Automated Technology for Verification and Analysis*, pages 269–286, 2017.

[89] Francisco Eiras, Motasem Alfarra, M Pawan Kumar, Philip HS Torr, Puneet K Dokania, Bernard Ghanem, and Adel Bibi. Ancer: Anisotropic certification via sample-wise volume maximization. *Transactions of Machine Learning Research*, 2022.

[90] Francisco Eiras, Adel Bibi, Rudy R Bunel, Krishnamurthy Dj Dvijotham, Philip Torr, and M Pawan Kumar. Efficient error certification for Physics-informed neural networks. In *International Conference on Machine Learning*, 2024.

[91] Francisco Eiras, Kemal Oksuz, Adel Bibi, Philip HS Torr, and Puneet K Dokania. Segment, select, correct: A framework for weakly-supervised referring segmentation. *European Conference on Computer Vision Workshop Proceedings*, 2024.

[92] Francisco Eiras, Aleksandar Petrov, Bertie Vidgen, Christian Schroeder de Witt, Fabio Pizzati, Katherine Elkins, Supratik Mukhopadhyay, Adel Bibi, Botos Csaba, Fabro Steibel, et al. Position: Near to mid-term risks and opportunities of open-source generative ai. In *International Conference on Machine Learning*, 2024.

[93] Francisco Eiras, Aleksandar Petrov, Philip Torr, M Pawan Kumar, and Adel Bibi. Do as i do (safely): Mitigating task-specific fine-tuning risks in large language models. In *International Conference on Learning Representations*, 2025.

[94] Andre Esteva, Brett Kuprel, Roberto A Novoa, Justin Ko, Susan M Swetter, Helen M Blau, and Sebastian Thrun. Dermatologist-level classification of skin cancer with deep neural networks. *Nature*, pages 115–118, 2017.

[95] European Parliament. Artificial Intelligence Act, 2021. URL `https://eur-lex.europa.eu/legal-content/EN/TXT/?uri=celex`.

[96] Zhiwei Fang and Justin Zhan. Deep physical informed neural networks for metamaterial design. *IEEE Access*, 2019.

[97] Zhiwei Fang and Justin Zhan. A physics-informed neural network framework for pdes on 3d surfaces: Time independent problems. *IEEE Access*, pages 26328–26335, 2019.

[98] Mahyar Fazlyab, Manfred Morari, and George J Pappas. Safety verification and robustness analysis of neural networks via quadratic constraints and semidefinite programming. *IEEE Transactions on Automatic Control*, pages 1–15, 2020.

[99] Benedikt Fecher, Marcel Hebing, Melissa Laufer, Jörg Pohle, and Fabian Sofsky. Friend or foe? Exploring the implications of large language models on the science system. *arXiv pre-print arxiv:2306.09928*, 2023.

[100] Emilio Ferrara. GenAI against humanity: Nefarious applications of generative artificial intelligence and large language models. *arXiv pre-print arxiv:2310.00737*, 2023.

[101] Claudio Ferrari, Mark Niklas Muller, Nikola Jovanovic, and Martin Vechev. Complete verification via multi-neuron relaxation guided branch-and-bound. *arXiv pre-print arxiv:2205.00263*, 2022.

[102] Joseph Saveri Law Firm and Matthew Butterick. LLM litigation. URL `https://llmlitigation.com/`.

[103] Marc Fischer, Maximilian Baader, and Martin Vechev. Certified defense to image transformations via randomized smoothing. In *Advances in Neural Information Processing Systems*, 2020.

[104] Carl Franzen. Mistral CEO confirms "leak"' of new open source AI model nearing GPT-4 performance. *VentureBeat*, 2024.

[105] Timo Freiesleben and Thomas Grote. Beyond generalization: a theory of robustness in machine learning. *Synthese*, 2023.

[106] Kunihiko Fukushima. Neocognitron: A self-organizing neural network model for a mechanism of pattern recognition unaffected by shift in position. *Biological Cybernetics*, pages 193–202, 1980.

[107] Leo Gao, Stella Biderman, Sid Black, Laurence Golding, Travis Hoppe, Charles Foster, Jason Phang, Horace He, Anish Thite, Noa Nabeshima, et al. The Pile: An 800gb dataset of diverse text for language modeling. *arXiv pre-print arxiv:2101.00027*, 2020.

[108] Leo Gao, Jonathan Tow, Baber Abbasi, Stella Biderman, Sid Black, Anthony DiPofi, Charles Foster, Laurence Golding, Jeffrey Hsu, Alain Le Noac'h, Haonan Li, Kyle McDonell, Niklas Muennighoff, Chris Ociepa, Jason Phang, Laria Reynolds, Hailey Schoelkopf, Aviya Skowron, Lintang Sutawika, Eric

Tang, Anish Thite, Ben Wang, Kevin Wang, and Andy Zou. A framework for few-shot language model evaluation, 2023. URL `https://zenodo.org/records/10256836`.

[109] Saudi Gazette. SDAIA launches ALLAM AI application for Arabic chat. 2024.

[110] Timnit Gebru, Jamie Morgenstern, Briana Vecchione, Jennifer Wortman Vaughan, Hanna Wallach, Hal Daumé Iii, and Kate Crawford. Datasheets for datasets. *Communications of the ACM*, 2021.

[111] Timon Gehr, Matthew Mirman, Dana Drachsler-Cohen, Petar Tsankov, Swarat Chaudhuri, and Martin Vechev. Ai2: Safety and robustness certification of neural networks with abstract interpretation. In *2018 IEEE Symposium on Security and Privacy*, pages 3–18, 2018.

[112] Kristalina Georgieva. AI will transform the global economy. Let's make sure it benefits humanity. 2024.

[113] Fabio Giampaolo, Mariapia De Rosa, Pian Qi, Stefano Izzo, and Salvatore Cuomo. Physics-informed neural networks approach for 1d and 2d gray-scott systems. *Advanced Modeling and Simulation in Engineering Sciences*, pages 1–17, 2022.

[114] Igor Gilitschenski and Uwe D Hanebeck. A robust computational test for overlap of two arbitrary-dimensional ellipsoids in fault-detection of kalman filters. In *International Conference on Information Fusion*, 2012.

[115] Nicole Gillespie, Steven Lockey, Caitlin Curtis, Javad Pool, and Ali Akbari. Trust in artificial intelligence: A global study. 2023.

[116] Ian Goodfellow, Jonathon Shlens, and Christian Szegedy. Explaining and harnessing adversarial examples. In *International Conference on Learning Representations*, 2015.

[117] Ian J Goodfellow, Mehdi Mirza, Da Xiao, Aaron Courville, and Yoshua Bengio. An empirical investigation of catastrophic forgetting in gradient-based neural networks. *arXiv pre-print arxiv:1312.6211*, 2013.

[118] Sven Gowal, Krishnamurthy Dvijotham, Robert Stanforth, Rudy Bunel, Chongli Qin, Jonathan Uesato, Relja Arandjelovic, Timothy Mann, and Pushmeet Kohli. On the effectiveness of interval bound propagation for training verifiably robust models. *arXiv pre-print arxiv:1810.12715*, 2018.

[119] Sven Gowal, Krishnamurthy Dj Dvijotham, Robert Stanforth, Rudy Bunel, Chongli Qin, Jonathan Uesato, Relja Arandjelovic, Timothy Mann, and Pushmeet Kohli. Scalable verified training for provably robust image classification. In *IEEE International Conference on Computer Vision*, 2019.

[120] Roberto Gozalo-Brizuela and Eduardo C Garrido-Merchan. ChatGPT is not all you need. A State of the Art Review of large Generative AI models. *arXiv pre-print arxiv:2301.04655*, 2023.

[121] Daya Guo, Dejian Yang, Haowei Zhang, Junxiao Song, Ruoyu Zhang, Runxin Xu, Qihao Zhu, Shirong Ma, Peiyi Wang, Xiao Bi, et al. Deepseek-r1: Incentivizing reasoning capability in llms via reinforcement learning. *arXiv preprint arXiv:2501.12948*, 2025.

[122] Zishan Guo, Renren Jin, Chuang Liu, Yufei Huang, Dan Shi, Supryadi, Linhao Yu, Yan Liu, Jiaxuan Li, Bojian Xiong, and Deyi Xiong. Evaluating large language models: A comprehensive survey. *arXiv pre-print arxiv:2310.19736*, 2023.

[123] Philipp Hacker, Andreas Engel, and Marco Mauer. Regulating ChatGPT and other large generative AI models. In *Proceedings of the 2023 ACM Conference on Fairness, Accountability, and Transparency*, 2023. URL https://dl.acm.org/doi/10.1145/3593013.3594067.

[124] Valentin Hartmann, Anshuman Suri, Vincent Bindschaedler, David Evans, Shruti Tople, and Robert West. SoK: Memorization in general-purpose Large Language Models. *arXiv pre-print arxiv:2310.18362*, 2023.

[125] Thomas Hartvigsen, Saadia Gabriel, Hamid Palangi, Maarten Sap, Dipankar Ray, and Ece Kamar. Toxigen: A large-scale machine-generated dataset for adversarial and implicit hate speech detection. *arXiv pre-print arxiv:2203.09509*, 2022.

[126] Kaiming He, Xiangyu Zhang, Shaoqing Ren, and Jian Sun. Deep residual learning for image recognition. In *IEEE Conference on Computer Vision and Pattern Recognition*, 2016.

[127] Luxi He, Mengzhou Xia, and Peter Henderson. What's in your "safe" data?: Identifying benign data that breaks safety. *arXiv pre-print arxiv:2404.01099*, 2024.

[128] Matthias Hein and Maksym Andriushchenko. Formal guarantees on the robustness of a classifier against adversarial manipulation. *Advances in Neural Information Processing Systems*, 2017.

[129] Dan Hendrycks and Kevin Gimpel. A baseline for detecting misclassified and out-of-distribution examples in neural networks. *arXiv pre-print arxiv:1610.02136*, 2016.

[130] Dan Hendrycks, Collin Burns, Steven Basart, Andy Zou, Mantas Mazeika, Dawn Song, and Jacob Steinhardt. Measuring massive multitask language understanding. *arXiv pre-print arxiv:2009.03300*, 2020.

[131] Dan Hendrycks, Nicholas Carlini, John Schulman, and Jacob Steinhardt. Unsolved problems in ml safety. *arXiv pre-print arxiv:2109.13916*, 2021.

[132] Dan Hendrycks, Mantas Mazeika, and Thomas Woodside. An overview of catastrophic AI risks. *arXiv pre-print arxiv:2306.12001*, 2023.

[133] Birgit Hillebrecht and Benjamin Unger. Certified machine learning: A posteriori error estimation for physics-informed neural networks. *arXiv pre-print arxiv:2203.17055*, 2022.

[134] Andreseen Horowitz. House of Lords Communications and Digital Select Committee inquiry: Large language models, 2023. URL https://committees.parliament.uk/writtenevidence/127070/pdf.

[135] The White House. FACT SHEET: President Biden Issues Executive Order on Safe, Secure, and Trustworthy Artificial Intelligence, 2023. URL https://www.whitehouse.gov/briefing-room/statements-releases/2023/10/30/fact-sheet-president-biden-issues-executive-order-on-safe-secure-and-trustworthy-artificial-intelligence/.

[136] Xiaowei Huang, Marta Kwiatkowska, Sen Wang, and Min Wu. Safety verification of deep neural networks. In *International Conference on Computer Aided Verification*, 2017.

[137] Yangsibo Huang, Samyak Gupta, Mengzhou Xia, Kai Li, and Danqi Chen. Catastrophic jailbreak of open-source llms via exploiting generation. *arXiv pre-print arxiv:2310.06987*, 2023.

[138] Andrew Ilyas, Logan Engstrom, Anish Athalye, and Jessy Lin. Black-box adversarial attacks with limited queries and information. In *International Conference on Machine Learning*, pages 2137–2146, 2018.

[139] Hakan Inan, Kartikeya Upasani, Jianfeng Chi, Rashi Rungta, Krithika Iyer, Yuning Mao, Michael Tontchev, Qing Hu, Brian Fuller, Davide Testuggine, and Madian Khabsa. Llama Guard: LLM-based input-output safeguard for Human-AI conversations. *arXiv pre-print arxiv:2312.06674*, 2023.

[140] Infocomm. First of its kind Generative AI Evaluation Sandbox for Trusted AI by AI Verify Foundation and IMDA. *Infocomm Media Development Authority*.

[141] Geoffrey Irving, Paul Christiano, and Dario Amodei. Ai safety via debate. *arXiv pre-print arxiv:1805.00899*, 2018.

[142] Neel Jain, Avi Schwarzschild, Yuxin Wen, Gowthami Somepalli, John Kirchenbauer, Ping-yeh Chiang, Micah Goldblum, Aniruddha Saha, Jonas Geiping, and Tom Goldstein. Baseline defenses for adversarial attacks against aligned language models. *arXiv pre-print arxiv:2309.00614*, 2023.

[143] Samyak Jain, Robert Kirk, Ekdeep Singh Lubana, Robert P. Dick, Hidenori Tanaka, Edward Grefenstette, Tim Rocktäschel, and David Scott Krueger. Mechanistically analyzing the effects of fine-tuning on procedurally defined tasks. *arXiv pre-print arxiv:2311.12786*, 2023.

[144] Jeevan Jaisingh, Eric WK See-To, and Kar Yan Tam. The impact of open source software on the strategic choices of firms developing proprietary software. *Journal of Management Information Systems*, 2008.

[145] Jongheon Jeong and Jinwoo Shin. Consistency regularization for certified robustness of smoothed classifiers. In *Advances in Neural Information Processing Systems*, 2020.

[146] Jiaming Ji, Tianyi Qiu, Boyuan Chen, Borong Zhang, Hantao Lou, Kaile Wang, Yawen Duan, Zhonghao He, Jiayi Zhou, Zhaowei Zhang, et al. Ai alignment: A comprehensive survey. *arXiv pre-print arxiv:2310.19852*, 2023.

[147] Xiaowei Jin, Shengze Cai, Hui Li, and George Em Karniadakis. Nsfnets (navier-stokes flow nets): Physics-informed neural networks for the incompressible navier-stokes equations. *Journal of Computational Physics*, page 109951, 2021.

[148] Erik Jones, Anca Dragan, Aditi Raghunathan, and Jacob Steinhardt. Automatically auditing large language models via discrete optimization. In *International Conference on Machine Learning*, pages 15307–15329, 2023.

[149] Matt Jordan and Alexandros G Dimakis. Exactly computing the local lipschitz constant of relu networks. In *Advances in Neural Information Processing Systems*, 2020.

[150] Pratik Joshi, Sebastin Santy, Amar Budhiraja, Kalika Bali, and Monojit Choudhury. The state and fate of linguistic diversity and inclusion in the nlp world. *arXiv pre-print arxiv:2004.09095*, 2020.

[151] Oyvind Kaldestad. New report: Generative AI threatens. *Forbrukerrådet*, 2023. URL https://www.forbrukerradet.no/side/new-report-generative-ai-threatens-consumer-rights/.

[152] Rahul Kapoor, Shokoh H Yaghoubi, and Theresa T Kalathil. Ai regulation in india: Current state and future perspectives, 2024. URL https://www.morganlewis.com/blogs/sourcingatmorganlewis/2024/01/ai-regulation-in-india-current-state-and-future-perspectives.

[153] Sayash Kapoor and Arvind Narayanan. Licensing is neither feasible nor effective for addressing AI risks. *AI Snake Oil*, 2023.

[154] Sayash Kapoor and Arvind Narayanan. Three ideas for regulating generative AI. *AI Snake Oil*, 2023.

[155] Antonia Karamolegkou, Jiaang Li, Li Zhou, and Anders Søgaard. Copyright Violations and Large Language Models. In *Empirical Methods in Natural Language Processing*, 2023.

[156] Hamid Karimi, Tyler Derr, and Jiliang Tang. Characterizing the decision boundary of deep neural networks. *arXiv pre-print arxiv:1912.11460*, 2019.

[157] Richard M Karp. *Reducibility among combinatorial problems*. Springer, 2010.

[158] Guy Katz, Clark Barrett, David L Dill, Kyle Julian, and Mykel J Kochenderfer. Reluplex: An efficient smt solver for verifying deep neural networks. In *International Conference on Computer Aided Verification*, pages 97–117, 2017.

[159] Maurice G Kendall. *A Course in the Geometry of n Dimensions*. Courier Corporation, 2004.

[160] Zachary Kenton, Tom Everitt, Laura Weidinger, Iason Gabriel, Vladimir Mikulik, and Geoffrey Irving. Alignment of language agents. *arXiv pre-print arxiv:2103.14659*, 2021.

[161] Jintae Kim, Sera Park, Dongbo Min, and Wankyu Kim. Comprehensive survey of recent drug discovery using deep learning. *International Journal of Molecular Sciences*, page 9983, 2021.

[162] Jungeun Kim, Kookjin Lee, Dongeun Lee, Sheo Yon Jhin, and Noseong Park. Dpm: a novel training method for physics-informed neural networks in extrapolation. pages 8146–8154, 2021.

[163] Hannah Rose Kirk, Bertie Vidgen, Paul Röttger, and Scott A. Hale. Personalisation within bounds: A risk taxonomy and policy framework for the alignment of large language models with personalised feedback. *arXiv pre-print arxiv:2303.05453*, 2023.

[164] Will Knight. OpenAI's CEO says the age of giant AI models is already over. *Wired*, 2023. URL https://www.wired.com/story/openai-ceo-sam-altman-the-age-of-giant-ai-models-is-already-over/.

[165] Ching-Yun Ko, Zhaoyang Lyu, Lily Weng, Luca Daniel, Ngai Wong, and Dahua Lin. Popqorn: Quantifying robustness of recurrent neural networks. In *International Conference on Machine Learning*, pages 3468–3477, 2019.

[166] Dmitrii Kochkov, Alvaro Sanchez-Gonzalez, Jamie Alexander Smith, Tobias Joachim Pfaff, Peter Battaglia, and Michael Brenner. Learning latent field dynamics of pdes. In *Third Workshop on Machine Learning and the Physical Sciences (Advances in Neural Information Processing Systems)*, 2020.

[167] Leonie Koessler and Jonas Schuett. Risk assessment at agi companies: A review of popular risk assessment techniques from other safety-critical industries. *arXiv pre-print arxiv:2307.08823*, 2023.

[168] Aditi Krishnapriyan, Amir Gholami, Shandian Zhe, Robert Kirby, and Michael W Mahoney. Characterizing possible failure modes in physics-informed neural networks. *Advances in Neural Information Processing Systems*, pages 26548–26560, 2021.

[169] Alex Krizhevsky. Learning multiple layers of features from tiny images. Technical report, 2009.

[170] Alex Krizhevsky, Ilya Sutskever, and Geoffrey E Hinton. Imagenet classification with deep convolutional neural networks. *Advances in Neural Information Processing Systems*, 2012.

[171] Ajay Kumar and Tom Davenport. How to make generative ai greener. *Harvard Business Review*, 2023.

[172] Aounon Kumar, Alexander Levine, Tom Goldstein, and Soheil Feizi. Curse of dimensionality on randomized smoothing for certifiable robustness. In *International Conference on Machine Learning*, 2020.

[173] Alexey Kurakin, Ian Goodfellow, and Samy Bengio. Adversarial machine learning at scale. *arXiv pre-print arxiv:1611.01236*, 2016.

[174] Alexey Kurakin, Ian J Goodfellow, and Samy Bengio. Adversarial examples in the physical world. In *Artificial Intelligence Safety and Security*, pages 99–112. Chapman and Hall/CRC, 2018.

[175] Tom Kwiatkowski, Jennimaria Palomaki, Olivia Redfield, Michael Collins, Ankur Parikh, Chris Alberti, Danielle Epstein, Illia Polosukhin, Jacob Devlin, and Kenton Lee. Natural questions: a benchmark for question answering research. *Transactions of the Association for Computational Linguistics*, 2019.

[176] Emanuele La Malfa, Aleksandar Petrov, Simon Frieder, Christoph Weinhuber, Ryan Burnell, Raza Nazar, Anthony G. Cohn, Nigel Shadbolt, and Michael Wooldridge. Language Models as a Service: Overview of a new paradigm and its challenges. *arXiv pre-print arxiv:2309.16573*, 2023.

[177] Preethi Lahoti, Nicholas Blumm, Xiao Ma, Raghavendra Kotikalapudi, Sahitya Potluri, Qijun Tan, Hansa Srinivasan, Ben Packer, Ahmad Beirami, Alex Beutel, et al. Improving diversity of demographic representation in large language models via collective-critiques and self-voting. *arXiv pre-print arxiv:2310.16523*, 2023.

[178] LAION.ai. A call to protect open source AI in europe. 2023. Accessed: 2024-01-29.

[179] Balaji Lakshminarayanan, Alexander Pritzel, and Charles Blundell. Simple and scalable predictive uncertainty estimation using deep ensembles. *Advances in Neural Information Processing Systems*, 2017.

[180] Remi Lam, Alvaro Sanchez-Gonzalez, Matthew Willson, Peter Wirnsberger, Meire Fortunato, Ferran Alet, Suman Ravuri, Timo Ewalds, Zach Eaton-Rosen, Weihua Hu, et al. Graphcast: Learning skillful medium-range global weather forecasting. *arXiv pre-print arxiv:2212.12794*, 2022.

[181] Tom A Lamb, Rudy Brunel, Krishnamurthy DJ Dvijotham, M Pawan Kumar, Philip HS Torr, and Francisco Eiras. Faithful knowledge distillation. *arXiv pre-print arxiv:2306.04431*, 2023.

[182] Yann LeCun, Léon Bottou, Yoshua Bengio, and Patrick Haffner. Gradient-based learning applied to document recognition. *IEEE Transactions on Neural Networks*, pages 2278–2324, 1998.

[183] Mathias Lecuyer, Vaggelis Atlidakis, Roxana Geambasu, Daniel Hsu, and Suman Jana. Certified robustness to adversarial examples with differential privacy. In *IEEE Symposium on Security and Privacy*, 2019.

[184] Guang-He Lee, Yang Yuan, Shiyu Chang, and Tommi S Jaakkola. Tight certificates of adversarial robustness for randomly smoothed classifiers. *arXiv pre-print arxiv:1906.04948*, 2019.

[185] Jan Leike, David Krueger, Tom Everitt, Miljan Martic, Vishal Maini, and Shane Legg. Scalable agent alignment via reward modeling: a research direction. *arXiv pre-print arxiv:1811.07871*, 2018.

[186] Alexander Levine and Soheil Feizi. Robustness certificates for sparse adversarial attacks by randomized ablation. In *AAAI Conference on Artificial Intelligence*, 2020.

[187] Alexander Levine and Soheil Feizi. Improved, deterministic smoothing for l1 certified robustness. *arXiv pre-print arxiv:2103.10834*, 2021.

[188] Bai Li, Changyou Chen, Wenlin Wang, and Lawrence Carin. Certified adversarial robustness with additive noise. In *Advances in Neural Information Processing Systems*, 2019.

[189] Jiatong Li, Rui Li, and Qi Liu. Beyond static datasets: A deep interaction approach to LLM evaluation. *arXiv pre-print arxiv:2309.04369*, 2023.

[190] Juncheng Li, Frank Schmidt, and Zico Kolter. Adversarial camera stickers: A physical camera-based attack on deep learning systems. In *International Conference on Machine Learning*, pages 3896–3904, 2019.

[191] Linyi Li, Maurice Weber, Xiaojun Xu, Luka Rimanic, Tao Xie, Ce Zhang, and Bo Li. Provable robust learning based on transformation-specific smoothing. *arXiv pre-print arxiv:2002.12398*, 2020.

[192] Yunxiang Li, Zihan Li, Kai Zhang, Ruilong Dan, Steve Jiang, and You Zhang. ChatDoctor: A medical chat model fine-tuned on a large language model meta-ai (LLaMA) using medical domain knowledge. *arXiv pre-print arxiv:2303.14070*, 2023.

[193] Percy Liang, Rishi Bommasani, Tony Lee, Dimitris Tsipras, Dilara Soylu, Michihiro Yasunaga, Yian Zhang, Deepak Narayanan, Yuhuai Wu, Ananya Kumar, et al. Holistic evaluation of language models. *arXiv pre-print arxiv:2211.09110*, 2022.

[194] Percy Liang, Rishi Bommasani, Tony Lee, Dimitris Tsipras, Dilara Soylu, Michihiro Yasunaga, Yian Zhang, Deepak Narayanan, Yuhuai Wu, Ananya Kumar, et al. Holistic evaluation of language models. *arXiv pre-print arxiv:2211.09110*, 2023.

[195] Andreas Liesenfeld, Alianda Lopez, and Mark Dingemanse. Opening up ChatGPT: Tracking openness, transparency, and accountability in instruction-tuned text generators. In *5th International Conference on Conversational User Interfaces*, 2023.

[196] Hila Lifshitz-Assaf and Frank Nagle. The digital economy runs on open source. here's how to protect it. *Harvard Business Review*, 2021.

[197] Buhua Liu, Shitong Shao, Bao Li, Lichen Bai, Haoyi Xiong, James Kwok, Sumi Helal, and Zeke Xie. Alignment of diffusion models: Fundamentals, challenges, and future. *arXiv pre-print arxiv:2409.07253*, 2024.

[198] Dehao Liu and Yan Wang. Multi-fidelity physics-constrained neural network and its application in materials modeling. *Journal of Mechanical Design*, 2019.

[199] Zhengzhong Liu, Aurick Qiao, Willie Neiswanger, Hongyi Wang, Bowen Tan, Tianhua Tao, Junbo Li, Yuqi Wang, Suqi Sun, Omkar Pangarkar, et al. LLM360: Towards fully transparent open-source LLMs. *arXiv pre-print arxiv:2312.06550*, 2023.

[200] Alex Lockie. The wealthiest mafia in the world is undergoing a schism and it could get ugly. *Business Insider*, 2015.

[201] Alessio Lomuscio and Lalit Maganti. An approach to reachability analysis for feed-forward relu neural networks. *arXiv pre-print arxiv:1706.07351*, 2017.

[202] Jonathan Long, Evan Shelhamer, and Trevor Darrell. Fully convolutional networks for semantic segmentation. In *IEEE Conference on Computer Vision and Pattern Recognition*, pages 3431–3440, 2015.

[203] Shayne Longpre, Robert Mahari, Anthony Chen, Naana Obeng-Marnu, Damien Sileo, William Brannon, Niklas Muennighoff, Nathan Khazam, Jad Kabbara, Kartik Perisetla, et al. The Data Provenance Initiative: A Large Scale Audit of Dataset Licensing & Attribution in AI. *arXiv pre-print arxiv:2310.16787*, 2023.

[204] Lu Lu, Pengzhan Jin, Guofei Pang, Zhongqiang Zhang, and George Em Karniadakis. Learning nonlinear operators via deeponet based on the universal approximation theorem of operators. *Nature Machine Intelligence*, 2021.

[205] Björn Lütjens, Michael Everett, and Jonathan P How. Certified adversarial robustness for deep reinforcement learning. In *Conference on Robot Learning*, pages 1328–1337, 2020.

[206] Aleksander Madry, Aleksandar Makelov, Ludwig Schmidt, Dimitris Tsipras, and Adrian Vladu. Towards deep learning models resistant to adversarial attacks. *International Conference on Learning Representations*, 2018.

[207] Tegwen Malik, Laurie Hughes, Yogesh K Dwivedi, and Sandra Dettmer. Exploring the transformative impact of generative AI on higher education. In *Conference on e-Business, e-Services and e-Society*, 2023.

[208] Sourab Mangrulkar, Sylvain Gugger, Lysandre Debut, Younes Belkada, Sayak Paul, and Benjamin Bossan. Peft: State-of-the-art parameter-efficient fine-tuning methods. `https://github.com/huggingface/peft`, 2022.

[209] Yuhao Mao, Mark Müller, Marc Fischer, and Martin Vechev. Connecting certified and adversarial training. *Advances in Neural Information Processing Systems*, 2024.

[210] Matt Marshall. How enterprises are using Open Source LLMs: 16 examples. *VentureBeat*, 2024.

[211] Kayla Matteucci, Shahar Avin, Fazl Barez, and Sean O hEigeartaigh. AI systems of concern. *arXiv pre-print arxiv:2310.05876*, 2023.

[212] Mantas Mazeika, Long Phan, Xuwang Yin, Andy Zou, Zifan Wang, Norman Mu, Elham Sakhaee, Nathaniel Li, Steven Basart, Bo Li, et al. Harmbench: A standardized evaluation framework for automated red teaming and robust refusal. *arXiv pre-print arxiv:2402.04249*, 2024.

[213] Garth P McCormick. Computability of global solutions to factorable nonconvex programs: Part i—convex underestimating problems. *Mathematical Programming*, pages 147–175, 1976.

[214] Scott McLean, Gemma JM Read, Jason Thompson, Chris Baber, Neville A Stanton, and Paul M Salmon. The risks associated with artificial general intelligence: A systematic review. *Journal of Experimental and Theoretical Artificial Intelligence*, pages 649–663, 2023.

[215] Alex Mei, Anisha Kabir, Sharon Levy, Melanie Subbiah, Emily Allaway, John Judge, Desmond Patton, Bruce Bimber, Kathleen McKeown, and William Yang Wang. Mitigating covertly unsafe text within natural language systems. In *Findings of the Association for Computational Linguistics: EMNLP 2022*, 2022.

[216] Alex Mei, Sharon Levy, and William Wang. ASSERT: Automated safety scenario red teaming for evaluating the robustness of large language models. In *Findings of the Association for Computational Linguistics: EMNLP 2023*, 2023.

[217] Kevin Meng, David Bau, Alex Andonian, and Yonatan Belinkov. Locating and editing factual associations in gpt. *Advances in Neural Information Processing Systems*, pages 17359–17372, 2022.

[218] Meta. Meta and Microsoft Introduce the Next Generation of Llama. 2023.

[219] Cade Metz. Openai says new york times lawsuit against it is "without merit". *The New York Times*, 2024.

[220] Todor Mihaylov, Peter Clark, Tushar Khot, and Ashish Sabharwal. Can a suit of armor conduct electricity? a new dataset for open book question answering. *arXiv pre-print arxiv:1809.02789*, 2018.

[221] MinCiencia. Artículo: Ministerio De Ciencia Abre Consulta Ciudadana Para Actualizar Política Nacional De Inteligencia Artificial. URL http://www.minciencia.gob.cl/noticias/ministerio-de-ciencia-abre-consulta-ciudadana-para-actualizar-politica-nacional-de-inteligencia-artificial/.

[222] Matthew Mirman, Timon Gehr, and Martin Vechev. Differentiable abstract interpretation for provably robust neural networks. In *International Conference on Machine Learning*, pages 3578–3586, 2018.

[223] Siddhartha Mishra and Roberto Molinaro. Estimates on the generalization error of physics-informed neural networks for approximating pdes. *IMA Journal of Numerical Analysis*, 2022.

[224] Brent Mittelstadt, Chris Russell, and Sandra Wachter. Explaining explanations in AI. In *Conference on Fairness, Accountability, and Transparency*, 2019.

[225] Jeet Mohapatra, Ching-Yun Ko, Tsui-Wei Weng, Pin-Yu Chen, Sijia Liu, and Luca Daniel. Higher-order certification for randomized smoothing. *Advances in Neural Information Processing Systems*, 2020.

[226] Ethan Mollick. An Opinionated Guide to Which AI to Use, 2023. URL https://www.oneusefulthing.org/p/an-opinionated-guide-to-which-ai.

[227] Simone Monaco and Daniele Apiletti. Training physics-informed neural networks: One learning to rule them all? *Results in Engineering*, 2023.

[228] Monetary Authority of Singapore. MAS Partners Industry to Develop Generative AI Risk Framework for the Financial Sector. URL https://www.mas.gov.sg/news/media-releases/2023/mas-partners-industry-to-develop-generative-ai-risk-framework-for-the-financial-sector.

[229] Seyed-Mohsen Moosavi-Dezfooli, Alhussein Fawzi, and Pascal Frossard. Deepfool: a simple and accurate method to fool deep neural networks. In *IEEE Conference on Computer Vision and Pattern Recognition*, pages 2574–2582, 2016.

[230] Seyed-Mohsen Moosavi-Dezfooli, Alhussein Fawzi, Jonathan Uesato, and Pascal Frossard. Robustness via curvature regularization, and vice versa. In *IEEE Conference on Computer Vision and Pattern Recognition*, 2019.

[231] Marius Mosbach, Maksym Andriushchenko, Thomas Trost, Matthias Hein, and Dietrich Klakow. Logit pairing methods can fool gradient-based attacks. *arXiv pre-print arxiv:1810.12042*, 2018.

[232] Mark Niklas Müller, Marc Fischer, Robin Staab, and Martin Vechev. Abstract interpretation of fixpoint iterators with applications to neural networks. *ACM Transactions on Programming Languages and Systems*, pages 786–810, 2023.

[233] Jakob Mökander, Jonas Schuett, Hannah Rose Kirk, and Luciano Floridi. Auditing large language models: a three-layered approach. *AI and Ethics*, 2023.

[234] Milad Nasr, Nicholas Carlini, Jonathan Hayase, Matthew Jagielski, A. Feder Cooper, Daphne Ippolito, Christopher A. Choquette-Choo, Eric Wallace, Florian Tramèr, and Katherine Lee. Scalable extraction of training data from (production) language models. *arXiv pre-print arxiv:2311.17035*, 2023.

[235] OECD. OECD's live repository of AI strategies & policies. URL https://oecd.ai/en/dashboards.

[236] Courts of New Zealand. Guidelines for use of generative artificial intelligence in Courts and Tribunals — Courts of New Zealand. URL https://www.courtsofnz.govt.nz/going-to-court/practice-directions/practice-guidelines/all-benches/guidelines-for-use-of-generative-artificial-intelligence-in-courts-and-tribunals/.

[237] Chris Olah, Nick Cammarata, Ludwig Schubert, Gabriel Goh, Michael Petrov, and Shan Carter. Zoom in: An introduction to circuits. *Distill*, 2020.

[238] Daryna Oliynyk, Rudolf Mayer, and Andreas Rauber. I know what you trained last summer: A survey on stealing machine learning models and defences. *ACM Computing Surveys*, 2023.

[239] Long Ouyang, Jeffrey Wu, Xu Jiang, Diogo Almeida, Carroll Wainwright, Pamela Mishkin, Chong Zhang, Sandhini Agarwal, Katarina Slama, Alex Ray, et al. Training language models to follow instructions with human feedback. *Advances in Neural Information Processing Systems*, pages 27730–27744, 2022.

[240] Stephanie Palazzolo. Meta's free ai isn't cheap to use, companies say. *The Information*, 2023.

[241] Alexander Pan, Jun Shern Chan, Andy Zou, Nathaniel Li, Steven Basart, Thomas Woodside, Hanlin Zhang, Scott Emmons, and Dan Hendrycks. Do the rewards justify the means? measuring trade-offs between rewards and ethical behavior in the machiavelli benchmark. In *International Conference on Machine Learning*, pages 26837–26867, 2023.

[242] Guofei Pang, Lu Lu, and George Em Karniadakis. fpinns: Fractional physics-informed neural networks. *SIAM Journal on Scientific Computing*, 2019.

[243] Nicolas Papernot, Patrick McDaniel, Somesh Jha, Matt Fredrikson, Z Berkay Celik, and Ananthram Swami. The limitations of deep learning in adversarial settings. In *2016 IEEE European Symposium on Security and Privacy*, pages 372–387, 2016.

[244] Nicolas Papernot, Patrick McDaniel, Ian Goodfellow, Somesh Jha, Z Berkay Celik, and Ananthram Swami. Practical black-box attacks against machine learning. In *ACM Asia Conference on Computer and Communications Security*, pages 506–519, 2017.

[245] EU Parliament. EU AI Act. https://www.europarl.europa.eu/news/en/headlines/society/20230601STO93804/eu-ai-act-first-regulation-on-artificial-intelligence, 2023. Accessed: 2024-01-29.

[246] Alicia Parrish, Angelica Chen, Nikita Nangia, Vishakh Padmakumar, Jason Phang, Jana Thompson, Phu Mon Htut, and Samuel R Bowman. Bbq: A hand-built bias benchmark for question answering. *arXiv pre-print arxiv:2110.08193*, 2021.

[247] Adam Paszke, Sam Gross, Francisco Massa, Adam Lerer, James Bradbury, Gregory Chanan, Trevor Killeen, Zeming Lin, Natalia Gimelshein, Luca Antiga, Alban Desmaison, Andreas Kopf, Edward Yang, Zachary DeVito, Martin Raison, Alykhan Tejani, Sasank Chilamkurthy, Benoit Steiner, Lu Fang, Junjie Bai, and Soumith Chintala. PyTorch: An imperative style, high-performance deep learning library. In *Advances in Neural Information Processing Systems*. 2019.

[248] James W Paulson, Giancarlo Succi, and Armin Eberlein. An empirical study of open-source and closed-source software products. *IEEE Transactions on Software Engineering*, 2004.

[249] ShengYun Peng, Pin-Yu Chen, Matthew Hull, and Duen Horng Chau. Navigating the safety landscape: Measuring risks in finetuning large language models. *arXiv pre-print arxiv:2405.17374*, 2024.

[250] Ethan Perez, Saffron Huang, Francis Song, Trevor Cai, Roman Ring, John Aslanides, Amelia Glaese, Nat McAleese, and Geoffrey Irving. Red teaming language models with language models. *arXiv pre-print arxiv:2202.03286*, 2022.

[251] Ethan Perez, Sam Ringer, Kamilė Lukošiūtė, Karina Nguyen, Edwin Chen, Scott Heiner, Craig Pettit, Catherine Olsson, Sandipan Kundu, Saurav Kadavath, et al. Discovering language model behaviors with model-written evaluations. *arXiv pre-print arxiv:2212.09251*, 2022.

[252] Aleksandar Petrov, Francisco Eiras, Amartya Sanyal, Philip Torr, and Adel Bibi. Certifying ensembles: A general certification theory with s-lipschitzness. In *International Conference on Machine Learning*, pages 27709–27736, 2023.

[253] Aleksandar Petrov, Emanuele La Malfa, Philip HS Torr, and Adel Bibi. Language model tokenizers introduce unfairness between languages. *Advances in Neural Information Processing Systems*, 2023.

[254] Aleksandar Petrov, Philip HS Torr, and Adel Bibi. Prompting a pretrained transformer can be a universal approximator. *arXiv pre-print arxiv:2402.14753*, 2024.

[255] Lerrel Pinto, James Davidson, Rahul Sukthankar, and Abhinav Gupta. Robust adversarial reinforcement learning. In *International Conference on Machine Learning*, pages 2817–2826, 2017.

[256] Björn Plüster. Laion leolm: Linguistically enhanced open language model. URL `https://huggingface.co/LeoLM/leo-hessianai-7b-chat`.

[257] Vinay Uday Prabhu and Abeba Birhane. Large image datasets: A pyrrhic win for computer vision? *arXiv pre-print arxiv:2006.16923*, 2020.

[258] PricewaterhouseCoopers. Overview of 'The Executive Order on the Safe, Secure, and Trustworthy Development and Use of Artificial Intelligence', 2024. URL `https://www.pwc.com/jp/en/knowledge/column/generative-ai-regulation09.html`.

[259] Henry Pulver, Francisco Eiras, Ludovico Carozza, Majd Hawasly, Stefano V Albrecht, and Subramanian Ramamoorthy. Pilot: Efficient planning by imitation learning and optimisation for safe autonomous driving. In *2021 IEEE/RSJ International Conference on Intelligent Robots and Systems*, pages 1442–1449, 2021.

[260] Xiangyu Qi, Yi Zeng, Tinghao Xie, Pin-Yu Chen, Ruoxi Jia, Prateek Mittal, and Peter Henderson. Fine-tuning aligned language models compromises safety, even when users do not intend to! *arXiv pre-print arxiv:2310.03693*, 2023.

[261] J. Ross Quinlan. Induction of decision trees. *Machine Learning*, pages 81–106, 1986.

[262] Alec Radford, Jeffrey Wu, Rewon Child, David Luan, Dario Amodei, and Ilya Sutskever. Language models are unsupervised multitask learners. *OpenAI Blog*, 2019.

[263] Jack W. Rae, Sebastian Borgeaud, Trevor Cai, Katie Millican, Jordan Hoffmann, Francis Song, John Aslanides, Sarah Henderson, Roman Ring, Susannah Young, et al. Scaling Language Models: Methods, Analysis & Insights from Training Gopher. *arXiv pre-print arxiv:2112.11446*, 2022.

[264] Rafael Rafailov, Archit Sharma, Eric Mitchell, Stefano Ermon, Christopher D Manning, and Chelsea Finn. Direct preference optimization: Your language model is secretly a reward model. *arXiv pre-print arxiv:2305.18290*, 2023.

[265] Rafael Rafailov, Archit Sharma, Eric Mitchell, Christopher D Manning, Stefano Ermon, and Chelsea Finn. Direct preference optimization: Your language model is secretly a reward model. *Advances in Neural Information Processing Systems*, 2024.

[266] Colin Raffel, Noam Shazeer, Adam Roberts, Katherine Lee, Sharan Narang, Michael Matena, Yanqi Zhou, Wei Li, and Peter J Liu. Exploring the limits of transfer learning with a unified text-to-text transformer. *Journal of Machine Learning Research*, pages 1–67, 2020.

[267] Aditi Raghunathan, Jacob Steinhardt, and Percy Liang. Certified defenses against adversarial examples. In *International Conference in Learning Representations*, 2018.

[268] Maziar Raissi, Paris Perdikaris, and George E Karniadakis. Physics-informed neural networks: A deep learning framework for solving forward and inverse problems involving nonlinear partial differential equations. *Journal of Computational Physics*, pages 686–707, 2019.

[269] Maziar Raissi, Zhicheng Wang, Michael S Triantafyllou, and George Em Karniadakis. Deep learning of vortex-induced vibrations. *Journal of Fluid Mechanics*, pages 119–137, 2019.

[270] Maziar Raissi, Alireza Yazdani, and George Em Karniadakis. Hidden fluid mechanics: Learning velocity and pressure fields from flow visualizations. *Science*, pages 1026–1030, 2020.

[271] Vinay Venkatesh Ramasesh, Aitor Lewkowycz, and Ethan Dyer. Effect of scale on catastrophic forgetting in neural networks. In *International Conference on Learning Representations*, 2021.

[272] Charvi Rastogi, Marco Tulio Ribeiro, Nicholas King, Harsha Nori, and Saleema Amershi. Supporting human-ai collaboration in auditing llms with llms. In *AAAI/ACM Conference on AI, Ethics, and Society*, AIES '23', page 913–926, 2023.

[273] Shaoqing Ren. Faster r-cnn: Towards real-time object detection with region proposal networks. *arXiv pre-print arxiv:1506.01497*, 2015.

[274] Reuters. Abu Dhabi makes its Falcon 40B AI model open source. `https://www.reuters.com/technology/abu-dhabi-makes-its-falcon-40b-ai-model-open-source-2023-05-25/`, 2023.

[275] Matthias C Rillig, Marlene Ågerstrand, Mohan Bi, Kenneth A Gould, and Uli Sauerland. Risks and benefits of large language models for the environment. *Environmental Science and Technology*, 2023.

[276] Alexander Robey, Eric Wong, Hamed Hassani, and George J Pappas. Smoothllm: Defending large language models against jailbreaking attacks. *arXiv pre-print arxiv:2310.03684*, 2023.

[277] Anna Rogers. Closed AI Models Make Bad Baselines, 2023. URL `https://hackingsemantics.xyz/2023/closed-baselines/`.

[278] Lluís Ros, Assumpta Sabater, and Federico Thomas. An ellipsoidal calculus based on propagation and fusion. *IEEE Transactions on Systems, Man, and Cybernetics, Part B (Cybernetics)*, 2002.

[279] Jules Roscoe. Elon Musk's Grok AI is pushing misinformation and legitimizing conspiracies. *Vice*, 2023.

[280] Frank Rosenblatt. The perceptron: a probabilistic model for information storage and organization in the brain. *Psychological Review*, page 386, 1958.

[281] Paul Röttger, Hannah Rose Kirk, Bertie Vidgen, Giuseppe Attanasio, Federico Bianchi, and Dirk Hovy. Xstest: A test suite for identifying exaggerated safety behaviours in large language models. *arXiv pre-print arxiv:2308.01263*, 2023.

[282] David E Rumelhart, Geoffrey E Hinton, and Ronald J Williams. Learning representations by back-propagating errors. *Nature*, pages 533–536, 1986.

[283] Francesco Rundo, Francesca Trenta, Agatino Luigi Di Stallo, and Sebastiano Battiato. Machine learning for quantitative finance applications: A survey. *Applied Sciences*, page 5574, 2019.

[284] Tim De Ryck and Siddhartha Mishra. Generic bounds on the approximation error for physics-informed (and) operator learning. In *Advances in Neural Information Processing Systems*, 2022.

[285] Kate Saenko. A computer scientist breaks down generative ai's hefty carbon footprint. *Scientific American*, 2023.

[286] Oscar Sainz, Jon Ander Campos, Iker García-Ferrero, Julen Etxaniz, Oier Lopez de Lacalle, and Eneko Agirre. Nlp evaluation in trouble: On the need to measure llm data contamination for each benchmark. *arXiv pre-print arxiv:2310.18018*, 2023.

[287] Keisuke Sakaguchi, Ronan Le Bras, Chandra Bhagavatula, and Yejin Choi. Winogrande: An adversarial winograd schema challenge at scale. *Communications of the ACM*, pages 99–106, 2021.

[288] Hadi Salman, Jerry Li, Ilya P Razenshteyn, Pengchuan Zhang, Huan Zhang, Sébastien Bubeck, and Greg Yang. Provably robust deep learning via adversarially trained smoothed classifiers. In *Advances in Neural Information Processing Systems*, 2019.

[289] Hadi Salman, Greg Yang, Huan Zhang, Cho-Jui Hsieh, and Pengchuan Zhang. A convex relaxation barrier to tight robust verification of neural networks. In *Advances in Neural Information Processing Systems*, 2019.

[290] C Sanchez. Civil society can help ensure ai benefits us all. here's how. In *World Economic Forum*, 2021. URL https://www.weforum.org/agenda/2021/07/civil-society-help-ai-benefits/.

[291] David Sancho and Vincenzo Ciancaglini. Hype vs. reality: AI in the cybercriminal underground, 2023. URL https://www.trendmicro.com/vinfo/fi/security/news/cybercrime-and-digital-threats/hype-vs-reality-ai-in-the-cybercriminal-underground.

[292] Guido Schryen and Rouven Kadura. Open source vs. closed source software: towards measuring security. In *ACM Symposium on Applied Computing*, pages 2016–2023, 2009.

[293] Christoph Schuhmann, Romain Beaumont, Richard Vencu, Cade Gordon, Ross Wightman, Mehdi Cherti, Theo Coombes, Aarush Katta, Clayton Mullis, Mitchell Wortsman, et al. LAION-5B: An open large-scale dataset for training next generation image-text models. *Advances in Neural Information Processing Systems*, pages 25278–25294, 2022.

[294] John Schulman, Filip Wolski, Prafulla Dhariwal, Alec Radford, and Oleg Klimov. Proximal policy optimization algorithms. *arXiv pre-print arxiv:1707.06347*, 2017.

[295] Roy Schwartz, Jesse Dodge, Noah A. Smith, and Oren Etzioni. Green ai. *arXiv pre-print arxiv:1907.10597*, 2019.

[296] Melanie Sclar, Yejin Choi, Yulia Tsvetkov, and Alane Suhr. Quantifying language models' sensitivity to spurious features in prompt design or: How i learned to start worrying about prompt formatting. *arXiv pre-print arxiv:2310.11324*, 2023.

[297] Elizabeth Seger, Noemi Dreksler, Richard Moulange, Emily Dardaman, Jonas Schuett, K Wei, Christoph Winter, Mackenzie Arnold, Seán Ó hÉigeartaigh, Anton Korinek, et al. Open-sourcing highly capable foundation models: An evaluation of risks, benefits, and alternative methods for pursuing open-source objectives. *arXiv pre-print arxiv:2311.09227*, 2023.

[298] Andrew W Senior, Richard Evans, John Jumper, James Kirkpatrick, Laurent Sifre, Tim Green, Chongli Qin, Augustin Žídek, Alexander WR Nelson, Alex Bridgland, et al. Improved protein structure prediction using potentials from deep learning. *Nature*, pages 706–710, 2020.

[299] Ali Shafahi, Mahyar Najibi, Mohammad Amin Ghiasi, Zheng Xu, John Dickerson, Christoph Studer, Larry S Davis, Gavin Taylor, and Tom Goldstein. Adversarial training for free! *Advances in Neural Information Processing Systems*, 2019.

[300] Rusheb Shah, Soroush Pour, Arush Tagade, Stephen Casper, Javier Rando, et al. Scalable and transferable black-box jailbreaks for language models via persona modulation. *arXiv pre-print arxiv:2311.03348*, 2023.

[301] Matt Sheehan. China's AI Regulations and How They Get Made. URL `https://carnegieendowment.org/2023/07/10/china-s-ai-regulations-and-how-they-get-made-pub-90117`.

[302] Mohammad Shehab, Laith Abualigah, Qusai Shambour, Muhannad A Abu-Hashem, Mohd Khaled Yousef Shambour, Ahmed Izzat Alsalibi, and Amir H Gandomi. Machine learning in medical applications: A review of state-of-the-art methods. *Computers in Biology and Medicine*, page 105458, 2022.

[303] Simin Shekarpaz, Mohammad Azizmalayeri, and Mohammad Hossein Rohban. Piat: Physics informed adversarial training for solving partial differential equations. *arXiv pre-print arxiv:2207.06647*, 2022.

[304] Renee Shelby, Shalaleh Rismani, Kathryn Henne, AJung Moon, Negar Rostamzadeh, Paul Nicholas, N'Mah Yilla, Jess Gallegos, Andrew Smart, Emilio Garcia, and Gurleen Virk. Sociotechnical harms of algorithmic systems: Scoping a taxonomy for harm reduction. *arXiv pre-print arxiv:2210.05791*, 2023.

[305] Xinyue Shen, Zeyuan Chen, Michael Backes, Yun Shen, and Yang Zhang. " do anything now": Characterizing and evaluating in-the-wild jailbreak prompts on large language models. *arXiv pre-print arxiv:2308.03825*, 2023.

[306] Toby Shevlane, Sebastian Farquhar, Ben Garfinkel, Mary Phuong, Jess Whittlestone, Jade Leung, Daniel Kokotajlo, Nahema Marchal, Markus Anderljung, Noam Kolt, et al. Model evaluation for extreme risks. *arXiv pre-print arxiv:2305.15324*, 2023.

[307] Zhouxing Shi, Huan Zhang, Kai-Wei Chang, Minlie Huang, and Cho-Jui Hsieh. Robustness verification for transformers. In *International Conference on Learning Representations*, 2020.

[308] Yeonjong Shin, Jerome Darbon, and George Em Karniadakis. On the convergence of physics informed neural networks for linear second-order elliptic and parabolic type pdes. *arXiv pre-print arxiv:2004.01806*, 2020.

[309] Yash Raj Shrestha, Georg von Krogh, and Stefan Feuerriegel. Building open-source AI. *Nature Computational Science*, 2023.

[310] David Silver, Julian Schrittwieser, Karen Simonyan, Ioannis Antonoglou, Aja Huang, Arthur Guez, Thomas Hubert, Lucas Baker, Matthew Lai, Adrian Bolton, et al. Mastering the game of Go without human knowledge. *Nature*, pages 354–359, 2017.

[311] David Silver, Thomas Hubert, Julian Schrittwieser, Ioannis Antonoglou, Matthew Lai, Arthur Guez, Marc Lanctot, Laurent Sifre, Dharshan Kumaran, Thore Graepel, et al. A general reinforcement learning algorithm that masters chess, shogi, and Go through self-play. *Science*, pages 1140–1144, 2018.

[312] Shaden Smith, Mostofa Patwary, Brandon Norick, Patrick LeGresley, Samyam Rajbhandari, Jared Casper, Zhun Liu, Shrimai Prabhumoye, George Zerveas, Vijay Korthikanti, et al. Using deepspeed and megatron to train megatron-turing nlg 530b, a large-scale generative language model. *arXiv pre-print arxiv:2201.11990*, 2022.

[313] Richard Socher, Alex Perelygin, Jean Wu, Jason Chuang, Christopher D Manning, Andrew Y Ng, and Christopher Potts. Recursive deep models for semantic compositionality over a sentiment treebank. In *Empirical Methods in Natural Language Processing*, pages 1631–1642, 2013.

[314] Irene Solaiman. The Gradient of Generative AI Release: Methods and Considerations. *arXiv pre-print arxiv:2302.04844*, 2023.

[315] Irene Solaiman, Zeerak Talat, William Agnew, Lama Ahmad, Dylan Baker, Su Lin Blodgett, Hal Daumé III, Jesse Dodge, Ellie Evans, Sara Hooker, et al. Evaluating the social impact of generative ai systems in systems and society. *arXiv pre-print arxiv:2306.05949*, 2023.

[316] Aarohi Srivastava, Abhinav Rastogi, Abhishek Rao, Abu Awal Md Shoeb, Abubakar Abid, Adam Fisch, Adam R Brown, Adam Santoro, Aditya Gupta, Adrià Garriga-Alonso, et al. Beyond the imitation game: Quantifying and extrapolating the capabilities of language models. *arXiv pre-print arxiv:2206.04615*, 2022.

[317] Aarohi Srivastava, Abhinav Rastogi, Abhishek Rao, Abu Awal Md Shoeb, Abubakar Abid, Adam Fisch, Adam R. Brown, et al. Beyond the imitation game: Quantifying and extrapolating the capabilities of language models. *arXiv pre-print arxiv:2206.04615*, 2023.

[318] Jacob Steinhardt. Emergent deception and emergent optimization. *Emergent deception and emergent optimization*, 2023.

[319] Emma Strubell, Ananya Ganesh, and Andrew McCallum. Energy and policy considerations for deep learning in NLP. *arXiv pre-print arxiv:1906.02243*, 2019.

[320] Lichao Sun, Yue Huang, Haoran Wang, Siyuan Wu, Qihui Zhang, Chujie Gao, Yixin Huang, Wenhan Lyu, Yixuan Zhang, Xiner Li, et al. Trustllm: Trustworthiness in large language models. *arXiv pre-print arxiv:2401.05561*, 2024.

[321] Luning Sun, Han Gao, Shaowu Pan, and Jian-Xun Wang. Surrogate modeling for fluid flows based on physics-constrained deep learning without simulation data. *Computer Methods in Applied Mechanics and Engineering*, page 112732, 2020.

[322] Christian Szegedy, Wojciech Zaremba, Ilya Sutskever, Joan Bruna, Dumitru Erhan, Ian Goodfellow, and Rob Fergus. Intriguing properties of neural networks. In *International Conference on Learning Representations*, 2014.

[323] Makoto Takamoto, Timothy Praditia, Raphael Leiteritz, Daniel MacKinlay, Francesco Alesiani, Dirk Pflüger, and Mathias Niepert. Pdebench: An extensive benchmark for scientific machine learning. *Advances in Neural Information Processing Systems*, pages 1596–1611, 2022.

[324] Rohan Taori, Ishaan Gulrajani, Tianyi Zhang, Yann Dubois, Xuechen Li, Carlos Guestrin, Percy Liang, and Tatsunori B. Hashimoto. Stanford alpaca: An instruction-following llama model. `https://github.com/tatsu-lab/stanford_alpaca`, 2023.

[325] Gemini Team, Rohan Anil, Sebastian Borgeaud, Yonghui Wu, Jean-Baptiste Alayrac, Jiahui Yu, Radu Soricut, Johan Schalkwyk, Andrew M Dai, Anja Hauth, et al. Gemini: a family of highly capable multimodal models. *arXiv pre-print arxiv:2312.11805*, 2023.

[326] The UK Government. The Bletchley Declaration by Countries Attending the AI Safety Summit, 1-2 November 2023, 2023. URL https://www.gov.uk/government/publications/ai-safety-summit-2023-the-bletchley-declaration/the-bletchley-declaration-by-countries-attending-the-ai-safety-summit-1-2-november-2023.

[327] TII. Falcon. https://falconllm.tii.ae/, 2023.

[328] Vincent Tjeng, Kai Xiao, and Russ Tedrake. Evaluating robustness of neural networks with mixed integer programming. In *International Conference in Learning Representations*, 2019.

[329] Hugo Touvron, Louis Martin, Kevin Stone, Peter Albert, Amjad Almahairi, Yasmine Babaei, Nikolay Bashlykov, Soumya Batra, Prajjwal Bhargava, Shruti Bhosale, et al. Llama 2: Open foundation and fine-tuned chat models. *arXiv pre-print arxiv:2307.09288*, 2023.

[330] Hugo Touvron, Louis Martin, Kevin Stone, Peter Albert, Amjad Almahairi, Yasmine Babaei, Nikolay Bashlykov, Soumya Batra, Prajjwal Bhargava, Shruti Bhosale, et al. Llama 2: Open foundation and fine-tuned chat models. *arXiv pre-print arxiv:2307.09288*, 2023.

[331] Florian Tramèr, Nicolas Papernot, Ian Goodfellow, Dan Boneh, and Patrick McDaniel. The space of transferable adversarial examples. *arXiv pre-print arxiv:1704.03453*, 2017.

[332] Florian Tramèr, Alexey Kurakin, Nicolas Papernot, Ian Goodfellow, Dan Boneh, and Patrick McDaniel. Ensemble adversarial training: Attacks and defenses. In *International Conference on Learning Representations*, 2018.

[333] China Law Translate. Interim Measures for the Management of Generative Artificial Intelligence Services, 2023. URL https://www.chinalawtranslate.com/generative-ai-interim/.

[334] A. Tumadóttir. Supporting Open Source and Open Science in the EU AI Act. https://creativecommons.org/2023/07/26/supporting-open-source-and-open-science-in-the-eu-ai-act/, 2023. Accessed: 2024-01-29.

[335] A. M. Turing. Computing machinery and intelligence. *Mind*, pages 433–460, 1950.

[336] UAE. UAE Strategy for Artificial Intelligence, 2023. https://u.ae/en/about-the-uae/strategies-initiatives-and-awards/strategies-plans-and-visions/government-services-and-digital-transformation/uae-strategy-for-artificial-intelligence.

[337] Jonathan Uesato, Brendan O'Donoghue, Aaron van den Oord, and Pushmeet Kohli. Adversarial risk and the dangers of evaluating against weak attacks. *International Conference in Machine Learning*, 2018.

[338] UK-gov. Safety and security risks of generative artificial intelligence to 2025. 2023.

[339] Roberto Verdecchia, June Sallou, and Luís Cruz. A systematic review of Green AI. *Wiley Interdisciplinary Reviews: Data Mining and Knowledge Discovery*, page e1507, 2023.

[340] Pranshu Verma. They thought loved ones were calling for help. It was an AI scam, 2023. URL https://www.washingtonpost.com/technology/2023/03/05/ai-voice-scam/.

[341] Bertie Vidgen, Hannah Rose Kirk, Rebecca Qian, Nino Scherrer, Anand Kannappan, Scott A Hale, and Paul Röttger. SimpleSafetyTests: a Test Suite for Identifying Critical Safety Risks in Large Language Models. *arXiv pre-print arxiv:2311.08370*, 2023.

[342] Georg Von Krogh and Sebastian Spaeth. The open source software phenomenon: Characteristics that promote research. *The Journal of Strategic Information Systems*, pages 236–253, 2007.

[343] Ben Wang and Aran Komatsuzaki. GPT-J-6B: A 6 billion parameter autoregressive language model. https://github.com/kingoflolz/mesh-transformer-jax, 2021.

[344] Chuwei Wang, Shanda Li, Di He, and Liwei Wang. Is l^2 physics-informed loss always suitable for training physics-informed neural network? *arXiv pre-print arxiv:2206.02016*, 2022.

[345] Shiqi Wang, Yizheng Chen, Ahmed Abdou, and Suman Jana. Mixtrain: Scalable training of verifiably robust neural networks. *arXiv pre-print arxiv:1811.02625*, 2018.

[346] Shiqi Wang, Huan Zhang, Kaidi Xu, Xue Lin, Suman Jana, Cho-Jui Hsieh, and J Zico Kolter. Beta-crown: Efficient bound propagation with per-neuron split constraints for complete and incomplete neural network verification. *arXiv pre-print arxiv:2103.06624*, 2021.

[347] Sifan Wang, Xinling Yu, and Paris Perdikaris. When and why pinns fail to train: A neural tangent kernel perspective. *Journal of Computational Physics*, page 110768, 2022.

[348] Stefan Webb, Tom Rainforth, Yee Whye Teh, and M Pawan Kumar. A statistical approach to assessing neural network robustness. *arXiv pre-print arxiv:1811.07209*, 2018.

[349] Hui Wei, Hao Tang, Xuemei Jia, Zhixiang Wang, Hanxun Yu, Zhubo Li, Shin'ichi Satoh, Luc Van Gool, and Zheng Wang. Physical adversarial attack meets computer vision: A decade survey. *IEEE Transactions on Pattern Analysis and Machine Intelligence*, 2024.

[350] Laura Weidinger, Maribeth Rauh, Nahema Marchal, Arianna Manzini, Lisa Anne Hendricks, Juan Mateos-Garcia, Stevie Bergman, Jackie Kay, Conor Griffin, Ben Bariach, et al. Sociotechnical Safety Evaluation of Generative AI Systems. *arXiv pre-print arxiv:2310.11986*, 2023.

[351] Tsui-Wei Weng, Huan Zhang, Hongge Chen, Zhao Song, Cho-Jui Hsieh, Duane Boning, Inderjit S Dhillon, and Luca Daniel. Towards fast computation of certified robustness for relu networks. In *International Conference on Machine Learning*, 2018.

[352] Tsui-Wei Weng, Huan Zhang, Pin-Yu Chen, Jinfeng Yi, Dong Su, Yupeng Gao, Cho-Jui Hsieh, and Luca Daniel. Evaluating the robustness of neural networks: An extreme value theory approach. *arXiv pre-print arxiv:1801.10578*, 2018.

[353] Yotam Wolf, Noam Wies, Yoav Levine, and Amnon Shashua. Fundamental limitations of alignment in large language models. *arXiv pre-print arxiv:2304.11082*, 2023.

[354] Eric Wong and Zico Kolter. Provable defenses against adversarial examples via the convex outer adversarial polytope. In *International Conference on Machine Learning*, pages 5286–5295, 2018.

[355] Eric Wong, Frank Schmidt, Jan Hendrik Metzen, and J Zico Kolter. Scaling provable adversarial defenses. *Advances in Neural Information Processing Systems*, 2018.

[356] Eric Wong, Leslie Rice, and J Zico Kolter. Fast is better than free: Revisiting adversarial training. *arXiv pre-print arxiv:2001.03994*, 2020.

[357] Cleve R. Wootson. It's time to stop laughing at Nigerian scammers – because they're stealing billions of dollars. *The Washington Post*, 2023.

[358] Carole-Jean Wu, Ramya Raghavendra, Udit Gupta, Bilge Acun, Newsha Ardalani, Kiwan Maeng, Gloria Chang, Fiona Aga, Jinshi Huang, Charles Bai, et al. Sustainable AI: Environmental implications, challenges and opportunities. *Machine Learning and Systems*, pages 795–813, 2022.

[359] Kangxi Wu, Liang Pang, Huawei Shen, Xueqi Cheng, and Tat-Seng Chua. LLMDet: A third party large language models generated text detection tool. In *Findings of the Association for Computational Linguistics: EMNLP 2023*, pages 2113–2133, 2023.

[360] Yonghui Wu. Google's neural machine translation system: Bridging the gap between human and machine translation. *arXiv pre-print arxiv:1609.08144*, 2016.

[361] Weiming Xiang, Hoang-Dung Tran, and Taylor T Johnson. Reachable set computation and safety verification for neural networks with relu activations. *arXiv pre-print arxiv:1712.08163*, 2017.

[362] Frank F. Xu, Uri Alon, Graham Neubig, and Vincent J. Hellendoorn. A systematic evaluation of large language models of code. *arXiv pre-print arxiv:2202.13169*, 2022.

[363] Kaidi Xu, Zhouxing Shi, Huan Zhang, Yihan Wang, Kai-Wei Chang, Minlie Huang, Bhavya Kailkhura, Xue Lin, and Cho-Jui Hsieh. Automatic perturbation analysis for scalable certified robustness and beyond. *Advances in Neural Information Processing Systems*, pages 1129–1141, 2020.

[364] Kaidi Xu, Huan Zhang, Shiqi Wang, Yihan Wang, Suman Jana, Xue Lin, and Cho-Jui Hsieh. Fast and complete: Enabling complete neural network verification with rapid and massively parallel incomplete verifiers. *arXiv pre-print arxiv:2011.13824*, 2020.

[365] Zihao Xu, Yi Liu, Gelei Deng, Yuekang Li, and Stjepan Picek. Llm jailbreak attack versus defense techniques–a comprehensive study. *arXiv pre-print arxiv:2402.13457*, 2024.

[366] Linting Xue, Noah Constant, Adam Roberts, Mihir Kale, Rami Al-Rfou, Aditya Siddhant, Aditya Barua, and Colin Raffel. mt5: A massively multilingual pre-trained text-to-text transformer. *arXiv pre-print arxiv:2010.11934*, 2020.

[367] Chengrun Yang, Xuezhi Wang, Yifeng Lu, Hanxiao Liu, Quoc V Le, Denny Zhou, and Xinyun Chen. Large language models as optimizers. *arXiv pre-print arxiv:2309.03409*, 2023.

[368] Greg Yang, Tony Duan, J Edward Hu, Hadi Salman, Ilya Razenshteyn, and Jerry Li. Randomized smoothing of all shapes and sizes. In *International Conference on Machine Learning*, 2020.

[369] Zheng-Xin Yong, Cristina Menghini, and Stephen H Bach. Low-resource languages jailbreak GPT-4. *arXiv pre-print arxiv:2310.02446*, 2023.

[370] Youliang Yuan, Wenxiang Jiao, Wenxuan Wang, Jen tse Huang, Pinjia He, Shuming Shi, and Zhaopeng Tu. GPT-4 Is Too Smart To Be Safe: Stealthy Chat with LLMs via Cipher. *arXiv pre-print arxiv:2308.06463*, 2023.

[371] Rowan Zellers, Ari Holtzman, Yonatan Bisk, Ali Farhadi, and Yejin Choi. Hellaswag: Can a machine really finish your sentence? *arXiv pre-print arxiv:1905.07830*, 2019.

[372] Runtian Zhai, Chen Dan, Di He, Huan Zhang, Boqing Gong, Pradeep Ravikumar, Cho-Jui Hsieh, and Liwei Wang. Macer: Attack-free and scalable robust training via maximizing certified radius. In *International Conference on Learning Representations*, 2019.

[373] Qiusi Zhan, Richard Fang, Rohan Bindu, Akul Gupta, Tatsunori Hashimoto, and Daniel Kang. Removing rlhf protections in gpt-4 via fine-tuning. *arXiv pre-print arxiv:2311.05553*, 2023.

[374] Dinghuai Zhang, Mao Ye, Chengyue Gong, Zhanxing Zhu, and Qiang Liu. Filling the soap bubbles: Efficient black-box adversarial certification with non-gaussian smoothing, 2019.

[375] Dongkun Zhang, Ling Guo, and George Em Karniadakis. Learning in modal space: Solving time-dependent stochastic pdes using physics-informed neural networks. *SIAM Journal on Scientific Computing*, pages A639–A665, 2020.

[376] Hongyang Zhang, Yaodong Yu, Jiantao Jiao, Eric Xing, Laurent El Ghaoui, and Michael Jordan. Theoretically principled trade-off between robustness and accuracy. In *International Conference on Machine Learning*, pages 7472–7482, 2019.

[377] Huan Zhang, Tsui-Wei Weng, Pin-Yu Chen, Cho-Jui Hsieh, and Luca Daniel. Efficient neural network robustness certification with general activation functions. *Advances in Neural Information Processing Systems*, 2018.

[378] Huan Zhang, Pengchuan Zhang, and Cho-Jui Hsieh. Recurjac: An efficient recursive algorithm for bounding jacobian matrix of neural networks and its applications. In *AAAI Conference on Artificial Intelligence*, pages 5757–5764, 2019.

[379] Huan Zhang, Shiqi Wang, Kaidi Xu, Linyi Li, Bo Li, Suman Jana, Cho-Jui Hsieh, and J Zico Kolter. General cutting planes for bound-propagation-based neural network verification. *Advances in Neural Information Processing Systems*, pages 1656–1670, 2022.

[380] Zhexin Zhang, Jiale Cheng, Hao Sun, Jiawen Deng, Fei Mi, Yasheng Wang, Lifeng Shang, and Minlie Huang. Constructing highly inductive contexts for dialogue safety through controllable reverse generation. *arXiv pre-print arxiv:2212.01810*, 2022.

[381] Hao Zhao, Maksym Andriushchenko, Francesco Croce, and Nicolas Flammarion. Long is more for alignment: A simple but tough-to-beat baseline for instruction fine-tuning. *arXiv pre-print arxiv:2402.04833*, 2024.

[382] Tan Zhi-Xuan, Micah Carroll, Matija Franklin, and Hal Ashton. Beyond preferences in ai alignment. *arXiv pre-print arxiv:2408.16984*, 2024.

[383] Chunting Zhou, Pengfei Liu, Puxin Xu, Srinivasan Iyer, Jiao Sun, Yuning Mao, Xuezhe Ma, Avia Efrat, Ping Yu, Lili Yu, et al. Lima: Less is more for alignment. *Advances in Neural Information Processing Systems*, 2024.

[384] Jiawei Zhou, Yixuan Zhang, Qianni Luo, Andrea G Parker, and Munmun De Choudhury. Synthetic lies: Understanding ai-generated misinformation and evaluating algorithmic and human solutions. In *CHI Conference on Human Factors in Computing Systems*, pages 1–20, 2023.

[385] Kun Zhou, Yutao Zhu, Zhipeng Chen, Wentong Chen, Wayne Xin Zhao, Xu Chen, Yankai Lin, Ji-Rong Wen, and Jiawei Han. Don't make your LLM an evaluation benchmark cheater. *arXiv pre-print arxiv:2311.01964*, 2023.

[386] Andy Zou, Long Phan, Sarah Chen, James Campbell, Phillip Guo, Richard Ren, Alexander Pan, Xuwang Yin, Mantas Mazeika, Ann-Kathrin Dombrowski, et al. Representation engineering: A top-down approach to ai transparency. *arXiv pre-print arxiv:2310.01405*, 2023.

[387] Andy Zou, Zifan Wang, J Zico Kolter, and Matt Fredrikson. Universal and transferable adversarial attacks on aligned language models. *arXiv pre-print arxiv:2307.15043*, 2023.